Assessment of Chromate Effects on the Galvanic-Coupling-Induced Localized Corrosion of AA7050-T7451

A Dissertation

Presented to the Faculty of the School of Engineering and Applied Science

University of Virginia

In Partial Fulfillment
Of the Requirements for the Degree of

Doctor of Philosophy in Materials Science and Engineering

By

Utibe-Eno Charles-Granville

December 12, 2022

APPROVAL SHEET

This

Dissertation

is submitted in partial fulfillment of the requirements
for the degree of

Doctor of Philosophy

Author: Utibe-Eno Charles-Granville

This Dissertation has been read and approved by the examining committee:

Advisor: Dr. John R. Scully

Advisor: Dr. Robert G. Kelly

Committee Member: Dr. Petra Reinke

Committee Member: Dr. James M. Fitz-Gerald

Committee Member: Dr. Bi-Cheng Zhou

Committee Member: Dr. Andres Clarens

Committee Member:

Committee Member:

Accepted for the School of Engineering and Applied Science:

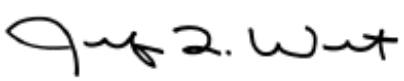

Jennifer L. West, School of Engineering and Applied Science

May 2023

Executive Summary

Dissimilar metal assemblies are frequently encountered in complex structures such as in aerospace applications and pose a major challenge involving galvanic-induced corrosion. One example of such assemblies is that of precipitation-strengthened aluminum alloy (AA) components and stainless steel (SS) fasteners. These precipitation-strengthened AA components are inherently susceptible to localized corrosion due to *micro*-galvanic interactions that develop between the Al matrix and the constituent (or intermetallic) particles that form as a result of the strengthening process. In addition, the strengthening process renders these AAs unsuitable for traditional welding, and as an alternative, they are commonly joined with 316SS fasteners. Although the structures are coated to mitigate galvanic-induced localized corrosion of the AA component, defects in these coating systems are inevitable during the operational and maintenance life cycles of the AA-based structures. In natural corrosive environments, including the thin electrolyte films present under atmospheric conditions, this situation would often create a *macro*-galvanic cell in the vicinity of the fastener joint, including within the confined fastener crevice, between the localized corrosion-susceptible base AA component – the anode in the galvanic cell – and the 316SS fastener – the cathode in the galvanic cell – in which the AA component may be polarized above critical potential thresholds (e.g., pitting and repassivation potentials), resulting in greater localized corrosion than if there was no external 316SS cathode. These aggravated attack sites, particularly the hidden deep fissures within the fastener crevice, can serve as locations for crack initiation with the potential for accelerated crack propagation rates, which would be detrimental to the service and fatigue life of the AA-based structure. This situation has warranted an increasing body of research with regards to the macro-galvanic-induced corrosion of these AAs with the intent to develop an understanding of the physical, electrochemical, and metallurgical factors that govern both the location and mode of corrosion damage in a fastener geometry, including the rationalization of how an inhibitor, such as chromate, can influence these factors. Although extensive work has been carried out on chromate effects on the *micro*-galvanic corrosion behavior of base precipitation-strengthened AAs, information is generally lacking on the impact of chromate on the damage distribution and morphology pertinent to complex geometries such as plate-fastener configuration and how the

unique fastener crevice environments affect the activity of chromate compared to the boldly exposed surface conditions under atmospheric conditions. Although the dangers of chromate have been widely recognized, with a mandate to phase out chromate-based inhibitor systems, a comprehensive understanding of its role in the galvanic-induced corrosion phenomena is crucial for the optimization of testing frameworks and design of environmentally-friendly inhibitor technologies needed to replace toxic chromate-based corrosion mitigation systems. This work aims to improve the mechanistic understanding of the galvanic-induced localized corrosion of AA7050-T7451 coupled to 316SS in simulated atmospheric environments from the perspectives of damage distribution dependence on cathodic activity and inhibitor action on the main cathodic contributors. This understanding is accomplished by means of a combination of experimental and modeling techniques through three main areas: 1) characterization of the baseline cathodic behavior of AA7XXX in an attempt to establish the factors that affect the degree of suppression of cathodic reactions on this class of AAs, 2) assessment of the current capacities of the individual cathodic contributors to drive anodic dissolution of AA7050 in simulated atmospheric environments, 3) correlation of the findings from areas 1 and 2 to those attained on actual AA7050-316SS galvanic couples under various environmental conditions pertinent to atmospheric exposure.

The rotating disk electrode (RDE) technique provided a means to simulate the effects of water layer thickness to differentiate thin film conditions from full immersion conditions, and enabled the study of the mass-transport-limited oxygen reduction reaction (ORR) on AA7XXX alloys as a function of chromate concentration. The ORR current density decreased by up to two orders of magnitude upon addition of 10^{-2} M chromate, however, the degree of inhibition was observed to depend on the Cu content of the alloy. Chromate was reduced irreversibly to form a Cr(III)-rich film on the alloy surface that blocked cathodic sites and hindered the ORR. This film was confirmed by X-ray photoelectron spectroscopic characterization of the chemistry and thickness of the chromate-induced layer formed on the specimens after exposure to chromate. The layer was approximately 13 nm in thickness and consisted of mixed Cr(III)/Cr(VI) oxides with some metallic Cr.

The RDE technique was extended to investigate the impact of chromate on the cathodic behavior of 316SS and high-purity Cu in dilute and elevated chloride environments. The objective was to determine which electrode would be the more significant cathode that would drive galvanic corrosion of AA7050 as a function of environment, and to assess the role of chromate in modifying their cathodic activity to mitigate the attack. In 0.6 M NaCl, the ORR kinetics on 316SS was suppressed by more than two orders of magnitude upon addition of 10^{-4} M chromate, and high-purity Cu produced the largest cathodic currents with and without chromate in solution. In 5 M NaCl, chromate was assessed to be less effective on all the studied cathodes, with high-purity Cu remaining the most significant cathode. Upon introduction of Al ions to 5 M Cl^- in order to simulate pre-corrosion of AA7050 leading to the release of Al^{3+} into a concentrated chloride environment, cathodic reactions were accelerated on the electrodes regardless of the presence of chromate. In this situation, 316SS became the dominant cathode compared to high-purity Cu.

The efficacy of chromate in protecting AA7050 coupled to 316SS in simulated external and fastener crevice environments was investigated utilizing a number of electrochemical and surface characterization techniques. The influence of pH and Al ions on the galvanic coupling behavior and damage evolution on AA7050 as a function of chromate concentration were assessed. The degree of chromate inhibition was observed to decrease as pH decreased, owing to chromate speciation and reduced capacity to suppress the hydrogen evolution reaction (HER) compared to the ORR. The addition of Al ions significantly increased HER kinetics and produced a large buffer effect which overwhelmed the ability of chromate to slow damage propagation on AA7050. Assessment of cathodes indicated that Cu was more important than 316SS in driving damage initiation, but less active than 316SS in supporting high-rate damage propagation in simulated crevice environments.

An existing steady-state finite element method (FEM) modeling framework based on the Laplace equation was adapted to predict the macro-galvanic current distributions on an AA7050-316SS couple, in environments representative of the boldly exposed surface of an actual fastener couple. Boundary conditions had to be modified from that of the bulk experimental environment in order to achieve better agreement between the total currents calculated with the model and

those measured experimentally with the scanning vibrating electrode technique (SVET) at a certain height above the electrode surface. Once validated, the model was used to predict the current densities at the electrode/electrolyte interface and better interpret the results obtained with SVET, even though it was incapable of capturing localized events that occurred experimentally such as pitting and precipitation of corrosion products.

Lastly, the galvanic current interactions on an AA7050-316SS couple in chromate-containing NaCl environments under thick films and conditions of wet-dry cycling were investigated utilizing the coupled micro-electrode array (CMEA) approach. The CMEA approach provided a means to analyze the in-situ electrochemical kinetics as a function of spatial location and time. In Inhibitor-free environments, the total net anodic charge increased with increasing conductivity and aggressiveness of the environment, with AA7050 electrodes supplying greater than 50% of the total net cathodic charge in the more aggressive environments. Under thick films, chromate was less effective at suppressing cathodic kinetics on the 316SS and AA7050 net cathodes as chloride concentration increased. Under wet-dry cycling conditions, the effectiveness of chromate was diminished when compared to thick film conditions, due to the alternation in equilibrium chloride concentration as electrolyte thickness changed upon onset of drying and wetting. Furthermore, chromate exhibited a diminished ability to suppress cathodic currents on the AA7050 net cathodes in comparison to the 316SS electrodes.

This dissertation provided clarifications and further insights into the mechanistic understanding of the galvanic-coupling-induced corrosion phenomena as regards precipitation-strengthened AAs, including the shortcomings of chromate as regards protection of these AAs when exposed to conditions pertinent to aerospace service environments. This work highlighted the importance of Cu-rich intermetallic particles and replated Cu when considering the driving force of cathodes in sustaining anodic dissolution in typical AA macro-galvanic systems exposed to atmospheric conditions. From the technological perspective, it is intended that the knowledge acquired through this work will aid inform the principal attributes that should be exploited in the testing and development of potential chromate-free inhibitor alternatives.

Acknowledgements

I would like to thank my advisors, Dr. John Scully and Dr. Rob Kelly for taking a chance on me and giving me an opportunity to pursue my PhD program. I came into the program with barely any fundamental knowledge of core materials science. At the time, the term 'crystal' meant something like a gemstone – like an emerald or a ruby. Now I know better. Crystal = Lattice + Basis! This dissertation would not be possible without their mentorship and immense support. Thank you for all the life lessons you taught me… and for the free group lunches too!

I would also like to thank my dissertation committee members, Dr. Petra Reinke, Dr. James Fitz-Gerald, Dr. Bi-Cheng Zhou, and Dr. Andres Clarens for their time and invaluable input into my research. Not forgetting the wonderful members of CESE who were always so kind and supportive, always happy to assist me whenever I ran into challenging situations. It was very rewarding to learn and grow together as young researchers. Special thanks to the kindhearted MSE staff, Kimberly Fitzhugh, Kari Werres, Jeannie Reese, Tonya Reynolds, Sherri Sullivan, Peggy Gibson, Bryana Amador, Eric Newsome, Richard White (thank heavens I graduated without breaking the SEM!), Joe Thompson, Tanner Fitzgerald, and Ig Jakovac, who in one way or the other made a positive impact on my student life. Thank you to Ms. Cathy Dukes for teaching me how to deal with the XPS!

I am also thankful for the unwavering support of my family. I am especially thankful to my young son, Sobomate, who exercised so much patience dealing with an 'absent' mom for five long years.

Financial support provided by the Office of Naval Research, managed by W. Nickerson and A. Rahman under grant N00014-14-1-0012 is most gratefully acknowledged.

Bibliography

The publications that resulted/will result from this dissertation are listed below:

- U.-E. Charles-Granville, C. Liu, J. R. Scully, R. G. Kelly, "An RDE Approach to Investigate the Influence of Chromate on the Cathodic Kinetics on 7XXX Series Al Alloys under Simulated Thin Film Electrolytes", *J. Electrochem. Soc.*, **167**, 111507 (2020).
- U.-E. Charles-Granville, C. F. Glover, J. R. Scully, R. G. Kelly, "Effect of pH and Al Cations on Chromate Inhibition of Galvanic-Induced Corrosion of AA7050-T7451 Macro-Coupled to 316SS", *J. Electrochem. Soc.*, **168**, 121509 (2021).
- U.-E. Charles-Granville*, R. S. Marshall*, C. V. Moraes*, C. F. Glover, J. R. Scully, R. G. Kelly, "Application of Finite Element Modeling to Macro-Galvanic Coupling of AA7050 and SS316: Validation Using the Scanning Vibrating Electrode Technique", *J. Electrochem. Soc.*, **169**, 031502 (2022). * Equal contribution
- U.-E. Charles-Granville, J. R. Scully, R. G. Kelly, "Impact of Chromate on the Current Capacities of Cathodes Pertinent to AA7050-316SS Galvanic Couples in Simulated Atmospheric Environments", TBD (2023)
- U.-E. Charles-Granville, J. R. Scully, R. G. Kelly, "Galvanic Couple Behavior Between AA7050-T7451 and 316SS in Chromate-Containing NaCl Solutions Assessed with a Coupled Micro-Electrode Array Under Thick Film and Cyclic Wet-Dry Conditions", TBD (2023)

Table of Contents

List of Figures

List of Tables

List of Abbreviations and Symbols

AA	Aluminum Alloy
IMP	Intermetallic Particle
ORR	Oxygen Reduction Reaction
HER	Hydrogen Evolution Reaction
SS	Stainless Steel
RH	Relative Humidity
RDE	Rotating Disk Electrode
OCP	Open Circuit Potential
WL	Water Layer Thickness
XPS	X-ray Photoelectron Spectroscopy
SVET	Scanning Vibrating Electrode Technique
ZRA	Zero Resistance Ammeter
FEM	Finite Element Modeling
CMEA	Coupled Micro-Electrode Array
PTFE	Polytetrafluoroethylene
SCE	Saturated Calomel Electrode
SEM	Scanning Electron Microscope
EDS	Energy Dispersive Spectroscopy
BSE	Backscattered Electron
OM	Optical Microscope
EIS	Electrochemical Impedance Spectroscopy
UPD	Underpotential Deposition
PDS	Potentiodynamic Scan
MPT	Mixed Potential Theory
d	Film Thickness
Q	Charge
W	Molecular Weight

A	Area of Electrode
F	Faraday's Constant
n	Number of electrons transferred in a reaction
ρ	Density
i_{lim}	Limiting Current Density
D	Diffusion Coefficient
C	Concentration
δ	Boundary Layer Thickness
δ_{nc}	Natural Convection Boundary Layer Thickness
ω	Electrode Rotation Rate
ν	Kinematic Viscosity
a	Atomic Weight
f	Mass Fraction
Δm	Mass Loss
V_{pp}	Peak-to-Peak Voltage
j_z	SVET Current Density
A_{pp}	Peak-to-Peak Amplitude of Vibration of the SVET Probe
J	SVET Area-averaged Current Density
κ	Solution Conductivity
E_{couple}	Galvanic Couple Potential
i_{couple}	Galvanic Couple Current Density
b	Tafel Slope
E_{eq}	Equilibrium Potential
φ	Electrolyte Potential
i_0	Pseudo-exchange Current Density
i_{ct}	Charge Transfer Current Density
E_0	Reversible Potential

1. Introduction

1.1 Motivation and Overview of Dissertation Problem

The growing desire for higher payloads and fuel efficiency in the aerospace industry have made high-strength Al alloys the preferred materials for constructing light-weight aerospace vehicles. In order to achieve the high strength required in aerospace components whilst optimally balancing other material properties of interest, certain alloying elements such as Zn, Mg, and Cu have to be added to Al, and the resulting alloy subsequently precipitation-strengthened to the desired temper to produce fine strengthening precipitates.[1,3] Unfortunately, the strengthening process also yields constituent particles that adversely affect the corrosion and fracture properties of these Al alloys.[3] In natural corrosive environments, including the thin electrolyte layers present under atmospheric exposure, micro-galvanic interactions develop between the Al matrix and the constituent particles leading to localized corrosion; the constituent particles can be anodic or cathodic to the Al matrix depending on their electrochemical characteristics relative to the Al matrix.[3,4]

Despite their superior properties, these precipitation-strengthened Al alloys pose a huge challenge in weldability. The use of traditional welding techniques to join them often leaves undesirable weld joints with deteriorated properties due to weld porosity and weld cracking during solidification.[5] As an alternative, high-strength, noble fasteners such as stainless steels (SS) are often used in joining the Al alloy parts in aerospace structures. Under corrosive conditions, in addition to the micro-galvanic interactions with the constituent particles described previously, the damage on the Al alloy is exacerbated in the vicinity of the fastener joint, including within the fastener hole, due to the macro-galvanic interactions with the more noble fastener.[6–10] The damage on the Al-based component, particularly hidden corrosion fissures within the fastener hole, coupled with the inherent high stresses imposed by the joint, can transition into fatigue cracks which would negatively impact the lifespan of the Al-based structure.[11] A 2009 US Air Force airframe teardown analysis report highlighted that such corrosion-accelerated fatigue cracks accounted for ~ 80% of all fatigue failures.[12] This report has prompted a body of research

into understanding why this situation was occurring despite the presence of protective coating systems.

From a corrosion control perspective, protective chromate-based barrier coating systems have historically been used to maximize the in-service life of Al-based structures. These cost-effective and high-performance coating systems are typically multifaceted, consisting of a chromate conversion coating underlying a chromate-pigmented primer and an ultraviolet-resistant organic barrier top coat.[13,14] Nevertheless, these coatings may become compromised owing to different factors ranging from poor surface preparation or mechanical impact to the nature of the operating environment, ultimately exposing the bare Al-based substrate to corrosive conditions, as depicted in Figure 1.1.

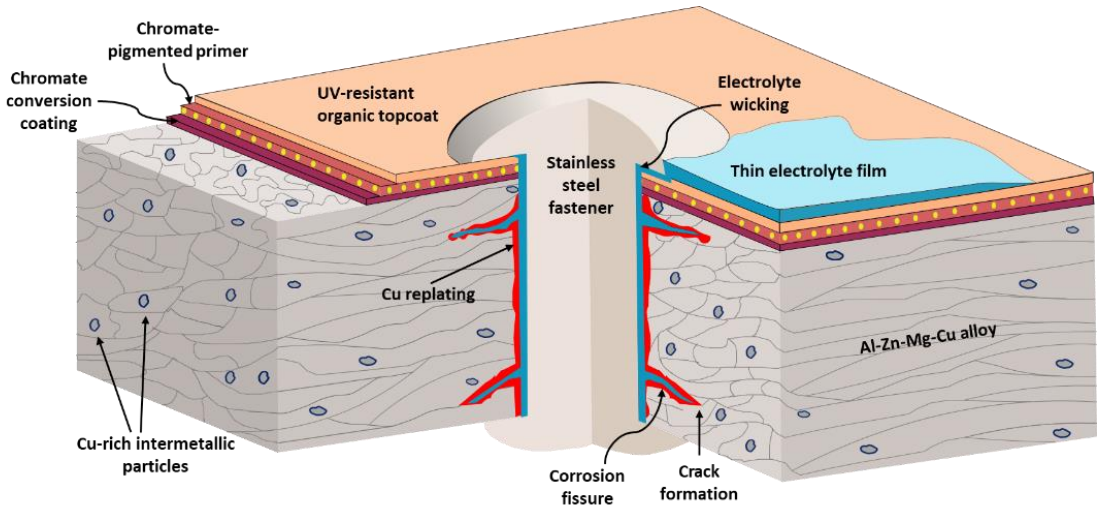

Figure 1.1. Schematic of AA plate-SS fastener configuration with compromised coating allowing ingress of electrolyte into the fastener hole.

One important role of the conversion coating and/or the primer is to facilitate the release of soluble chromate to the damaged area(s) of the coating in order to mitigate dissolution of the exposed substrate.[15–17] Although extensive work has been carried out on chromate effects on the corrosion behavior of precipitation-strengthened Al alloys,[18–36] information is generally lacking on the impact of chromate on the damage distribution and morphology pertinent to complex

geometries such as plate-fastener configuration and how the unique fastener crevice environments affect the activity of chromate compared to surface conditions.

The overall objective of this work therefore was to elucidate the effects of chromate and possible inhibition mechanism(s) as it pertains to the corrosion behavior of aerospace Al-based structures with micro- and macro-galvanic couples through combined experimental and modeling techniques.

1.2 Background

1.2.1 Microstructure-Electrochemical Behavior Correlations for Precipitation-Strengthened Al Alloys

Precipitation-strengthened Al alloys commonly used in aerospace applications consist of AA2XXX and AA7XXX alloys. Although the AA2XXX alloys such as AA2024-T3 have been most widely used due to their superior damage tolerance, e.g., in aircraft fuselage structures,[1] their strength is inferior compared to AA7XXX alloys which exhibit a higher mechanical strength-to-weight ratio with a good balance of fracture toughness and stress corrosion cracking (SCC) resistance.[2] As aircraft manufacturers are exploring several avenues to minimize the number of parts in new aircraft, it is advantageous to work with larger and thicker plates with equivalent or better physical and mechanical properties than thin plates.[1] In this context, AA7050 which retains its high strength, fracture and fatigue properties in thicker sections, is more attractive than AA2024 in many applications. The superior properties of the AA7XXX alloys have warranted increased research into their electrochemical behaviors and corrosion inhibition strategies.

AA7050 (Al-6.7wt%Zn-2.6wt%Cu-2.6wt%Mg) contains three main types of secondary phase particles: strengthening precipitates - $MgZn_2$ (η-phase, 4-10 nm), dispersoids to control recrystallization (e.g., Al_3Zr, 20-50 nm), and coarse (5-30 μm) constituent/intermetallic particles (IMP) - Al_2CuMg (S-phase), Al_7Cu_2Fe (β-phase), and Mg_2Si.[37] Tempering has a significant effect on the microstructure of Al alloys.[38] The T7451 temper is an overaging treatment to allow coarser, discontinuous grain boundary precipitation as well as the incorporation of Cu in the grain boundary η-phase (Figure 1.2) to decrease the potential difference between the η-phase and the matrix.[39–41] The result is an improved fracture toughness, intergranular corrosion (IGC) and stress

corrosion cracking (SCC) resistance along the grain boundaries, compared to the T6 (peak-aged) temper, albeit at lower strength.[40,42,43]

Localized corrosion is the common corrosion mechanism in Al-Zn-Cu-Mg alloys due to their heterogeneous microstructure. The heterogeneous nature of their microstructure results in the formation of micro-galvanic couples between the various phases which leads to enhanced anodic and cathodic reactions. These enhanced reactions ultimately increase the susceptibility of these alloys to localized corrosion damage primarily in the form of pitting corrosion.[44] Other relevant forms of localized corrosion of these alloys in chloride-containing environments include crevice corrosion, filiform corrosion, IGC and exfoliation corrosion.[3] Table 1.1 shows a summary of the electrochemical characteristics of the secondary phase particles in AA7050 compared to that of the base alloy in quiescent 0.6 M NaCl.

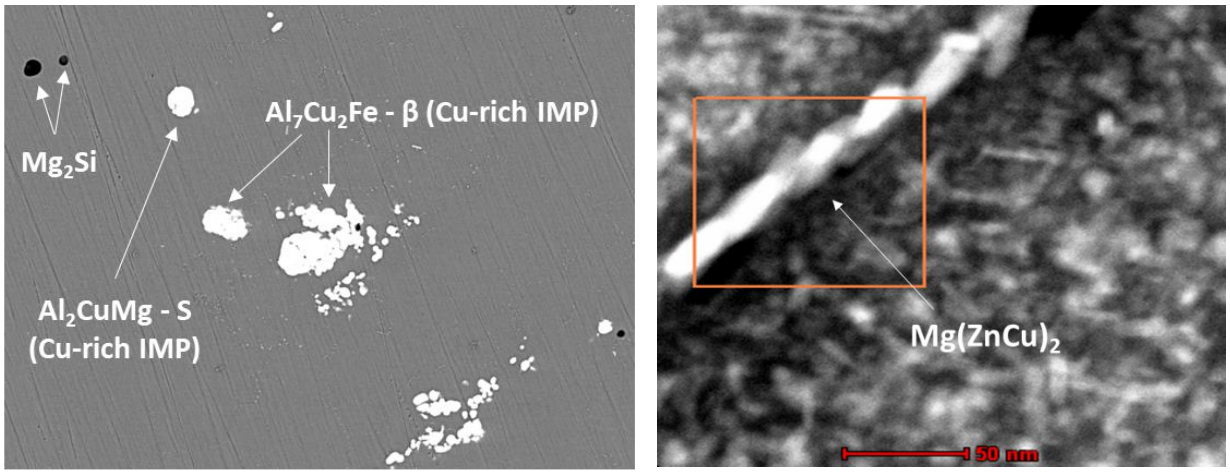

Figure 1.2. (a) SEM image of a polished AA7050-T7451 surface showing the IMPs;[45] (b) corresponding TEM image showing the grain boundary precipitate. TEM image after Rafla (2018).

Reports in literature have demonstrated that the Cu-rich IMPs (i.e., Al_2CuMg and Al_7Cu_2Fe) are the major facilitators of localized corrosion of high-strength Al alloys in chloride-containing environments.[4,9,44-46] In the context of cathodic activity, these Cu-rich IMPs catalyze the fast oxygen reduction reaction (ORR) rates required to sustain anodic dissolution of the peripheral Al-rich matrix and/or preferential dealloying of active elemental constituent(s) of the Cu-rich IMPs.[4,46–48] Figure 1.3 displays a schematic of the dealloying process of Al_2CuMg. When coupled to the Al matrix, the Mg and Al components of the particle will selectively dissolve, leaving behind a porous Cu particle which can mechanically detach, dissolve in solution, and then replate on the Al-rich surface. The replated Cu provides additional cathodic sites to support secondary pitting of the Al matrix.

Table 1.1. Electrochemical characteristics of second phase particles in AA7050 on exposure to 0.6 M NaCl solution[4]

Type of Phase	Phase	Corrosion Potential (V_{SCE})	Electrochemical effect relative to AA7050 matrix
Strengthening precipitate	$MgZn_2$ (η)	-1.1	Active particle. Anodic to matrix. Self dissolves
Dispersoid	Al_3Zr	-0.8	Noble particle but electrochemically inert
Intermetallic particle	Al_2CuMg (S)	-1.06	Initially active particle. Anodic to matrix. Al and Mg dissolve leaving porous Cu particle which becomes cathodic to matrix
	Al_7Cu_2Fe (β)	-0.65	Noble particle. Cathodic to matrix
	Mg_2Si	-1.5	Active particle. Anodic to matrix. Self dissolves
AA7050-T7451 bulk	-	-0.81	-

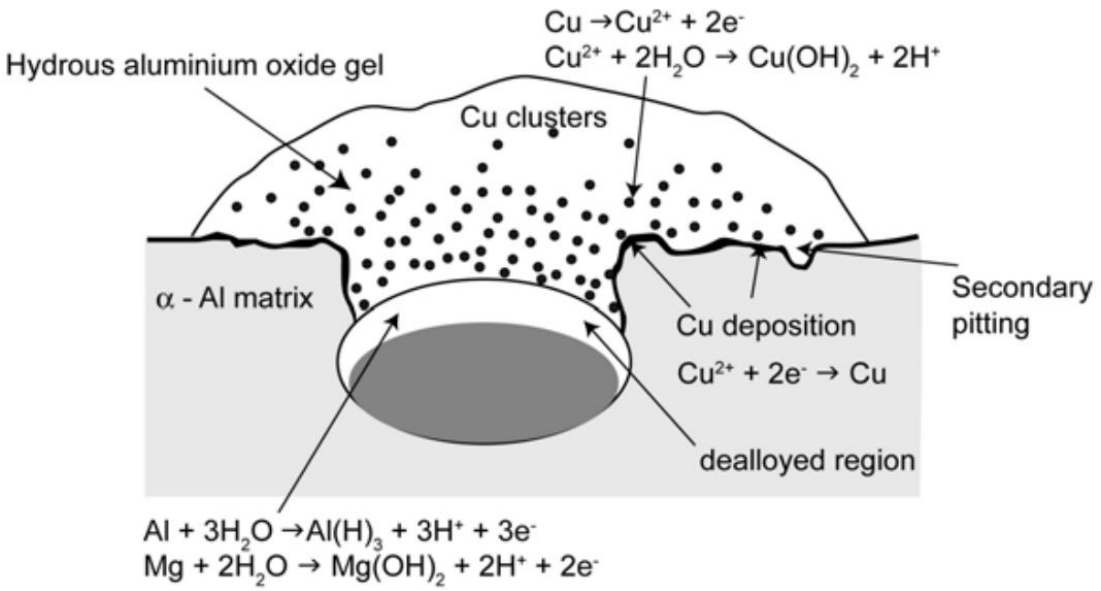

Figure 1.3. Schematic of the dealloying process of Al_2CuMg (S-phase) within an AA matrix.[49]

1.2.2 Micro- and Macro-Galvanic-Induced Corrosion of Precipitation-Strengthened Al Alloys under Atmospheric Conditions

Galvanic corrosion is induced when two dissimilar metals are in electrical contact (or coupled) in a corrosive electrolyte. In this situation, the rate of corrosion of the less noble metal, generally termed the anode, is increased compared to the case where it was uncoupled and freely corroding. On the other hand, the more noble metal, generally termed the cathode, corrodes slower (or not at all) than it would if it were free corroding. Thermodynamically, the driving force for galvanic corrosion increases with increasing electrochemical potential difference between the coupling metals.

As mentioned previously, aerospace Al-Zn-Cu-Mg alloys are often joined using high-strength noble bare metal fasteners, notably 316SS. The structure is then coated for protection against the aggressive environment. However, damage to the coating within the vicinity of the fastener joint aids wicking of the aggressive electrolyte into tight crevices typical of this joint location as illustrated in the schematic in Figure 1.1. This situation leads to severe local environment both outside and inside the fastener hole where a macro-galvanic cell can be established between the Al alloy (AA) component (anode) and the 316SS fastener (cathode),

triggering an enhanced corrosion damage of the AA component. The 316SS fastener is speculated to also increase the driving force for Cu replating, and the replated Cu in turn sustains fast cathodic reaction kinetics.[9]

The fastener geometry described above presents a crevice environment where dissolved oxygen is plentiful at the external surface and depleted deep inside the crevice. As a result, the ORR cannot be sustained inside the crevice. This situation creates a highly corrosive environment inside the crevice because of metal dissolution without a cathodic reaction locally balancing the anodic reaction, leading to metal ion hydrolysis, acidification, and migration of aggressive anion species (e.g., Cl^-) to maintain electroneutrality.[50] In the case of AA-SS galvanic couples, the presence of the wetted external SS cathode renders the situation more dire, as the SS provides large cathodic currents from the ORR and the hydrogen evolution reaction (HER) occurring at the surface and inside the crevice, respectively, to sustain high rates of anodic Al dissolution inside the crevice. Any replated Cu (due to the release of Cu ions from Cu-rich IMPs) inside the crevice would aggravate the situation. The resulting corrosion fissures can serve as crack initiation sites which may propagate in fatigue-prone operating environments.

Atmospheric conditions complicate galvanic-induced corrosion of AA-SS couples. Changes in electrolyte layer thickness resulting from the dynamic nature of environmental conditions, e.g., temperature, relative humidity (RH), presence of hygroscopic salts and pollutants, can remarkably impact corrosion kinetics.[51] Electrolyte layer thickness can affect the mass transport of dissolved oxygen, concentration of soluble species (i.e., salts, metal ions, and corrosion products), and solvation of dissolved metal ions. Tomashov presented a model to elucidate the dependence of metal corrosion rate on electrolyte layer thickness.[52] In this model, adapted in Figure 1.4, the rate of corrosion is at a minimum in the dry region because there is not enough adsorbed water molecules to form a continuous water layer, and corrosion proceeds via dry chemical oxidation. In region II, increasing RH increases the electrolyte layer thickness on the metal surface, and there is a gradual increase in corrosion rate up to a maximum as the corrosion process transitions from purely oxidation in dry air to a mechanism where rapid oxygen transport through the relatively thin electrolyte layer plays a dominant role. In region III, the corrosion rate gradually declines with further increases in electrolyte thickness due to decreasing rate of oxygen

transport through the thicker layer. In region IV, a constant diffusion boundary layer is established due to natural convection such that further increasing electrolyte thickness has no effect on corrosion rate, and the corrosion rate plateaus. In this situation, the metal is described to be under full immersion.[52]

In this dissertation work, experimental methods are used to study the effect of atmospheric conditions on electrochemical kinetics on simulated AA7050-316SS couple. One method is based on the rotating disk electrode (RDE) technique to simulate thin electrolyte layers, and the other involves the use of an environmental chamber to simulate wet-dry cycle conditions, in relation to full immersion conditions.

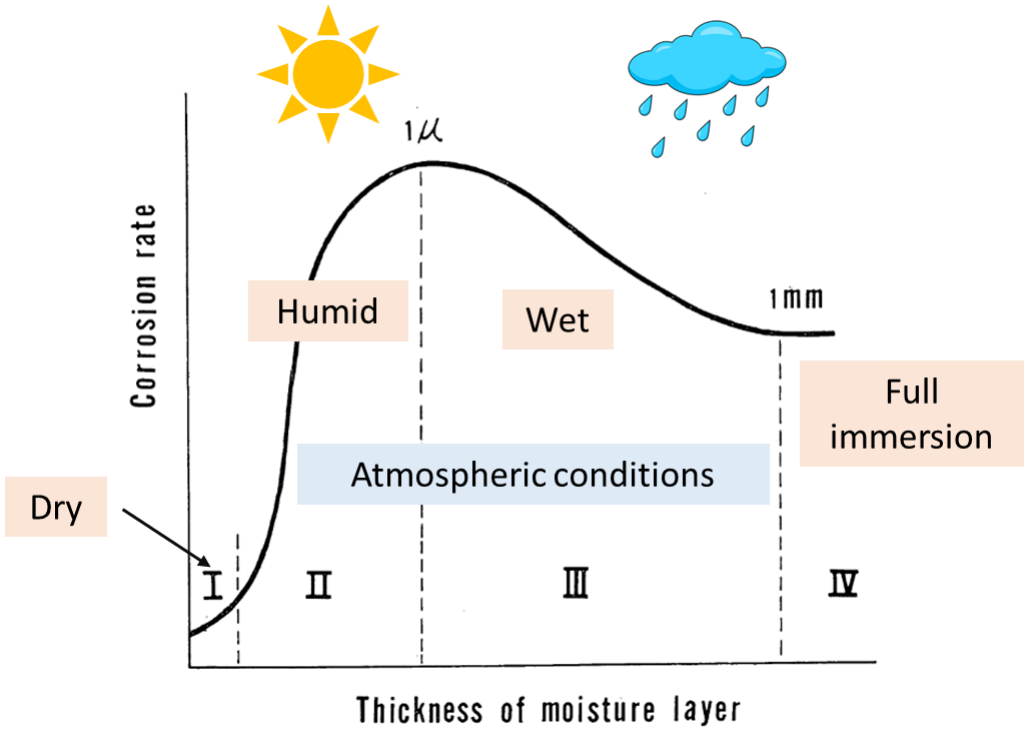

Figure 1.4. Metal corrosion rate as a function of electrolyte layer thickness. (I) Region of dry atmospheric corrosion (WL < 10 nm); (II) region of humid atmospheric corrosion (10 nm < WL < 1 µm); (III) region of wet atmospheric corrosion (1 µm < WL < 1 mm); (IV) region of complete immersion (WL > 1 mm).[52]

1.2.3 Corrosion Mitigation of Precipitation-Strengthened Al Alloys

Conventionally, chromate-based coating systems have been used to protect precipitation-strengthened AAs from corrosion. The inhibitive power of chromate species lies in their ability to be reduced from their soluble and oxidizing Cr(VI) state to an insoluble and irreversible Cr(III) product that effectively protects the underlying corroding metal substrate from the aggressive environment (Figure 1.5). This universal mechanism has been shown to inhibit both anodic and cathodic reactions on Al alloys in many environments.[15,17,30,33,34,53] Clark et al.[53] observed an increase in the pitting potential of AA2024-T3 on addition of 5mM dichromate to 0.1 M NaCl. Similar observation was made by Ilevbare et al.[30] where the pitting potential of AA2024-T3 was raised on addition of 10 mM chromate to 0.1 M Na_2SO_4 + 0.005 M NaCl. The elevation in pitting potential was indicative of anodic inhibition and was attributed to the suppression of metastable pitting and repassivation of small, stable pits. From the cathodic inhibition perspective, chromates are known to effectively suppress ORR kinetics at concentrations much lower than the threshold concentrations observed to significantly raise pitting potentials on AAs.[17] ORR kinetics were reduced by up to one order of magnitude on AA2024-T3 in oxygen-sparged 1 M NaCl upon introduction of 0.01 mM dichromate to solution as reported by Sehgal et al.[33] This concentration of dichromate had no effect on anodic or pit kinetics. Although suppression of pitting susceptibility via increases in pitting potential can be important, actual aerospace structures are at their open circuit potential (OCP) when in service. Under open circuit conditions, the determination of the degree of pitting can be controlled by either the anodic or cathodic behavior of the material, i.e., sufficient suppression of cathodic reactions can drive the OCP well below the pitting potential measured in polarization experiments. The implication of predominant cathodic inhibition is that for electrochemical processes under cathodic control, barring other governing factors, a very low concentration of chromate could dramatically reduce the cathodic current available to drive anodic dissolution. It would be valuable to assess if this apparent impressive cathodic inhibitive power of chromate extends to AA-SS couples under various environmental conditions.

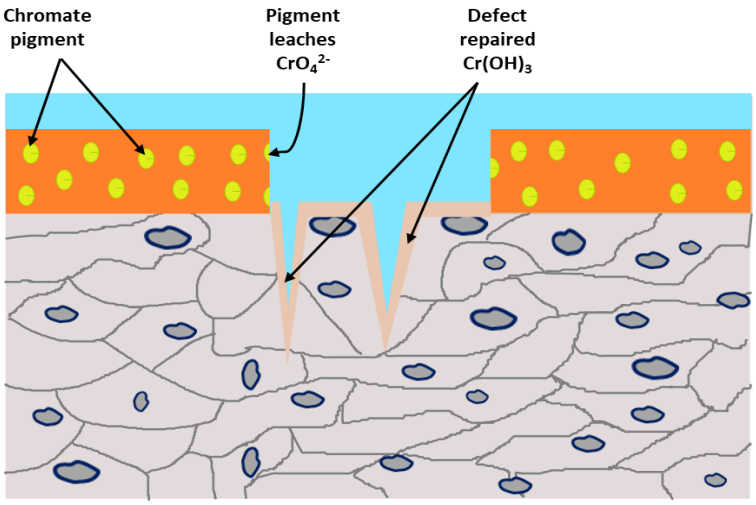

Figure 1.5. Universal mechanism of chromate inhibition. Chromate leaches from coating into the electrolyte and is reduced to insoluble and electronically non-conductive Cr(III) oxide/hydroxide on the exposed alloy surface.

Despite their superior inhibitive capability and cost efficiency, chromate species are known to be toxic and carcinogenic; thus, Cr(VI)-based inhibitor technologies are mandated to be phased out in favor of greener inhibitor alternatives. This situation has motivated ongoing extensive research into a wide variety of potential alternatives including metal-based coating systems such as Mg, [54–59] as well as ionic-based systems such as Ce[60–63] and molybdates.[61,64,65]

Several studies have shown that Mg-rich primers provide sacrificial anode-based cathodic protection to AAs.[54–59] The mechanism involves the Mg pigment being galvanically coupled to the AA so that the Mg pigment (anode) preferentially dissolves or corrodes while the AA (cathode) is cathodically polarized to potentials more negative than its pitting potentials and remains protected. In addition, precipitated Mg corrosion products, e.g., MgO, $Mg(OH)_2$ and $MgCO_3$ can provide some degree of secondary barrier protection to the AA. That said, there is a major drawback with Mg-rich primers. Because Mg is a highly reactive element, it is susceptible to remote self-corrosion (without coupling to the AA), which would result to a premature pigment depletion in the primer.[55,56]

Ce-based compounds have shown some promise as cathodic inhibitors for precipitation-strengthened AAs. A recent study on different IMPs in AA2024-T3 by Kosari et al.[63] provided insights into the nano-galvanic coupling process within corroding IMPs that induces local alkaline conditions that encourage local cerium oxide/hydroxide precipitation. However, unlike chromate, Ce-based inhibitors are unable to mitigate dealloying of Cu-rich IMPs in the first place. Cerium oxide/hydroxide precipitation occurs only after dealloying of the Cu-rich IMP - particularly the S-phase - has occurred to produce Cu aggregates or replated Cu. Furthermore, the precipitated Ce-rich layer was shown to be porous, with the potential for continuous dealloying and trenching corrosion underneath the Ce-rich layer after long exposure times.

Molybdates are weaker oxidants than chromates,[66] but have been shown to inhibit both anodic and cathodic reactions via the formation of a passivating hydroxide layer on the metal surface.[61,65] However, higher molybdate concentrations compared to chromate may be required to adequately suppress anodic and cathodic reactions on AAs.[65,67] Madden et al.[64] compared the performance of chromate and molybdate ions in repassivating defects on AA2024-T351 and AA7075-T6. They observed that chromate concentrations as low as 5 mM were adequate to suppress scratch current densities as well as total charge after depassivation. On the other hand, molybdate showed no inhibition of scratch current densities, even at higher concentrations.

Although extensive research into potential chromate replacements have been underway for the last three decades, only minor advances have been made with regards to finding a sustainable alternative that meets the versatility and cost effectiveness of chromates. For this reason, the aerospace industry is still heavily reliant on chromates, and research is still ongoing to explore the limits of chromate protection particularly in relation to the galvanic corrosion behavior of complex structures complicated with micro- and macro-galvanic couples. A comprehensive understanding of chromate inhibition mechanism(s) with regards to the galvanic corrosion phenomena is considered essential for the optimization of testing frameworks to aid in the engineering of future corrosion mitigation strategies.

1.3 Critical Unresolved Issues

In light of chromate effects on the corrosion behavior of high-strength aerospace Al alloys, most of the investigations have focused on AA2XXX, particularly AA2024-T3 due to its wide use, and only a few recent studies have focused on the effects of chromate on AA7XXX alloys. The growing interest in AA7XXX alloys has warranted increased research into their unique base electrochemical behaviors and corrosion control strategies. AA7XXX alloys generally contain less Cu than AA2XXX. In addition, they contain Zn as the primary alloying element as opposed to Cu in AA2XXX. It is plausible that these compositional differences may influence their microstructure and electrochemical behaviors, in comparison to AA2XXX.

Most studies involving chromate on AA7XXX alloys have been limited to the anodic behavior and conducted under quiescent conditions. Because chromates have been assessed to be potent cathodic inhibitors on AA2XXX, it is important to characterize this effect on AA7XXX as well as on 316SS and (replated) Cu. In addition, quiescent (or full immersion) conditions are not representative of real-life atmospheric exposure. Under atmospheric conditions, fluctuating water layer thickness (WL) stemming from wet-dry cycling impacts electrolyte chemistry and the mass transport of dissolved species in solution. It is probable that the behavior of chromate may change with the aggressive conditions that prevail under thin electrolyte films.

Macro-galvanic coupling has been observed to be deleterious to chromate inhibition of Al-Zn-Cu-Mg alloys.[7,8,28,68] However, there is inadequate information on chromate effects on the electrochemical and geometric variables that control galvanic interactions in AA-SS couples in atmospheric environments. Investigations into the effects of the individual actors could provide further insights into why chromate appears to be less effective in mitigating macro-galvanic corrosion.

Experimental studies of localized corrosion in complex geometries can be time-consuming and, in some cases, not even feasible. Computational models, once validated with experimental data, can offer the powerful advantage of designing and optimizing test matrices, as well as understanding corrosion processes, in a cost-effective and timely fashion. The results

can be applied to full scale structures to predict lifespan and guide maintenance and repair strategies. In light of AA-SS galvanic interactions, recent studies in the literature have proposed a validated modeling framework to predict the damage on the surface and within the fastener hole of AA7XXX-316SS fastener assembly.[10,69] However, these studies did not consider the influence of replated Cu and the effect of chromate in solution.

1.4 Overarching Dissertation Question

By what mechanisms does chromate influence the different factors – electrochemical, microstructural and geometric – that govern galvanic corrosion-induced damage on AA7050-T7451 coupled to 316SS in a plate-fastener configuration under conditions representative of atmospheric exposure?

1.5 Objectives of Research

As schematically summarized in Figure 1.6, the overall objectives of this work are to (1) quantitatively assess the influence of chromate on the thin-film cathodic behavior of base AA7XXX alloys in simulated atmospheric environments and determine what external (environmental) and internal (microstructural) factors affect the degree of ORR suppression, (2) explore various laboratory methods to elucidate the impact of chromate on the micro- and macro-cathode current contributions pertinent to a typical AA7050-316SS galvanic couple under various environmental conditions, (3) leverage the findings in (1) and (2) to adapt an existing modeling framework to predict electrochemical distributions across AA7050-316SS couple surface under conditions that are experimentally difficult to investigate.

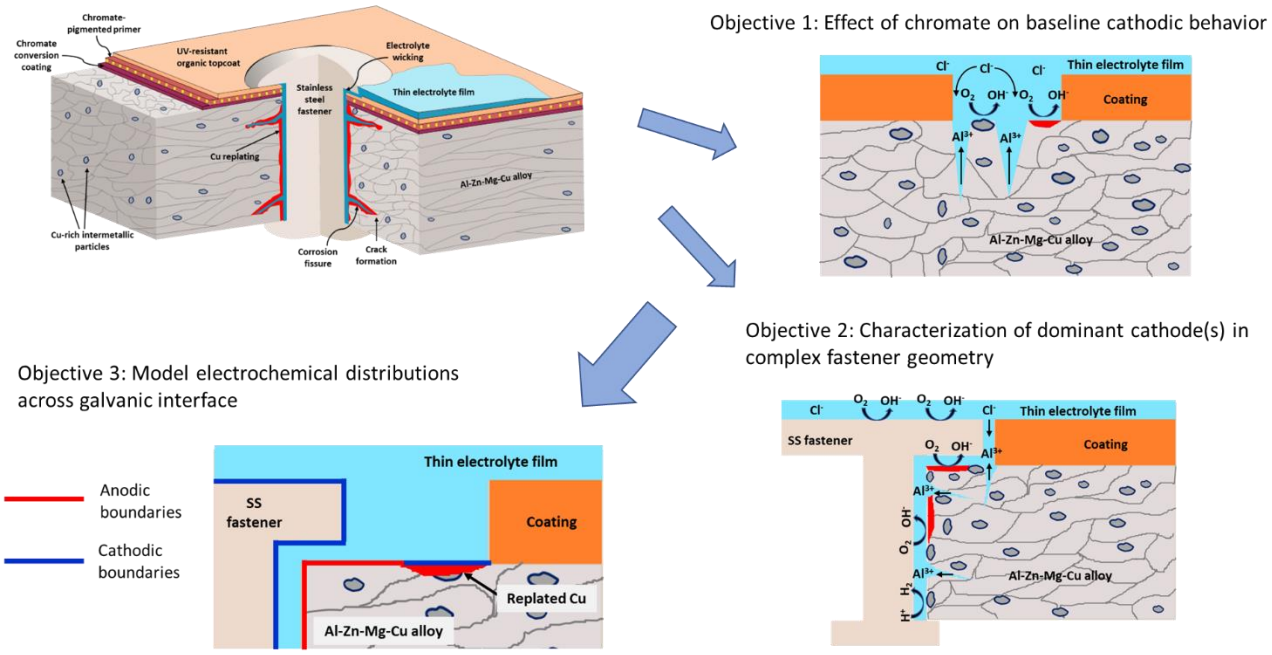

Figure 1.6. Diagrammatic representation of the objectives of research work

1.6 Organization of Dissertation

Chapter 2 describes the use of the RDE technique to investigate the effect of WL on the activity of chromate on the mass-transport-limited ORR behavior of base (uncoupled) AA7XXX alloys under conditions representative of atmospheric exposure. As the corrosion of precipitation-strengthened AAs have been shown to be controlled by the available cathodic current, it was necessary to examine the effect of chromate on the cathodic kinetics on these alloys. The study enabled a mechanistic understanding of the roles of environmental and material (composition, surface conditions – size and spatial distribution of IMPs) factors on the mass-transport-limited ORR kinetics on AA7XXX as a function of chromate concentration, compared to the case of an inert electrode, Pt. X-ray photoelectron spectroscopy (XPS) was used to estimate the thickness of the chromate-induced layer formed on the surface of AA7XXX.

Chapter 3 extends the RDE approach to study the impact of chromate on the ability of the main cathodic actors pertinent to AA7050-316SS galvanic couple to support fast cathodic reaction rates under various environmental conditions. In this study, AA7050 was used to

represent the Cu-rich IMPs, and high-purity Cu was used to represent replated Cu. Experiments were also carried out on Cu electroplated onto AA7050 in an attempt to more realistically simulate Cu replating on AA7050. It is noted that the RDE technique only accounts for WL effects with the assumption of a constant solution chemistry at the electrode surface. In order to simulate concentration effects, test solutions were adjusted to higher chloride concentration (i.e., 5 M, with and without the addition of Al^{3+} in solution) and chromate concentrations (up to 10^{-1} M), as might expected in real atmospheric environments.

Chapter 4 investigates the effect of solution chemistry on the efficacy of chromate in protecting AA7050-316SS couple using different electrochemical techniques. The first part of this work used the scanning vibrating electrode technique (SVET) to visualize the local current density distributions *in-situ* over the boldly exposed surface of an actual AA7050-316SS fastener couple, in comparison with uncoupled AA7050, under simulated external conditions. In addition, the performance of Mg^{2+} in comparison to chromate was assessed. Zero resistance ammeter (ZRA) experiments on planar coupled samples were used in combination with the SVET analysis to explain the observations. The second part of the study utilized the ZRA technique in combination with gravimetric mass loss measurements and cross-sectional corrosion damage characterization to rationalize the low degree of chromate inhibition in simulated AA7050-316SS fastener crevice environments.

Chapter 5 assesses the applicability of the Laplace approach in finite element modeling (FEM) in predicting macro-galvanic current distributions on a typical AA7050-SS316 couple. The study utilized the SVET-derived data in Chapter 4 with modified boundary conditions to experimentally validate the steady-state model results under full immersion conditions. Sources of the observed discrepancies were elucidated.

Chapter 6 examines the galvanic couple interactions between AA7050 and 316SS in chromate-containing chloride solutions assessed with a coupled microelectrode array (CMEA) under various environmental conditions. In contrast to the SVET, which is limited to low conductivity electrolyte and full immersion studies, CMEAs offer the advantage of thin and thick film measurements in more concentrated saline environments as well as wet-dry cycling in a

controlled humidity and temperature chamber. The AA7050-316SS CMEA investigated in this work was constructed in a similar geometry to that used in the SVET experiments discussed in Chapter 4. The ZRA technique was used investigated the in-situ spatial current interactions and correlations of local anodes and cathodes on AA7050 as a function of position from the 316SS under different solution chemistries. In addition, studies were carried out under wet-dry cycling conditions to assess the ability of chromate to suppress current spikes expected during the onset of wetting following a dry period.

Chapter 7 summarizes the conclusions and key highlights from each chapter. Suggestions for future work based on the findings obtained from this dissertation work are also presented.

1.7 References

1. T. Dursun and C. Soutis, *Mater. Des.*, **56**, 862–871 (2014).

2. A. Azarniya, A. K. Taheri, and K. K. Taheri, *J. Alloys Compd.*, **781**, 945–983 (2019).

3. J. R. Davis, *Corrosion of Aluminum and Aluminum Alloys*, ASM International, New York, (1999).

4. N. Birbilis and R. G. Buchheit, *J. Electrochem. Soc.*, **152**, B140–B151 (2005).

5. D. Olson, T. Siewert, S. Liu, and G. Edwards, *ASM Handbook Vol 6: Welding, Brazing, and Soldering*, ASM International, New York, (1993).

6. C. A. Matzdorf et al., *Corrosion*, **69**, 1240–1246 (2013).

7. Z. Feng and G. S. Frankel, *Corrosion*, **70**, 95 (2014).

8. Z. Feng, G. S. Frankel, W. H. Abbott, and C. A. Matzdorf, *Corrosion*, **72**, 342–355 (2016).

9. V. N. Rafla, A. D. King, S. Glanvill, A. Davenport, and J. R. Scully, *Corrosion*, **74**, 5–23 (2018).

10. R. S. Marshall, R. G. Kelly, A. Goff, and C. Sprinkle, *Corrosion*, **75**, 1461–1473 (2019).

11. N. E. C. Co and J. T. Burns, *Int. J. Fatigue*, **103**, 234–247 (2017).

12. G. A. Shoales, S. A. Fawaz, and M. R. Walters, in *ICAF 2009, Bridging the Gap between Theory and Operational Practice*,, p. 187–207 (2009).

13. G. P. Bierwagen and D. E. Tallman, *Prog. Org. Coatings*, **41**, 201–216 (2001).

14. F. H. Scholes et al., *Prog. Org. Coatings*, **56**, 23–32 (2006).

15. G. S. Frankel and R. L. Mccreery, *Electrochem. Soc. Interface*, **10**, 34–38 (2001).

16. G. S. Frankel, *Mechanism of Al alloy corrosion and the role of chromate inhibitors*, (2001).

17. M. W. Kendig and R. G. Buchheit, *Corrosion*, **59**, 379–400 (2003).

18. J. Zhao, G. Frankel, and R. 1 Mccreery, *J. Electrochem. Soc.*, **145**, 2258–2264 (1998).

19. J. D. Ramsey and R. L. Mccreery, *J. Electrochem. Soc.*, **146**, 4076–4081 (1999).

20. D. Chidambaram, M. J. Vasquez, G. P. Halada, and C. R. Clayton, *Surf. Interface Anal.*, **35**, 226–230 (2003).

21. D. Chidambaram, C. R. Clayton, and G. P. Halada, *J. Electrochem. Soc.*, **151**, B151–B159 (2004).

22. D. Chidambaram, C. R. Clayton, G. P. Halada, and M. W. Kendig, *J. Electrochem. Soc.*, **151**, B605 (2004).

23. D. Chidambaram, C. R. Clayton, M. W. Kendig, and G. P. Halada, *J. Electrochem. Soc.*, **151**, B613 (2004).

24. Q. Meng and G. S. Frankel, *Corrosion*, **60**, 897–905 (2004).

25. J. Li, N. Birbilis, and R. G. Buchheit, *Corros. Sci.*, **101**, 155–164 (2015).

26. S. C. Morton and G. S. Frankel, *Mater. Corros.*, **65**, 351–361 (2014).

27. R. K. Gupta, B. R. W. Hinton, and N. Birbilis, *Corros. Sci.*, **82**, 197–207 (2014).

28. V. N. Rafla and J. R. Scully, *Corrosion*, **75**, 587–603 (2019).

29. J. Zhao et al., *Surf. Coatings Technol.*, **140**, 51–57 (2001).

30. G. O. Ilevbare, J. R. Scully, J. Yuan, and R. G. Kelly, *Corrosion*, **56**, 227–242 (2000).

31. G. O. Ilevbare and J. R. Scully, *Corrosion*, **57**, 134–152 (2001).

32. G. O. Ilevbare and J. R. Scully, *J. Electrochem. Soc.*, **148**, 196–207 (2001).

33. A. Sehgal, G. S. Frankel, B. Zoofan, and S. Rokhlin, *J. Electrochem. Soc.*, **147**, 140–148 (2000).

34. A. Kolics, A. S. Besing, and A. Wieckowski, *J. Electrochem. Soc.*, **148**, 322–331 (2001).

35. Y. Baek and G. S. Frankel, *J. Electrochem. Soc.*, **150**, B1–B9 (2003).

36. D. Chidambaram, C. R. Clayton, and G. P. Halada, *J. Electrochem. Soc.*, **150**, B224 (2003).

37. J. E. Hatch, *Aluminum: Properties and Physical Metallurgy*, ASM International, Metals Park, Ohio, (1984).

38. D. Dumont, A. Deschamps, and Y. Brechet, *Mater. Sci. Eng. A*, **356**, 326–336 (2003).

39. D. Wang, D. R. Ni, and Z. Y. Ma, *Mater. Sci. Eng. A*, **494**, 360–366 (2008).

40. N. M. Han, X. M. Zhang, S. D. Liu, B. Ke, and X. Xin, *Mater. Sci. Eng. A*, **528**, 3714–3721 (2011).

41. F. Wang, Y. Gong, Y. Du, and M. Song, *J. Mater. Eng. Perform.*, 1–8 (2020).

42. D. A. Little, B. J. Connolly, and J. R. Scully, *Corros. Sci.*, **49**, 347–372 (2007).

43. J. Wloka, T. Hack, and S. Virtanen, *Corros. Sci.*, **49**, 1437–1449 (2007).

44. G. S. Chen, M. Gao, and R. P. Wei, *Corrosion*, **52**, 8–15 (1996).

45. U.-E. Charles-Granville, C. Liu, J. R. Scully, and R. G. Kelly, *J. Electrochem. Soc.*, **167**, 111507 (2020).

46. O. Schneider, G. O. Ilevbare, R. G. Kelly, and J. R. Scully, *J. Electrochem. Soc.*, **154**, C397–C410 (2007).

47. M. A. Jakab, D. A. Little, and J. R. Scully, *J. Electrochem. Soc.*, **152**, B311–B320 (2005).

48. G. O. Ilevbare, O. Schneider, R. G. Kelly, and J. R. Scully, *J. Electrochem. Soc.*, **151**, B453–B464 (2004).

49. R. G. Buchheit, M. A. Martinez, and L. P. Montes, *J. Electrochem. Soc.*, **147**, 119–124 (2000).

50. P. R. Roberge, *Handbook of Corrosion Engineering*, McGraw-Hill, New York, (1999).

51. A. Nishikata, V. Ichihara, V. Hayashi, and T. Tsuru, *J. Electrochem. Soc*, **144**, 1244 (1997).

52. N. D. Tomashov, *Corrosion*, **20**, 7t-14t (1964).

53. W. J. Clark, J. D. Ramsey, R. L. McCreery, and G. S. Frankel, *J. Electrochem. Soc.*, **149**, B179–B185 (2002).

54. D. Battocchi, A. M. Simões, D. E. Tallman, and G. P. Bierwagen, *Corros. Sci.*, **48**, 1292–1306 (2006).

55. A. D. King, B. Kannan, and J. R. Scully, *Corrosion*, **70**, 512–535 (2014).

56. B. Kannan and J. R. Scully, *Corrosion*, **72**, 1363–1384 (2016).

57. B. Kannan, C. F. Glover, H. N. McMurray, G. Williams, and J. R. Scully, *J. Electrochem. Soc.*, **165**, C27–C41 (2018).

58. R. J. Santucci, B. Kannan, W. Abbott, and J. R. Scully, *Corrosion*, **75**, 440–456 (2019).

59. R. J. Santucci, M. D. Holleman, and J. R. Scully, *Surf. Coatings Technol.*, **383**, 125245 (2020).

60. M. A. Jakab, F. Presuel-Moreno, and J. R. Scully, *Corrosion*, **61**, 246–263 (2005).

61. M. A. Jakab, F. Presuel-Moreno, and J. R. Scully, *J. Electrochem. Soc.*, **153**, B244 (2006).

62. P. Rodič and I. Milošev, *J. Electrochem. Soc.*, **163**, C85–C93 (2016).

63. A. Kosari et al., *J. Electrochem. Soc.*, **168**, 041505 (2021).

64. S. B. Madden, D. J. Moosbauer, and J. R. Scully, *ECS Trans.*, **50**, 57–78 (2013).

65. O. Lopez-Garrity and G. S. Frankel, *J. Electrochem. Soc.*, **161**, C95–C106 (2014).

66. M. Becker, *Corros. Rev.*, **37**, 321–342 (2019).

67. M. G. Mahjani, M. Sabzali, M. Jafarian, and J. Neshati, *Anti-Corrosion Methods Mater.*, **55**, 208–216 (2008).

68. Z. Feng, J. Boerstler, G. S. Frankel, and C. A. Matzdorf, *Corrosion*, **71**, 771–783 (2015).

69. C. Liu, V. N. Rafla, J. R. Scully, and R. G. Kelly, in *CORROSION 2015,*, p. Paper 5579.

2. Assessment of the Influence of Chromate on the Thin-Film Cathodic Behavior of Base AA7XXX Alloys in Simulated Atmospheric Environments

The work presented in this chapter has been reported in the following publication:

U.-E. Charles-Granville, C. Liu, J. R. Scully, R. G. Kelly, "An RDE Approach to Investigate the Influence of Chromate on the Cathodic Kinetics on 7XXX Series Al Alloys under Simulated Thin Film Electrolytes", *J. Electrochem. Soc.*, **167**, 111507 (2020).

2.1 Abstract

The effect of sodium chromate on the cathodic current availability pertinent to the micro-galvanic-induced corrosion of high-strength AA7XXX alloys under simulated thin electrolyte films representative of atmospheric conditions was investigated utilizing a combination of electrochemical and surface characterization techniques. The rotating disk electrode technique provided a means to simulate the effects of water layer thickness to differentiate thin film conditions from full immersion conditions, and enabled the study of the mass-transport-limited oxygen reduction reaction (ORR) on AA7XXX alloys as a function of chromate concentration. The ORR current density decreased by up to two orders of magnitude upon addition of 10 mM chromate, however, the degree of inhibition was observed to depend on the Cu content of the alloy. Chromate was reduced irreversibly to form a Cr^{3+}-rich film on the alloy surface that blocked cathodic sites and hindered ORR. This film was confirmed by X-ray photoelectron spectroscopic characterization of the chemistry and thickness of the chromate-induced layer formed on the specimens after exposure to chromate. The layer was approximately 13 nm in thickness and consisted of mixed Cr^{3+}/Cr^{6+} oxides with some metallic Cr. Studies on a Pt electrode demonstrated the intrinsic ability of chromate as an effective inhibitor for the ORR.

2.2 Introduction

The ever-increasing desires for higher payloads and fuel efficiency in the aerospace industry have made high-strength Al alloys the materials of choice for constructing light-weight aerospace vehicles. In order to achieve the high strength required in aerospace service whilst

optimally balancing other material properties of interest, certain alloying elements such as Zn, Mg, and Cu have to be added to Al and the resulting alloy subsequently precipitation-hardened to the desired temper to produce fine hardening precipitates.[1,2] Unfortunately, the strengthening process also yields intermetallic particles (IMPs) that adversely affect the corrosion and fracture properties of these Al alloys.[3] In natural corrosive environments, including the thin electrolyte layers present under atmospheric exposure, micro-galvanic interactions leading to localized corrosion develop between the Al matrix and the IMPs; the latter can be anodic or cathodic to the Al matrix depending on their electrochemical characteristics relative to the Al matrix.[3,4] Numerous reports in literature have demonstrated that the Cu-rich IMPs are the major facilitators of localized corrosion of high-strength Al alloys in chloride-containing environments.[4-14] In the context of cathodic activity, these Cu-rich IMPs catalyze the fast oxygen reduction reaction (ORR) rates required to sustain anodic dissolution of the peripheral Al matrix and/or preferential dealloying of active elemental constituent(s) of the Cu-rich IMPs.[4,6,12-14]

From a corrosion control perspective, protective chromate-based barrier coating systems have historically been used to maximize the in-service life of Al alloy-based structures. These cost-effective and high-performance coating systems are typically multifaceted, consisting of a chromate conversion coating underlying a chromate-pigmented primer and an ultraviolet-resistant organic barrier top coat.[11,15] Nevertheless, these coatings may become compromised owing to different factors ranging from poor surface preparation or mechanical impact to the nature of the operating environment, ultimately exposing the bare Al-based substrate to corrosive conditions. One important role of the conversion coating and/or the primer is to facilitate the release of soluble chromate to the damaged area(s) of the coating in order to mitigate dissolution of the exposed substrate.[15-17]

Extensive work has been carried out in order to understand the mechanism(s) of corrosion protection of precipitation-hardened Al alloys. Most of the investigations have focused on AA2024-T3[10,18-29] and only a few recent studies[30-33] have focused on the effects of chromate on AA7XXX alloys. Nonetheless, the general consensus from the investigations is that the inhibitive power of chromate species lies in their ability to be reduced from their soluble and

oxidizing Cr^{6+} state to an insoluble and irreversible Cr^{3+} product that effectively protects the underlying corroding metal substrate from the aggressive environment. This universal mechanism has been shown to inhibit both anodic and cathodic reactions.[15-17,23,24,26,34] Clark et al.[26] observed an increase in the pitting potential of AA2024-T3 on addition of 5 mM dichromate to 0.1 M NaCl. Similar observation was made by Ilevbare et al.[23] where the pitting potential of AA2024-T3 was raised on addition of 10 mM chromate to 0.1 M Na_2SO_4 + 0.005 M NaCl. The elevation in pitting potential was indicative of anodic inhibition and was attributed to the suppression of metastable pitting and repassivation of small stable pits.

Although suppression of pitting susceptibility via increases in pitting potential can be important, actual aerospace structures are at their open circuit potential (OCP) when in service. Under open circuit conditions, the determination of the degree of pitting can be controlled by either the anodic or cathodic behavior of the material, i.e., sufficient suppression of cathodic reactions can drive the OCP well below the pitting potential measured in polarization experiments. From the cathodic inhibition perspective, chromates are known to effectively suppress ORR kinetics at concentrations much lower than the threshold concentrations observed to significantly raise pitting potentials of Al alloys.[15] ORR kinetics reduced by up to one order of magnitude on AA2024-T3 in oxygen-sparged 1 M NaCl upon introduction of 0.01 mM dichromate to solution as reported by Sehgal et al.[24] This concentration of dichromate had no effect on anodic or pit kinetics. The effects of chromate on apparent cathodic reactions on heterogeneous electrodes are, however, complex, with the debate of prior degree of open circuit corrosion and/or other mechanisms at play.[22] For instance, suppression of open circuit corrosion, i.e., the minimization of Al_2CuMg (S-phase) attack and subsequent Cu replating by chromate could be considered a subtle and indirect anodic inhibitive effect that mainly manifests as an impressive cathodic effect, albeit not in the form of classic cathodic inhibition.[22] One way to eliminate the indirect anodic effect on cathodic inhibition might be to conduct cathodic reaction kinetics studies on materials that do not corrode at open circuit.

AA2024-T3 has been one of the most widely used Al alloys for aerospace applications requiring superior damage tolerance, e.g., in aircraft fuselage structures,[1] however, its strength

is inferior compared to AA7XXX alloys which exhibit a higher mechanical strength-to-weight ratio with a good balance of fracture toughness and stress corrosion cracking (SCC) resistance.[2] As aircraft manufacturers are exploring several avenues to minimize the number of parts in new aircraft, it may be advantageous to work with larger and thicker plates with equivalent or better physical and mechanical properties than thin plates.[1] In this context, AA7050 which retains its high strength, fracture and fatigue properties in thicker sections, may be more attractive than AA2024 in many applications. The superior properties of the AA7XXX alloys have warranted increased research into their electrochemical behaviors and corrosion inhibition strategies.

In light of chromate effects on the corrosion behavior of Al alloys, very few investigations have been conducted on AA7XXX alloys as previously noted. Gupta et al.[32] studied the effect of chromate concentration on the pit kinetics on AA7075-T651 in quiescent 0.01 M NaCl. It was found that the pitting potential did not increase significantly until a chromate concentration of 10^{-3} M was added, and deaeration did not cause any notable effects. Metastable pitting rate and pit density were shown to decrease with increasing chromate concentration. Interestingly, although this study did not focus on cathodic kinetics, it was noted that the OCP became increasingly negative with increasing chromate concentration which the authors attributed to dominant cathodic inhibition. This observation in OCP evolution with chromate concentration is in line with the results of a more recent work by Rafla and Scully[33] on chromate effects on the anodic behavior of AA7050-T7451 in quiescent 0.5 M NaCl. While the results of this work did not record a dramatic increase in pitting potentials on addition of chromate, the OCP values did appear to decrease with further additions of chromate. The apparent discrepancy in the degree of anodic inhibition via the rise in pitting potentials at a constant chromate concentration, say at 10^{-3} M, could lie in the degree of aggressiveness (or conductivity) of the electrolyte (in this instance, 0.01 M vs. 0.5 M NaCl) and/or the compositional/microstructural variations in the alloys. A comparative study on both alloys under the same environmental conditions could provide more insights. Moreover, the aforementioned studies are not comprehensive enough as they do not address the effect of chromate on cathodic kinetics even as the results suggest an important role of cathodic inhibition under some conditions. The implication of predominant cathodic inhibition is that for electrochemical processes under cathodic control, barring other

governing factors, a very low concentration of chromate could dramatically reduce the cathodic current available to drive anodic dissolution.

The aim of the present work was therefore to assess the influence of chromate on the mass-transport limited ORR kinetics on AA7XXX alloys under thin film conditions representative of atmospheric exposure. As the world moves into an era of green technologies, the results of this work are intended to add to the comprehensive understanding of chromate inhibition mechanism(s) to serve as a standard for the development of next-generation non-toxic inhibitor systems for aerospace applications.

2.3 Experimental

2.3.1 Materials Preparation

Two types of high-strength Al alloys were utilized in this study: AA7050-T7451 (UNS A97050) and AA7075-T6 (UNS A97075), the former being the principal material under investigation. Both alloys were obtained from Alcoa in the form of 50 mm plates. The samples were constructed in the rotating disk electrode (RDE) configuration with a diameter of 1.27 cm (exposed area 1.27 cm^2) surrounded by a PTFE holder with an internal Ni wire electrical connection. Table 2.1 shows the composition of both Al alloys. High-purity Cr obtained from Alfa Aesar was used to achieve a $Cr(OH)_3$ sputter rate standard. Studies were also conducted on a Pt RDE (exposed area 0.196 cm^2) obtained from Pine Research. Immediately preceding each experiment, the Al alloy RDEs and the high-purity Cr were wet-ground successively from 120 grit to a surface finish of 1200 grit with SiC paper, rinsed in acetone and then with deionized water, and finally dried with clean compressed air. The Pt electrode was electrochemically cleaned with 10 cycles of cyclic voltammetry between -1.0 V and 1.0 V at 10 mV/s in 0.1 M H_2SO_4, rinsed with deionized water and dried with clean compressed air.

Table 2.1. Composition of AA7050-T7451 and AA7075-T6 (in wt%).

	Zn	Mg	Cu	Fe	Si	Zr	Mn	Ti	Cr	Al
AA7050-T7451	6.7	2.6	2.6	0.15	0.12	0.15	0.1	0.06	0.04	balance
AA7075-T6	5.7	2.6	1.6	0.13	0.06	0.01	0.02	0.02	0.21	balance

2.3.2 Electrochemical Measurements

Experiments were conducted on the samples in unbuffered 0.6 M NaCl solution (pH 5.6) and with additions of 10^{-4} M (pH 6.3), 10^{-3} M (pH 7.2), and 10^{-2} M Na_2CrO_4 (pH 8.3). These chromate concentrations represent those expected after 0.1 h, 1 h, and 10 h respectively of chromate leaching from a conversion coating into solution based on previous work by Ilevbare and coworkers.[23] The pH of the solutions were measured and not adjusted; measured values were consistent with those expected from calculations using OLI^{TM} Studio Analyzer 9.2 (from OLI Systems, NJ).

Cathodic polarization scans were carried out after a 1 h exposure at open circuit in a standard three-electrode cell with a Pt-Nb mesh counter electrode and a saturated calomel electrode (SCE) as reference. The scans were performed from 0 V_{OCP} (in order to avoid surface alterations from prior anodic dissolution) to -1.2 V_{SCE} at a scan rate of 0.2 mV/s and at various rotation rates from 0 to 1440 rpm using a Gamry Reference 600+^{TM} potentiostat/galvanostat/ZRA. In inhibitor-free 0.6 M NaCl solution, electrochemical kinetics on Pt taken at a reference potential of -0.75 V_{SCE} were used to analyze the current density as a function of diffusional boundary layer thickness, eliminating the effects of a native oxide film that can pose as an additional barrier to the diffusion of oxygen to the electrode surface. Chromate tests on Pt were also carried out to assess the effectiveness of chromate solely as a cathodic inhibitor without the effects of a native oxide layer.

Polarization curves were also generated in deaerated solution on AA7050 to assess the effect of chromate on the cathodic kinetics in O_2-depleted conditions. The tests were conducted in a vertical flat cell (as opposed to a horizontal cell) to maintain the same orientation as the RDE

setup, i.e., electrode surface perpendicular to gravity vector, which permits the assumption of an equivalent diffusional boundary layer thickness for natural convection. Prior to the scans, the solutions were purged with nitrogen gas for 10 min, and purging continued for the duration of the experiments.

2.3.3 X-ray Photoelectron Spectroscopy

High-resolution XPS spectra were taken from a PHI VersaProbe III™ scanning XPS microprobe equipped with a monochromatic Al Kα x-ray source (1486.7 eV) and at a pass energy of 26 eV in order to probe the chemistry of the surface film formed on the samples on exposure to chromate-containing solution. Preliminary survey spectra at a pass energy of 224 eV were acquired for a general assessment of the major elements on the sample surface. The survey spectra of the AA7050 surface identified major Al, Cr and O peaks. With this qualitative information, high-resolution Al2p and $Cr2p_{3/2}$ data were thereafter collected in order to resolve the chemical states of the respective elements. Spectra were fitted using KolXPD software version 1.8.0 (provided by kolibrik.net, Czech Republic) after calibrating to the standard binding energy of 285 eV for the C1s peak. Deconvolution of the peaks was based on binding energies found in the literature.[35-37] A summary of the binding energies is given in Table 2.2.

Table 2.2. Summary of binding energies for different chemical states of the major elements detected on chromate-exposed AA7050 and Pt surfaces.[35-37]

Element	Peak	Binding Energy (eV)
Cr	$2p_{3/2}$	Cr^0: 574.4; Cr_2O_3: 576.3; $Cr(OH)_3$: 577.1; CrO_4^{2-}: 579.6
	3s	75
Al	2p	Al^0: 72.3; Al_2O_3: 74.4
Cu	$3p_{3/2}$	75

Areas of the deconvoluted peaks were also determined using the KolXPD software. For the Al2p peak, it was necessary to delineate the metal and oxide contributions as well as any overlapping peaks from other species. Samples were sputter-depth profiled to measure the thickness of the Cr^{3+} surface layer by rastering a 3 keV Ar^+ beam over a 3 mm x 3 mm area.

Analyses were performed after every 0.1 min of sputtering to a total sputter time of 5 min, alternating with zalar rotation. A $Cr(OH)_3$ sputter rate standard was achieved by sputtering through an 18 nm thick $Cr(OH)_3$ film on high-purity Cr metal using the same sputter parameters. The $Cr(OH)_3$ film was electrochemically grown by potentiostatically holding high-purity Cr at 0.2 V_{SCE} (within the passive region) in 0.6 M NaCl for 30 min following 1 h exposure at open circuit. To exclude the additive effect of the air-formed $Cr(OH)_3$, prior reduction of the air-formed hydroxide was carried out at -1.4 V_{SCE} for 10 min in the same solution. It is noted that the air-formed oxide Cr_2O_3 is highly thermodynamically stable and may not have been reduced at the potential chosen. However, its room temperature air-formed thickness is expected to be very small (on the order of 1 nm)[38] compared to the electrochemically-grown $Cr(OH)_3$ thickness of 18 nm, and hence, should not significantly alter the calculated $Cr(OH)_3$ sputter rate. The $Cr(OH)_3$ film thickness was estimated using Faraday's law:

$$d_{Cr(OH)_3} = \frac{QW_{Cr(OH)_3}}{AnF\rho_{Cr(OH)_3}} \tag{2.1}$$

where Q is the quantity of charge passed, W is the molecular weight of $Cr(OH)_3$, A is the exposed area of the electrode, n is the number of electrons transferred, F is Faraday's constant and ρ is the density of $Cr(OH)_3$.

2.3.4 Surface Characterization

Where applicable, surface characterization was performed utilizing a Quanta 650™ scanning electron microscope (SEM) equipped with energy dispersive spectroscopy (EDS) capability and Oxford Instruments AZtec™ software. Backscattered electron (BSE) images of the polished AA7XXX surfaces were taken and Image J™ software was used to estimate the average Cu-rich IMP size and spacing. The average Cu-rich IMP sizes (in terms of area) on AA7050 and AA7075 were 10.3 μm^2 and 4.5 μm^2 respectively; average particle spacing values were 9.0 µm and 15.8 µm respectively. A Hirox RH 8800™ optical microscope (OM) was also used to image sample surfaces as required to assess the extent of corrosion damage. In every case, imaging was carried out within 5 min of completion of the experiment. Prior to imaging, the surfaces were rinsed with deionized water and dried with clean compressed air.

2.4 Results

The results presented herein experimentally assessed the influence of chromate concentration and water layer (WL) thickness on the mass-transport limited cathodic behavior of AA7XXX alloys. Cathodic polarization data on Pt RDE were employed to bound WL thickness corresponding to conditions typical of atmospheric exposure; an upper limit above which natural convection dominates the diffusion process and a lower limit below which flow regime transitions from laminar to turbulent conditions were defined. Evolution in OCP as a function of chromate concentration was examined to understand the mode(s) of inhibition. The surfaces of chromate-free and chromate-exposed samples were characterized with SEM, OM, and XPS to acquire information on damage morphology, chemistry and thickness of chromate-induced layers.

2.4.1 Determination of Water Layer Thickness as a Function of Rotation Rate

The RDE technique was utilized in this work to investigate the effect of WL thickness on electrochemical kinetics on AA7XXX under thin electrolytes representative of atmospheric conditions. A schematic of the setup is depicted in Figure 2.1a. As the structure rotates, centrifugal forces maintain a steady stream of fresh solution containing an equilibrium concentration of dissolved oxygen from the bulk solution to the electrode surface; this creates a uniform and reproducible diffusional boundary layer immediately adjacent to the electrode surface. Thus, the rotation rate can be used to define a diffusional boundary layer thickness to represent the effect of WL thickness (Figure 2.1b) on the diffusion of dissolved oxygen to the electrode surface under atmospheric exposure conditions.

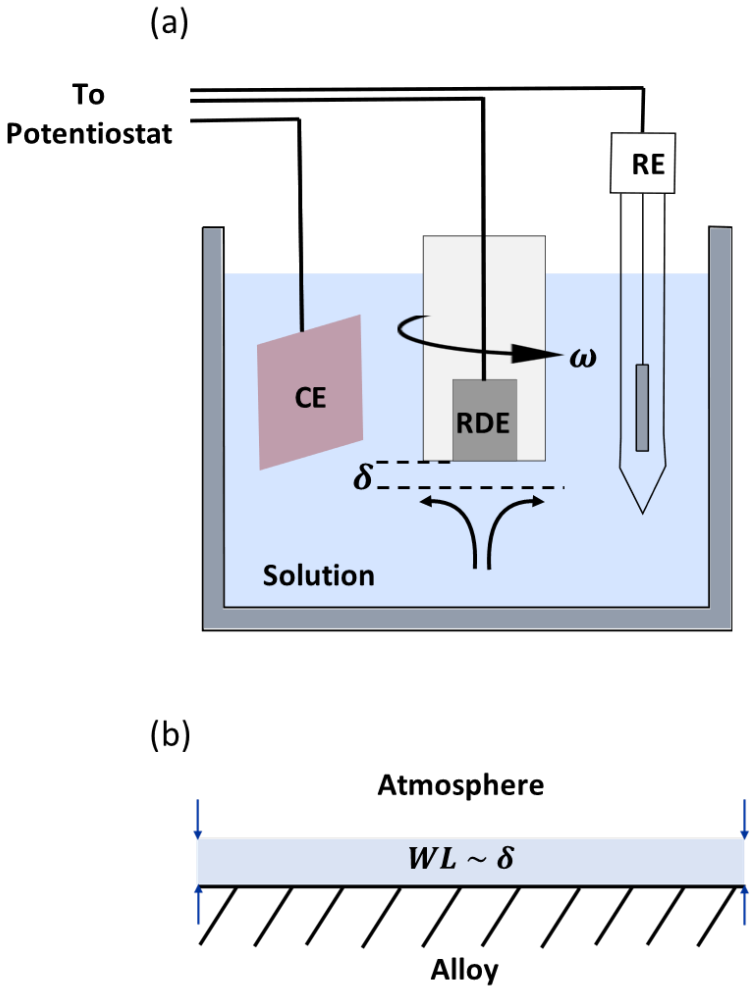

Figure 2.1. (a) Schematic of the setup representative of all RDE experiments carried out in this work; (b) representation of a thin WL on an alloy surface exposed to atmospheric conditions. The thickness of the WL is considered equivalent to that of the diffusional boundary layer imposed by electrode rotation for WL less than the natural convection boundary layer thickness.

By equating the Fick[39] and Levich[40] expressions for limiting current density (Equations 2.2 and 2.3 respectively), the diffusional boundary layer thickness as a function of rotation rate of the electrode can be estimated using Equation 2.4:[39]

$$i_{lim} = \frac{nFD_{O_2}C_{O_2}}{\delta} \tag{2.2}$$

$$i_{lim} = 0.62nFD_{O_2}{}^{2/3}\omega^{1/2}\nu^{-1/6}C_{O_2} \tag{2.3}$$

$$\delta = 1.61D_{O_2}{}^{1/3}\nu^{1/6}\omega^{-1/2} \tag{2.4}$$

where n is the number of electrons transferred (assumed to be 4 in this work), D_{O_2} is the diffusivity of dissolved oxygen in solution (= 2.0 x 10^{-5} cm^2/s in ambient 0.6 M NaCl, calculated with OLI™ Studio Analyzer 9.2), C_{O_2} is the concentration of dissolved oxygen in solution (= 2.3 x 10^{-7} mol/cm^3 in ambient 0.6 M NaCl, calculated with OLI™ Studio Analyzer 9.2), ν is the kinematic viscosity of solution (= 9.2 x 10^{-3} cm^2/s for ambient 0.6 M NaCl, calculated with OLI™ Studio Analyzer 9.2) and ω is the rotation rate of the electrode in rad/s. By inspection of the above equations, it follows that a stationary electrode (i.e., at 0 rpm) should have an infinite diffusional boundary layer thickness and the limiting current should be zero. However, in reality the limiting current is not zero for stationary electrodes or quiescent solutions because of the role of natural convection in the diffusion process. The Levich equation is not applicable under these conditions, so a different approach is required to estimate the true natural convection boundary layer thickness, δ_{nc}. Figure 2.2 shows the cathodic polarization curves of Pt RDE in 0.6 M NaCl as a function of rotation rate. Corresponding diffusional boundary layer thicknesses are given for when $\omega \neq 0$. To estimate δ_{nc}, the technique proposed by Liu et al.[41] was adopted; the limiting current density value at 0 rpm is used in combination with RDE Levich analysis to determine the critical WL thickness beyond which natural convection controls diffusional boundary layer. The result is shown in Figure 2.3a where the RDE i_{lim} data are taken at a reference potential of -0.75 V_{SCE}. The intersection of the limiting current density value at 0 rpm, $i_{lim,nc}$ with the RDE Levich line defines δ_{nc} to be 555 µm (Figure 2.3b). In this work, this value of δ_{nc} is taken to be the critical WL thickness above which environmental conditions transition from atmospheric to full immersion with respect to the kinetics of oxygen reduction.

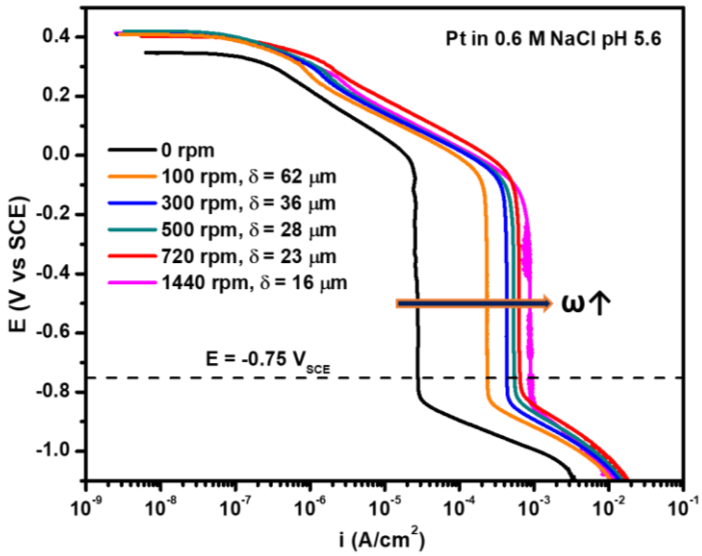

Figure 2.2. Cathodic polarization curves of Pt RDE in 0.6 M NaCl (pH = 5.6) as a function of electrode rotation rate. Diffusional boundary layer thicknesses calculated assuming D_{O_2} = 2.0 x 10^{-5} cm^2/s, C_{O_2} = 2.3 x 10^{-7} mol/cm^3, and ν = 9.2 x 10^{-3} cm^2/s, all calculated for ambient 0.6 M NaCl with OLI™ Studio Analyzer 9.2.

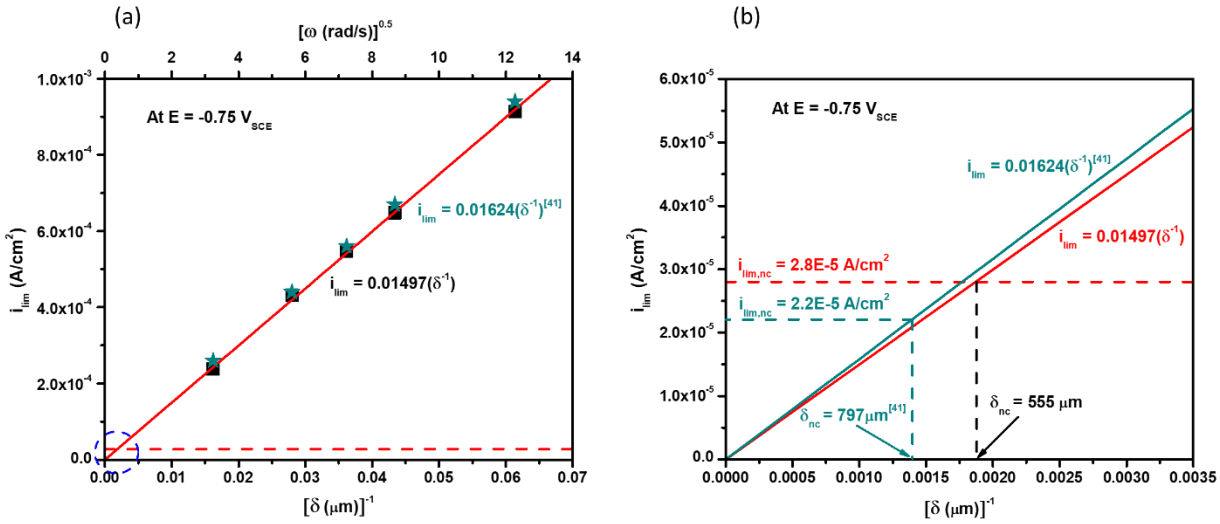

Figure 2.3. (a) Mass-transport limiting current density on Pt shown in Figure 2.2 at -0.75 V_{SCE} as a function of diffusional boundary layer thickness. The green stars represent RDE data obtained by Liu et al.[41] for the same electrochemical system. The red dashed line represents the value of i_{lim} on Pt at 0 rpm (for which natural convection controls the boundary layer); (b) Circled region in (a) zoomed-in to estimate natural convection boundary layer thickness. A value of 555 μm was estimated in this work compared to 797 μm obtained by Liu et al.[41]

2.4.2 Cathodic Kinetics on AA7050-T7451 as a Function of Chromate Concentration

To evaluate the baseline cathodic kinetic behavior of AA7050 in inhibitor-free conditions, the mass-transport ORR kinetics in 0.6 M NaCl (taken at a reference potential of -0.95 V_{SCE}) were compared with those on Pt and Levich-predicted data. As illustrated in Figure 2.4, although kinetics on Pt reasonably matched Levich-predicted kinetics (which theoretically should be independent of electrode material), the limiting current density on AA7050 was much lower than Levich-predicted kinetics, by up to an order of magnitude as diffusional boundary layer thickness decreased with increased rotation rate. In addition, AA7050 exhibited a non-linear ORR rate dependence on δ^{-1}.

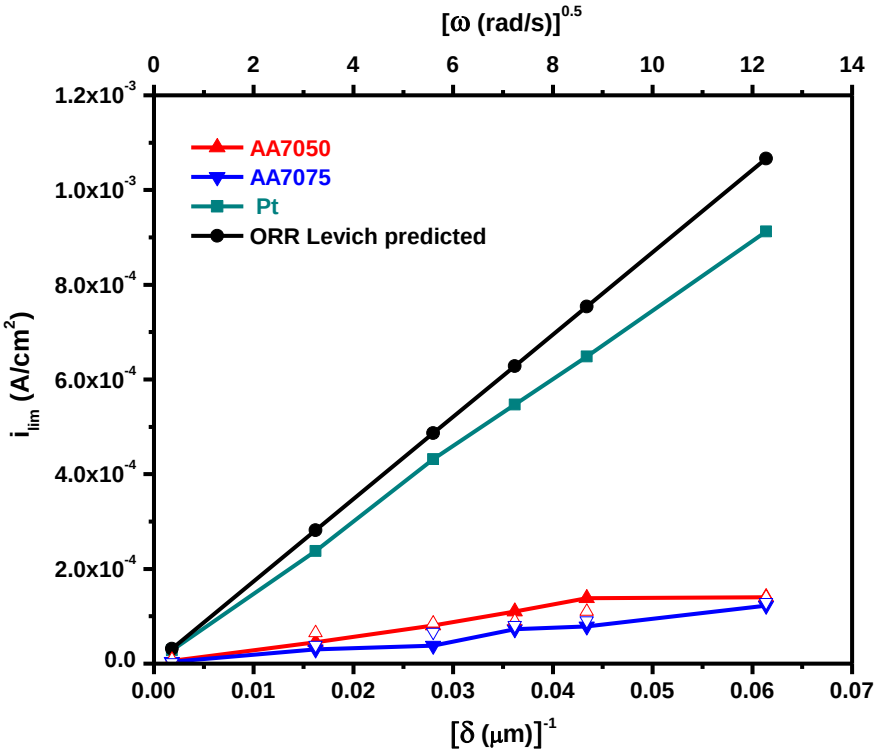

Figure 2.4. Mass-transport ORR kinetics on AA7050-T7451 and AA7075-T6 (taken at a reference potential of -0.95 V_{SCE}) and on Pt (taken at a reference potential of -0.75 V_{SCE}) compared with Levich-predicted data in 0.6 M NaCl (pH = 5.6) as a function of diffusional boundary layer thickness. Open symbols represent data from replicate experiments on the respective AA7XXX alloy. The AA7XXX alloys are shown to substantially deviate from Levich-predicted behavior. Levich prediction based on D_{O_2} = 2.0 x 10^{-5} cm^2/s, C_{O_2} = 2.3 x 10^{-7} mol/cm^3, ν = 9.2 x 10^{-3} cm^2/s, all calculated for ambient 0.6 M NaCl with OLI™ Studio Analyzer 9.2, and n = 4.

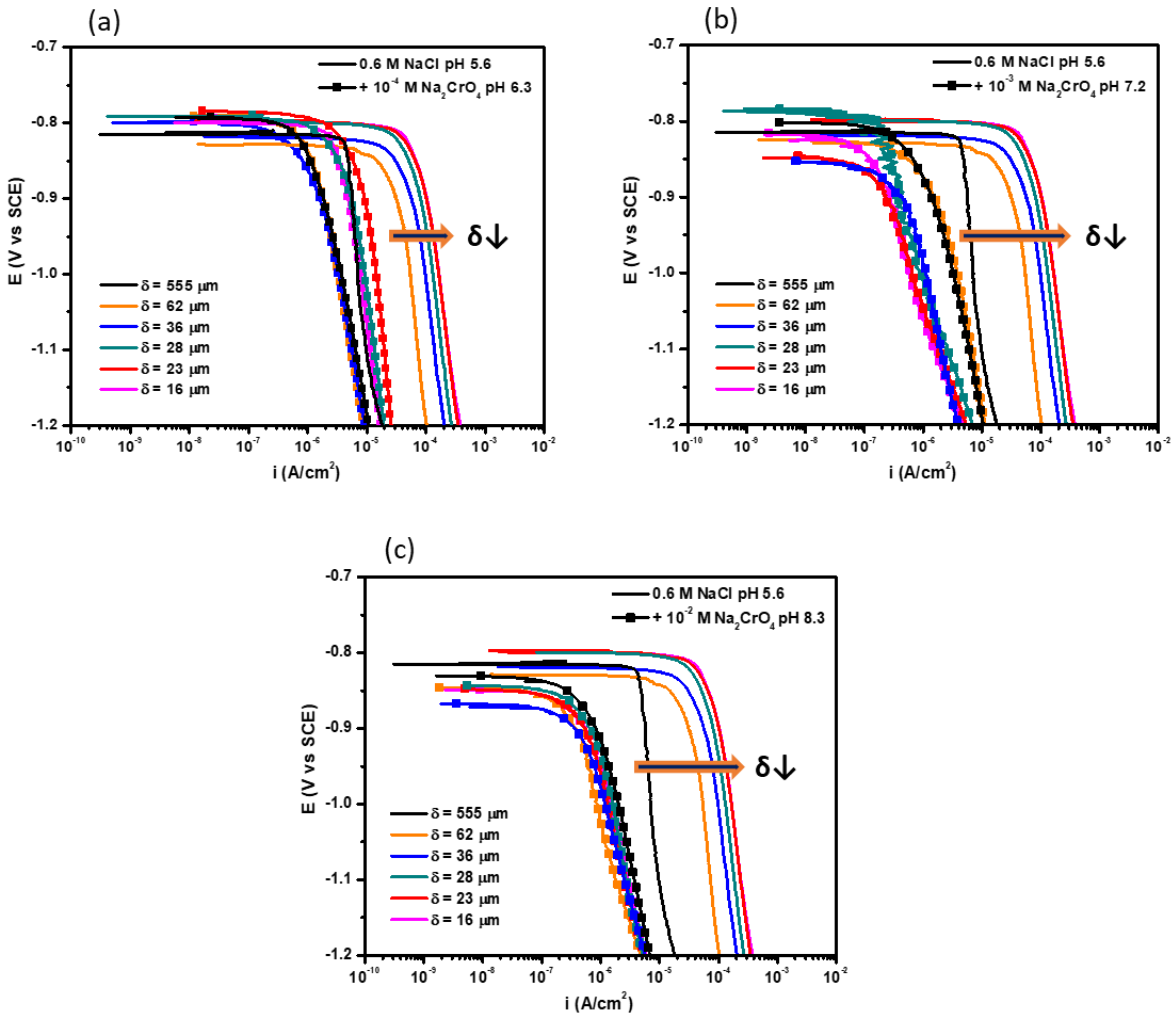

Figure 2.5. Cathodic polarization behavior for RDE of AA7050-T7451 in 0.6 M NaCl pH 5.6 compared with behaviors on addition of (a) 10^{-4} M Na_2CrO_4 pH 6.3, (b) 10^{-3} M Na_2CrO_4 pH 7.2, and (c) 10^{-2} M Na_2CrO_4 pH 8.3.

ORR kinetics on AA7050 decreased as chromate concentration increased. The cathodic polarization curves of AA7050 in inhibitor-free 0.6 M NaCl and with varying concentrations of sodium chromate are displayed in Figure 2.5. In the lowest chromate concentration used (i.e., 10^{-4} M), ORR was suppressed on rotated electrodes by at least one order of magnitude compared to inhibitor-free solution. On the stationary electrode, inhibition was far less significant, implying an influence of the thick diffusional boundary layer (δ = 555 µm) on the transport of the chromate anions to the electrode surface. It was also observed that OCP values remained largely unchanged, if not slightly ennobled, suggesting inhibition of both ORR activity and anodic

dissolution at a comparable level. When the chromate concentration was increased to 10^{-3} M, the degree of suppression was enhanced with lower values of δ, by up to two orders of magnitude reduction with a small general decrease in OCP values. At δ > 36 µm, there appeared to be no improvement in the degree of ORR suppression from that observed with 10^{-4} M chromate. However, with the highest concentration of 10^{-2} M, significant inhibition occurred independent of δ. Furthermore, OCP values were clearly lowered, suggesting predominantly cathodic inhibition at higher chromate concentrations. Figure 2.6 displays SEM images of AA7050 surfaces as polished and after 1 h OCP exposure followed by cathodic polarization in quiescent inhibitor-free and 10^{-2} M chromate-bearing 0.6 M NaCl solutions. Deep, coalesced pits as well as intergranular fissures were visible on the sample surface exposed to inhibitor-free conditions. With addition of chromate, very shallow pits were noticed in the vicinity of Cu-rich IMPs as confirmed by EDS. The Al matrix away from the IMPs were largely corrosion- and fissure-free.

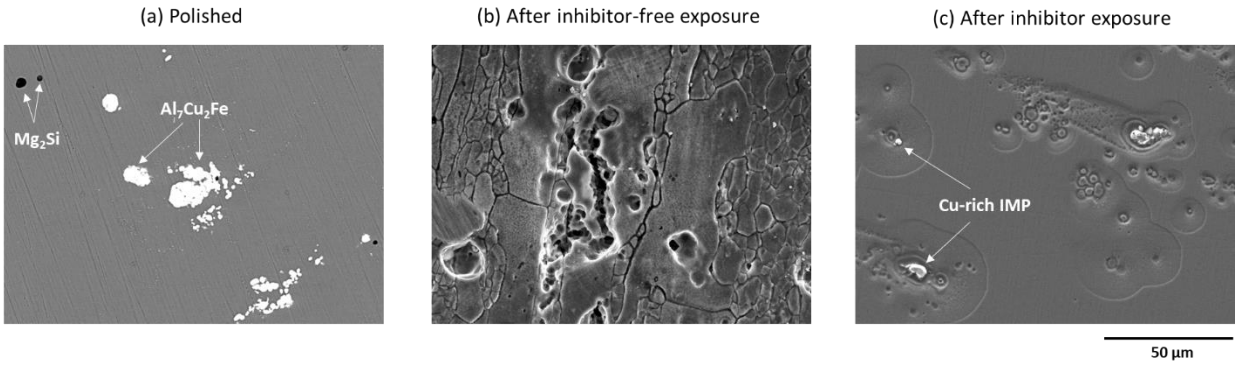

Figure 2.6. SEM images of AA7050-T7451 surface after (a) polishing, (b) 1 h OCP exposure followed by cathodic polarization in 0.6 M NaCl, and (c) 1 h OCP exposure followed by cathodic polarization in 0.6 M NaCl + 10^{-2} M Na_2CrO_4, under quiescent conditions.

2.4.3 Comparison of AA7050-T7451 and AA7075-T6 Electrochemistry as a Function of Chromate Concentration

In an attempt to gain insights into possible trends in the electrochemical behavior across 7XXX series Al alloys, the effects of chromate on the cathodic kinetics on AA7050 and AA7075 were compared. Similar experiments as on AA7050 were carried on AA7075 and the results at δ = 16 µm are summarized in Figure 2.7.

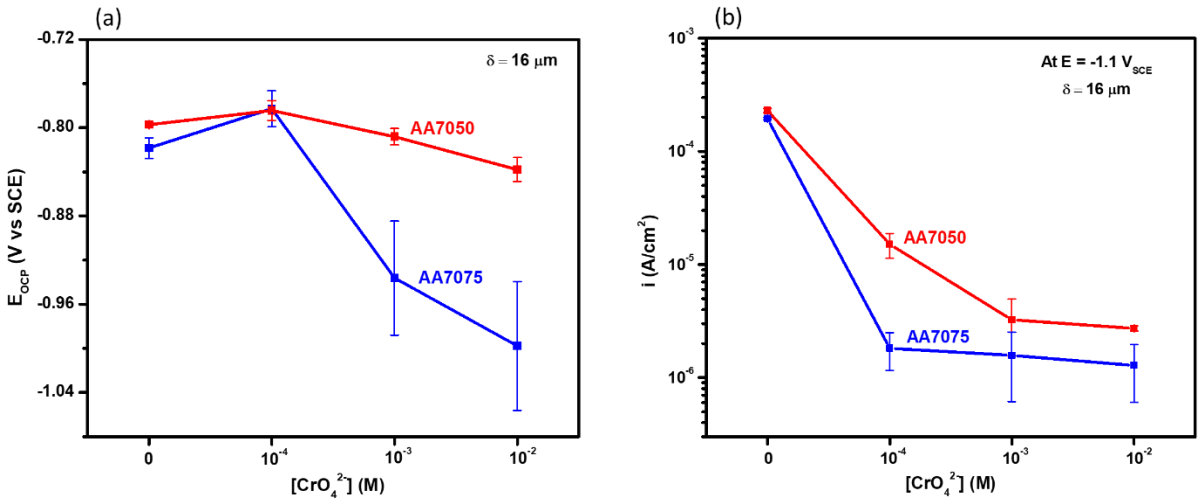

Figure 2.7. Comparison of the electrochemical behaviors of AA7050-T7451 and AA7075-T6 in 0.6 M NaCl solutions with and without chromate. Evolution in (a) OCP and (b) ORR kinetics as a function of chromate concentration. Error data obtained from one to two replicate experiments.

In terms of OCP evolution with chromate concentration on AA7075, there was a clear ennoblement of OCP with the lowest chromate concentration but a sharp decrease in values as the inhibitor concentration increased (Figure 2.7a). This behavior was similar to that of AA7050, albeit much more dramatic. In terms of the ORR current density, kinetic data were taken at a reference potential of -1.1 V_{SCE} for both AA7050 and AA7075 (as a result of the much lower OCP values on AA7075 at high chromate concentrations) to enable a direct comparison. As shown in Figure 2.7b, addition of 10^{-4} M chromate to solution dramatically reduced ORR kinetics on AA7075 by almost two orders of magnitude, compared to approximately one order of magnitude on AA7050 at the same chromate concentration. Although increasing the concentration of chromate on AA7075 further decreased current density, the additional beneficial effect with higher concentration was not as significant as that attained with 10^{-4} M chromate. This result suggests that very low chromate concentrations may effectively suppress corrosion on AA7075 compared to AA7050. Nevertheless, the key result in this section is that same trends were observed with both AA7XXX alloys: with increasing chromate concentration, 1) the cathodic current density decreased by up to two orders of magnitude with no clear dependence on diffusional boundary layer thickness and 2) the OCP became increasingly negative.

2.4.4 XPS Characterization of Chromate-Exposed AA7050-T7451 Surface

XPS surface analyses were conducted on AA7050 RDE after 1 h OCP exposure followed by cathodic polarization in 0.6 M NaCl containing 10^{-2} M chromate at 1440 rpm (δ = 16 μm) to study the chemistry of the surface film formed and to determine the film thickness. Figure 2.8a presents the deconvoluted Al2p peak. As expected, Al^{3+} was present in the surface film. The overlapping $Cu3p_{3/2}$ peak was from the elemental contribution of Cu alloying component in the substrate while that of Cr3s was from the Cr-based inhibitor in the surface film. Although there is a trace amount of Cr alloying component in AA7050, the quantity was too low to create a detectable peak. This result was confirmed by conducting a high-resolution scan of a polished, bare AA7050 surface within the binding energy range of $Cr2p_{3/2}$ which showed no peak. As such, all identified Cr peaks were attributed solely to the inhibitor. For the deconvoluted $Cr2p_{3/2}$ peak (Figure 2.8b), Cr^{3+} hydroxide was found to be the dominant Cr species in the surface film, making up 73% of the total peak area. Cr^{3+} oxide constituted 20%. A smaller amount (2%) of absorbed and unreduced Cr^{6+} was also detected which is consistent with literature.[15] Furthermore, it appeared some Cr^{3+} were further reduced to metallic Cr (Cr^0), constituting 5% of the $Cr2p_{3/2}$ peak area.

Sputter depth profiling was conducted on the same chromate-exposed sample to estimate the thickness of the chromate-induced layer. Layer thickness was initially taken as sputter time and then converted to nm based on experimentally-determined Cr^{3+} hydroxide sputter rate on high-purity Cr. The Cr^{3+} hydroxide sputter rate standard of ~ 0.5 nm/s was achieved by sputtering through an 18 nm thick electrochemically-grown Cr^{3+} hydroxide layer on 99.998 wt% Cr, and based on the sputter time taken for the O1s signal to attenuate to half of the initial value which was approximated to be 36 s (Figure 2.9a). For the chromate-exposed AA7050 sample, the sputter time taken for the $Cr2p_{3/2}$ signal to attenuate to half of its initial value was 25 s (Figure 2.9b). This sputter time of 25 s converted to chromate-induced layer thickness of 13 nm based on the Cr^{3+} hydroxide sputter rate standard of ~ 0.5 nm/s on high-purity Cr. Similar experiments conducted at lower rotation rates (higher values of δ) at the same chromate concentration (10^{-2} M) yielded approximately same chromate-induced layer thickness, which is

consistent with the comparable i_{lim} data that appears to be independent of δ in solution containing 10^{-2} M chromate (Figure 2.5c).

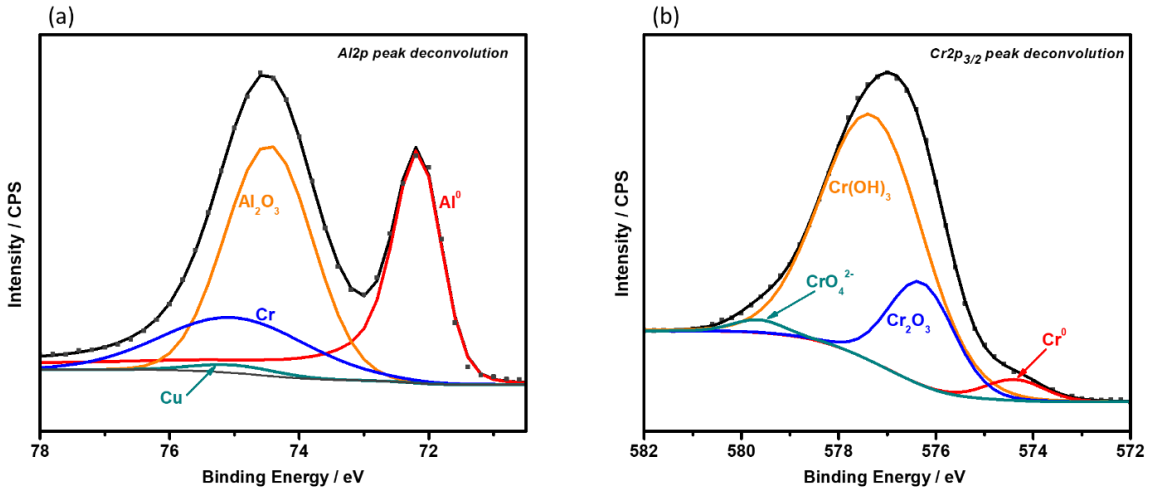

Figure 2.8. High-resolution XPS spectra analysis of the major elements on AA7050-T7451 surface after 1 h OCP exposure followed by cathodic polarization in 0.6 M NaCl + 10^{-2} M Na_2CrO_4 at 1440 rpm (δ = 16 µm). Deconvolution of (a) Al2p and (b) $Cr2p_{3/2}$ peaks shows chemistry of surface layer.

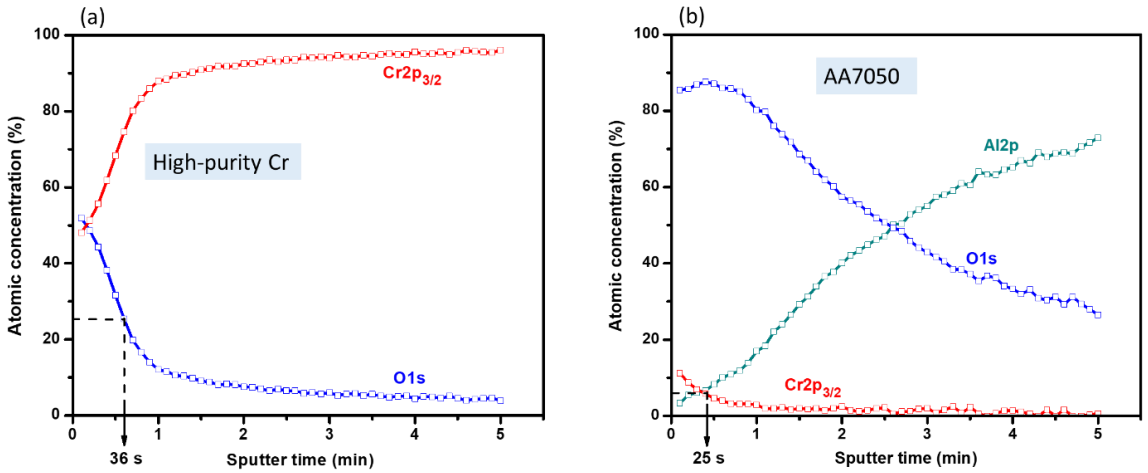

Figure 2.9. Sputter depth profile data of (a) an 18 nm thick electrochemically-grown Cr^{3+} hydroxide layer on high-purity Cr, and (b) chromate-induced layer on AA7050-T7451 after 1 h OCP exposure followed by cathodic polarization in 0.6 M NaCl + 10^{-2} M Na_2CrO_4 at 1440 rpm (δ = 16 µm). Analysis showed thickness of Cr^{3+} film on AA7050 was ~ 13 nm based on Cr^{3+} hydroxide sputter rate of 0.5 nm/s on high-purity Cr.

2.4.5 Effect of Chromate on ORR Kinetics on Pt to Exclude Effects of Anodic Activity

The goal of this portion of the study was to investigate the effectiveness of chromate solely as a cathodic inhibitor of the ORR without the complications of a native oxide layer or the effects of anodic dissolution as would be the case with Al alloys in general. The ideal candidates for this study would be materials that neither corrode nor possess air-formed oxides and/or passive films that might interfere with or alter the intrinsic cathodic inhibitive activity of chromate and/or introduce other species that may be reduced and add on to the total cathodic limiting current density in addition to O_2 reduction and Cr^{6+} to Cr^{3+} reduction. Pure Pt was assessed to fit this category of materials and was chosen for use in this study. Figure 2.10a presents the cathodic kinetics on Pt in inhibitor-free 0.6 M NaCl and with addition of 10^{-2} M chromate at δ = 16 µm. This lowest value of δ within our experimental range produced the highest ORR kinetics in inhibitor-free conditions, representing the worst-case scenario and it was considered an excellent choice to assess the cathodic inhibitive effect of chromate under this condition. In this case, it was observed that chromate reduced both the mass-transport-limited

and activation-controlled ORR kinetics by up to one order of magnitude while also decreasing the activation-controlled HER kinetics, albeit to a lesser extent. OCP decreased as well, indicative of inhibition of cathodic ORR. These results supported the presence of a low porosity, adherent and electronically non-conductive layer that restricted the diffusion of oxygen to the Pt surface.

To investigate this theory, XPS analysis was performed on Pt RDE surface after exposure to chromate. Preliminary survey spectrum of the surface identified Cr and O peaks, giving an indication of a chromate-induced surface layer. High resolution $Cr2p_{3/2}$ data was collected to determine layer chemistry. As evident in Figure 2.10b, the layer was very rich (82%) in Cr^{3+} hydroxide, with smaller amounts of Cr^{3+} (11.4%) and Cr^{6+} (6%) oxides. Cr^{0} was barely detectable (< 1%) in this layer, unlike in the case of AA7050.

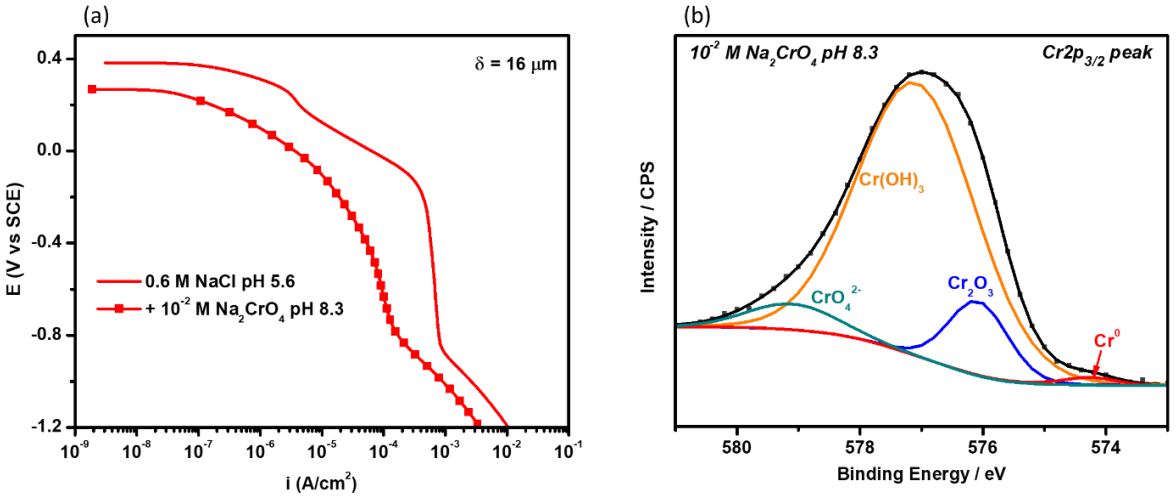

Figure 2.10. (a) Comparison of cathodic kinetics on Pt in chromate-free and chromate-bearing 0.6 M NaCl solutions; (b) High-resolution XPS surface chemistry analysis of the film formed on Pt after 1 h OCP exposure followed by cathodic polarization in 0.6 M NaCl + 10^{-2} M Na_2CrO_4 at 1440 rpm (δ = 16 μm).

2.4.6 Persistence of Cr^{3+} Layer on AA7050-T7451 on Removal of Chromate from Solution

Studies were conducted to assess the persistence of the Cr^{3+} layer formed on pretreated AA7050 after the inhibitor was subsequently removed from solution. If Cr^{6+} to Cr^{3+} reduction is

indeed irreversible,[15,17] then it would be reasonable to hypothesize that once the reduction reaction occurred, the resulting Cr^{3+}-rich film should remain stable and sustain ORR inhibition despite changes in electrolyte conditions where the inhibitor may no longer be available. Figure 2.11a highlights the cathodic kinetics on inhibitor-pretreated AA7050 in inhibitor-free 0.6 M NaCl solution compared to the kinetics on polished electrodes in inhibitor-free and inhibitor-bearing 0.6 M NaCl solutions at δ = 555 µm, 62 µm and 16 µm, taken at a reference potential of -1 V_{SCE}. The cathodic current data were collected after 1 h exposure at OCP. In the former case, a polished AA7050 sample was pretreated (1 h OCP exposure followed by cathodic potentiodynamic scan from 0 V_{OCP} to -1.2 V_{SCE}) in solution containing 10^{-2} M chromate and was thereafter rinsed gently in deionized water and lightly dried with clean compressed air immediately before transferring to inhibitor-free solution for similar testing.

On polished AA7050 electrode in inhibitor-free conditions, the rotation-rate-dependent limiting current density increased dramatically as the diffusional boundary layer thickness decreased. Optical micrographs on the top row in Figure 2.11b show the resulting differences in surface damage morphology. In quiescent conditions (δ = 555 µm), there was a number of isolated deep pits; with electrode rotation (decreasing δ) however, pit density increased and the pits appeared to coalesce, forming stringers along IMPs. Upon introduction of chromate to solution, the current density significantly decreased to the order of 10^{-6} A/cm^2 and the rotation rate dependence disappeared. This inhibition of the cathodic current density was accompanied by the formation of only a few shallow pits on the optical micrographs (Figure 2.11b, middle row). Interestingly, upon removal of chromate from solution after prior inhibitor exposure, ORR remained inhibited on AA7050 with no appreciable increase in pit density (Figure 2.11b, bottom row).

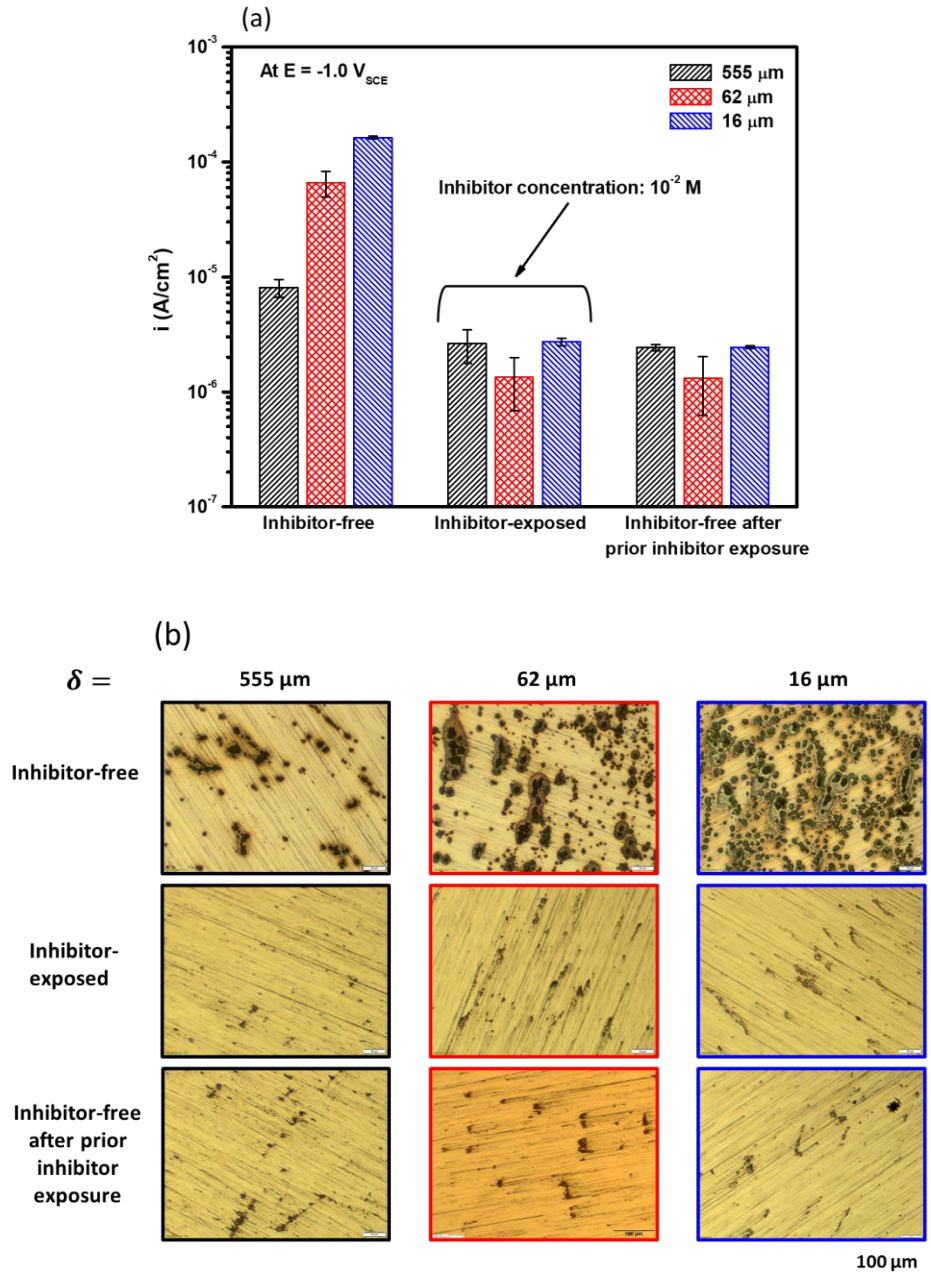

Figure 2.11. Persistence of protection of Cr^{3+} layer on AA7050-T7451 demonstrated. (a) ORR kinetics on polished AA7050 in inhibitor-free and chromate-bearing 0.6 M NaCl compared with kinetics on chromate-pretreated AA7050 in inhibitor-free 0.6 M NaCl at different boundary layer thicknesses obtained at a reference potential of -1 V_{SCE}. Error data obtained from one to two replicate experiments; (b) corresponding optical micrographs of the electrode surfaces post experiments.

2.4.7 Damage Morphology on AA7050-T7451 after Constant Solution Exposure Time: 2 h OCP vs. 1 h OCP followed by Cathodic Polarization

The purpose of this investigation was to decouple the effect of cathodic polarization from that of OCP exposure on the corrosion morphology of AA7050 and assess the role of chromate on damage evolution. In this investigation, two sets of polished AA7050 RDEs were subjected to either OCP-only or 1 h OCP + cathodic polarization exposure for a total time of 2 h in chromate-free or chromate-bearing 0.6 M NaCl solutions. Experiments were conducted at rotation rates of 0, 100 and 1440 rpm. After each experiment, the electrode surface was immediately rinsed in deionized water, dried and viewed under the optical microscope. The micrographs are displayed in Figure 2.12. In the chromate-free conditions, a trend was observed where the cathodically-polarized samples exhibited more pitting damage than their OCP-only exposed counterparts, suggesting that cathodic polarization of AA7050 in this environment causes more damage than OCP corrosion. In contrast, chromate addition to solution appeared to mitigate corrosion at OCP and during cathodic polarization.

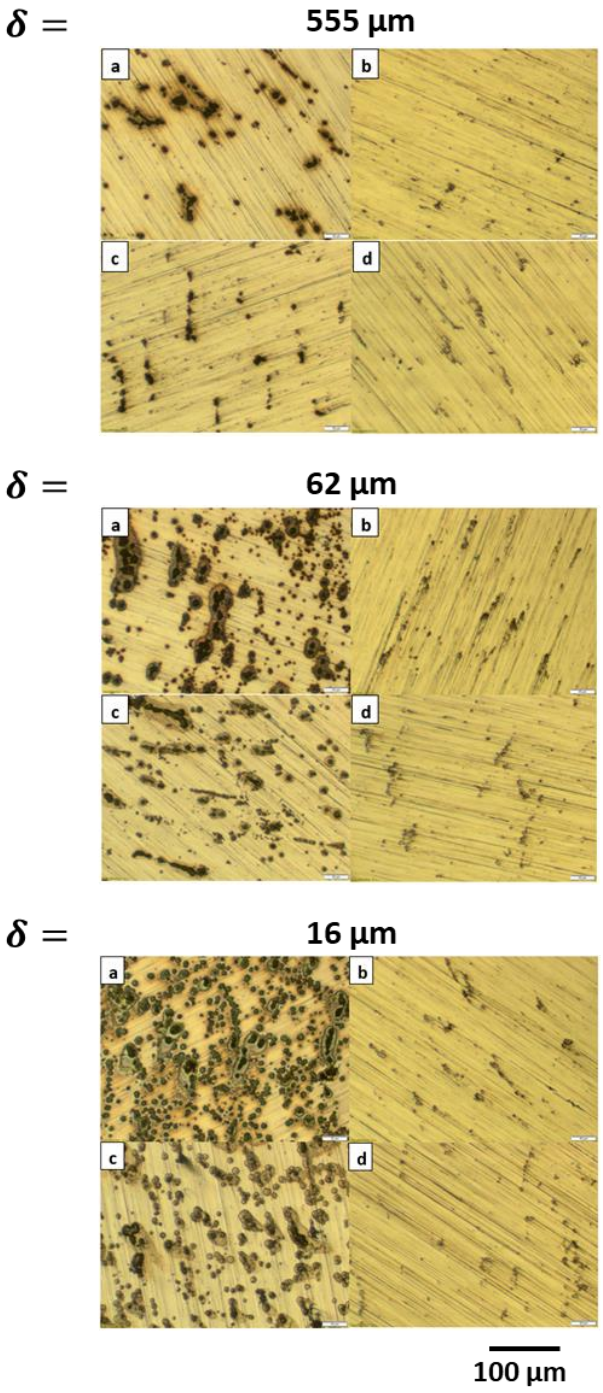

Figure 2.12. Optical micrographs of AA7050-T7451 surface after (a) 1 h OCP exposure followed by cathodic polarization in 0.6 M NaCl and (b) with addition of 10^{-2} M Na_2CrO_4; (c) 2 h OCP-only exposure in 0.6 M NaCl and (d) with addition of 10^{-2} M Na_2CrO_4, at δ = 555 µm, 62 µm and 16 µm. All exposure times roughly totaled 2 h.

2.4.8 Effect of Chromate on Kinetics on AA7050-T7451 in Deaerated Conditions Compared to Quiescent Conditions

Experiments were also carried out in O_2-depleted conditions to quantify the kinetics of chromate reduction on AA7050 whilst minimizing the effects of the ORR. It is expected that in chromate-bearing solutions, there will be some cathodic current associated with chromate reduction because it occurs over the potential range of mass-transport-controlled ORR on AA7050. Also, because Cr^0 was detected on AA7050 on exposure to chromate, the total cathodic limiting current density can be represented as follows in Equation 2.5:

$$i_c = i_{ORR} + i_{Cr^{6+/3+}} + i_{Cr^{3+/0}} \quad (2.5)$$

where i_{ORR}, $i_{Cr^{6+/3+}}$, $i_{Cr^{3+/0}}$ are current densities associated with ORR, Cr^{6+} to Cr^{3+} reduction and Cr^{3+} to Cr^0 reduction respectively. Figure 2.13 compares the cathodic behavior of AA7050 with and without chromate in quiescent and deaerated conditions. Two key observations can be made. First, it can be estimated that the limiting current density associated with just the chromate reduction reactions is on the order of 10^{-7} A/cm^2 and therefore too low to significantly contribute to the total cathodic limiting current density on AA7050. Second, there is an apparent discrepancy in OCP evolution between quiescent and deaerated conditions on addition of chromate. Although the OCP fell in the case of quiescent conditions, the reverse was the case for deaerated conditions where clear ennoblement in OCP was registered.

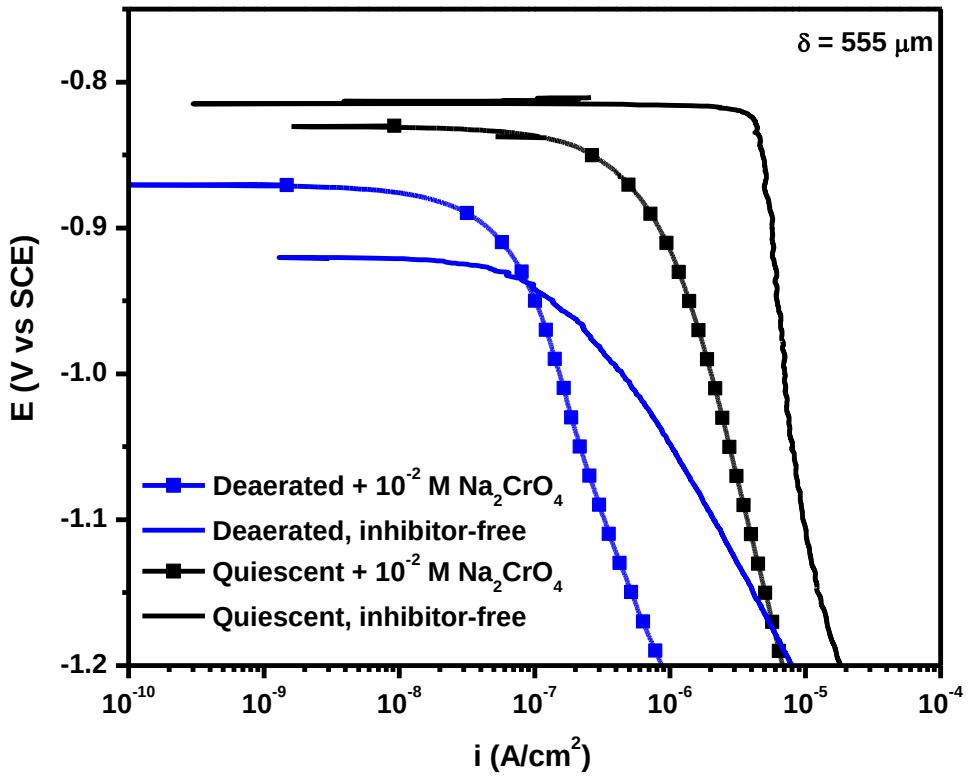

Figure 2.13. Comparison of the cathodic behavior of AA7050-T7451 in deaerated and quiescent 0.6 M NaCl with and without chromate in solution. It is assumed that the main cathodic reaction in deaerated conditions with chromate is Cr^{6+} to Cr^{3+} reduction; this implies that the kinetics associated with just chromate reduction is on the order of 10^{-7} A/cm^2.

2.5 Discussion

Studies conducted under simulated atmospheric conditions require the use of a robust approach that can quantitatively delineate thin film exposure from full immersion exposure because the corrosion kinetics can be markedly different in each environment. This study employed the RDE technique to explore the effect of water layer thickness on cathodic kinetics on AA7XXX alloys and to define natural convection boundary thickness above which full immersion conditions prevail with respect to the kinetics of oxygen reduction. Data from the literature are compared to corroborate the value obtained herein. We note that one limitation of using the RDE technique to simulate atmospheric conditions is that it does not account for the changes in concentration of dissolved species under thin film conditions in response to the electrochemical reactions, including dissolution, ORR, and homogeneous reactions. Under open

circuit conditions, the pH of the surface will tend towards 7-8 due to the combination of partial Al^{3+} hydrolysis creating H^+ and ORR creating OH^-. This pH results from the fact that there is not a separation of anodic and cathodic reactions on the surface, in a similar manner as occurs in crevices or occluded regions for which no wetted external surface is present.[42-44] The slightly higher pH will decrease the reversible potential for ORR and lead to a slightly higher passive current density, but when combined with an approximately constant cathodic current density, the effect would be a small change in the OCP. That said, it is also possible that concentration effects can result to lower O_2 diffusion rates particularly for very thin diffusional boundary layers.[45]

The electrochemical behaviors of two AA7XXX alloys are discussed in light of the presence of the native Al-rich oxide film, solution conditions, and alloy Cu content, considering information reported in the literature. The mode of corrosion inhibition of AA7XXX as a function of chromate concentration and oxygen concentration is elucidated as well as the implications of the Cu-rich IMPs on the reduction of the chromate anions on AA7050 surface. The ramifications of the results of the present study towards environmentally-assisted fatigue cracking are discussed.

2.5.1 The Natural Convection Boundary Layer Thickness is Poorly Controllable

Convection, whether natural or forced, controls the thickness of the diffusional boundary layer established adjacent to electrode surfaces in electrochemical reactions and can control the rate of those reactions. Although natural convection is present in every solution regardless of state, its influence on the RDE is rather minimal and often disregarded under most conditions. Forced convection dominates in most applications of the RDE process and controls the flow pattern in such a way that electrochemical kinetics are reproducible,[46] provided electrolyte properties remain the same. The results here illustrate this reproducibility as they are consistent with the RDE data obtained by Liu et al.[41] for the same electrochemical system (Figure 2.3a). In contrast, the estimated values of δ_{nc} are somewhat different. While a value of 555 µm is obtained in this work, Liu et al.[41] attained a value of 797 µm (Figure 2.3b). The discrepancy arises mainly as a result of the non-steady state i_{lim} values measured under quiescent conditions which are dominated by natural convection. Natural convection arises from small vibrations in the

laboratory and/or small thermal or local density gradients[47] and is poorly controllable due to the time-based variations in these factors. Moreover, system geometry in relation to gravity vector may also play an important role. Upward facing horizontal electrodes (perpendicular to solution gravity vector) may have easier natural convection compared to electrodes whose surfaces are parallel to solution gravity vector as a result of the relatively higher degree of direct fluid motion in the vicinity of the surface in the former orientation.[48] Considering the aforementioned factors, it appears rather impracticable to establish a definitive value of δ_{nc} regardless of electrochemical system. Nonetheless, the value of δ_{nc} herein falls within the range of δ_{nc} values reported in the literature[49-53] with the lower bound of 200 μm[49] and the upper bound of 1000 μm.[53]

2.5.2 Factors Contributing to AA7XXX Deviation from Levich-Predicted ORR Behavior in Inhibitor-Free Conditions

In inhibitor-free solution, the mass-transport-limited ORR kinetics on Pt reasonably agreed with Levich-predicted kinetics. In contrast, the kinetics on AA7050 and AA7075 substantially deviated from Levich-predicted data for ORR at all rotation rates as shown in Figure 2.4. Not only were the kinetics slower on AA7XXX, but also i_{lim} appeared to lose its linear dependence of δ^{-1}. This result indicates some other rate limitation on the diffusion of oxygen to the AA7XXX surface than the mass transport of oxygen in solution. Possible reasons for this deviation include the microelectrode array effect of the cathodic-catalytic Cu-rich IMPs,[6] an additional barrier control due to the presence of a native oxide film,[21,22] and cathodic Al dissolution causing local surface pH increases and leading to cycles of oxide film dissolution and reformation,[54] such that the net cathodic current density is much smaller than predicted.

The heterogeneous nature of an electrode can cause non-linear diffusion of cathodic reactants to the electrode surface – hemispherical diffusion at small particle on planar electrode – such that the mass-transport-limited ORR rate increases as a complex function of δ.[6,55] This notion is consistent with the non-linear ORR behavior of both AA7XXX alloys compared to that of Pt as shown in Figure 2.4. However, it does not explain the slower kinetics on the AA7XXX alloys compared to Pt and Levich-predicted kinetics given that the microelectrode array of the Cu-rich

IMPs is expected to behave like a planar Cu electrode as the average IMP sizes and spacings are much smaller than δ_{nc}.[56]

Previous reports in the literature have demonstrated that oxide films on pure Al in chloride-containing electrolytes lower the mass-transport-limited ORR current density compared to other air-formed oxide-covered electrodes like Cu and Fe.[6,21,22,56] The behavior of high-purity Al in these studies was attributed to the slow step of electron transport through the highly electronic-resistant Al-oxide film to support ORR at the oxide/electrolyte interface compared to the faster rate of electron supply through the more electronically conductive Cu- and Fe-oxide layers. Furthermore, this rate-limiting step is shown to be slower as the Al-oxide film thickness increases[22] as a result of increased electronic resistance with oxide film thickness.[57] Our experiments on anodized AA7075 at a fixed rotation rate of 720 rpm (Figure 2.14) exhibited similar tendencies, albeit with slightly higher i_{lim} values than on pure Al, arguably due to the presence of the more cathodically-catalytic Cu- and Fe-rich IMPs covered with presumably more electronically conductive and/or defective Cu- / Fe-altered Al-rich oxide films. These factors could in combination enable electron and oxygen transport to the oxide/solution and metal/oxide interfaces, respectively. At these cathodic sites, electron transport should not be a rate limitation and control of ORR should be solely the mass transport of dissolved oxygen through the oxide film.

Cathodic Al dissolution requires the generation of a copious amount of OH^- to cause a large surface pH shift sufficient to destabilize and solubilize the Al oxide film. In unbuffered solutions, this requirement can be met by cathodically polarizing the Al-based alloy away from its OCP into the mass-transport-limited ORR region.[27,54,58] For precipitation-hardened Al alloys, the ORR occurring on the IMPs causes a rapid pH increase in the vicinity of the IMPs which results to the alkaline dissolution of the peripheral Al matrix.[58] In the present work, the increased ORR rate on the IMPs compared to the Al matrix upon application of cathodic overpotentials was manifested as enhanced pitting damage in the vicinity of the IMPs compared to freely-corroding conditions at OCP (Figure 2.12). Ogle et al.[54] demonstrated that although the cathodic Al dissolution rate on pure Al significantly affected the net cathodic limiting current density, the

true cathodic limiting current density was still small compared to the cathodic limiting current density that would be observed on Pt. It therefore follows that the oxide film on AA7XXX, in addition to the effects of cathodic corrosion, plays an important role in limiting ORR rates as noted previously.

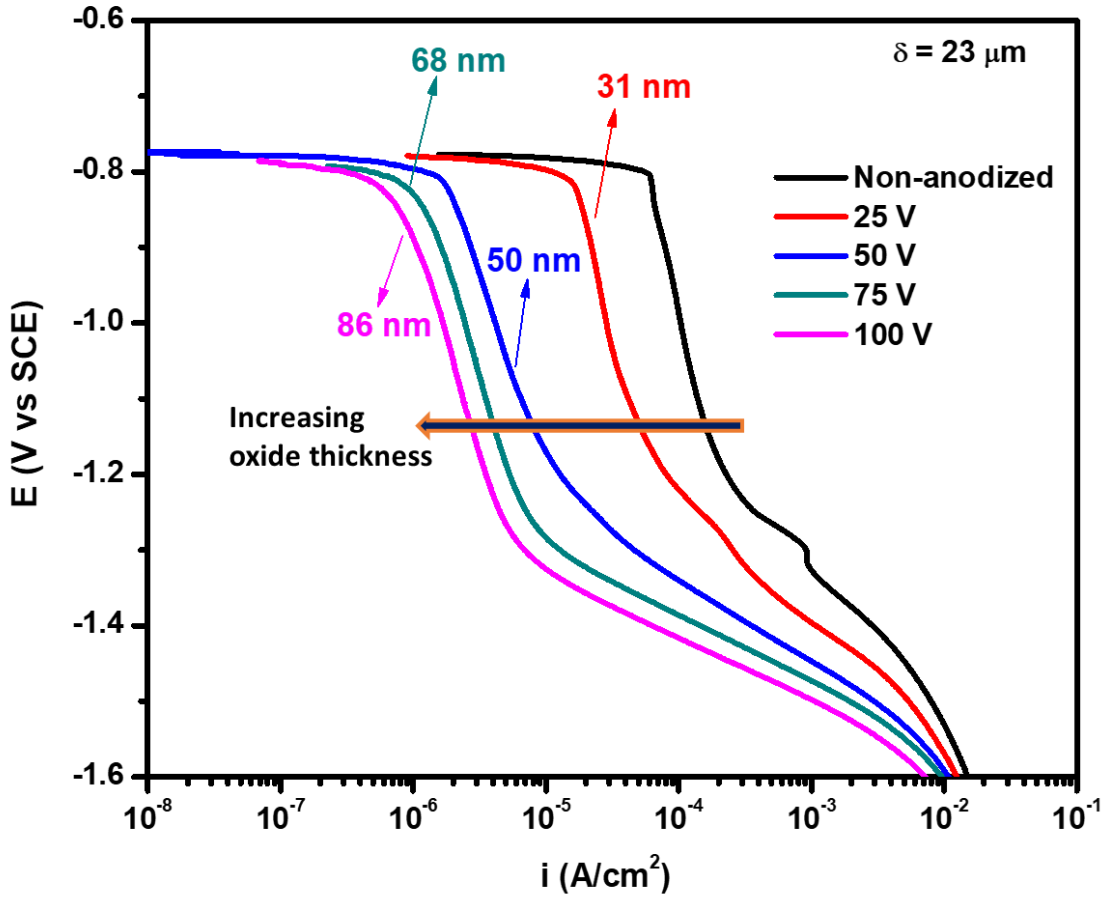

Figure 2.14. Impact of oxide film thickness on the E-log i behavior of AA7075-T6 RDE in 0.6 M NaCl at 720 rpm. Oxide films were electrochemically grown on AA7075-T6 by anodizing at various elevated voltages in 3 wt% ammonium tartrate for 4 min prior to the application of single frequency EIS at 1 kHz for 1 h to obtain oxide film capacitance for estimation of oxide film thickness using the relation: $d_{ox} = \frac{\varepsilon\varepsilon_o}{C}$*, where C is capacitance,* ε_o *is vacuum permittivity (= 8.85 x* 10^{-12} *F/m), and* ε *is the dielectric constant (= 9, assuming the oxide film is* γ*-*Al_2O_3*).*

2.5.3 Primary vs. Secondary Mode of Inhibition of AA7XXX by Chromate

At issue is whether or not chromate is an effective cathodic inhibitor of the ORR on AA7XXX under atmospheric conditions. The analysis shown in Figure 2.7b revealed that the addition of a small concentration of chromate (10^{-4} M) which represents early times of chromate leaching out of a coating system in response to potential change signaling the onset of corrosion, would dramatically decrease cathodic current density. This concentration of chromate barely raises the pitting potentials of AA7075 and AA7050.[32,33] Much higher chromate concentrations, > 10^{-3} M, are required to raise the pitting potentials of AA7075 appreciably.[31,32] Thus, the cathodic inhibition may be the first and primary step in the protection afforded by chromate in service applications. XPS analyses of chromate-exposed AA7050 and Pt surfaces (Figures 2.8b and 2.10b) revealed a Cr^{3+}-rich film consisting of Cr_2O_3 and $Cr(OH)_3$. These Cr^{3+} species are hypothesized to constitute an irreversible barrier film over the Cu-rich IMPs, directly inhibiting ORR on the cathodically-catalytic phases, e.g., Al_7Cu_2Fe, and indirectly through passivation of the anodically-active phases, e.g., Al_2CuMg which minimizes Cu replating. Anodic inhibition through elevation of pitting potentials would then be a secondary effect which enhances with increasing chromate concentration, making the material surface increasingly more resistant to pitting. Damage suppression on AA7XXX at OCP occurs because the Cr^{6+} to Cr^{3+} reduction reaction is thermodynamically stable over the OCP range of these alloys such that subsequent cathodic polarization does not aggravate damage (Figure 2.12).

2.5.4 Chromate Concentration and Oxygen Availability Influence Mechanism of Corrosion Protection of AA7XXX by Chromate

Corrosion inhibitors can be classified as anodic, cathodic or mixed based on the partial reaction in the corrosion couple that they predominantly retard. Anodic inhibitors primarily retard anodic reactions, typically by stabilizing protective native oxide films on metal surfaces; cathodic inhibitors primarily retard cathodic reactions by forming or precipitating a low porosity film of an insoluble oxide/hydroxide or salt on the metal surface.[59,60] This film is adherent and electronically non-conductive, and thus, restricts the diffusion of oxygen to the metal surface. Mixed inhibitors retard both anodic and cathodic reactions. Based on Mixed Potential Theory, the change in OCP coupled with its effect on corrosion rate on addition of the inhibitor is key to

identifying which electrochemical reaction is being affected. A positive change in OCP combined with a decreased corrosion rate indicates anodic inhibition, whereas a negative change in OCP combined with a decreased corrosion rate indicates cathodic inhibition; little or no change in OCP indicates similar levels of inhibition of both reactions.[60]

Inferences can therefore be made from the observed trend in the change in OCP and corrosion rate as a function of chromate concentration of both AA7XXX alloys (Figure 2.7a) and its relation to protection of a scribe by chromate leaching. At early leach times after a coating breach when the inhibitor concentration in the scribe is small, inhibition of both Al dissolution and cathodic ORR is implicated given the slight positive change in OCP at 10^{-4} M chromate. It is speculated that at this early stage in the leaching process, chromate migrates to the local corroding region(s) on the metal surface and promotes repairs of the oxide film by interacting with the metal ions to form stable oxide or hydroxide complexes. The ORR activity on the adjacent cathodic site, e.g., at a Cu-rich IMP may also be impacted; this may be more important as stated earlier. At longer leach times when the inhibitor concentration is high, cathodic ORR is predominantly suppressed. This interpretation is supported by the relatively large negative change in OCP of both AA7XXX alloys as the chromate concentration is increased, largely in agreement with the literature.[32,33] Higher chromate concentrations made available at longer leach times promote more global chromate anion transport for adsorption and subsequent reduction to form a Cr^{3+}-rich film over the entire electrode surface. The Cr^{3+}-rich film then blocks adsorption and diffusion of oxygen and chloride ions to the electrode surface. The Cr^{3+} film forms irreversibly (Figure 2.11), further supporting the notion that the Cr^{6+} to Cr^{3+} reduction products are tightly bound to Al alloy surfaces and limit electron transfer to effectively block ORR cathodic sites.[21,22] The inhibition of ORR on inert Pt on exposure to 10^{-2} M chromate occurred with attendant negative change in OCP (Figure 2.10a), lending further support to the intrinsic ability of chromate to function as a cathodic inhibitor without the requirement of a native oxide layer in order for chromate to adsorb and be subsequently reduced to Cr^{3+}. In contrast, the OCP was ennobled on AA7050 exposed to chromate in O_2-depleted conditions (Figure 2.13). Based on this result, it is speculated that chromate activity in deaerated conditions may be primary suppression of anodic Al dissolution even though ORR kinetics may still be reduced. This notion is consistent

with the observations made by Clark and coworkers[26] in their investigation of AA2024-T3 in deaerated 0.1 M NaCl where 5 mM dichromate addition had less effect on the cathodic ORR rates but more significant effect on passive current densities and pitting potentials compared to inhibitor-free conditions. This apparent discrepancy could possibly be due to a change from cathodic control of the electrochemical system in aerated conditions to anodic control in deaerated conditions. The threshold range of dissolved oxygen concentration in the deaerated chromate-containing system in the present study was estimated to be 2.5×10^{-10} mol/cm^3 (lower limit) to 8.6×10^{-9} mol/cm^3 (upper limit). It is hypothesized that below this critical range of dissolved oxygen concentration in solution, chromate at 10^{-2} M switches from a predominantly cathodic inhibitor to a predominantly anodic inhibitor; increasing the chromate concentration would not affect cathodic reactions but would affect anodic kinetics by lowering the passive current density and raising the pitting potential. OCP would increase with attendant decrease in corrosion current density according to Mixed Potential Theory.

2.5.5 Degree of ORR Suppression on AA7XXX by Chromate Depends on Cu Content of Alloy

The degree of suppression appears to be a function of the Cu content in the Al alloy, increasing as alloy Cu content decreases. Regardless of temper, AA7075 contains 1 wt% less Cu than AA7050 (Table 2.1) and exhibits better performance than the latter with 10^{-4} M chromate to the extent that increasing the chromate concentration to up to 10^{-2} M does not add significant additional benefits. In contrast, up to 10^{-3} M chromate is needed for the kinetics on AA7050 to be suppressed to the level attained on AA7075 with 10^{-4} M chromate. For Cu-containing Al alloys, the tendency for more surface area to be covered by Cu-rich IMPs and replated Cu (i.e., cathodic favored sites) increases with Cu content.[5,61] It therefore follows that as the Cu content of AA7XXX increases, higher chromate concentration may be required to form a thick enough barrier film over the Cu-rich IMPs and any replated Cu to adequately suppress ORR rates. The same logic can be applied to the Pt electrode. The Pt electrode utilized in this work is considered to be a homogeneous electrode (analogous to pure Cu electrode) in the sense that ORR occurs at the same rate over the entire surface. Chromate at 10^{-2} M decreases ORR kinetics on Pt by just an order of magnitude, indicating that further suppression of ORR requires higher inhibitor concentrations than 10^{-2} M (Figure 2.10a).

2.5.6 Cu-rich IMPs Enhance Formation of Metallic Cr on AA7050-T7451 on Exposure to Chromate

XPS analyses revealed the formation of a Cr^{3+}-rich layer with minor incorporation of Cr^{6+} on both AA7050 and Pt surfaces on exposure to 10^{-2} M chromate at potentials ≥ -1.2 V_{SCE}. This finding is consistent with similar analysis carried out on AA2024-T3.[25] In the present work, it appeared some Cr^{3+} were further reduced to Cr^0. This particular finding has not been previously reported in the literature on chromate effects on Al-Zn-Mg-Cu alloys in NaCl solutions. One possible explanation could be the photoreduction of the higher valence Cr species during XPS exposure. However, reports in the literature have only demonstrated the photoreduction of Cr^{6+} to CrO_2, and no indication of the photoreduction of Cr^{3+} to Cr^0.[36,37] In the present study, no CrO_2 peaks were observed which would have been detected at a binding energy of 575.2 eV, [37,38] and so, the impact of XPS exposure on Cr oxidation state could be eliminated.

From the viewpoint of thermodynamics, it is interesting to note that the Cr^{3+} to Cr^0 reduction reaction is not energetically favorable on pure Cr under the conditions of this study. Nonetheless, the reaction appeared favorable on AA7050 surface, an indication of underpotential deposition (UPD) of metallic Cr on AA7050. The process of UPD seemingly violates the Nernst equation and necessitates the anomalous electrodeposition of a less noble metal phase on a more noble metal substrate at more positive potentials relative to the reversible Nernst potential for deposition of the less noble metal on itself.[62] The E-pH diagram displayed in Figure 2.15a shows that the Cr^{3+} to Cr^0 reduction on AA7050 at pH 8.3 corresponding to the pH of the test solution (0.6 M NaCl + 10^{-2} M chromate) occurs at a higher potential E ≥ -0.959 V_{SHE} (≥ -1.2 V_{SCE}) than its reversible (or equilibrium) potential at E ≤ -1.07 V_{SHE} (≤ -1.311 V_{SCE}), giving a minimum underpotential shift of 0.111 V_{SCE}. In light of the concept of UPD, it is conjectured that the deposition of Cr^0 is confined to the Cu-rich IMPs because Cu is the only stable major metallic species in AA7050 in the potential range investigated in this study, as is evident on the E-pH diagram of Cu superposed on that of Cr in Figure 2.15b. The relatively non-existent Cr^0 in the chromate-induced layer on Pt implies that surface conditions on Pt in this work were not favorable for UPD of Cr. It is probable that the deposited Cr^0 provided additional barrier to the

diffusion of oxygen to the Cu-rich IMPs on AA7050, further inhibiting ORR as opposed to the case on Pt.

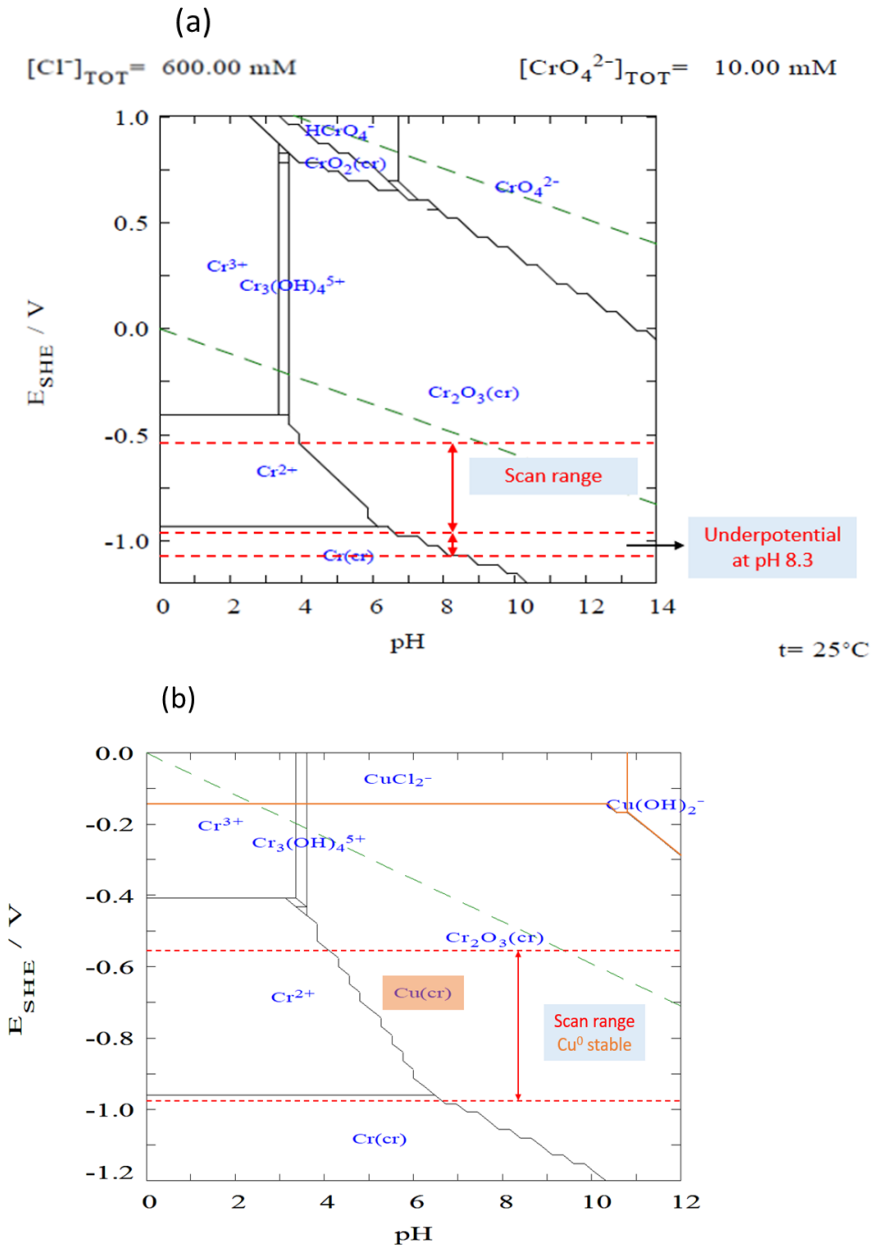

Figure 2.15. E-pH diagram of (a) Cr under the conditions of study showing underpotential shift for UPD of Cr^0 on AA7050 surface; (b) Cu superposed on that of Cr in (a) showing the stability of Cu^0 within the potential range of interest. E-pH diagrams were constructed with Medusa™ software.

2.5.7 Ramifications Towards Corrosion-Induced Fatigue Crack Initiation Life

It is well established that corrosion features, e.g., pits, have a deleterious effect on the fatigue life of Al-based components in the sense that they can serve as initiation sites for fatigue cracks.[63-67] Therefore, it is of utmost importance to retard stable pit formation and growth rates on these alloys when operating in fatigue-prone service conditions. The results of the present study indicate that the presence of chromate may slow the pit-to-crack transition rates on AA7050 and AA7075 through the suppression of the cathodic current available to support stabilization and growth of metastable pits. The implication would be an improvement in fatigue life. This supposition agrees with the results of previous work on chromate effects on the crack nucleation and early stage crack propagation on AA7XXX alloys exposed to chloride solutions.[68-71] Chromate was shown to improve the pit-to-crack transition life through slowing the development of pitting corrosion, as well as slow the growth rates of small cracks, attributed to the formation of Cr^{3+}-rich films which were posited to act as barrier to hydrogen production and subsequent embrittlement of the crack tip.[68-71]

It should be noted that the results of the present work may be different when extended to complex geometries, such as fastener holes, where the bare noble fasteners and the adjacent corroding Al matrix located far away from the surface may not benefit from the chromate inhibition concentrated at the surface. In such cases, the growth of any existing corrosion pits or fissures would be sustained by the large cathodic currents provided by the noble fastener,[72,73] thus, accelerating fatigue crack initiation and subsequent crack propagation rates.

2.6 Conclusions

The work presented herein experimentally assessed the effects of aqueous chromate on the mass-transport-limited ORR behavior of AA7XXX alloys under thin film electrolyte conditions representative of atmospheric exposure. Based on the results, the following conclusions were made:

- Chromate suppressed ORR kinetics on AA7050 by up to two orders of magnitude over the chromate-free case; the effect became greater with thinner diffusional boundary layer as rotation rate increased.
- Chromate was reduced irreversibly to form a Cr^{3+}-rich film on the electrode surface that blocked cathodic sites and hindered ORR. ORR inhibition was sustained when chromate was subsequently removed from solution.
- Comparison of AA7050 and AA7075 electrochemical behaviors indicated that same trends may apply across AA7XXX alloys; however, the degree of inhibition may be smaller as the Cu content of alloy increases. Better corrosion performance on AA7075 upon addition of chromate was attributed to its lower Cu content, and hence, reduced cathodic area (fewer Cu-rich IMPs and/or less Cu replating) requiring lower concentration of chromate to adequately suppress ORR kinetics.
- Surface film after cathodic polarization in chromate consisted of mixed Cr^{3+}/ Cr^{6+} oxides with some underpotentially deposited Cr^{0} on AA7050 surface. Cu-rich IMPs on AA7050 were speculated to promote the UPD of Cr.
- Chromate acted as an intrinsic cathodic inhibitor on Pt by forming a Cr^{3+}-rich surface film that reduced ORR kinetics on Pt by up to one order of magnitude.

2.7 References

1. T. Dursun and C. Soutis, *Mater. Des.* **56**, 862 (2014).
2. A. Azarniya, A. K. Taheri, and K. K. Taheri, *J. Alloys Compd.* **781**, 945 (2019).
3. J. R. Davis, *Corrosion of Aluminum and Aluminum Alloys*, ASM International, West Conshohocken, PA (1999).
4. N. Birbilis and R. G. Buchheit, *J. Electrochem. Soc.* **152**, B140 (2005).
5. Q. Meng and G. S. Frankel, *J. Electrochem. Soc.* **151**, B271 (2004).
6. M. A. Jakab, D. A. Little, and J. R. Scully, *J. Electrochem. Soc.* **152**, B311 (2005).
7. D. A. Little, M. A. Jakab, and J. R. Scully, *Corrosion* **62**, 300 (2006).
8. A. Boag, A. E. Hughes, A. M. Glenn, T. H. Muster, and D. McCulloch, *Corros. Sci.* **53**, 17 (2011).

9. Y. Zhu, K. Sun, and G. S. Frankel, *J. Electrochem. Soc.* **165**, C807 (2018).
10. J. Li, N. Birbilis, and R. G. Buchheit, *Corros. Sci.* **101**, 155 (2015).
11. V. N. Rafla, A. D. King, S. Glanvill, A. Davenport, and J. R. Scully, *Corrosion* **74**, 5 (2018).
12. G. O. Ilevbare, O. Schneider, R. G. Kelly, and J. R. Scully, *J. Electrochem. Soc.* **151**, B453 (2004).
13. O. Schneider, G. O. Ilevbare, J. R. Scully, and R. G. Kelly, *J. Electrochem. Soc.* **151**, B465 (2004).
14. O. Schneider, G. O. Ilevbare, R. G. Kelly, and J. R. Scully, *J. Electrochem. Soc.* **154**, C397 (2007).
15. M. W. Kendig and R. G. Buchheit, *Corrosion* **59**, 379 (2003).
16. M. Kendig, S. Jeanjaquet, R. Addison, and J. Waldrop, *Surf. Coatings Technol.* **140**, 58 (2001).
17. G. S. Frankel and R. L. Mccreery, *Electrochem. Soc. Int.* 34 (2001).
18. J. Zhao, G. S. Frankel, and R. L. Mccreery, *J. Electrochem. Soc.* **145**, 2258 (1998).
19. J. D. Ramsey and R. L. Mccreery, *J. Electrochem. Soc.* **146**, 4076 (1999).
20. J. Zhao, L. Xia, A. Sehgal, D. Lu, R. L. McCreery, and G. S. Frankel, *Surf. Coatings Technol.* **140**, 51 (2001).
21. G. O. Ilevbare and J. R. Scully, *J. Electrochem. Soc.* **148**, 196 (2001).
22. G. O. Ilevbare and J. R. Scully, *Corrosion* **57**, 134 (2001).
23. G. O. Ilevbare, J. R. Scully, J. Yuan, and R. G. Kelly, *Corrosion* **56**, 227 (2000).
24. A. Sehgal, G. S. Frankel, B. Zoofan, and S. Rokhlin, *J. Electrochem. Soc.* **147**, 140 (2000).
25. A. Kolics, A. S. Besing, and A. Wieckowski, *J. Electrochem. Soc.* **148**, 322 (2001).
26. W. J. Clark, J. D. Ramsey, R. L. McCreery, and G. S. Frankel, *J. Electrochem. Soc.* **149**, B179 (2002).
27. Y. Baek and G. S. Frankel, *J. Electrochem. Soc.* **150**, B1 (2002).
28. D. Chidambaram, M. J. Vasquez, G. P. Halada, and C. R. Clayton, *Surf. Interface Anal.* **35**, 226 (2003).
29. D. Chidambaram, C. R. Clayton, M. W. Kendig, and G. P. Halada, *J. Electrochem. Soc.* **151**, B613 (2004).

30. Q. Meng and G. S. Frankel, *Corrosion* **60**, 897 (2004).
31. S. C. Morton and G. S. Frankel, *Mater. Corros.* **65**, 351 (2014).
32. R. K. Gupta, B. R. W. Hinton, and N. Birbilis, *Corros. Sci.* **82**, 197 (2014).
33. V. N. Rafla and J. R. Scully, *Corrosion* **75**, 587 (2019).
34. S. T. Pride, J. R. Scully, and J. L. Hudson, *J. Electrochem. Soc* **141**, 3028 (1994).
35. D. Chidambaram, C. R. Clayton, G. P. Halada, and M. W. Kendig, *J. Electrochem. Soc.* **151**, B605 (2004).
36. G. P. Halada and C. R. Clayton, *J. Electrochem. Soc.* **138**, 2921 (1991).
37. D. Chidambaram, G. P. Halada, and C. R. Clayton, *Appl. Surf. Sci.* **181**, 283 (2001).
38. G. Thurner and P. H. Holoway, *Acta Phys. Pol. A* **81**, 273 (1992).
39. A. J. Bard and L. R. Faulkner, *Electrochemical Methods: Fundamentals and Applications*, 2nd ed., John Wiley & Sons, Inc., New York (2001).
40. V. G. Levich, *Acta Physicochim. Urss* **17**, 257 (1942).
41. C. Liu, J. Srinivasan, and R.G. Kelly, *J. Electrochem. Soc.* **164**, C845 (2017).
42. S. Guo, "*The Distribution of pH within Corrosion Crevices without External Surface*," in Aluminum Alloys '90, held Oct. 9-13 (Beijing, China: International Academic Publishers, 1990).
43. K. S. Ferrer and R. G. Kelly, *Corrosion* **58**, 452 (2002).
44. M. P. Ciccone, R. P. Gangloff, and R. G. Kelly, *Corrosion* **61**, 571 (2005).
45. C. S. Ho, L. K. Ju, R. F. Baddour, and D. I. C. Wang, *Chem. Eng. Sci.* **43**, 3093 (1988).
46. R. N. Adams, *Electrochemistry at Solid Electrodes*, Marcel Dekker Inc., New York (1969).
47. J. Nikolic, E. Exposito, J. Iniesta, J. Gonzalez-Garcia, and V. Montiel, *J. Chem. Educ.* **77**, 1191 (2000).
48. M. Becker, *Heat Transfer: A Modern Approach*, Springer, New York (1986).
49. Y. L. Cheng, Z. Zhang, F. H. Cao, J. F. Li, J. Q. Zhang, J. M. Wang, and C. N. Cao, *Corros. Sci.* **46**, 1649 (2004).
50. G. S. Frankel, M. Stratmann, M. Rohwerder, A. Michalik, B. Maier, J. Dora, and M. Wicinski, *Corros. Sci.* **49**, 2021 (2007).
51. O. Dolgikh, A. C. Bastos, A. Oliveira, C. Dan, and J. Deconinck, *Corros. Sci.* **102**, 338 (2016).

52. C. Amatore, S. Szunerits, L. Thouin, and J. S. Warkocz, *J. Electroanal. Chem.* **500**, 62 (2001).
53. N. D. Tomashov, *Corrosion* **20**, 7t (1964).
54. K. Ogle, M. Serdechnova, M. Mokaddem, and P. Volovitch, *Electrochim. Acta* **56**, 1711 (2011).
55. M. B. Vukmirovic, N. Dimitrov, and K. Sieradzki, *J. Electrochem. Soc.* **149**, B428 (2002).
56. M. J. Pryor and D. S. Kern, *J. Electrochem. Soc.* **102**, 605 (1955).
57. M. A. Heine and M. J. Pryor, *J. Electrochem. Soc.* **110**, 1205 (1963).
58. J. C. Seegmiller, R. C. Bazito, and D. A. Buttry, *Electrochem. Solid-State Lett.* **7**, B1 (2004).
59. E. Mccafferty, *Introduction to Corrosion Science*, Springer, New York (2010).
60. P. R. Roberge, *Handbook of Corrosion Engineering*, McGraw-Hill, New York (1999).
61. C. Liu, P. Khullar, and R. G. Kelly, *J. Electrochem. Soc.* **166**, C153 (2019).
62. S. Szabó, *Int. Rev. Phys. Chem.* **10**, 207 (1991).
63. C. Lin and S. Yang, *Eng. Fract. Mech.* **59**, 779 (1998).
64. K. Jones and D. W. Hoeppner, *Corros. Sci.* **47**, 2185 (2005).
65. K. Jones and D. W. Hoeppner, *Int. J. Fatigue* **31**, 686 (2009).
66. P. S. Pao, C. R. Feng, and S. J. Gill, *Corrosion* **56**, 1022 (2000).
67. N. E. C. Co and J. T. Burns, *Int. J. Fatigue* **103**, 234 (2017).
68. W. J. Lee and S. I. Pyun, *Mater. Sci. Eng. A* **279**, 172 (2000).
69. X. F. Liu, S. J. Huang, and H. C. Gu, *Corros. Sci.* **45**, 1921 (2003).
70. K. R. Cooper and R. G. Kelly, *Corros. Sci.* **49**, 2636 (2007).
71. S. E. G. Dorman and Y. Lee, *Procedia Eng.* **10**, 1220 (2011).
72. Z. Feng, G. S. Frankel, W. H. Abbott, and C. A. Matzdorf, *Corrosion* **72**, 342 (2016).
73. R. S. Marshall, R. G. Kelly, A. Goff, and C. Sprinkle, *Corrosion* **75**, 1461 (2019).

3. Cathode Capacities of Cu-rich IMPs (micro-cathodes), Replated Cu and 316SS Fastener (macro-cathodes) to Support Fast Cathodic Reaction Rates on AA7050-316SS Galvanic Couple in the Presence of Chromate in Simulated Atmospheric Environments

3.1 Abstract

The driving forces of Cu-rich intermetallic particles (IMPs) on AA7050, 316SS and high-purity Cu to support galvanic-induced localized corrosion of the boldly exposed surface of AA7050 coupled to 316SS under simulated atmospheric conditions were assessed using the RDE technique. In a low chloride environment (i.e., 0.6 M NaCl), the cathodic kinetics on 316SS was suppressed by more than two orders of magnitude upon addition of 10^{-4} M chromate, and high-purity Cu produced the largest cathodic currents with and without chromate in solution. In an elevated chloride environment (i.e., 5 M NaCl), although cathodic kinetics in inhibitor-free conditions were generally lower than observed in the low chloride environment, chromate was assessed to be less effective on all the studied cathodes, with high-purity Cu remaining the most significant cathode. However, upon introduction of Al ions to the elevated chloride environment, cathodic reactions were accelerated on the electrodes regardless of the presence of chromate. In this situation, 316SS became the dominant cathode compared to high-purity Cu. The implications of these observations are discussed in light of real service environments.

3.2 Introduction

Structural aerospace aluminum alloy (AA) components are commonly joined with high-strength noble fasteners, notably 316SS, as an alternative to welding due to challenges encountered during traditional welding of precipitation-strengthened materials.[1] Although the structures are coated to mitigate galvanic-induced localized corrosion of the AA component, defects in these coating systems are inevitable during the operational and maintenance life cycles of the Al-based structures. In natural corrosive environments, including the thin electrolyte films present under atmospheric conditions, this situation would often create a macro-galvanic cell between the localized corrosion-susceptible base AA component and the 316SS, in which the AA

component may be polarized above its pitting potential, resulting in greater localized corrosion than if there was no external 316SS cathode.[2–6] The damage on the AA component, particularly the hidden corrosion fissures within the fastener hole coupled with the inherent high stresses imposed by the joint, can transition into fatigue cracks which would negatively impact the lifespan of the Al-based structure.[7]

Conventionally, chromate-based coating systems have been used to protect precipitation-strengthened AAs from corrosion. Upon creation of a defect, chromate is released from the coating in a controlled fashion and transports to the corroding site where it is reduced from its soluble and oxidizing Cr(VI) state to an insoluble and irreversible Cr(III) product that effectively protects the underlying corroding metal substrate from the aggressive environment. This universal mechanism has been shown to inhibit both anodic and cathodic reactions on base AAs in many environments.[8–13] That said, a number of studies have shown that macro-galvanic coupling can defeat chromate inhibition of these alloys.[3,4,14–16] It is noted that most of these studies were carried out on chromate-coated, scribed AA panels containing bare 316SS fasteners, where the 316SS fasteners were physically distant from any chromate that may have been released from the coating adjacent to the scribes. In addition, a measured concentration of chromate that might have leached out into the scribes was not reported. Although the SS fasteners utilized in actual service are bare, the joint surfaces are often coated after the fasteners have been installed. The present work will circumvent the leaching process and will utilize measured chromate concentrations to investigate the effectiveness of chromate in inhibiting cathodic reactions on 316SS and other cathodic contributors in a typical AA-316SS galvanic couple.

Atmospheric conditions complicate galvanic-induced corrosion of AA-316SS couples. Corrosion kinetics under atmospheric conditions can be markedly different from those under full immersion. Corrosion under full immersion can proceed continuously at a steady state for long periods of time due to the constant presence of bulk solution with stable solution chemistry at the metal surface. Atmospheric corrosion on the other hand is not a continuous process due to wet-dry cycling imposed by diurnal changes in temperature and relative humidity (RH). Changes

in electrolyte thickness affect solution chemistry which can impact the mass-transport-limited kinetics on the corroding metal. In natural atmospheric environments, the NaCl concentration equilibrates at ~ 0.6 M at 98% RH. However, as RH decreases, the thickness of the electrolyte layer decreases for a constant salt loading density, and the equilibrium chloride concentration increases. For instance, at 80% RH, the NaCl concentration equilibrates at ~ 5 M. An increase in the equilibrium chloride concentration that occurs as RH decreases can alter the electrochemical kinetics due to decreased oxygen solubility.[17] Katona et al.[18] reported a decrease in mass-transport-limited kinetics on Pt and 304SS with increasing chloride concentration. These considerations are important as most RH in service are well below 98%, and service environments also go through wet-dry cycles. Therefore, experiments limited to dilute chloride environments may not be representative of the service conditions of aerospace structures. In addition, the behavior of chromate may change with the aggressive conditions that prevail under thin electrolyte films.

This work will extend the RDE approach previously described in Chapter 2 to investigate the impact of chromate on the cathodic behavior of the micro- and macro-cathodes pertinent to AA7050-316SS galvanic couple in dilute and elevated chloride environments. The objective is to determine which cathode would be the more significant actor that would drive galvanic corrosion of AA7050 as a function of environment, and to assess the role of chromate in modifying their cathodic activity to mitigate the attack. It is noted that AA7050 is used to represent the Cu-rich IMPs with the assumption that cathodic activity occurs mainly on the more cathodically-catalytic Cu-rich IMPs covered with presumably more electronically conductive and/ or defective Cu-altered Al-rich oxide films in relation to the Al matrix covered with a more electronically insulating Al oxide film.[19,20] The average Cu-rich IMP size, spacing and area fraction on AA7050 were 10.3 μm^2, 9.0 µm, and 3%, respectively, estimated with Image J™ software.[21] High-purity Cu is used to represent Cu replated on AA7050 that results from the preferential dealloying of active elemental constituent(s) of the Cu-rich IMPs and subsequent electrodeposition on the surface.[22–24]

3.3 Experimental

3.3.1 Materials Preparation

The materials utilized in this work were AA7050-T7451 (obtained from ALCOA) in the form of 2" thick plates, 316SS (obtained from McMaster-Carr Supply Company) and 99.99 wt% Cu (obtained from Alfa Aesar), both in the form of 0.5" diameter rods. Table 3.1 shows the composition of AA7050-T7451 and 316SS. The samples were constructed in the rotating disk electrode (RDE) configuration with a diameter of 1.27 cm (exposed area 1.27 cm^2) surrounded by a PTFE holder with an internal Ni wire electrical connection. An AFASR rotator acquired from Pine Research was used to run the RDE experiments on AA7050, 316SS, and high-purity Cu. Studies were also conducted on a Pt RDE (exposed area 0.196 cm^2) fitted on an AFMSRCE rotator also obtained from Pine Research. Immediately preceding each experiment, the AA7050, 316SS and Cu RDEs were wet-ground successively from 120 grit to a surface finish of 1200 grit with SiC paper, rinsed in acetone and then with deionized water, and finally dried with clean compressed air. The Pt electrode was electrochemically cleaned with 10 cycles of cyclic voltammetry between -1.0 V and 1.0 V at 10 mV/s in 0.1 M H_2SO_4, rinsed with deionized water and dried with clean compressed air.

Table 3.1. Nominal Composition of AA7050-T7451 and 316SS (in wt%).

AA7050	**Zn**	**Mg**	**Cu**	**Fe**	**Si**	**Zr**	**Mn**	**Ti**	**Cr**	**Al**	
	6.7	2.6	2.6	0.15	0.12	0.15	0.1	0.06	0.04	balance	
316SS	**C**	**Mn**	**P**	**S**	**Si**	**Ni**	**Mo**	**Cu**	**Cr**	**N**	**Fe**
	0.019	1.75	0.039	0.028	0.46	10.16	2.05	0.44	17.03	0.071	balance

3.3.2 Electrochemical Measurements

Experiments were conducted on the samples in unbuffered 0.6 M NaCl (base pH 5.6) and 5 M NaCl (base pH 8.1) solutions and with additions of Na_2CrO_4 ranging from 10^{-4} M to 10^{-1} M. In separate experiments, 0.1 M Al^{3+} was added to the 5 M NaCl environment to simulate pre-corrosion of AA7050 leading to the release of Al^{3+} into a concentrated chloride environment. The pH of the solutions was measured but not adjusted.

Cathodic polarization scans were carried out after a 1 h exposure at open circuit in a standard three-electrode cell with a Pt-Nb mesh counter electrode and a saturated calomel electrode (SCE) as reference. The scans were performed from 0 V_{OCP} (in order to avoid surface alterations from prior anodic dissolution) to -1.2 V_{SCE} at a scan rate of 0.2 mV/s and at various rotation rates from 0 to 1440 rpm using a Gamry Reference 600+^{TM} potentiostat/galvanostat/ZRA. In inhibitor-free 0.6 M and 5 M NaCl solutions, electrochemical kinetics on Pt taken at a reference potential of -0.7 V_{SCE} were used to analyze the current density as a function of boundary layer thickness (δ) and to determine the effect of chloride concentration on boundary layer thickness.

Polarization curves were also generated on Cu electroplated on AA7050 in an attempt to more realistically simulate replated Cu on AA7050. Cu was plated onto AA7050 by potentiostatically holding AA7050 at -1 V_{SCE} for 600 s in 0.1 M $CuSO_4$ at pH 3. This produced ~ 800 nm thick layer of Cu on the AA7050 surface, calculated based on Faraday's law:

$$d_{Cu} = \frac{QW_{Cu}}{AnF\rho_{Cu}} \tag{3.1}$$

where Q is the quantity of charge passed, W is the molecular weight of Cu, A is the exposed area of the electrode, n is the number of electrons transferred, F is Faraday's constant and ρ is the density of Cu.

3.4 Results

The results presented herein experimentally assessed the influence of chromate on the cathodic behavior of the micro- and macro-cathodes pertinent to AA7050-316SS galvanic couple (as depicted in Figure 3.1) as a function of WL and chloride concentration representative of atmospheric environments. Cathodic polarization data on Pt RDE were employed to bound WL thickness corresponding to conditions typical of atmospheric exposure; an upper limit above which natural convection dominates the diffusion process and a lower limit below which flow regime transitions from laminar to turbulent conditions were defined and compared for both NaCl environments tested. In addition, the effect of chromate on Al^{3+} on the cathodes was

assessed to identify the probable dominant cathode that would drive damage propagation on AA7050-316SS galvanic couple after initiation of corrosion.

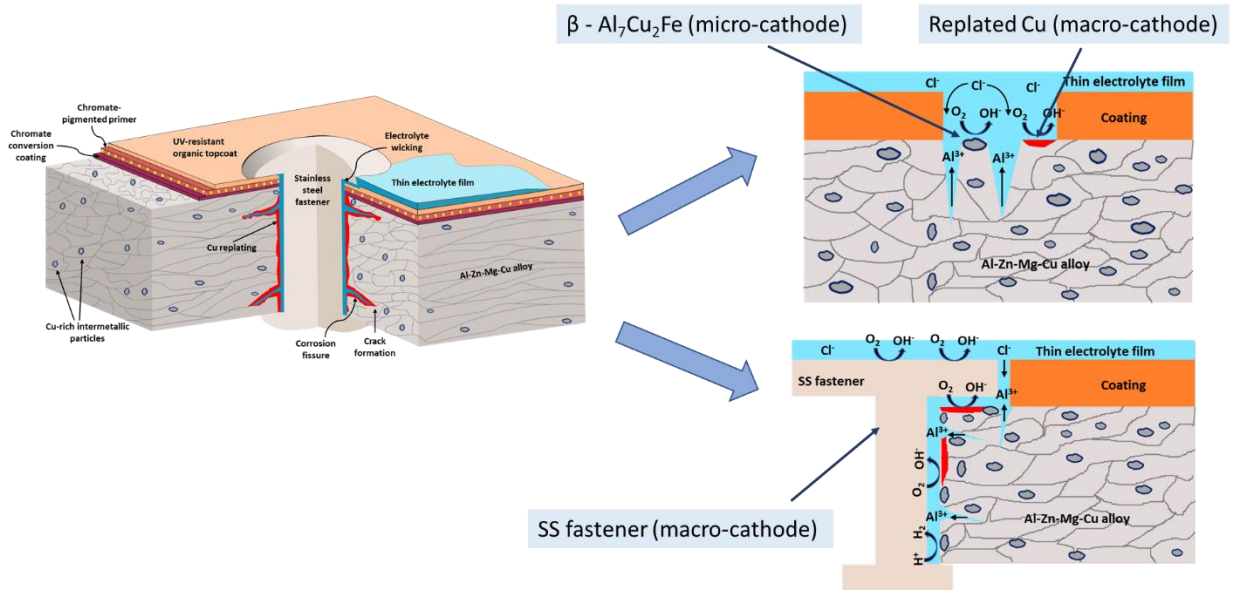

Figure 3.1. Depiction of cathodes in AA7050-316SS galvanic couple.

3.4.1 Cathodic Kinetics on 316SS and High-Purity Cu in Inhibitor-Free 0.6 M NaCl

The RDE technique described previously in Chapter 2 was utilized in this work to determine the probable dominant cathode in AA7050-316SS galvanic couple under thin electrolytes representative of atmospheric conditions. Figure 3.2 shows the cathodic polarization behaviors for 316SS and high-purity Cu RDEs in inhibitor-free 0.6 M NaCl. Boundary layer thickness values were previously determined on Pt RDE in Chapter 2. The orange bar highlights the range of AA7050 open circuit potentials (OCP), -0.75 V_{SCE} to -0.85 V_{SCE}, obtained under the same conditions and reported in Chapter 2. It is noted that Al alloys in these solutions are highly non-polarizable when considered anodes undergoing local corrosion, and so the AA7050-316SS/-Cu galvanic couple potentials are generally near the AA7050 OCP (Figure 3.3). It can be seen in Figure 3.2 that within the range of AA7050 OCP, the kinetics on Cu were slightly enhanced compared to the kinetics on 316SS, regardless of δ.

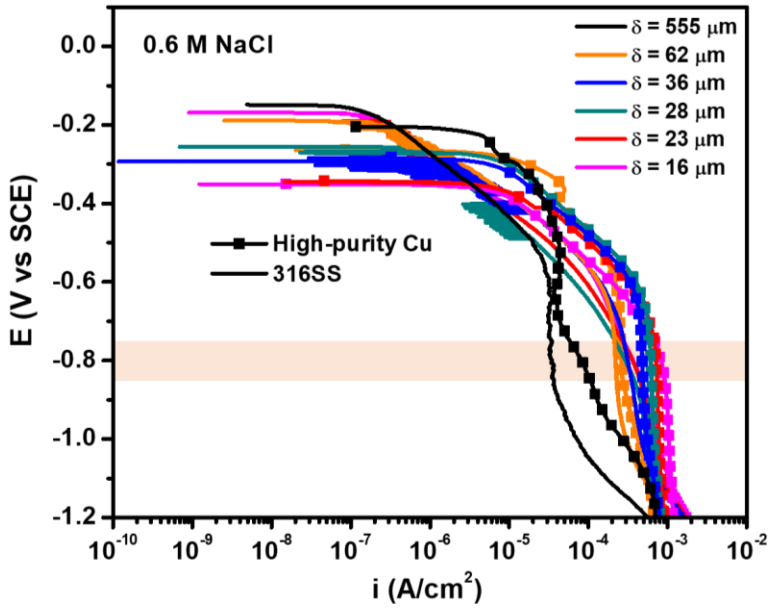

Figure 3.2. Cathodic polarization behaviors for 316SS and high-purity Cu RDEs in inhibitor-free 0.6 M NaCl pH 5.6. Orange box highlights the range of AA7050 OCP in the same environment.

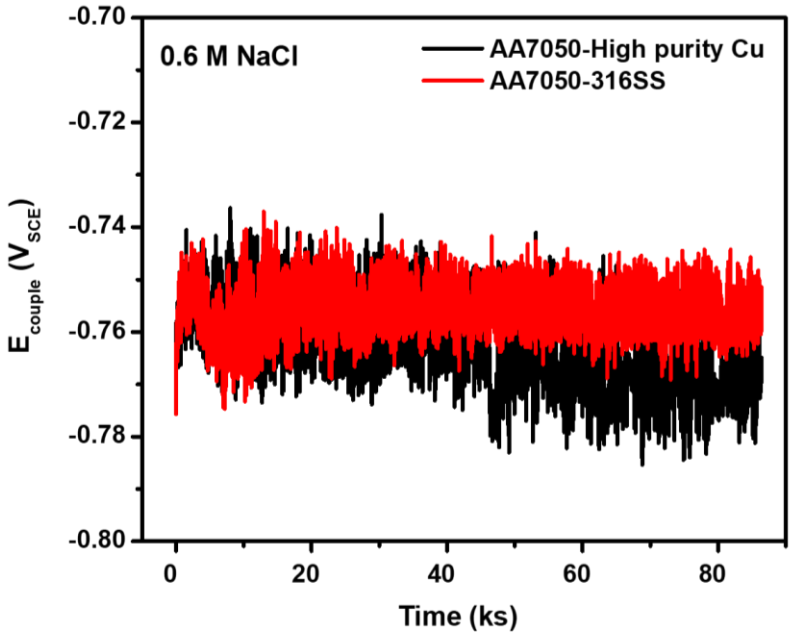

Figure 3.3. Galvanic couple potentials as a function of time on AA7050-high purity Cu and AA7050-316SS planar couples (cathode:anode area = 1) immersed in inhibitor-free 0.6 M NaCl pH 5.6.

Levich analysis was carried out on the polarization curves on 316SS and high-purity Cu at a reference potential of -0.8 V_{SCE} to extract the limiting current density data. The data were compared with those on Pt, AA7050, and Levich-predicted kinetics for the oxygen reduction reaction (ORR) based on oxygen diffusivity and solution viscosity values calculated with OLI™ Studio Analyzer 9.2. As illustrated in Figure 3.4, the kinetics on Cu very closely matched Levich-predicted kinetics across the range of δ, whereas the kinetics on 316SS was lower than Levich-predicted data and deviated from the linear ORR rate dependence on δ as δ decreased with increased electrode rotation rate.

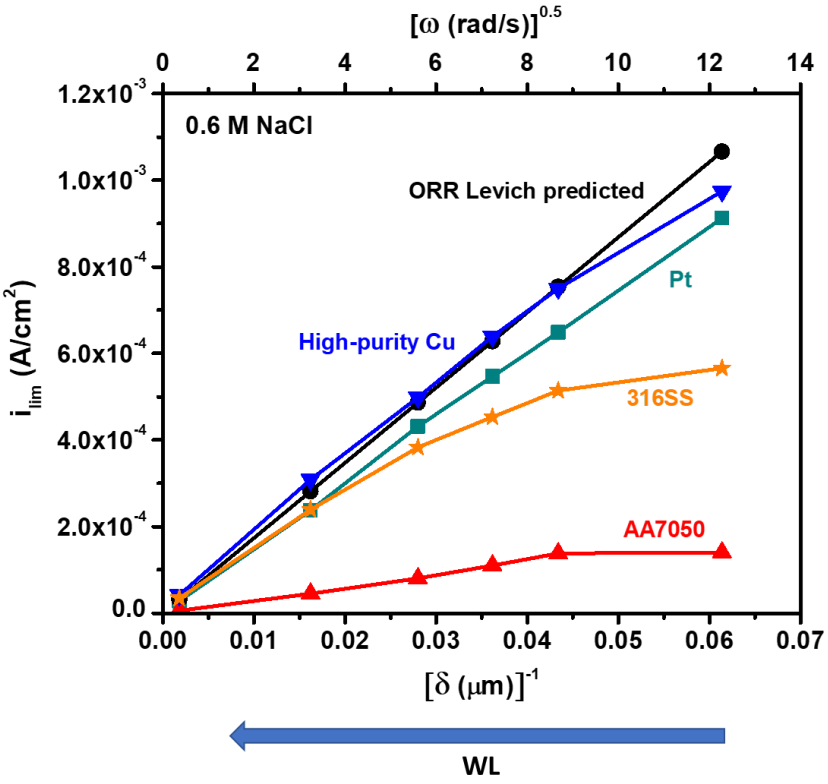

Figure 3.4. Mass-transport ORR kinetics on 316SS and high-purity Cu (taken at a reference potential of -0.8 V_{SCE}), AA7050 (taken at a reference potential of -0.95 V_{SCE}) and Pt (taken at a reference potential of -0.75 V_{SCE}) compared with Levich-predicted data in inhibitor 0.6 M NaCl (pH = 5.6) as a function of boundary layer thickness.

3.4.2 Effect of Chromate on Cathodic Kinetics on High-Purity Cu and 316SS in 0.6 M NaCl

The cathodic behavior of a high-purity Cu RDE in 0.6 M NaCl as a function of chromate concentration is presented in Figure 3.5. Generally, ORR kinetics decreased as chromate concentration increased. In the lowest chromate concentration used in this work, i.e., 10^{-4} M, kinetics were barely suppressed within the range of AA7050 OCP, and the degree of ORR suppression appeared to diminish with decreasing δ. When the chromate concentration was increased to 10^{-3} M, there was improved but small degree of suppression (less than an order of magnitude) across the range of δ. However, with the highest chromate concentration of 10^{-2} M, appreciable inhibition occurred independent of δ by at least an order of magnitude reduction compared to inhibitor-free conditions.

The effect of chromate on 316SS is presented in Figure 3.6. On exposure to chromate-containing 0.6 M NaCl, ORR current density on 316SS decreased by more than two orders of magnitude with no clear dependence on δ. The addition of the lowest concentration of chromate (i.e., 10^{-4} M) to solution dramatically reduced ORR kinetics by at least two orders of magnitude. Further additions of chromate did not add any significant benefits.

A comparison of the cathodic behaviors of high-purity Cu and 316SS is presented in Figure 3.7. It can be seen that chromate appears to perform better on 316SS than on high-purity Cu in 0.6 M NaCl regardless of δ. The lowest concentration of chromate (i.e., 10^{-4} M) suppressed kinetics on 316SS by at least two orders of magnitude whereas on high-purity Cu, as high as 10^{-2} M chromate was required to suppress kinetics by even one order of magnitude. The results at δ = 16 μm are summarized in Figure 3.8.

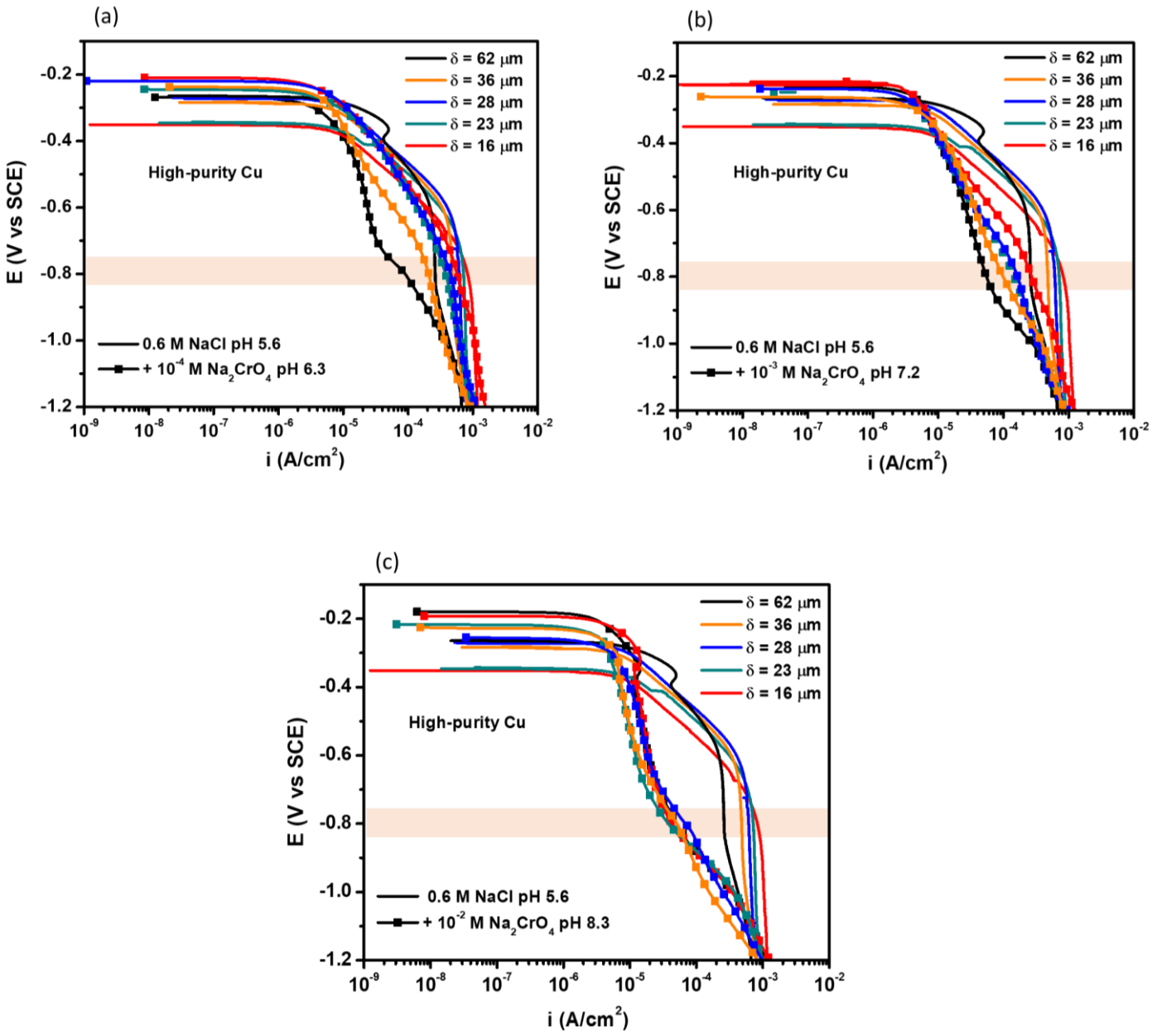

Figure 3.5. Cathodic polarization behavior of high-purity Cu RDE in 0.6 M NaCl pH 5.6 compared with behavior on addition of (a) 10^{-4} M Na_2CrO_4 pH 6.3, (b) 10^{-3} M Na_2CrO_4 pH 7.2, and (c) 10^{-2} M Na_2CrO_4 pH 8.3. Orange boxes highlight the range of AA7050 OCP in the same environments.

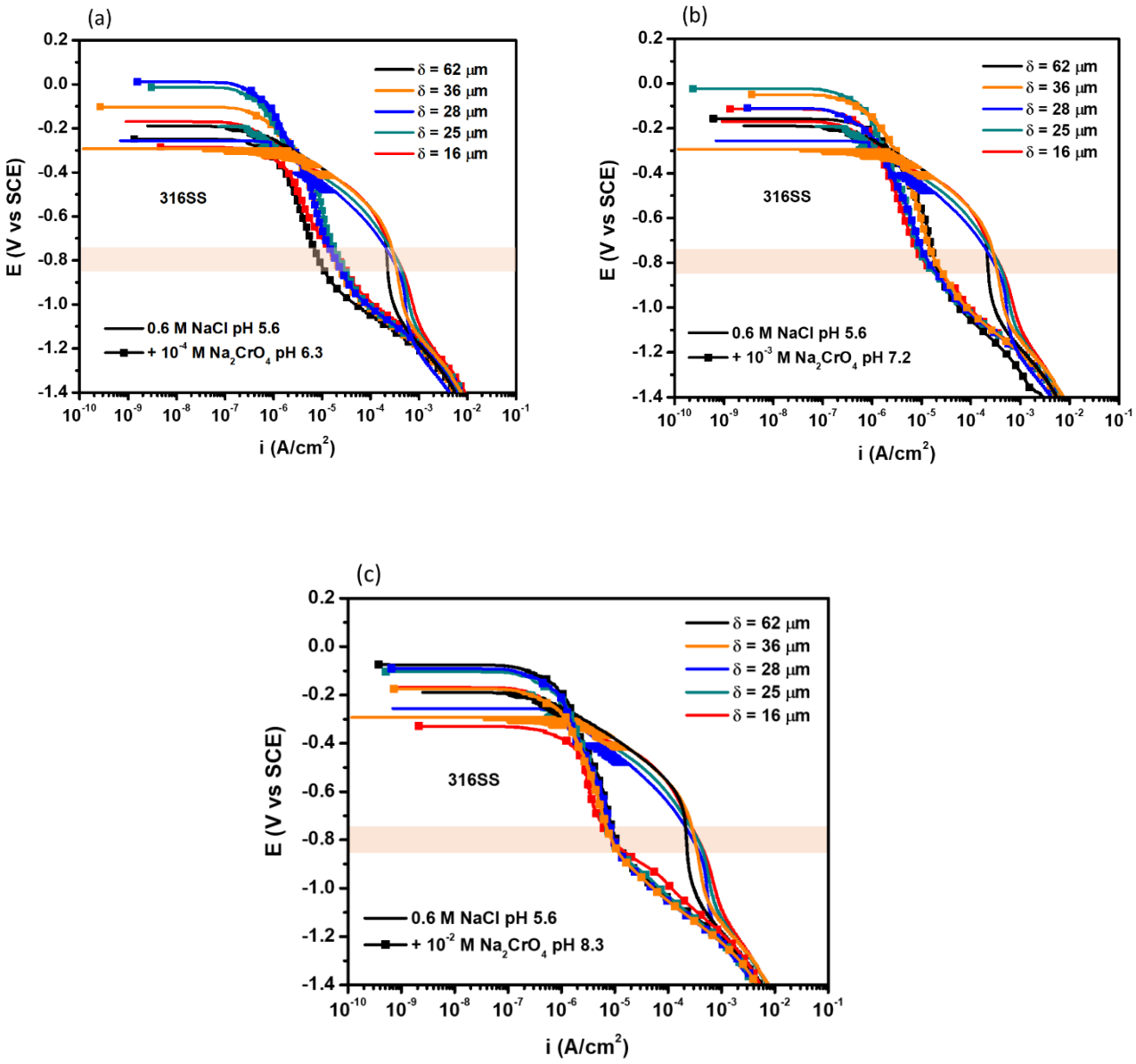

Figure 3.6. Cathodic polarization behavior of 316SS RDE in 0.6 M NaCl pH 5.6 compared with behavior on addition of (a) 10^{-4} M Na_2CrO_4 pH 6.3, (b) 10^{-3} M Na_2CrO_4 pH 7.2, and (c) 10^{-2} M Na_2CrO_4 pH 8.3. Orange boxes highlight the range of AA7050 OCP in the same environments.

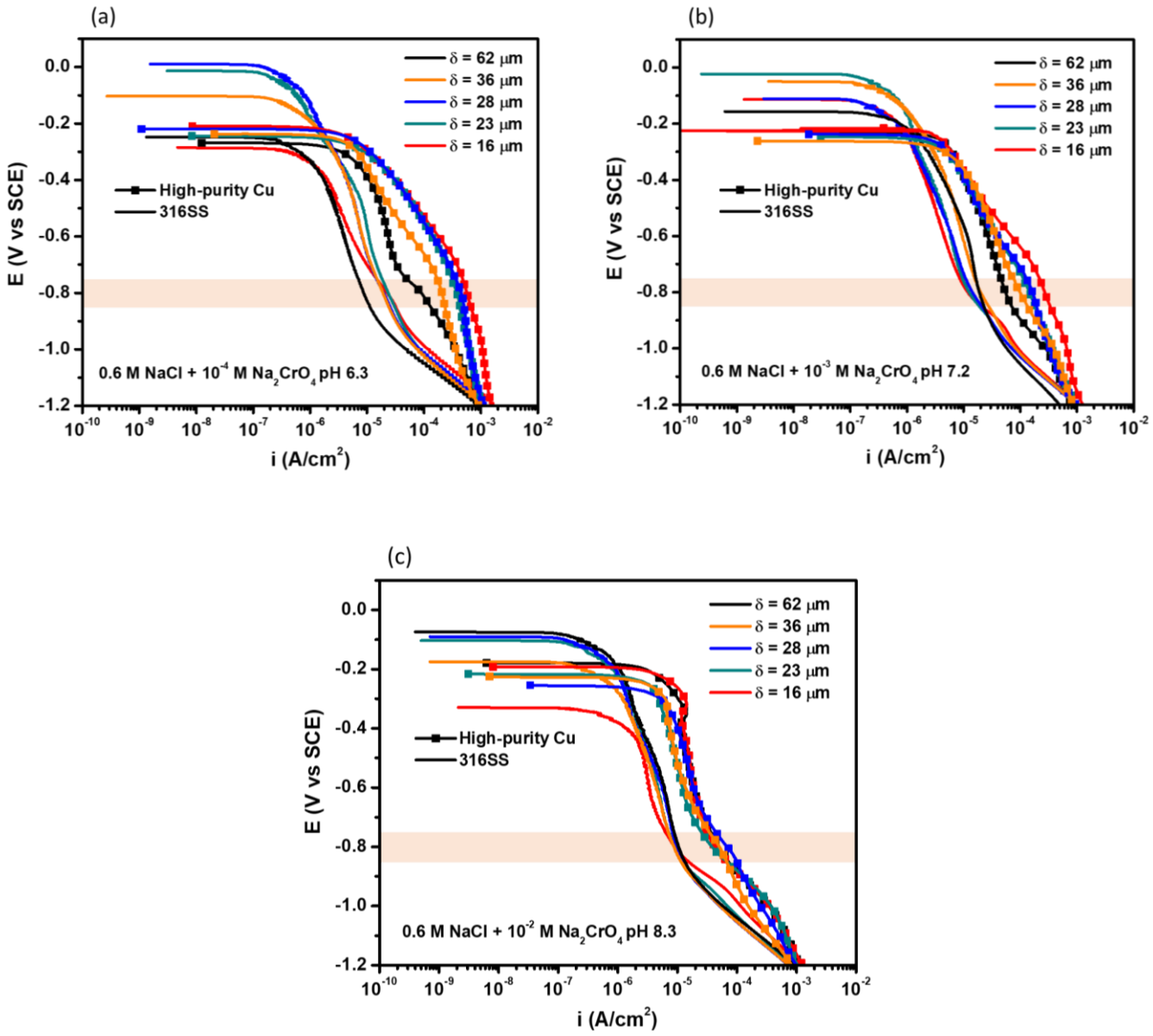

Figure 3.7. Comparison of the cathodic polarization behaviors of high-purity Cu and 316SS RDE in 0.6 M NaCl with addition of (a) 10^{-4} M Na_2CrO_4 pH 6.3, (b) 10^{-3} M Na_2CrO_4 pH 7.2, and (c) 10^{-2} M Na_2CrO_4 pH 8.3. Orange boxes highlight the range of AA7050 OCP in the same environments.

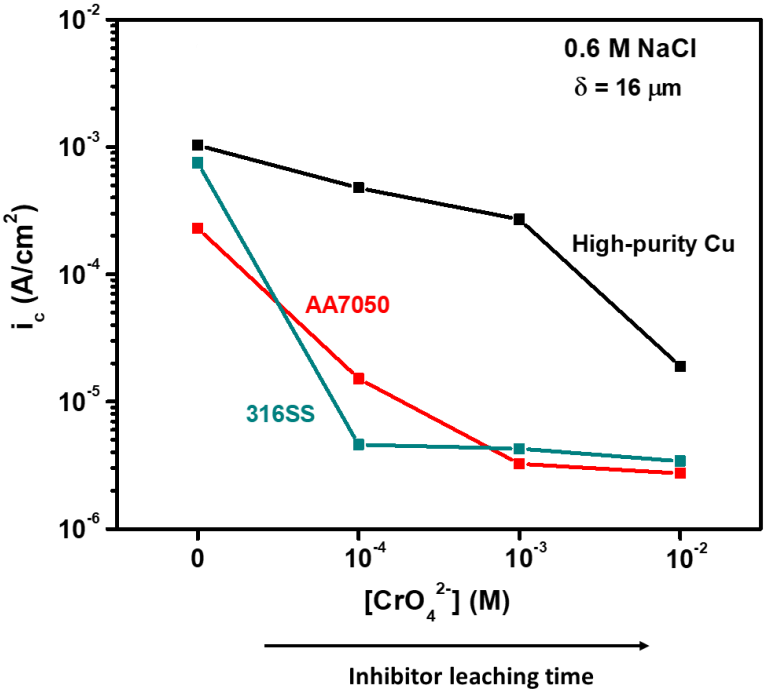

Figure 3.8. Comparison of the ORR behaviors of high-purity Cu, 316SS, and AA7050 in 0.6 M NaCl at δ = 16 μm as a function of chromate concentration.

To further investigate the effect of chromate on replated Cu on AA7050, similar experiments were carried out on Cu electroplated on AA7050 in an attempt to more realistically simulate replated Cu on AA7050. The scanned and optical surface images of the electroplated Cu on AA7050 in comparison with those of polished AA7050 and high-purity Cu are displayed in Figure 3.9. With the pre-determined threshold chromate concentration of 10^{-2} M required for appreciable ORR inhibition on high-purity Cu, cathodic polarization scans were carried out on Cu electroplated on AA7050 at different values of δ. The results were compared with those obtained on polished AA7050, high-purity Cu and 316SS electrodes, as displayed in Figure 3.10. Interestingly, it was observed that upon exposure to chromate, the degree of ORR inhibition on Cu electroplated on AA7050 compared to high-purity Cu was far less significant at all values of δ. In fact, inhibition did not occur under quiescent conditions which is consistent with the results of Rafla and Scully.[16] Nonetheless, the results suggest that regardless of WL, replated Cu may be more detrimental than 316SS to galvanic corrosion inhibition of AA7050 even at high bulk chromate concentrations.

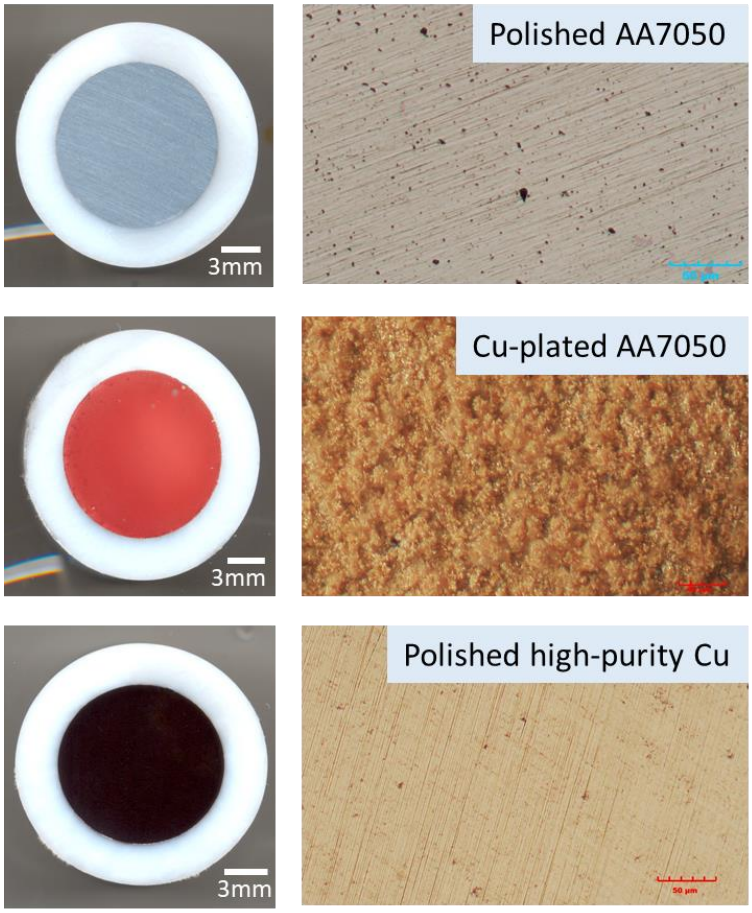

Figure 3.9. Scanned and optical images of polished AA7050, Cu electroplated on AA7050, and polished high-purity Cu.

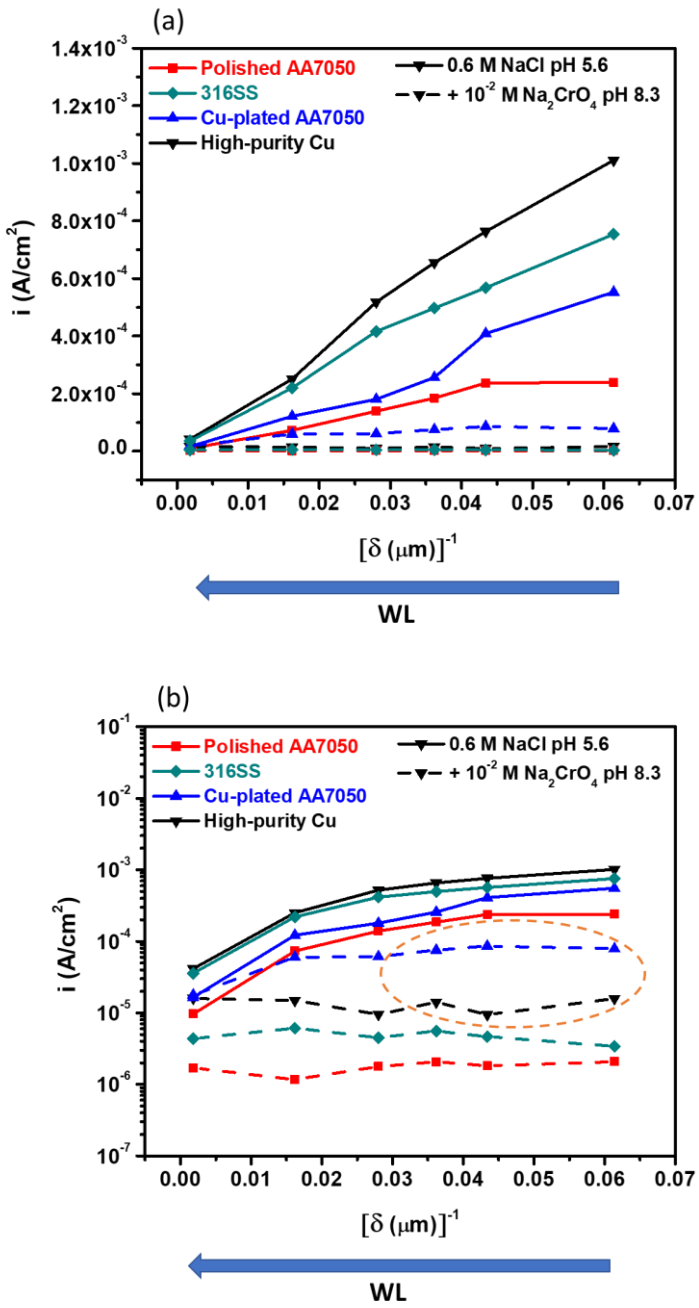

Figure 3.10. Comparison of the ORR current densities on polished AA7050, high-purity Cu, 316SS and Cu electroplated on AA7050 in 0.6 M NaCl and with the addition of 10^{-2} M Na_2CrO_4 as a function of boundary layer thickness. (a) Linear scale; (b) Semi-log plot. Orange oval in (b) highlights the differences in kinetics on high-purity Cu and Cu electroplated on AA7050 on addition of chromate.

3.4.3 Effect of Chloride Concentration on Boundary Layer Thickness

To determine if chloride concentration has any influence on boundary layer thickness, cathodic polarization scans were obtained on Pt RDE in 5 M NaCl and values of δ were determined using the same approach utilized previously in Chapter 2. Figure 3.11 shows the polarization curves obtained on Pt RDE in inhibitor-free 0.6 M NaCl and 5 M NaCl at various rotation rates. When comparing the two sets of polarization curves, it can be seen that the ORR limiting current density is reduced in 5 M NaCl compared to 0.6 M NaCl.

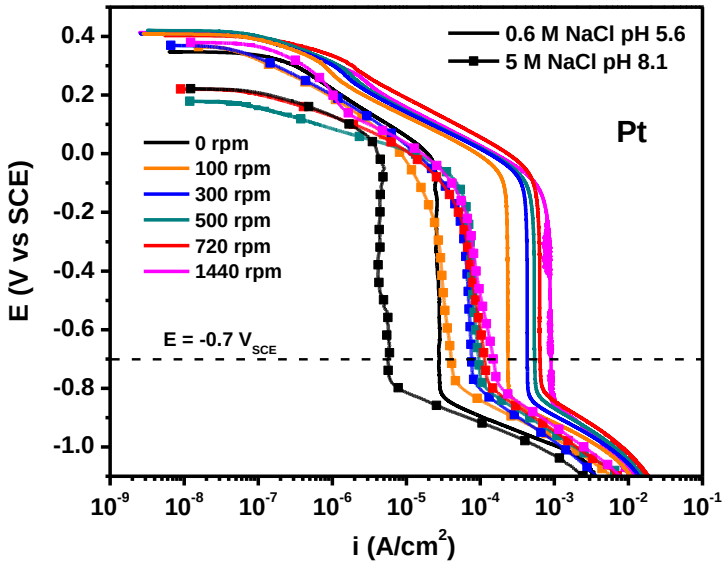

Figure 3.11. Cathodic polarization curves of Pt RDE in 0.6 M NaCl and 5 M NaCl as a function of electrode rotation rate.

OLI™ Studio Analyzer 9.2 was used to calculate the parameters - oxygen concentration (C_{O_2}), solution viscosity (ν), and oxygen diffusivity (D_{O_2}) - required for determining δ for rotated electrodes. The values of the parameters for 0.6 M NaCl and 5 M NaCl are shown in Table 3.2.

Table 3.2. Solution parameters used to estimate boundary layer thickness.

	0.6 M NaCl	5 M NaCl
C_{O_2}	2.3×10^{-7} mol/cm^3	9.0×10^{-8} mol/cm^3
v	9.2×10^{-3} cm^2/s	1.3×10^{-2} cm^2/s
D_{O_2}	2.0×10^{-5} cm^2/s	1.3×10^{-5} cm^2/s

The Levich analysis in combination with the technique proposed by Liu et al.[25] was utilized to define the natural convection boundary layer thickness, δ_{nc} (Figure 3.12). Data were taken from the two sets of polarization curves at a reference potential of -0.7 V_{SCE}. Values of the range of δ for both 0.6 M NaCl and 5 M NaCl are compared in Table 3.3. The results indicated that chloride concentration has a minimal effect on δ, even though there is a much greater effect on ORR limiting current density through its effect on oxygen concentration and diffusivity. The small decrease in δ with increase in chloride concentration is attributed to a greater decrease in diffusive mass transport in comparison to an overall increase in mass transport.[18]

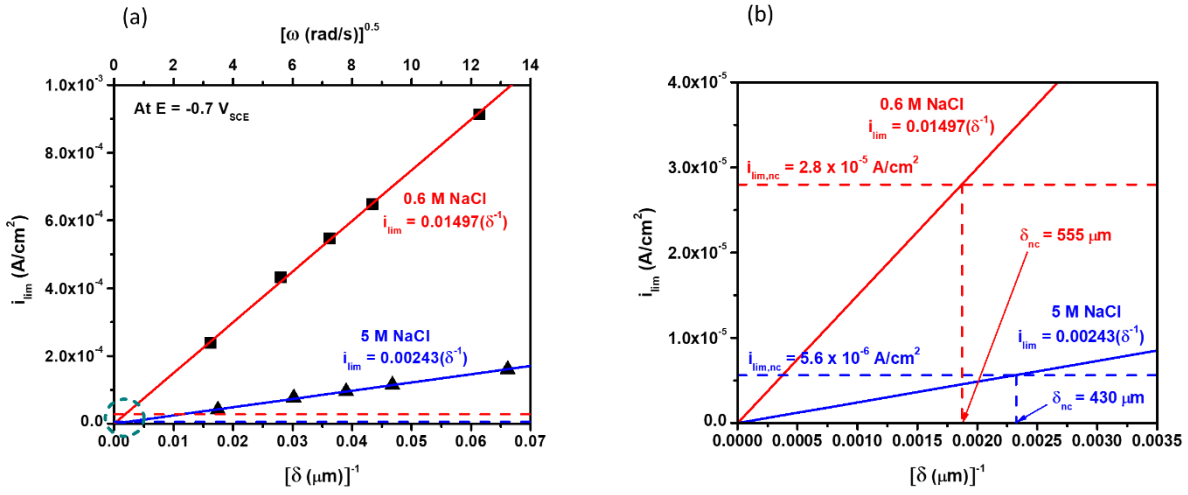

Figure 3.12. (a) ORR limiting current density on Pt shown in Figure 3.11 at -0.7 V_{SCE} as a function of boundary layer thickness; (b) Circled region in (a) zoomed-in to estimate natural convection boundary layer thickness in 0.6 M NaCl and 5 M NaCl.

Table 3.3. Boundary layer thickness values in 0.6 M NaCl and 5 M NaCl.

Rotation rate (rpm)		Quiescent	100	300	500	720	1440
Boundary layer thickness (μm)	0.6 M NaCl	555	62	36	28	23	16
	5 M NaCl	430	57	33	26	21	15

3.4.4 Cathodic Behavior of AA7050, 316SS and High-Purity Cu in 5 M NaCl compared to 0.6 M NaCl

Similar observations as on Pt were made on AA7050, 316SS and high-purity Cu as displayed in Figure 3.13. On each electrode, the kinetics as a function of electrode rotation rate in 5 M NaCl were decreased compared to the respective case in 0.6 M NaCl. On AA7050, the kinetics were generally decreased by up to an order of magnitude, but only about a three-fold and five-fold suppression on 316SS and high-purity Cu, respectively. It is also noted that on high-purity Cu, the kinetics appeared to plateau above electrode rotation rate of 300 rpm ($\delta \leq 33$ μm). These observations can be clearly seen on the Levich plots shown in Figure 3.14. Please note the same scale on both plots to permit a direct comparison of the kinetics of the respective electrodes in both 0.6 M NaCl and 5 M NaCl solutions.

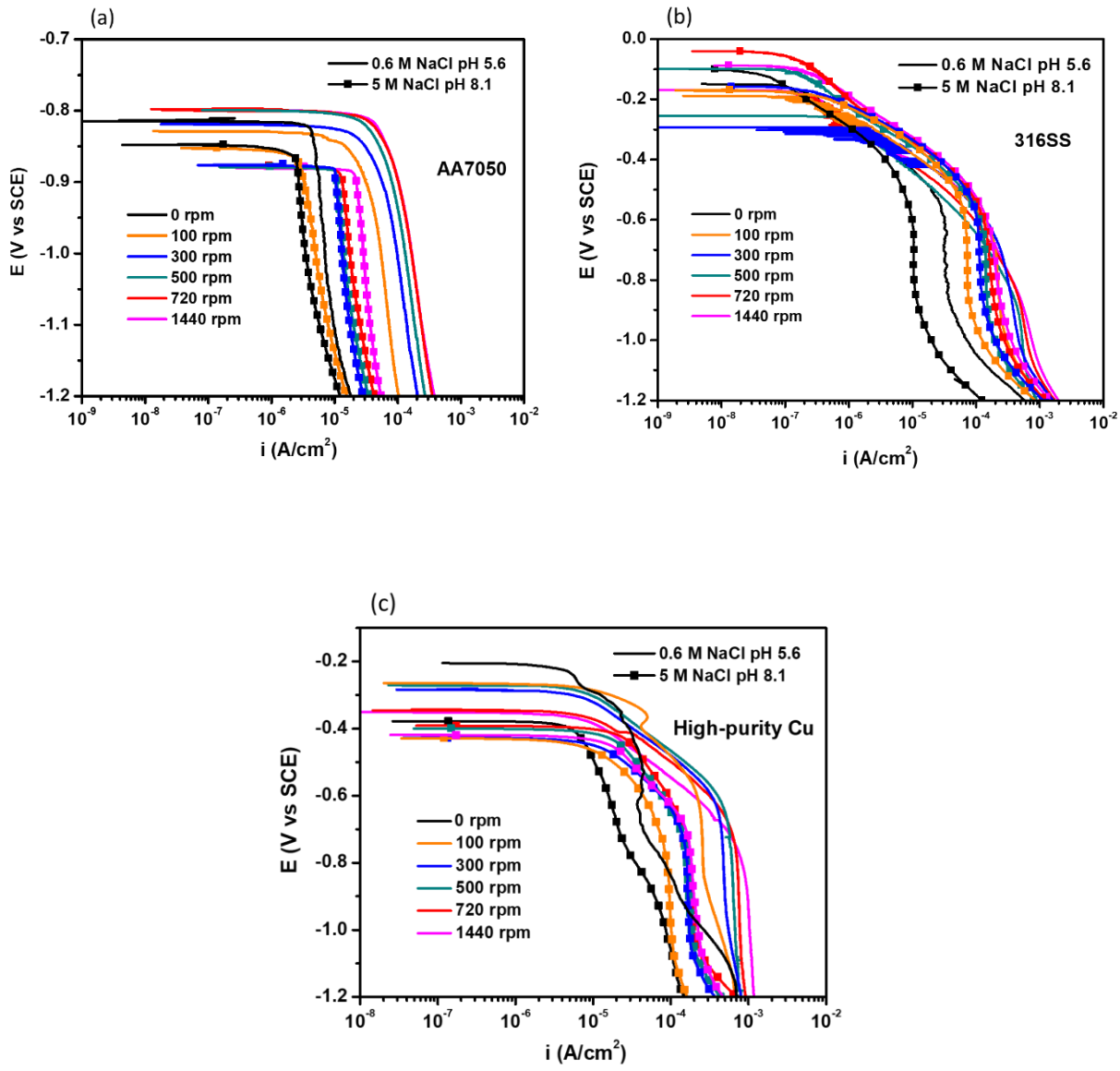

Figure 3.13. Cathodic polarization behavior of (a) AA7050, (b) 316SS, and (c) high-purity Cu in 0.6 M NaCl compared with behaviors in 5 M NaCl as a function of electrode rotation rate.

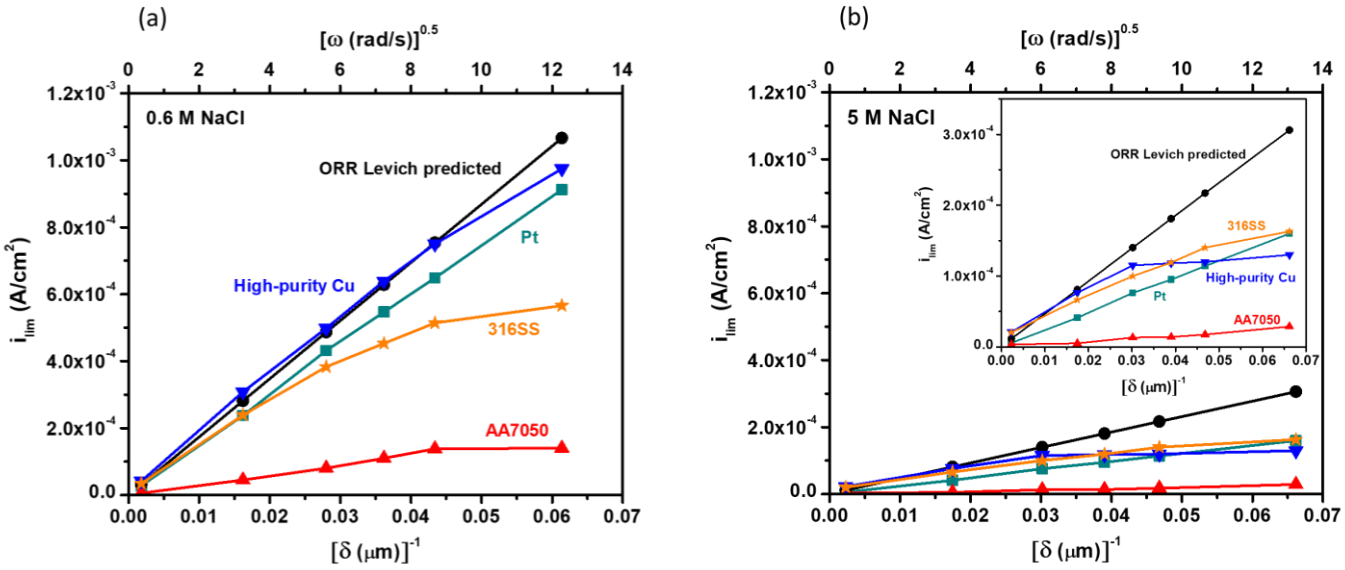

Figure 3.14. Levich plots comparing mass-transport ORR kinetics on AA7050 (taken at a reference potential of -0.95 V_{SCE}), 316SS and high-purity Cu (taken at a reference potential of -0.8 V_{SCE}) in (a) 0.6 M NaCl, and (b) 5 M NaCl as a function of boundary layer thickness. Data on Pt (taken at a reference potential of -0.7 V_{SCE}) and ORR Levich-predicted data are included for reference.

On addition of chromate to 5 M NaCl, kinetics was decreased on all three electrodes as expected. The degree of ORR suppression increased with increasing chromate concentration, regardless of δ (Figure 3.15). However, when compared to the results obtained in 0.6 M NaCl, it appeared that chromate functions better in the 0.6 M NaCl environment than the 5 M NaCl environment, particularly in thinner δ (Figure 3.15). On AA7050, the addition of 10^{-2} M chromate to 5 M NaCl reduced ORR kinetics by fifteen times compared to two orders of magnitude in 0.6 M NaCl (Figure 3.15b). On 316SS, the degree of suppression on addition of 10^{-2} M chromate to solution was about five-fold in 5 M NaCl compared to over two orders of magnitude in 0.6 M NaCl. On high-purity Cu, the degree of suppression was about two-fold in 5 M NaCl compared to almost two orders of magnitude in 0.6 M NaCl. In relation to AA7050-316SS galvanic couple, chromate still appears to be more effective on 316SS than on replated Cu at higher chloride concentration. It is worth noting that although increasing the chromate concentration to 10^{-1} M in 5 M NaCl further suppressed kinetics on 316SS and high-purity Cu, the cathodic current density

levels attained were still higher than those attained in 0.6 M NaCl with the addition of a lower chromate concentration of 10^{-2} M. (Figure 3.15b).

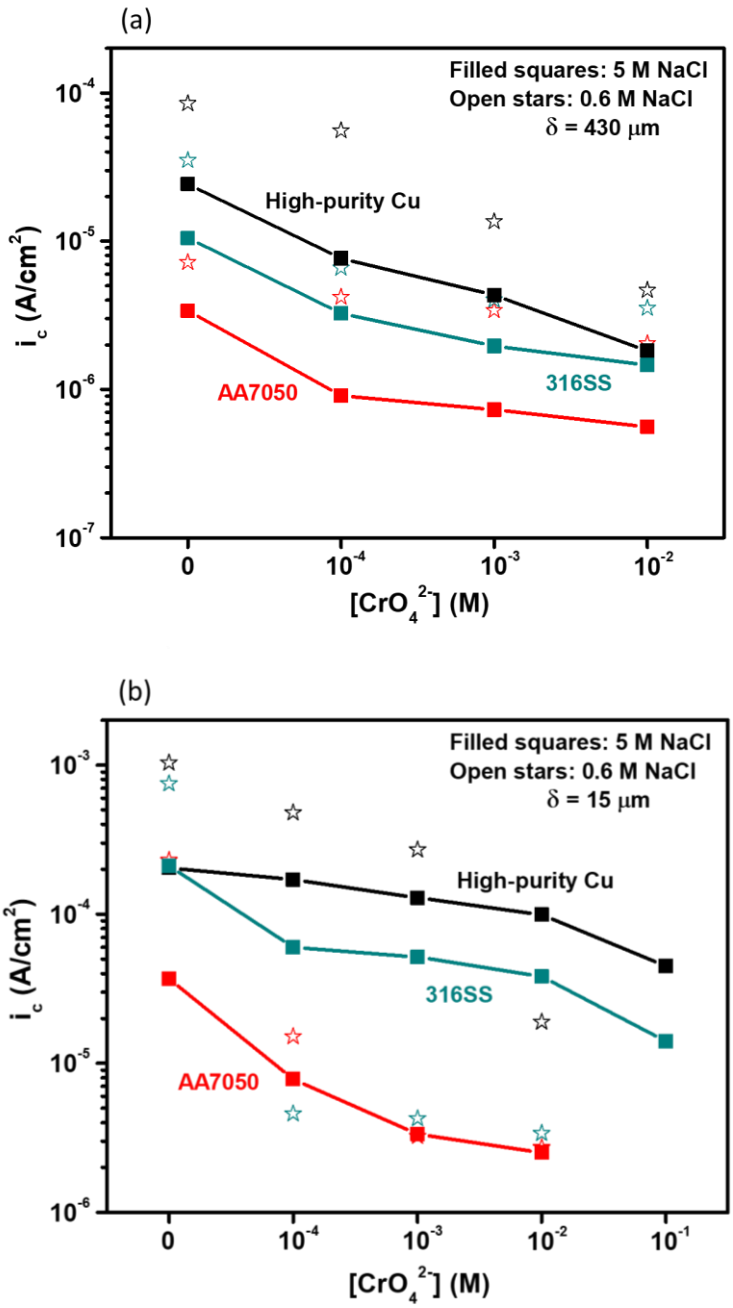

Figure 3.15. Comparison of the ORR behaviors of high-purity Cu, 316SS, and AA7050 in 0.6 M NaCl and 5 M NaCl as a function of chromate concentration at (a) δ = 430 μm (full immersion conditions), and (b) at δ = 15 μm (thin film conditions). Data on the electrodes were taken at the respective reference potential as noted in Figure 3.14.

3.4.5 Effect of Al^{3+} on the Cathodic Behaviors of AA7050, 316SS and High-Purity Cu in 5 M Cl^-

By definition, when corrosion occurs on an Al alloy, Al^{3+} would be released and these would be at a high concentration on the surface if undergoing active localized corrosion. It is important to understand how the presence of this metallic ion would influence the cathodic current available to propagate damage in the case of AA7050-316SS galvanic couple, as well as its effect on the activity of chromate. To this end, RDE experiments were carried out on the electrodes in 4.7 M NaCl + 0.1 M $AlCl_3$ and with the addition of 10^{-2} M chromate. Figure 3.16 compares the cathodic polarization curves generated on AA7050 in inhibitor-free 5 M NaCl and 4.7 M NaCl + 0.1 M $AlCl_3$, and with the addition of 10^{-2} M chromate to 4.7 M NaCl + 0.1 M $AlCl_3$ for different δ. In inhibitor-free conditions, it was observed that the addition of Al^{3+} enhanced cathodic kinetics on AA7050 by more than one order of magnitude, regardless of δ (Figure 3.16a). This observation is in line with the results obtained by Liu et al.[26] in 0.6 M Cl^- environment. On addition of 10^{-2} M chromate, kinetics was reduced by up to two orders of magnitude (Figure 3.16b), albeit not decreased to the levels achieved in 0.6 M NaCl and 5 M NaCl with the same chromate concentration.

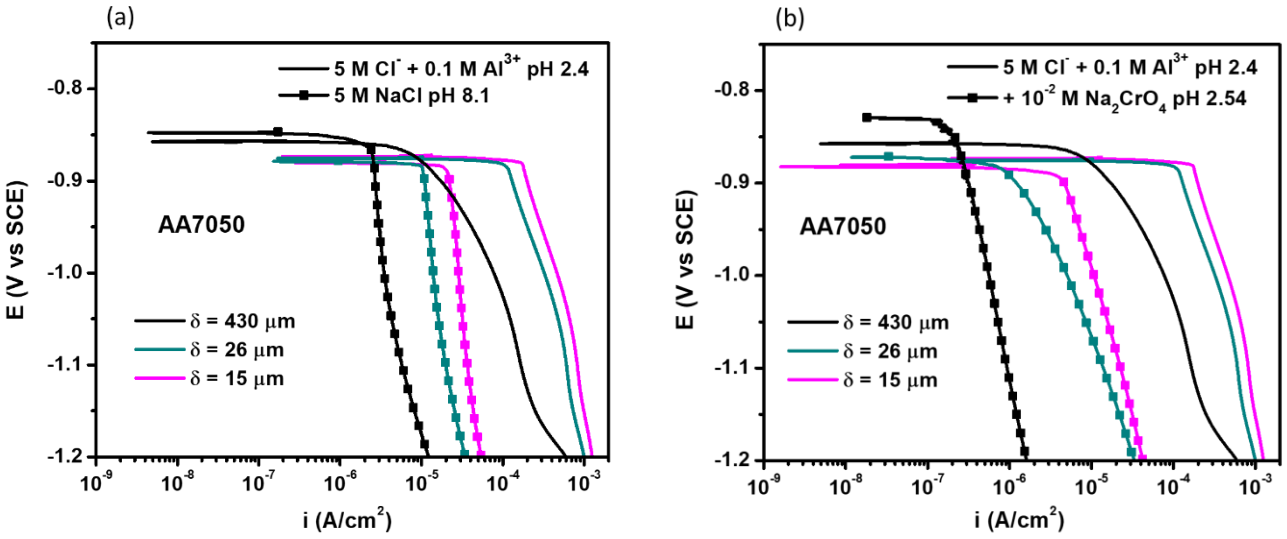

Figure 3.16. Comparison of the cathodic polarization behavior of AA7050 in (a) 5 M NaCl and 4.7 M NaCl + 0.1 M $AlCl_3$, and (b) 4.7 M NaCl + 0.1 M $AlCl_3$ and with the addition of 10^{-2} M Na_2CrO_4 at various values of δ.

Cathodic polarization curves generated on 316SS and high-purity Cu in inhibitor-free 5 M NaCl and 4.7 M NaCl + 0.1 M $AlCl_3$ are compared in Figure 3.17. The polarization curves were characterized by the ORR region from OCP to ~ -0.5 V_{SCE} and ~ -0.75 V_{SCE} for 316SS and high-purity Cu, respectively. Beyond those regions, which included the range of AA7050 OCP (-0.8 V_{SCE} to -0.9 V_{SCE}) in the same environment (Figure 3.16), the curves were dominated by activation-controlled hydrogen evolution reaction (HER) kinetics, as opposed to the diffusion-controlled ORR kinetics in 5 M NaCl (without the addition of Al^{3+}) within the same potential range. Overall, the kinetics in the Al^{3+} -containing solution were up to two orders of magnitude higher with 316SS and four times higher with high-purity Cu than the values obtained in 5 M NaCl. It is also noted that there was no dependence of the HER kinetics on δ, and Al^{3+} did not appear to have any significant effect on ORR kinetics.

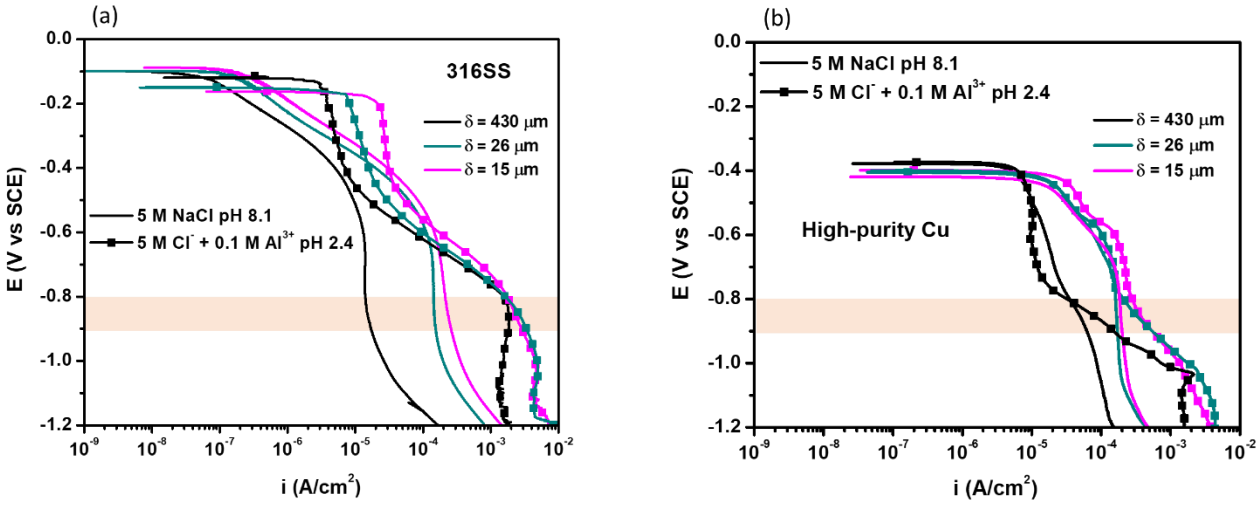

Figure 3.17. Comparison of the cathodic polarization behavior of (a) 316SS, and (b) High-purity Cu in 5 M NaCl and 4.7 M NaCl + 0.1 M $AlCl_3$, at various values of δ. Orange boxes highlight the range of AA7050 OCP in the same environments.

Similar observations were made on experiments conducted on Pt (Figure 3.18). It can be clearly seen within the potential range of 0 V_{SCE} to ~ -0.35 V_{SCE} that Al^{3+} had barely any effect on the ORR kinetics, but facilitated the HER kinetics beyond that potential range with no dependence on δ.

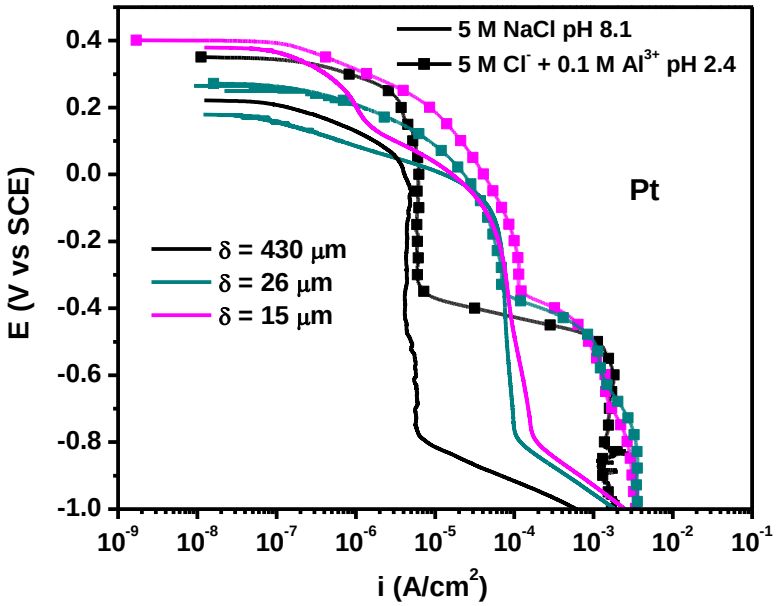

Figure 3.18. Comparison of the cathodic polarization behavior of Pt in 5 M NaCl and 4.7 M NaCl + 0.1 M $AlCl_3$, at various values of δ.

Figure 3.19 overlaps the polarization curves generated on 316SS and high-purity Cu in 4.7 M NaCl + 0.1 M $AlCl_3$ and with the addition of 10^{-2} M chromate at δ = 15 μm. Within the range of AA7050 OCP, kinetics was up to ten times higher on 316SS than on high-purity Cu, and chromate had negligible impact on the HER kinetics. Interestingly, it appears that in the presence of Al^{3+}, 316SS becomes the more significant cathode in AA7050-316SS galvanic couple, as opposed to high-purity Cu in Al^{3+}-free environments.

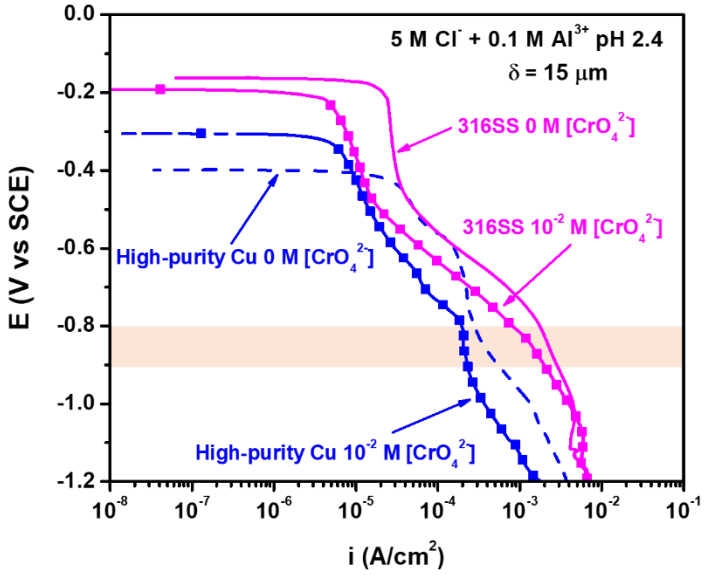

Figure 3.19. Comparison of the cathodic kinetics on 316SS and high-purity Cu polarization in 4.7 M NaCl + 0.1 M $AlCl_3$, and with the addition of 10^{-2} M Na_2CrO_4 at δ = 15 μm. Orange box highlights the range of AA7050 OCP in the same environments.

3.5 Discussion

Atmospheric conditions generally fluctuate with time and location due to the existence of wet-dry cycles as a result of diurnal changes in temperature and RH. This situation influences the volume of electrolyte and thickness of electrolyte layer available which can lead to dramatic changes in solution chemistry which in turn may impact the electrochemical behavior of a substrate. In the case of AA7050-316SS galvanic couple where localized corrosion of AA7050 is largely controlled by the amount of current available from the various cathodic materials, phases, and evolving surface in the couple,[3,6,15] any change in solution chemistry would be considered important. This work discusses how the changes in solution chemistry impact the ability of chromate to suppress cathodic currents on the governing cathodic contributors through assessment of the electrochemical response of the electrodes in dilute and concentrated chloride environments as a function of chromate concentration. Speculations are made as to why chromate may be more potent in one environment or on one cathode than the other. Implications in service environments are discussed.

3.5.1 Nature of Environment Governs the Dominant Cathode in AA7050-316SS Galvanic Couple

In the 0.6 M NaCl environment, it is speculated that replated Cu would be the more significant cathode with fast ORR kinetics to support high rates of anodic dissolution of AA7050 occurring at a localized corrosion site (Figure 3.4). It is worth noting that on a polished AA7050-316SS couple, replated Cu is not initially present (prior to initiation of corrosion); it only results from the dealloying of the Cu-rich IMPs which would be facilitated by the cathodic ORR activity on the 316SS.[5] However, once Cu has replated, it sustains faster ORR kinetics than the 316SS. In the context of chromate activity under these conditions, it appears chromate provides a superior degree of ORR inhibition on 316SS than on high-purity Cu (Figure 3.7). The addition of the lowest concentration of chromate, i.e., 10^{-4} M dramatically suppressed ORR kinetics on 316SS by at least two orders of magnitude, compared to only ~ three times on high-purity Cu. As indicated by Figure 3.8, a low concentration of chromate under the right conditions can effectively stifle kinetics on 316SS such that any corrosion occurring on AA7050 is supported mainly by local cathodic reactions occurring on the Cu-rich IMPs. It is also conceivable that early cathodic inhibition on 316SS would mitigate Cu replating on the Al alloy by limiting corrosion. However, if Cu replates, then it becomes a dominant cathode and sustains corrosion of the Al alloy, albeit at a lower rate than if chromate were not present.

In the case of 5 M NaCl environment, ORR kinetics were reduced on the electrodes in inhibitor-free conditions in comparison to the levels attained in 0.6 M NaCl (Figure 3.14). This result would be expected due to reduced oxygen solubility/concentration and diffusivity as chloride concentration increases. Under thin δ, 316SS and high-purity Cu displayed comparable kinetics in inhibitor-free conditions, indicating equivalent capacities as cathodes in this environment. Interestingly, the addition of chromate to 5 M NaCl appeared to be less effective at suppressing kinetics on the electrodes, compared to the respective cases in 0.6 M NaCl (Figure 3.15). Addition of a substantial amount of chromate, i.e., 10^{-1} M – which would be impractical to attain in the field[27,28] – was still insufficient to lower the cathodic currents on 316SS and high-purity Cu to levels attained in 0.6 M NaCl with the addition of a lower chromate concentration of 10^{-2} M (Figure 3.15b). This result suggests that something else other than the ORR was controlling

the electrochemical processes in this environment, and impeded the ability of chromate to perform effectively. One speculation may be related to the competitive adsorption between the chloride anion and the chromate anion. The chloride anion is not only a highly mobile ion,[29] but it is also smaller in size than the chromate anion, and so would be expected to migrate more easily in response to an electric field than the chromate anion. For instance, the mobility of the chloride ion in dilute aqueous solutions is ~ 8.0 x 10^{-8} m^2/Vs[30] and is only considerably less mobile than H^+ and OH^-.[31] Coupled with the vast concentration of chloride in relation to chromate in this environment, chloride would be disproportionately favored over chromate in terms of surface adsorption and coverage of the 316SS and high-purity Cu electrodes. That said, the inhibitive effect of chromate on high-purity Cu was minimal compared to 316SS. The addition of 10^{-1} M chromate to the solution decreased kinetics on 316SS by thirteen times as opposed to just four times on high-purity Cu. It follows that in concentrated chloride environments, chromate may not adequately protect AA7050 due to the availability of elevated cathodic current from replated Cu in addition to the contribution from 316SS.

The aforementioned situation would lead to damage propagation on AA7050 with attendant accumulation of a substantial concentration of Al^{3+} on the surface. To this end, experiments were conducted in 5 M Cl^- with the addition of 0.1 M Al^{3+}. Figures 3.16 and 3.17 suggest that under these conditions, the cathodic current available to sustain damage propagation on AA7050 would be even more substantial, particularly from the 316SS, due to high-rate HER kinetics facilitated by the activity of Al^{3+}. It is noted that pH of the 5 M Cl^- solution on addition of Al^{3+} became acidic. Liu et al.[26] proposed a mechanism based on the Grotthuss Theory to explain the activity of Al^{3+} resulting to the high-rate HER kinetics. According to Liu, Al^{3+} coordinates with O bonds in water, weakening the O-H bond, resulting in enhanced H^+ diffusivity to the electrode surface. The apparent considerably sluggish HER kinetics on Cu may be attributed to the very slow step of H adsorption on the surface.[32,33]

The addition of 10^{-2} M chromate to the Al^{3+}-containing solution barely raised the pH from that of the inhibitor-free solution, and provided no significant inhibitive effect on the HER kinetics on both 316SS and high-purity Cu (Figure 3.19). This result indicates that high-rate damage

propagation on AA7050 will be sustained whether or not chromate is present, if there is little or no early inhibition of corrosion leading to release of Al^{3+}. In this situation, 316SS will be the major cathodic contributor in comparison to replated Cu. Interestingly, on AA7050, chromate appeared to provide significant inhibition – by up to two orders of magnitude (Figure 3.16b). This outcome may be attributed to the electrostatic interaction of chromate with the Al^{3+} to form stable oxide or hydroxide complexes which has been speculated to promote inhibition.[34] That said, the inhibited cathodic current levels on AA7050 were still higher than those achieved in the Al^{3+}-free environment. It can be inferred that chromate functions better at suppressing ORR kinetics than HER kinetics.

3.5.2 Chromate Performs Better on Oxide-Covered Surfaces than on Bare Surfaces

The investigations conducted on the various electrodes suggest that chromate is more effective at suppressing cathodic kinetics on oxide-covered surfaces than on oxide-free surfaces. AA7050 and 316SS have native oxide films; the AA7050 surface is covered with Al_2O_3 / $Al(OH)_3$, and the 316SS surface is covered with an inner layer enriched in Cr(III) oxide and an outer layer enriched in Fe(III) oxide. Pt possesses no oxide film, and high-purity Cu is oxide-free within the range of potentials relevant to this work.

Comparing inhibition efficiencies on AA7050, 316SS and high-purity Cu (and even on Pt - discussed in Chapter 2) in the respective environments (Figure 3.15), lower concentrations of chromate tend to provide considerable cathodic inhibition on oxide-covered AA7050 and 316SS than on high-purity Cu and Pt. For instance, in 0.6 M NaCl, the addition of 10^{-4} M chromate decreased kinetics on AA7050 and 316SS by more than one order of magnitude and more than two orders of magnitude, respectively, in comparison to only a two-fold decrease on high-purity Cu (Figure 3.8). It is speculated that on the oxide-covered surfaces, chromate acts to stabilize the oxide film through adsorption and subsequent reduction on defective or otherwise catalytic sites – which would be favorable sites for O_2 adsorption. On AA7050, such ORR-catalytic sites would include the Cu-rich IMPs and sites of cathodic Al dissolution.[35] On 316SS, favorable sites for O_2 adsorption include Fe(II) sites present following the reduction of Fe(III) oxide.[36] It is therefore reasonable to assume that a much lower concentration of chromate would be required in the

above-mentioned circumstances as opposed to the case for bare surfaces where there would be more widespread competitive adsorption with O_2, and a considerably larger surface area available for coverage.

3.5.3 Implications in Service Environments

Due to the nature of their service operations, aircraft structures experience diurnal cycles that result in the formation of thin electrolytes on their surfaces with fluctuating concentrations of chloride as RH changes. The results of this study indicate that if a defect occurs within the vicinity of the 316SS at the instance of high RH, say 98%, chromate - even at a low concentration - may effectively suppress cathodic current on the 316SS to protect AA7050 from localized corrosion. Because the Cr(III)-rich oxide film formed on reduction of chromate is irreversible and persistent,[21] further changes in RH that result in a concentrated solution chemistry during the course of day should have little or no impact on corrosion kinetics. However, in the event that the defect occurs when the RH is lower, say 80% - the consequence of which would include a transition to a much more aggressive Cl^- and Al^{3+} complicated electrolyte - then the demand for chromate may be much higher, making it more difficult for chromate to effect adequate cathodic inhibition on the 316SS fastener. In this situation, the driving force for AA7050 corrosion and subsequent Cu replating would increase. The released Al^{3+} resulting from AA7050 corrosion would enter solution, further enhancing the conductivity of the already aggressive electrolyte, and accelerating cathodic kinetics on the 316SS and replated Cu to advance damage propagation on AA7050. This interpretation may be used to elucidate the results reported by Feng et al.[4] where the damage on a chromate primer + top coated and scribed AA7075 galvanic panel was accelerated within the scribed region closest to uncoated 316SS fasteners. It is plausible that the bare 316SS fasteners did not benefit from any chromate that may have leached out of the coating adjacent to the scribes, resulting in damage initiation with attendant release of Al^{3+} and possible Cu replating. Over the course of time, the solution chemistry localized to the vicinity of the 316SS became concentrated and aggressive, resulting in accelerated damage inside the scribes on the AA7075 panel within that vicinity.

3.6 Conclusions

The work presented herein utilized the RDE technique to evaluate the current capacities of the cathodic contributors in AA7050-316SS galvanic couple to drive localized corrosion of AA7050 in the presence of chromate under simulated atmospheric conditions. The following conclusions were made based on the findings:

- The addition of 10^{-4} M chromate into dilute NaCl solution significantly reduced ORR kinetics on both 316SS and Cu-rich IMPs on AA7050. However, at least 10^{-2} M chromate was required to achieve a similar effect on high-purity Cu. It was speculated based on this result that early cathodic inhibition of 316SS may mitigate AA7050 corrosion and subsequent Cu replating. However, if Cu replates, it may become the more significant cathode weakly affected by chromate that drives further attack.
- The degree of chromate inhibition on the cathodes decreased with increasing chloride concentration.
- The addition of 10^{-1} M Al^{3+} to 5 M Cl^- solution enhanced HER kinetics making it the dominant cathodic reaction as opposed to the ORR. Chromate exhibited a diminished ability to inhibit the HER compared to the ORR.
- In the presence of 10^{-1} M Al^{3+}, 316SS was determined to be the more significant cathode in comparison to high-purity Cu, with an increased current capacity of up to one order of magnitude.

3.7 References

1. D. Olson, T. Siewert, S. Liu, and G. Edwards, *ASM Handbook Vol 6: Welding, Brazing, and Soldering*, ASM International, New York, (1993).
2. C. A. Matzdorf et al., *Corrosion*, **69**, 1240–1246 (2013).
3. Z. Feng and G. S. Frankel, *Corrosion*, **70**, 95 (2014).
4. Z. Feng, G. S. Frankel, and C. A. Matzdorf, *J. Electrochem. Soc.*, **161**, C42–C49 (2014).
5. V. N. Rafla, A. D. King, S. Glanvill, A. Davenport, and J. R. Scully, *Corrosion*, **74**, 5–23 (2018).
6. R. S. Marshall, R. G. Kelly, A. Goff, and C. Sprinkle, *Corrosion*, **75**, 1461–1473 (2019).

7. N. E. C. Co and J. T. Burns, *Int. J. Fatigue*, **103**, 234–247 (2017).

8. M. W. Kendig and R. G. Buchheit, *Corrosion*, **59**, 379–400 (2003).

9. G. S. Frankel and R. L. Mccreery, *Electrochem. Soc. Interface*, **10**, 34–38 (2001).

10. G. O. Ilevbare, J. R. Scully, J. Yuan, and R. G. Kelly, *Corrosion*, **56**, 227–242 (2000).

11. W. J. Clark, J. D. Ramsey, R. L. McCreery, and G. S. Frankel, *J. Electrochem. Soc.*, **149**, B179–B185 (2002).

12. A. Sehgal, G. S. Frankel, B. Zoofan, and S. Rokhlin, *J. Electrochem. Soc.*, **147**, 140–148 (2000).

13. A. Kolics, A. S. Besing, and A. Wieckowski, *J. Electrochem. Soc.*, **148**, 322–331 (2001).

14. Z. Feng, G. S. Frankel, W. H. Abbott, and C. A. Matzdorf, *Corrosion*, **72**, 342–355 (2016).

15. Z. Feng, J. Boerstler, G. S. Frankel, and C. A. Matzdorf, *Corrosion*, **71**, 771–783 (2015).

16. V. N. Rafla and J. R. Scully, *Corrosion*, **75**, 587–603 (2019).

17. W. Lang and R. Zander, *Ind. Eng. Chem. Fundam.*, **25**, 775–782 (1986).

18. R. M. Katona et al., *J. Electrochem. Soc.*, **168**, 031512 (2021).

19. M. A. Jakab, D. A. Little, and J. R. Scully, *J. Electrochem. Soc.*, **152**, B311–B320 (2005).

20. M. J. Pryor and D. S. Kern, *J. Electrochem. Soc.*, **102**, 605–607 (1955).

21. U.-E. Charles-Granville, C. Liu, J. R. Scully, and R. G. Kelly, *J. Electrochem. Soc.*, **167**, 111507 (2020).

22. N. Birbilis and R. G. Buchheit, *J. Electrochem. Soc.*, **152**, B140–B151 (2005).

23. Y. Zhu, K. Sun, and G. S. Frankel, *J. Electrochem. Soc.*, **165**, C807–C820 (2018).

24. A. Kosari et al., *J. Electrochem. Soc.*, **168**, 041505 (2021).

25. C. Liu, J. Srinivasan, and R. G. Kelly, *J. Electrochem. Soc.*, **164**, C845–C855 (2017).

26. C. Liu, P. Khullar, and R. G. Kelly, *J. Electrochem. Soc.*, **166**, C153–C161 (2019).

27. L. Xia, E. Akiyama, G. Frankel, and R. Mccreery, *J. Electrochem. Soc.*, **147**, 2556–2562 (2000).

28. J. D. Ramsey, L. Xia, M. W. Kendig, and R. L. McCreery, *Corros. Sci.*, **43**, 1557–1572 (2001).

29. C. A. Lucy and T. L. Mcdonald, *Anal. Chem*, **67**, 1074–1078 (1995).

30. J. Ma et al., *J. Am. Chem. Soc*, **141**, 4264–4272 (2019).

31. Y. Tanaka, *J. Memb. Sci.*, **350**, 347–360 (2010).

32. S. Trasatti, *Electroanal. Chem. Interfacial Electrochem.*, **39**, 163–184 (1972).

33. B. E. Conway and G. Jerkiewicz, *Solid State Ionics*, **150**, 93–103 (2002).

34. J. D. Ramsey and R. L. Mccreery, *J. Electrochem. Soc.*, **146**, 4076–4081 (1999).

35. K. Ogle, M. Serdechnova, M. Mokaddem, and P. Volovitch, *Electrochim. Acta*, **56**, 1711–1718 (2011).

36. C. Liu and R. G. Kelly, *Corrosion*, **75**, 1087–1099 (2019).

4. Efficacy of Chromate in Mitigating Galvanic-Induced Corrosion of AA7050-T7451 Macro-Coupled to 316SS in Simulated External Vs. Fastener Crevice Environments

Part of the work presented in this chapter has been reported in the following publication:

U.-E. Charles-Granville, C. F. Glover, J. R. Scully, R. G. Kelly, "Effect of pH and Al Cations on Chromate Inhibition of Galvanic-Induced Corrosion of AA7050-T7451 Macro-Coupled to 316SS", *J. Electrochem. Soc.*, **168**, 121509 (2021).

4.1 Abstract

The performance of chromate in protecting AA7050-T7451 coupled to 316SS in simulated fastener environments, including that representative of the boldly exposed surfaces and downhole conditions, was investigated utilizing a number of electrochemical and surface characterization techniques. The influence of pH and Al^{3+} on the galvanic coupling behavior and damage evolution on AA7050 as a function of chromate concentration were assessed. The degree of chromate inhibition was observed to decrease as pH decreased, owing to chromate speciation and reduced capacity to suppress the hydrogen evolution reaction (HER) compared to the oxygen reduction reaction (ORR). The addition of 0.1 M Al^{3+} significantly increased HER kinetics and produced a large buffer effect which overwhelmed the ability of chromate to slow damage propagation on AA7050. Assessment of cathodes indicated that Cu was more important than 316SS in driving damage initiation, but less active than 316SS in supporting high-rate damage propagation in simulated crevice environments. The implications of this study for actual bimetallic systems are discussed. Furthermore, an assessment of the performance of Mg(II) in mitigating galvanic corrosion on the boldly exposed surface of an AA7050-316SS fastener couple indicated an inferior inhibitive capacity compared to chromate at the same ion concentration.

4.2 Introduction

Dissimilar metal assemblies are frequently encountered in complex structures, such as in aerospace applications, and can pose a major challenge in terms of galvanic-induced localized

corrosion. One generic example of such an assembly is that of high-strength aluminum alloy (AA) components joined with stainless steel (SS) fasteners. Defects in the corrosion protection coating systems at these joint locations facilitate the wicking of aggressive electrolyte species into the confined fastener crevices, creating a hidden macro-galvanic corrosion cell which can aggravate attack and degrade the fatigue life of the localized corrosion-prone base AA component.[1–9] In this regard, inhibitor release from the coating system, and transport into the fastener crevice, would be crucial in mitigating the localized attack.

Although chromates are known to be excellent inhibitors for Al-based alloys,[10–27] a number of investigations have demonstrated that macro-galvanic coupling can defeat chromate inhibition of these alloys.[2,17,28–30] . It is noted that many of these studies were carried out on chromate-coated, scribed Al-based panels containing bare SS fasteners, and a measured concentration of chromate that might have leached out into the scribes was not reported. In principle, a higher chromate concentration may be needed to effectively inhibit anodic reactions in a situation where there is a bare and wetted external cathode with no inhibition of cathodic reactions than would be required for the base Al alloy without an external cathode. For instance, Feng et al.[28] carried out investigations on chromate-coated and scribed AA7075-T6 panels with and without bare 316SS fasteners exposed to continuous salt spray ASTM B117 tests. The panel containing the fasteners exhibited enhanced corrosion localized to the scribes, while the coating outside the scribed areas remained intact. The enhanced damage on the Al panel was attributed to the large cathodic currents associated with the bare 316SS fasteners that polarized the Al component above its pitting potential, potentially overwhelming any anodic inhibition that may have been afforded by chromate in the scribes. In contrast, no appreciable damage was observed on the non-galvanic panels. One limitation in this work was that the damage within the fastener hole was not analyzed.

Marshall et al.[4] observed damage both in the scribes and within the fastener holes of AA7075 panels coupled with bare 316SS. The damage observed was minimized with the application of a sol-gel coating to the 316SS fasteners. This result demonstrated the efficacy of impeding cathodic reactions as a means of corrosion mitigation for galvanic couples. However, damage to the sol-gel coating would be detrimental as the coating contained no inhibitive

pigment to provide either cathodic inhibition on the 316SS fastener or anodic inhibition of the AA7075. Rafla and Scully[17] demonstrated that chromate can suppress the ORR rates on 316SS in quiescent conditions by up to an order of magnitude. Guided by this preliminary information, they extended their studies to AA7050-316SS couples where chromate was added to the test solution, circumventing the leaching phase from a coating. They utilized 3D X-ray tomography to analyze damage within the fastener hole of a simulated AA7050-316SS rivet exposed to 4 M NaCl with and without addition of 10^{-2} M chromate. They observed that with 10^{-2} M chromate, there was no attack outside the hole, nor was there attack inside the hole near the surface. However, there was one large group of fissures occurring at the bottom of the hole. This result raised questions surrounding the possible effects of crevice depth on the solution chemistry in the fastener hole which may have affected the activity of chromate.

In the work presented herein, external and crevice environments were simulated to isolate the effect of pH and Al^{3+}, respectively, on chromate inhibition of AA7050 coupled to 316SS in an attempt to explain the findings of Rafla and Scully.[17] The results of the present work are aimed at advancing the understanding of the macro-galvanic-induced corrosion phenomena crucial for the optimization of testing frameworks. In addition, these results can be used to assist in the design of environmentally-friendly inhibitor strategies needed to replace toxic chromate-based corrosion mitigation systems.

4.3 Experimental

4.3.1 Materials Preparation

The materials utilized in this study were AA7050-T7451 (obtained from ALCOA), 316SS (obtained from McMaster-Carr Supply Company) and 99.99% Cu (obtained from Alfa Aesar), all in the form of 0.25” thick plates. Table 4.1 shows the composition of AA7050-T7451 and 316SS. Planar samples were cut to form square coupons with an exposed surface area of 1 cm^2. AA7050 exposed surfaces were in the SL orientation. An AA7050-316SS simulated fastener galvanic couple was constructed by pressing a short rod of 316SS into a AA7050 plate with the dimensions as shown in Figure 4.1. No intentional crevice gap was created. The structure was encapsulated in epoxy with an internal Ni wire electrical connection. Immediately preceding each experiment,

the samples were wet-ground successively from 120 grit to a surface finish of 1200 grit with SiC paper, rinsed in acetone and then with deionized water, and finally dried with clean compressed air.

Table 4.1. Composition of AA7050-T7451 and 316SS (in wt%).

AA7050	**Zn**	**Mg**	**Cu**	**Fe**	**Si**	**Zr**	**Mn**	**Ti**	**Cr**	**Al**	
	6.7	2.6	2.6	0.15	0.12	0.15	0.1	0.06	0.04	balance	
316SS	**C**	**Mn**	**P**	**S**	**Si**	**Ni**	**Mo**	**Cu**	**Cr**	**N**	**Fe**
	0.019	1.75	0.039	0.028	0.46	10.16	2.05	0.44	17.03	0.071	balance

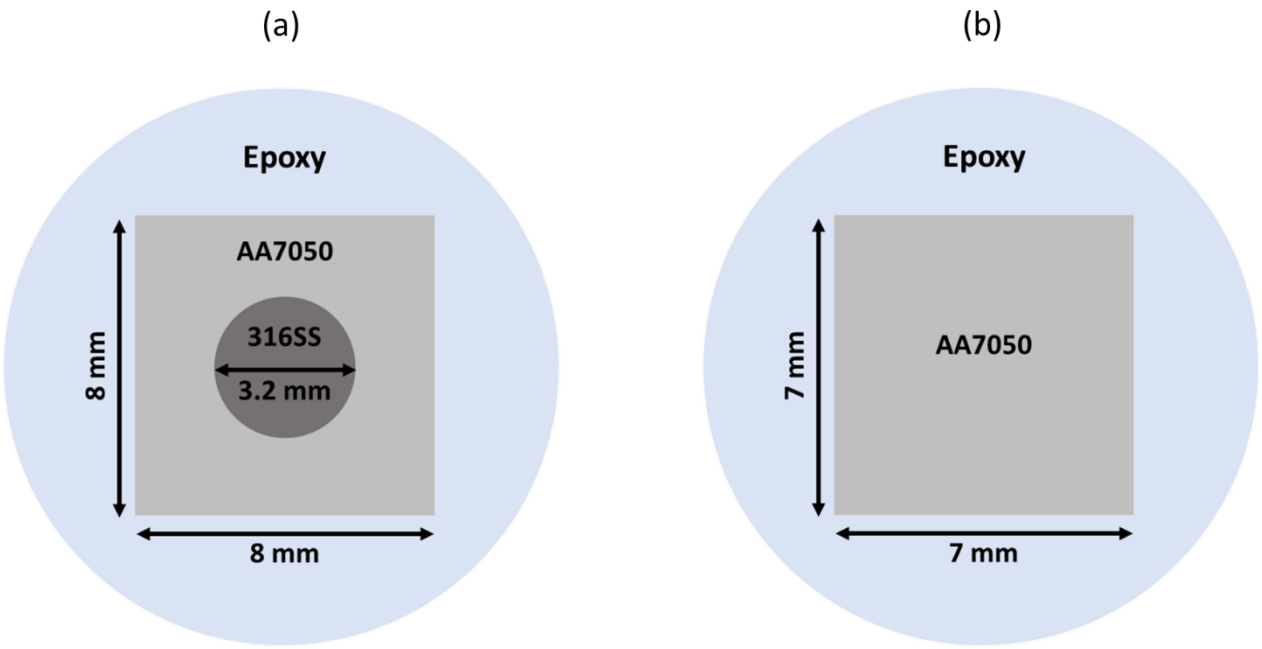

Figure 4.1. Schematic of the (a) simulated AA7050-316SS fastener galvanic couple, and (b) uncoupled base AA7050 (i.e., without 316SS) used for the SVET experiments.

4.3.2 Electrochemical Measurements

Experiments were conducted in various unbuffered aqueous NaCl solutions with and without the addition of 0.1 M $AlCl_3$ to simulate environments relating to the external surface as well as different stages of damage evolution within a fastener crevice, as displayed in Table 4.2,

and with addition of various concentrations of chromate. The pH of the solutions was either measured or adjusted depending on the type of environment that was being simulated. Measured pH values were consistent with those expected from calculations using OLI^{TM} Studio Analyzer 9.2 (from OLI Systems, NJ). Experiments were performed in quiescent (open to lab air) and deaerated (purged with nitrogen gas for 30 min prior to test, and throughout the duration of test) conditions as indicated in Table 4.2, and each test was repeated at least once to ensure reproducibility.

Table 4.2. Base test solutions and environment simulated.

Base solution	pH	Environment simulated
Quiescent 0.001 M NaCl	Natural, 5.8	External surface, near-neutral
Quiescent 0.001 M NaCl	Adjusted, 3.0	External surface, acid rain
Deaerated 5 M NaCl	Adjusted, 2.4	Deep crevice, damage initiation/low-rate damage propagation
Deaerated 4.7 M NaCl + 0.1 M $AlCl_3$	Natural, 2.4	Deep crevice, high-rate damage propagation

Zero resistance ammeter (ZRA) experiments were carried out over 24 h after an initial 10-min exposure at open circuit to measure the galvanic potentials and current densities on AA7050-316SS and AA7050-high purity Cu planar couples. A three-electrode flat cell configuration was used with AA7050 as the working electrode, 316SS or high-purity Cu as the counter electrode, and a saturated calomel electrode (SCE) as reference. Measurements were made using a Gamry Reference 600+^{TM} potentiostat/galvanostat/ZRA. The cathode-to-anode area ratio was 1:1. High-purity Cu was used to represent Cu-rich intermetallic particles (IMP) and/or Cu replated onto either AA7050 or 316SS after the dissolution of Cu-bearing IMP. AA7050 specimens were weighed (with ± 0.0001 g resolution) before and after each ZRA experiment, to enable measurement of the gravimetric mass loss which was converted to anodic charge density associated with metal dissolution ($Q_{\Delta m}$) via Faraday's law:

$$Q_{\Delta m} = \frac{\Delta m F}{W_{eq} A} \quad (4.1)$$

where Δm is mass loss, F is Faraday's constant, A is the exposed area of the electrode, and W_{eq} is the equivalent weight of AA7050 calculated to be 9.54 g/eq. W_{eq} was calculated using Equation 2 assuming incongruent dissolution where Al, Zn, Mg dissolve and Cu does not dissolve:

$$W_{eq} = \sum \frac{a_i}{f_i n_i} \quad (4.2)$$

where a_i, f_i and n_i are the atomic weight, mass fraction, and the number of electrons required to complete a half-cell reaction of the *ith* dissolving alloying element, respectively.

Separate to the ZRA experiments, open circuit potential (OCP) and gravimetric mass loss measurements were made on freely-corroding uncoupled AA7050 over 24 h in the same solutions used for the ZRA exposures. This enabled the correction of the charge measured in the ZRA experiments such that the anodic charge density associated with open circuit corrosion was removed, providing a true reflection of AA7050 corrosion strictly due to galvanic coupling to 316SS or high-purity Cu.

Anodic and cathodic potentiodynamic polarization curves were generated on AA7050 and 316SS/high-purity Cu, respectively, after a 3-h exposure at open circuit. The open circuit exposure time of 3 h was based on the average time observed for galvanic currents in the ZRA experiments to settle to steady state values. The scans were performed at a scan rate of 0.5 mV/s, starting from 0 V_{OCP} in order to avoid surface alterations from prior cathodic or anodic dissolution.

4.3.3 Scanning Vibrating Electrode Technique

A Biologic SP instrument was utilized for all SVET experiments. Experiments were conducted in freely corroding (i.e., unpolarized) conditions and the exposed bare area of the planar fastener couple with dimensions of ~ 8 mm x 8 mm was scanned in each case. The vibrating SVET probe consisted of a platinum probe with a diameter specified by the manufacturer as between 5 and 50 µm. A complete description of the design and calibration procedure for the SVET instrument is available in previous publications.[31,32] For each experiment, exposed

specimen surfaces were fully immersed in an electrolyte bath containing aqueous 0.001 M NaCl electrolyte and the relevant amount of Na_2CrO_4 dissolved in solution. Where applicable, separate experiments were carried out with the addition of Mg(II) for the purpose of a direct comparison of corrosion inhibition efficacy with chromate at the same ion concentrations. As several investigations have reported that Mg(II) provides an inhibitive effect on AAs,[33–38] it seemed reasonable to assess how it would perform compared to chromate in the case of a galvanic couple. The choice of 0.001 M NaCl was made based on the resolution limitations of the SVET as signal-to-noise ratios decrease with increasing solution conductivity.[39] However, in relation to the boldly exposed surfaces simulated in this work, the 0.001 M NaCl concentration would be relevant under rainy conditions, with the natural pH of 5.8 representing normal rain conditions, and pH 3 representing acid rain conditions. Spatial analyses of rainwater chemistry over the United States[40] and Europe[41,42] reported a maximum Cl^- concentration of ~ 0.0002 M and ~ 0.0012 M, respectively.

The vibrating SVET probe was positioned vertically and scanned at a constant of height of 100 µm above the experimental area with an amplitude of 30 µm and a frequency of 80 Hz. The peak-to-peak SVET voltage signal (V_{pp}) is related to the current flux density along the axis of probe vibration (j_z) by:

$$V_{pp} = j_z \left(\frac{A_{pp}}{\kappa}\right) \tag{4.3}$$

where κ is solution conductivity, and A_{pp} is the peak-to-peak amplitude of vibration of the SVET probe, such that a quantity $G = \kappa/A_{pp}$ may be defined as the SVET calibration factor.

SVET calibration was carried out galvanostatically using a point current source technique, and the setup can be found elsewhere.[43,44] Samples were scanned immediately following immersion, and continuously thereafter for a period of 24 h, and each scan took approximately 12 minutes. Area-averaged anodic current densities (J_a) and cathodic current densities (J_c) were obtained by the numerical area integration of j_z distributions to give an estimation of time-dependent total local corrosion currents, as described in details elsewhere.[31,45] Separate

experiments were carried out on uncoupled AA7050 (i.e., without 316SS) to collect baseline j_z distributions. j_z distributions were plotted using Surfer 8™ by Golden Software.

4.3.4 X-ray Photoelectron Spectroscopy

High-resolution $Cr2p_{3/2}$ XPS spectra were taken with a PHI VersaProbe III™ scanning XPS microprobe equipped with a monochromatic Al Kα X-ray source (1486.7 eV) and at a pass energy of 26 eV. The aim was to resolve the Cr chemical states of the chromate-induced surface film formed on the AA7050 ZRA samples after exposure to chromate-containing 0.001 M NaCl solutions at different pH's. Spectra were fitted using KolXPD software version 1.8.0 (provided by kolibrik.net, Czech Republic) after calibrating to the standard binding energy of 285 eV for the C1s peak. Deconvolution of the peaks was based on binding energies found in the literature.[12,46,47] A summary of the binding energies is given in Table 4.3. Areas of the deconvoluted peaks were also determined using the KolXPD software. Samples were sputter-depth profiled to calculate the percentage of total Cr species (independent of chemical state) across the depth of the surface layer by rastering a 3 keV Ar^+ beam over a 3 mm x 3 mm area. Analyses were performed after every 0.2 min of sputtering to a total sputter time of 5 min, alternating with zalar rotation.

Table 4.3. Summary of Binding Energies for Different Chemical States of $Cr2p_{3/2}$ Peak Detected on Chromate-Exposed AA7050 Surfaces.[12,46,47]

Species	Binding Energy (eV)
Cr^0	574.2
Cr_2O_3	575.9, 576.3, 577.1, 578.1, 578.5
$Cr(OH)_3$	577.3
Cr(VI) mixed species	579.1, 579.3, 579.8

4.3.5 Surface Corrosion Morphology Characterization

Where appropriate, surface characterization was performed utilizing a Quanta 650™ scanning electron microscope (SEM) equipped with energy dispersive spectroscopy (EDS) capability and Oxford Instruments AZtec™ software. A Hirox RH 8800™ optical microscope (OM) was also used to image sample cross-sections as required to assess the extent of corrosion damage. An in-house MATLAB code[4] was utilized to estimate the maximum damage penetration

depth as well as total area lost to corrosion from the cross-sectional images. Prior to optical imaging, the sample cross-sections were mounted in epoxy, polished to a surface finish of 1 µm, etched with Keller's Reagent, rinsed with deionized water and dried with clean compressed air.

4.4 Results

The results presented herein experimentally assessed the impact of solution parameters on the ability of chromate at various concentrations to protect AA7050 galvanically coupled to 316SS. First, the effect of pH was assessed in 0.001 M NaCl solutions using the SVET in combination with the ZRA technique, polarization scans, and XPS to assess the galvanic coupling behavior of AA7050 and 316SS under conditions meant to simulate those on the boldly exposed surfaces. Second, the effect of Al^{3+} in a crevice was assessed in deaerated 5 M total Cl^- using the ZRA technique in combination with polarization scans and damage characterization to identify the probable dominant cathode in a simulated AA7050-316SS fastener crevice during the damage initiation and damage propagation stages. The 5 M total Cl^- was considered an appropriate chloride concentration to represent crevice environments based on reports in the literature regarding occluded solution chemistry for Al alloys. For AA7XXX, crack tip pH has been reported to be as low as 2,[48–50] with crack tip [Al^{3+}] (as $AlCl_3$) up to ~ 2 M,[50] which translates to total [Cl^-] of up to ~ 6 M.

4.4.1 Galvanic Coupling of AA7050 and 316SS in Near-Neutral Surface Conditions

To evaluate the effect of galvanic coupling, SVET was conducted on freely-corroding, uncoupled AA7050 (i.e., without 316SS) to obtain baseline j_z distributions to enable a direct comparison with the j_z distributions obtained on the simulated AA7050-316SS fastener couple. Figure 4.2 presents the SVET maps on uncoupled AA7050 in inhibitor-free and chromate-containing 0.001 M NaCl at the natural pH values that occurred for each solution. It was observed that the baseline j_z distributions in inhibitor-free solution were so small ($< \pm 1$ µA/cm^2) such that there were barely any changes observed on addition of chromate, regardless of chromate concentration. Furthermore, there were no clear anodically or cathodically activated regions; the j_z distributions appeared to be consistent with uniform corrosion at the size scale of relevance to SVET measurements (~ 100 µm). These observations were in contrast to the current density maps

obtained on the fastener couple as illustrated in Figure 4.3a. In inhibitor-free solution, j_z distributions on the fastener couple were at least five times higher than on uncoupled AA7050 with approximate maximum values of +/- 10 $\mu A/cm^2$, and a clear pitting corrosion morphology was observed across the AA7050 surface that appeared to intensify over the course of 24 h. Upon addition of the lowest concentration of chromate studied (i.e., 10^{-4} M), j_z distributions over the 316SS were dramatically suppressed such that at longer times (≥ 10 h), the contribution of local cathodic reactions on the AA7050 to support a small anodically activated region became more significant (Figure 4.3b), albeit with j_z distributions comparable to those observed on the uncoupled AA7050. Further addition of chromate to 10^{-3} M appeared to fully suppress the galvanic coupling current after short times (~ 2 h), and thus, no additional beneficial effect was observed with the highest chromate concentration used (i.e., 10^{-2} M).

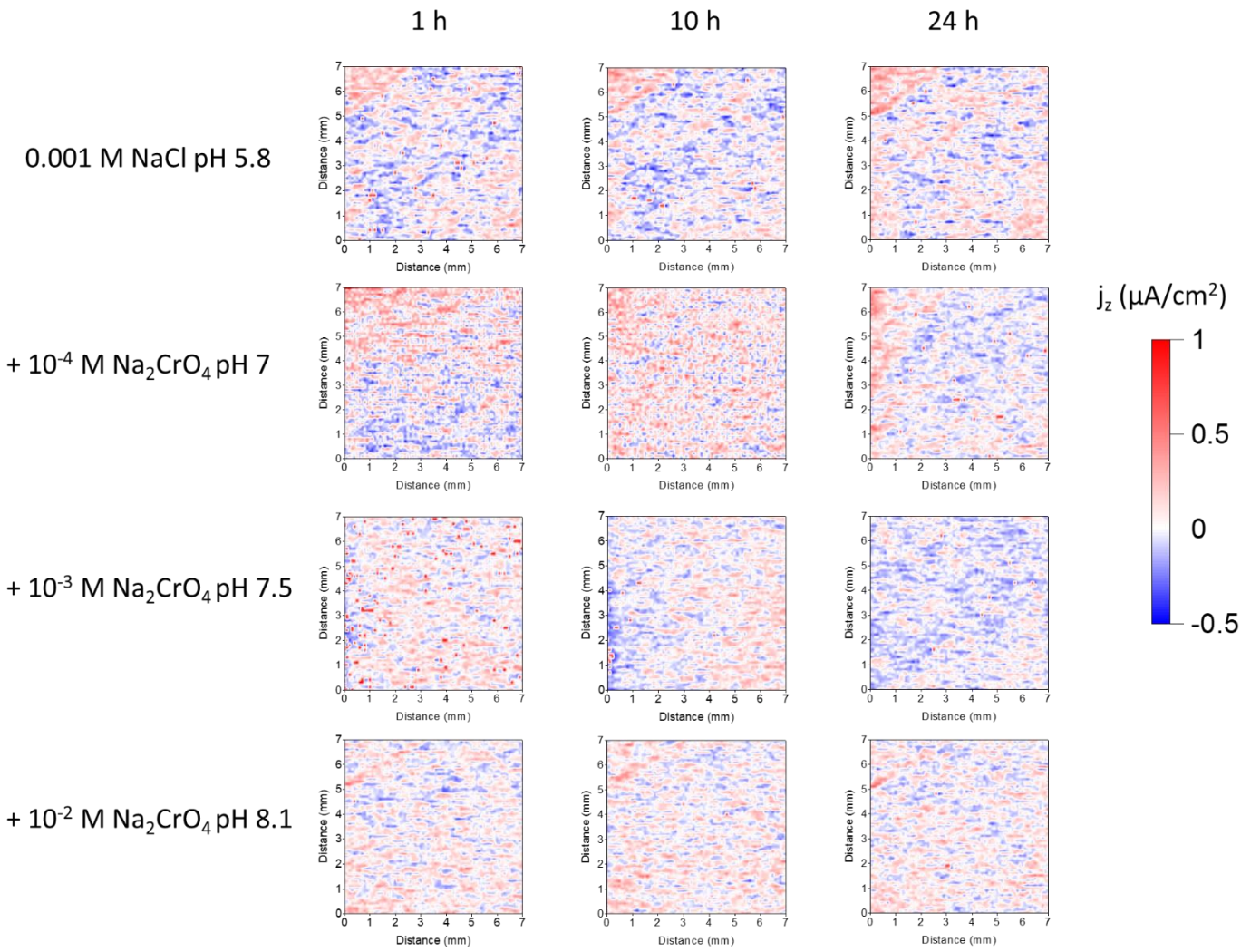

Figure 4.2. SVET-derived surface maps showing j_z distributions above a freely-corroding uncoupled AA7050 sample immersed in 0.001 M NaCl and with additions of chromate at different times. The pH of the solutions was not adjusted.

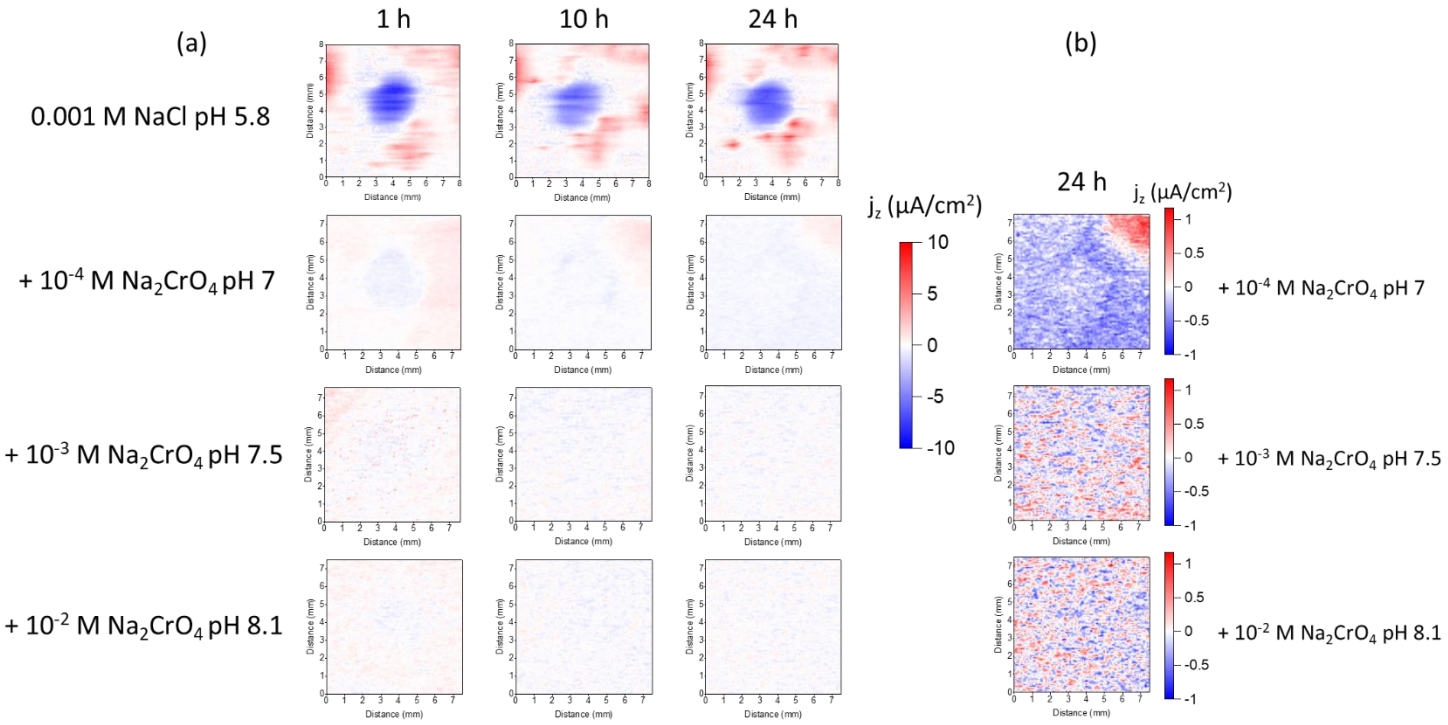

Figure 4.3. (a) SVET-derived surface maps showing j_z distributions above a freely-corroding AA7050-316SS couple sample immersed in 0.001 M NaCl and with additions of chromate at different times. The pH of the solutions was not adjusted; (b) zoomed-in 24 h maps in (a) to show limit of j_z distributions in chromate-containing solutions.

To further assess the galvanic couple behavior, ZRA experiments were performed on AA7050 coupled to 316SS in a 1:1 area ratio when immersed for 24 h in the same solutions used for the SVET measurements (Figure 4.4). In inhibitor-free conditions, the galvanic couple potential became relatively stable after the initial 5 h at ~ -0.54 V_{SCE} with a corresponding couple current density of ~ 4 μA/cm^2. The addition of 10^{-4} M chromate barely changed the galvanic couple potential. However, the couple current density decreased by nearly an order of magnitude. With higher concentrations of chromate, a trend was observed where at early times (0 to 8 h), the galvanic potentials steadily decreased with a corresponding decrease in couple current densities. At longer times (≥ 10 h), the galvanic couple potentials began to ennoble toward the potentials observed in inhibitor-free conditions while the couple current densities continued to decrease to ~ 0.1 μA/cm^2.

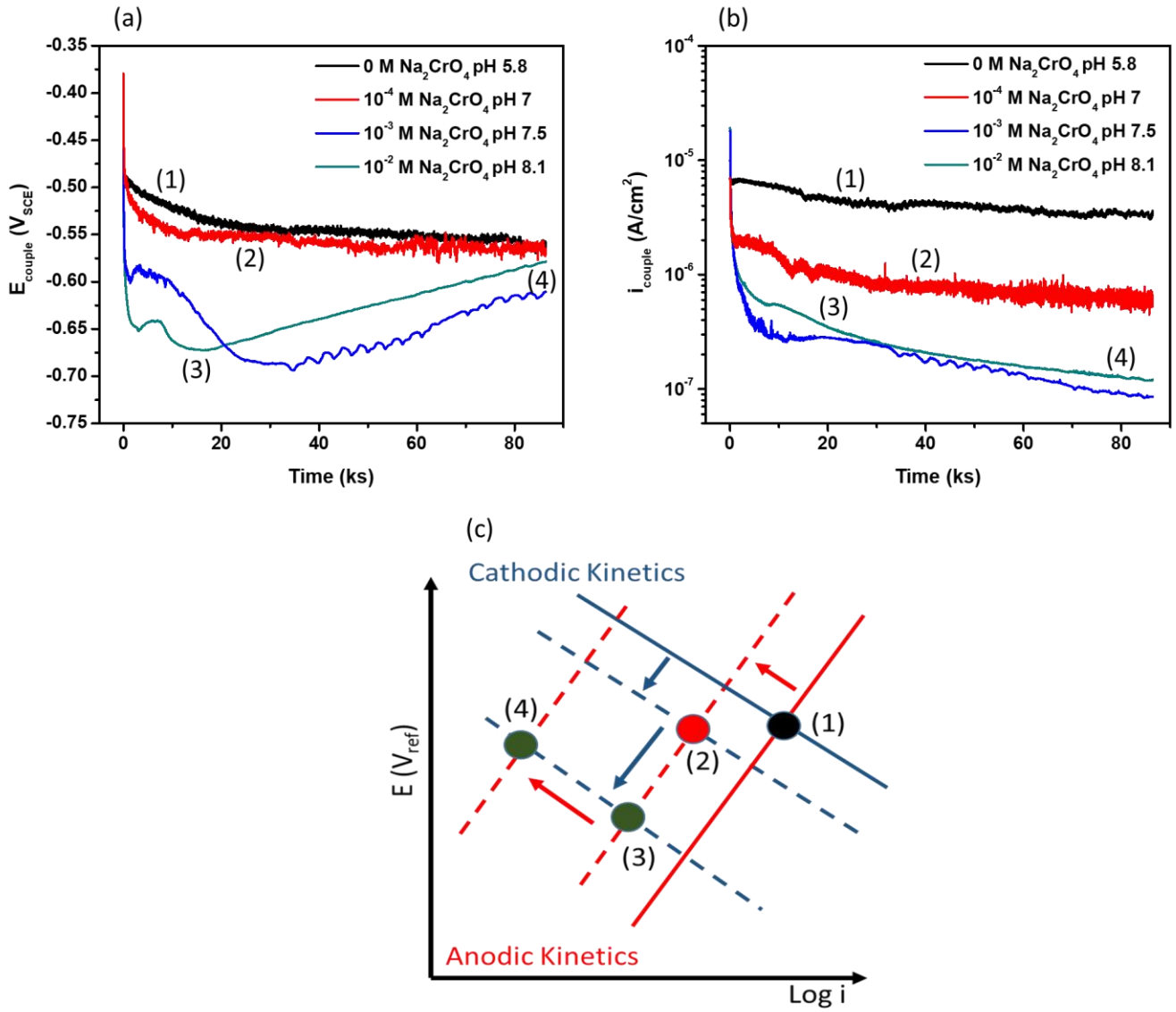

Figure 4.4. (a) Galvanic couple potentials and (b) couple current densities as a function of time on AA7050-316SS planar couples immersed in 0.001 M NaCl and with additions of chromate. The pH of the solutions was not adjusted; (c) schematic of the Evans diagram to show the controlling factors for the response in galvanic couple potential and couple current density based on Mixed Potential Theory.

Anodic and cathodic polarization curves on AA7050 and 316SS, respectively, were generated in the same environments (Figure 4.5) to assess the effect of chromate concentration on electrode kinetics. On 316SS, it was observed that cathodic ORR kinetics decreased as chromate concentration increased, within the range of galvanic potentials obtained in the ZRA

experiments (-0.5 to -0.7 V_{SCE}). On AA7050, the passive current density increased as chromate concentration increased, within the range of galvanic potentials obtained in the ZRA experiments.

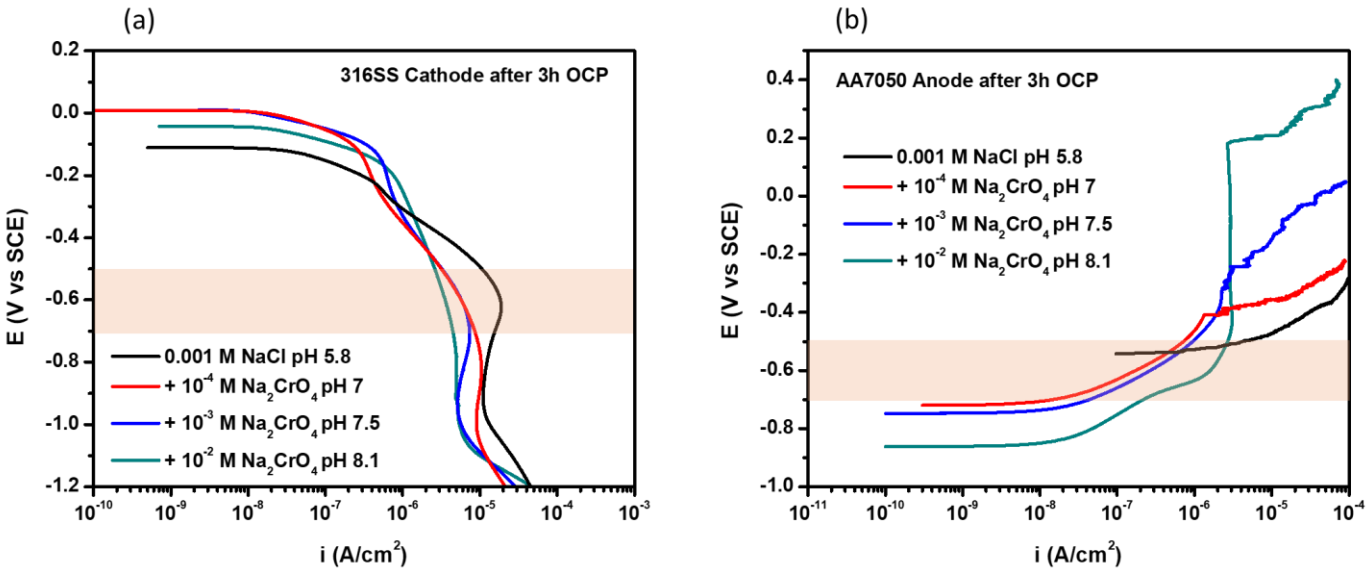

Figure 4.5. Polarization curves generated on (a) 316SS and (b) AA7050 in 0.001 M NaCl as a function of chromate concentration. The pH of the solutions was not adjusted. Orange boxes highlight the range of galvanic couple potentials obtained in the ZRA exposures.

4.4.2 Galvanic Coupling of AA7050 and 316SS in Acid Rain Surface Conditions

Figures 4.6 and 4.7 present the SVET maps on uncoupled AA7050 and simulated AA7050-316SS fastener couple, respectively, in inhibitor-free and chromate-bearing 0.001 M NaCl at pH 3. As illustrated in Figure 4.6, j_z distributions above the uncoupled AA7050 surface clearly showed anodically and cathodically activated regions with maximum current density values of +/- 25 µA/cm^2 that were up to twenty times higher than those observed at natural pH conditions. However, upon addition of 10^{-4} M chromate, j_z distributions decreased by up to an order of magnitude with no distinct anodically or cathodically activated regions observed after 24 h (Figure 4.6b). Further additions of chromate provided no significant beneficial effects. It is noted that the j_z distributions in chromate-containing solutions did not decrease to the levels attained at natural pH conditions, suggesting limited inhibitive activity of chromate at pH 3 conditions. For the fastener couple (Figure 4.7), increased cathodic current density over the 316SS up to 50

μA/cm^2 facilitated the anodic activation of nearly the entire exposed surface of AA7050 with an anodic j_z maximum of ~ 30 μA/cm^2. The j_z distributions measured above the 316SS were up to five times higher than the values observed over 316SS at natural pH conditions. The addition of 10^{-4} M chromate gradually decreased j_z distributions above the 316SS by up to an order of magnitude at the end of 24 h, and the attack on AA7050 transitioned to a more localized-type attack but there was still evidence of galvanic coupling. Increased chromate concentrations further suppressed j_z distributions, and a shutdown of galvanic coupling occurred in the presence of 10^{-2} M chromate, where j_z distributions were found to be comparable to those observed over uncoupled AA7050 surface in the same solution (Figure 4.6). It is noted that the chromate concentration required to shut down the 316SS cathode at pH 3 (i.e., 10^{-2} M) was ten times higher than that observed at natural pH conditions (i.e., 10^{-3} M).

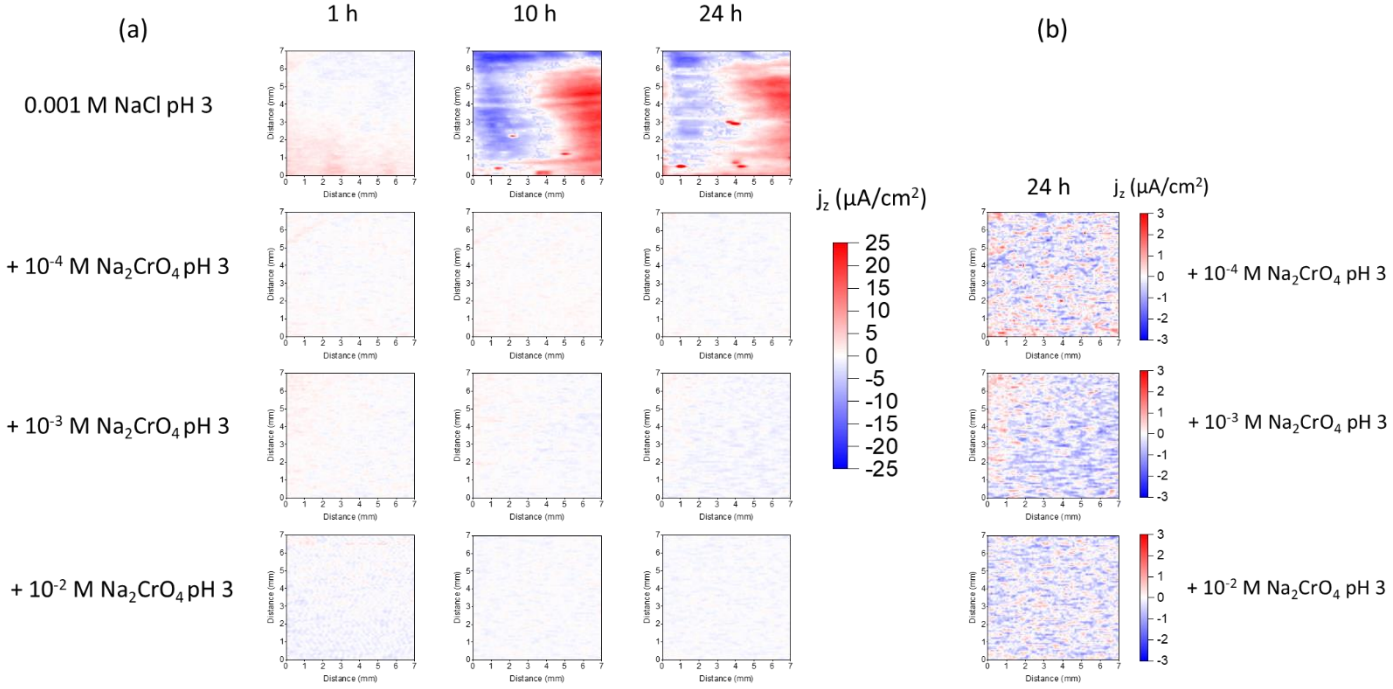

Figure 4.6. (a) SVET-derived surface maps showing j_z distributions above a freely-corroding uncoupled AA7050 sample immersed in 0.001 M NaCl and with additions of chromate at different times. The pH of each solution was adjusted to 3 using HCl; (b) zoomed-in 24 h maps in (a) to show limit of j_z distributions in chromate-containing solutions.

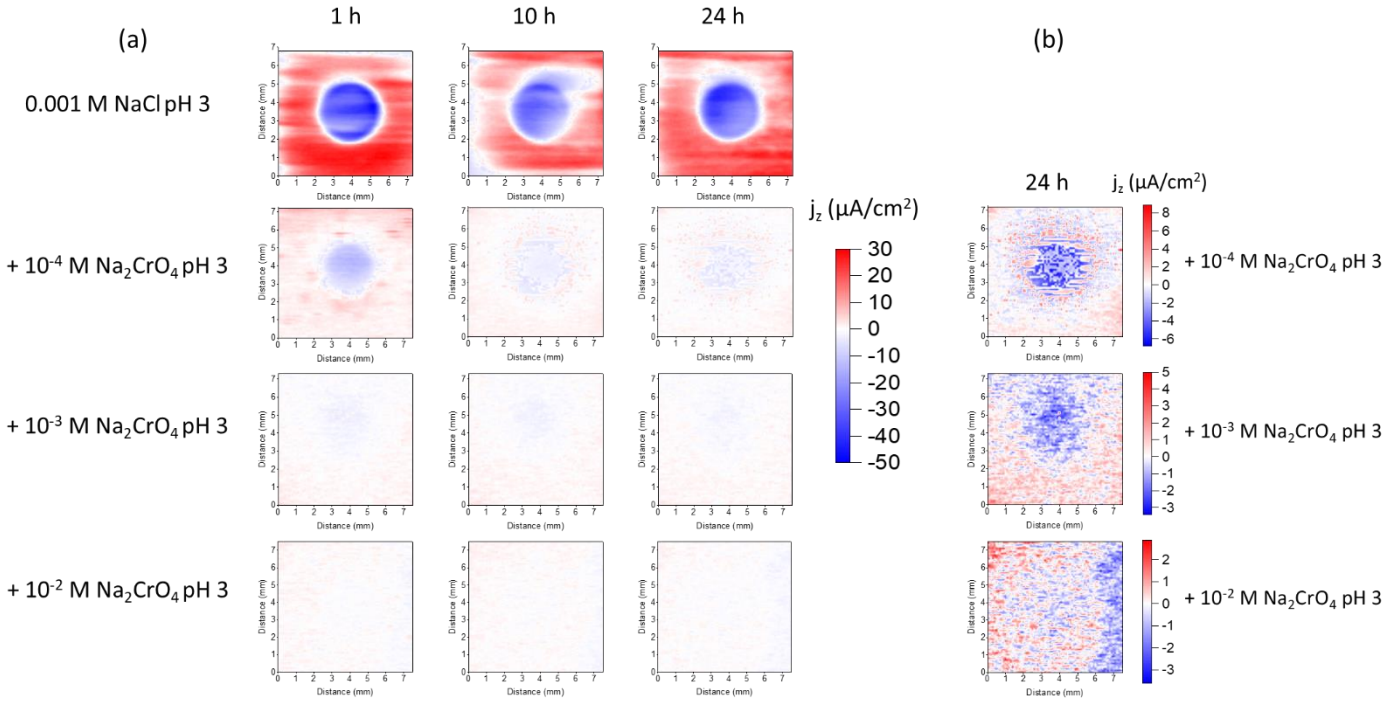

Figure 4.7. (a) SVET-derived surface maps showing j_z distributions above a freely-corroding AA7050-316SS couple sample immersed in 0.001 M NaCl and with additions of chromate at different times. The pH of each solution was adjusted to 3 using HCl; (b) zoomed-in 24 h maps in (a) to show limit of j_z distributions in chromate-containing solutions.

Figure 4.8 displays the galvanic couple potentials and couple current densities obtained from ZRA experiments performed on AA7050 coupled to 316SS (with a 1:1 area ratio) in inhibitor-free and chromate-containing 0.001 M NaCl at pH 3. In inhibitor-free conditions, there were occasional transient spikes in galvanic couple potential with corresponding transient spikes in couple current density. These transient spikes are indicative of metastable pitting events or transient micro-galvanic coupling-induced localized corrosion of various forms perhaps activated over time. Nonetheless, the galvanic couple potential averaged ~ -0.56 V_{SCE} with a corresponding average couple current density of ~ 6 µA/cm^2. The addition of 10^{-4} M chromate caused a minimal negative shift in the galvanic couple potential, however, the couple current density halved to ~ 3 µA/cm^2. Increased chromate concentration of 10^{-3} M also produced a small decrease in galvanic couple potential in the first 11 h, then slightly ennobled for the remaining duration of the experiment. However, the couple current density decreased by about an order of magnitude

compared to the inhibitor-free case. Interestingly, with the highest chromate concentration of 10^{-2} M, there was an appreciable decrease in galvanic couple potential but the couple current density (~ 1.5 µA/cm^2) was higher than that achieved with the addition of 10^{-3} M, but lower than that attained with 10^{-4} M chromate.

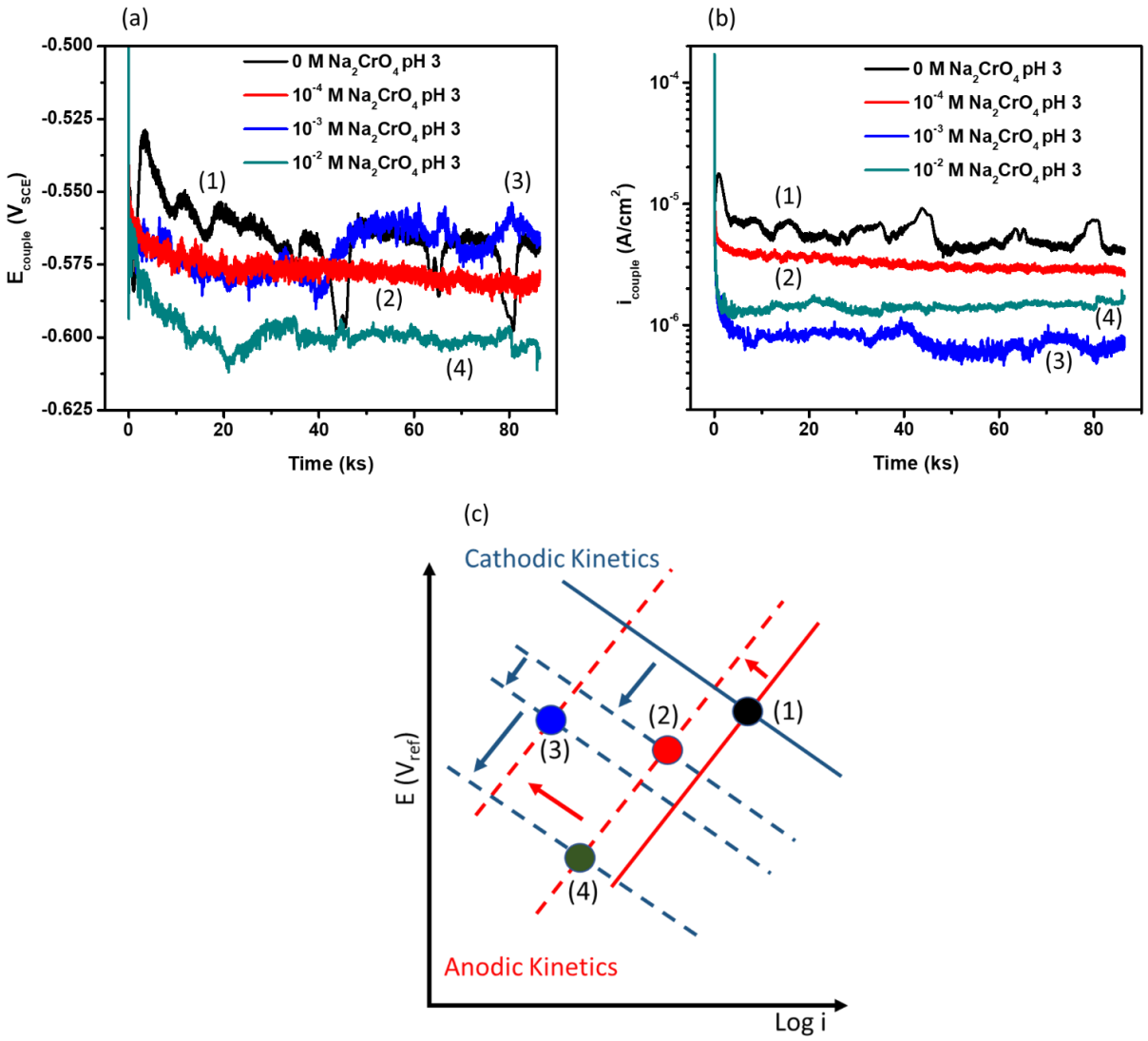

Figure 4.8. (a) Galvanic couple potentials and (b) couple current densities as a function of time on AA7050-316SS planar couples immersed in 0.001 M NaCl and with additions of chromate. The pH of each solution was adjusted to 3 using HCl; (c) schematic of the Evans diagram to show the controlling factors for the response in galvanic couple potential and couple current density based on Mixed Potential Theory.

Anodic and cathodic polarization curves generated on AA7050 and 316SS in pH 3 environments are displayed in Figure 4.9. On 316SS, it was observed that the range of galvanic potentials obtained in the ZRA experiments (-0.53 to -0.62 V_{SCE}) appeared to be dominated by activation-controlled HER kinetics unlike the case at natural pH conditions that was clearly controlled by ORR kinetics (Figure 4.5a). Nonetheless, cathodic kinetics appeared to decrease as chromate concentration increased. On AA7050, the passive current density decreased as chromate concentration increased such that at the highest concentration of 10^{-2} M, the open circuit potential was at or above the pitting potential, in contrast to the behavior observed under natural pH conditions.

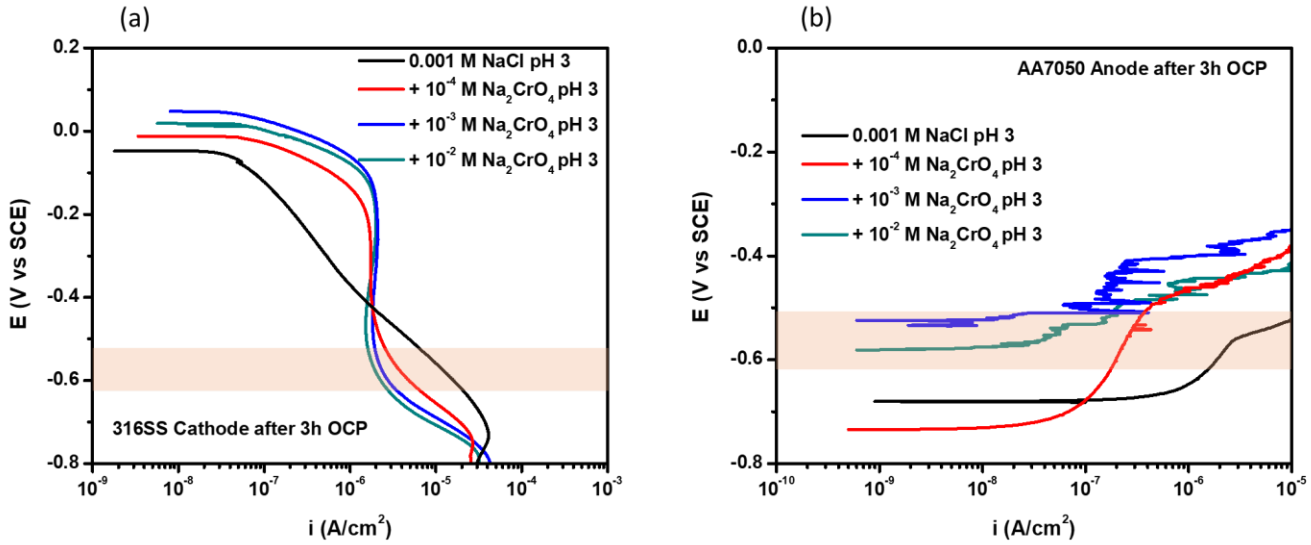

Figure 4.9. Polarization curves generated on (a) 316SS and (b) AA7050 in 0.001 M NaCl as a function of chromate concentration. The pH of each solution was adjusted to 3 using HCl. Orange boxes highlight the range of galvanic couple potentials obtained in the ZRA exposures.

4.4.3 Effect of Chromate on Galvanic Coupling Parameters as a Function of pH

SVET-derived local current density (j_z) vs. distance line profiles were taken across the center of the simulated fastener couple surface. Plotting the j_z data in this way enables localized interrogation of a region of interest. In this case, the effect of chromate at the lowest concentration (i.e., 10^{-4} M) on the cathodic current measured above the 316SS in the initial stages of exposure (i.e., after 30 min) was examined. The data are presented in Figure 4.10 where the

grey bar shows the size and position of the 316SS across the profile. First, in chromate-free conditions, the j_z distributions above the 316SS at pH 3 are up to eight times higher relative to the distributions at natural pH. The addition of 10^{-4} M chromate suppressed j_z distributions by at least an order of magnitude at natural pH conditions, compared to about a five-fold decrease at pH 3.

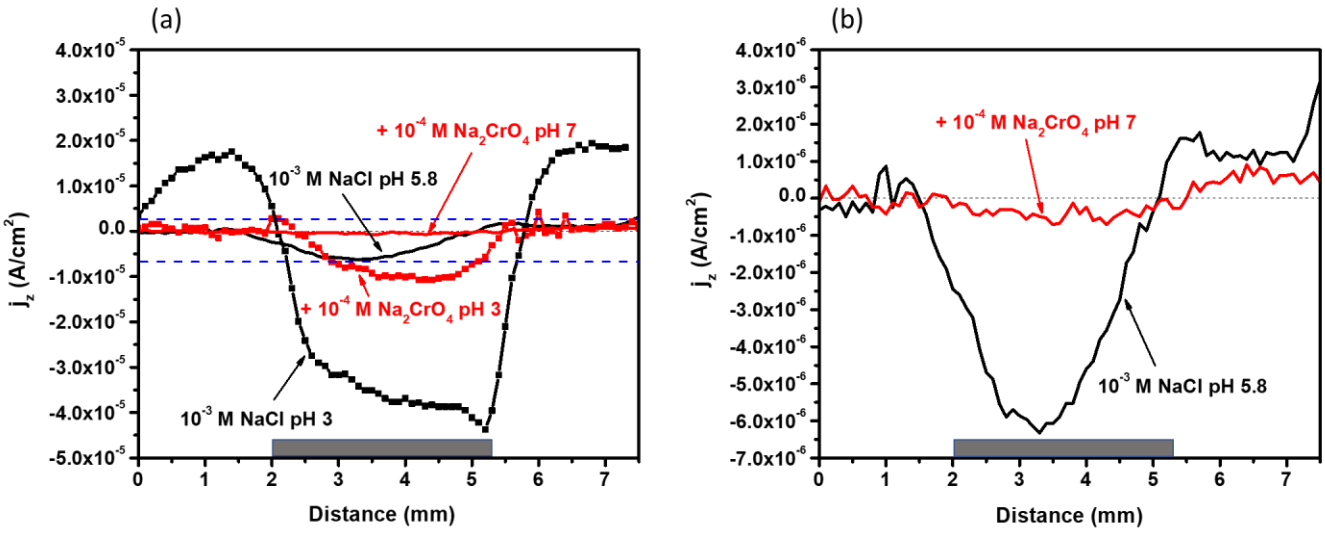

Figure 4.10. (a) SVET-derived line profile analysis across center of the AA7050-316SS couple surface comparing j_z distributions above 316SS in 0.001 M NaCl and with the addition of 10^{-4} M chromate after 30 min exposure at natural pH and pH 3 conditions; (b) Blue dashed region in (a) zoomed-in to highlight data limits under natural pH conditions. Grey bars show the size and position of the 316SS.

Semi-quantitative analysis of the corrosion activity on the simulated fastener couple as a function of time was carried out by calculating the SVET-derived area-averaged integrated total anodic (J_a) and cathodic (J_c) current density values, displayed as a function of time, in Figure 4.11. A trend can be seen where J_a and J_c values in pH 3 environments were generally higher than in natural pH environments regardless of chromate concentration. Another key observation was that although both J_a and J_c values decreased with increasing chromate regardless of pH, J_a and J_c values in pH 3 environments generally were not equal in magnitude, with slightly higher cathodic currents (+ 25% average). This discrepancy could have resulted from the underestimation of anodic currents due to masking effect of corrosion products, or non-detection of small transient currents that flow below the plane of the SVET measurement at

anodic sites, or edge effects (i.e., the SVET misses the anodic activity in the vicinity of the edges of the AA7050 surface but captures the cathodic activity occurring over the entire 316SS surface located at the center of the structure). In addition, cathodic currents could be overestimated due to increased diffusion of cathodic reactants (O_2, H^+) to the surface as the probe scans above cathodic sites.[51,52] Nonetheless, the discrepancies were relatively small and so J_a and J_c values were considered to be in reasonable agreement.

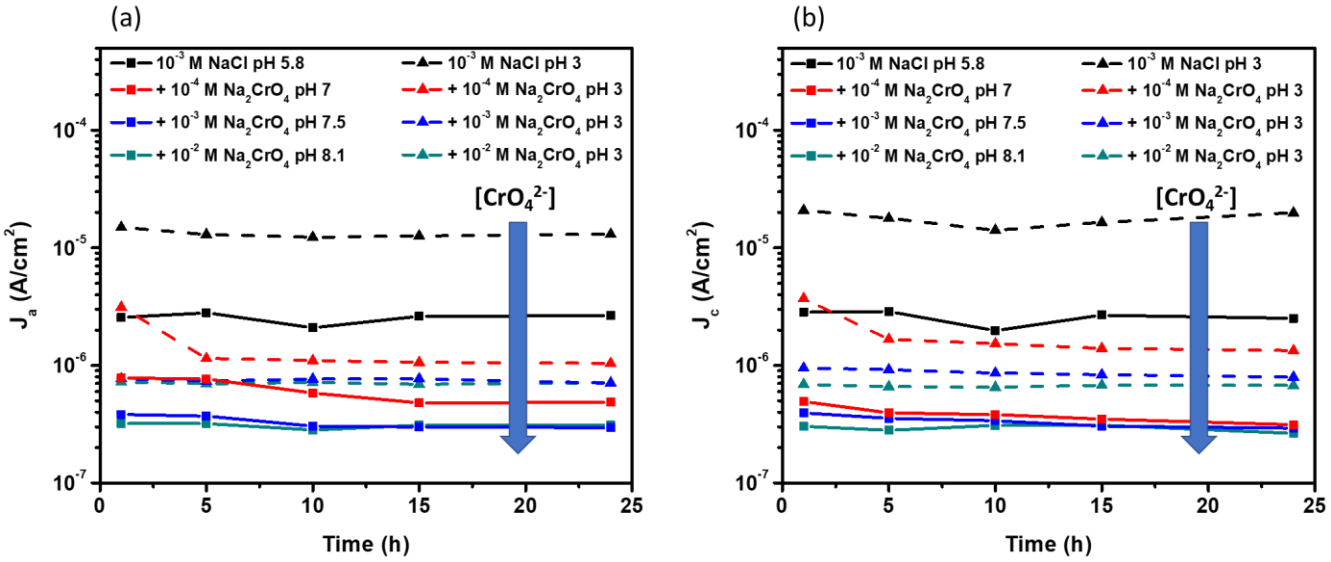

Figure 4.11. SVET-derived area-averaged integrated total (a) anodic and (b) cathodic current densities as a function of exposure time on a freely-corroding AA7050-316SS couple surface in 0.001 M NaCl and with additions of chromate at natural pH and pH 3 conditions.

Figure 4.12a compares the ZRA charge densities at natural pH and pH 3 conditions. A trend can be seen in which the charge densities at pH 3 conditions were at least twice those at natural pH conditions. Although charge density values were suppressed with increasing chromate concentration in both cases, it appeared chromate was not able to bring down the charge densities at pH 3 to the levels attained at natural pH conditions. This result is consistent with observations made with the SVET measurements. Figure 4.12b shows the corresponding optical micrographs of AA7050 surfaces after the ZRA exposures. On inspection it can be seen that in inhibitor-free solutions, the damage morphology at natural pH was characterized by isolated, large, deep pits while at pH 3 the damage was more of an intergranular-type attack (see inset)

accompanied with dense pitting. Interestingly, the addition of 10^{-4} M chromate suppressed the intergranular damage at pH 3 conditions, and the morphology transitioned to isolated shallow pitting similar to the nature of suppressed attack attained with the same chromate concentration at natural pH, albeit with considerably larger pit size. In both pH conditions, further additions of chromate decreased pit size and density.

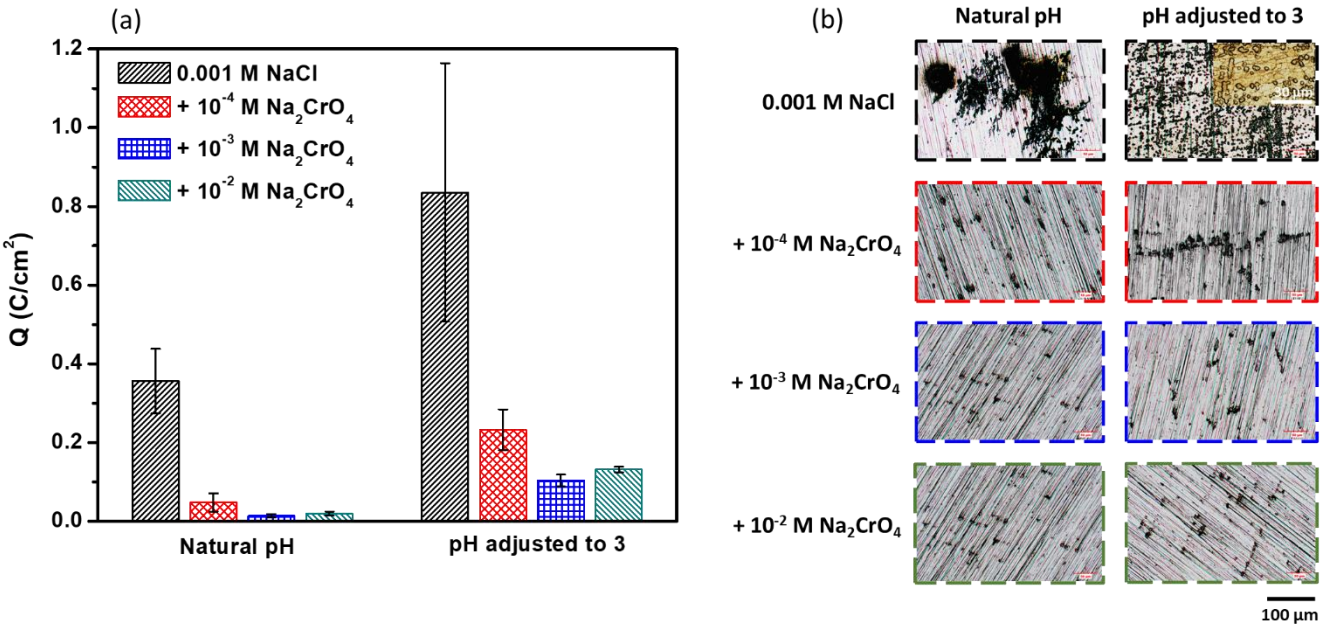

Figure 4.12. (a) ZRA charge densities on AA7050-316SS planar couples immersed in 0.001 M NaCl and with additions of chromate at natural pH and pH 3 conditions; (b) corresponding optical micrographs of the AA7050 surfaces after the 24 h ZRA experiments. Zoomed-in inset micrograph for 0.001 M NaCl pH 3 shows intergranular fissures.

4.4.4 XPS Characterization of Chromate-Exposed AA7050 Surface as a Function of pH

XPS analyses of the chromate-induced layer formed on AA7050 after 24 h full-immersion ZRA exposures in chromate-containing 0.001 M NaCl solutions were carried out. This enabled the resolution of the Cr chemical states and the composition of the surface film formed with respect to Cr species, as a function of pH. It is noted that Al_2O_3 was detected as the major component of the surface film, but for the purpose of this work, the chromate-induced components are the species of interest.

The $Cr2p_{3/2}$ peak deconvolution on AA7050 after ZRA experiments in 10^{-2} M chromate environments is shown in Figures 4.13a and 4.13b. Under natural pH conditions, Cr(III) hydroxide was found to be the dominant Cr species in the surface film, making up 69% of the total peak area. Cr(III) oxide constituted 22%. A smaller amount (8%) of adsorbed and unreduced Cr(VI) was also detected. Furthermore, a small but measurable amount of metallic Cr (Cr^0) was present, constituting ~ 1% of the $Cr2p_{3/2}$ peak area. This observation is consistent with our previous work on AA7050 in 0.6 M NaCl at natural pH.[19] Under pH 3 conditions, Cr(III) hydroxide was also found to be the dominant Cr species in the surface film, making up 65% of the total peak area. Cr(III) oxide constituted 19%, and adsorbed and unreduced Cr(VI) constituted a considerable 16%. It is noted that Cr^0, however slight, was not detected under pH 3 conditions.

Sputter depth profiling was conducted on the chromate-exposed AA7050 ZRA samples to estimate the composition of the surface film formed with respect to Cr species as a function of pH. The depth profile data collected after immersion in natural pH and pH 3 conditions are given as a function of chromate concentration in Figures 4.13c and 4.13d, respectively. Under natural pH conditions, the total amount of Cr species in the surface film increased with increasing chromate concentration, with a maximum surface Cr species concentration of ~ 50% upon exposure to 10^{-2} M chromate (Figure 4.13c). Under pH 3 conditions however, the concentration of the sum of the Cr species appeared to be less dependent on chromate concentration (Figure 4.13d). The maximum surface Cr species concentration was ~ 60% which was 10% higher than the value observed under natural pH conditions.

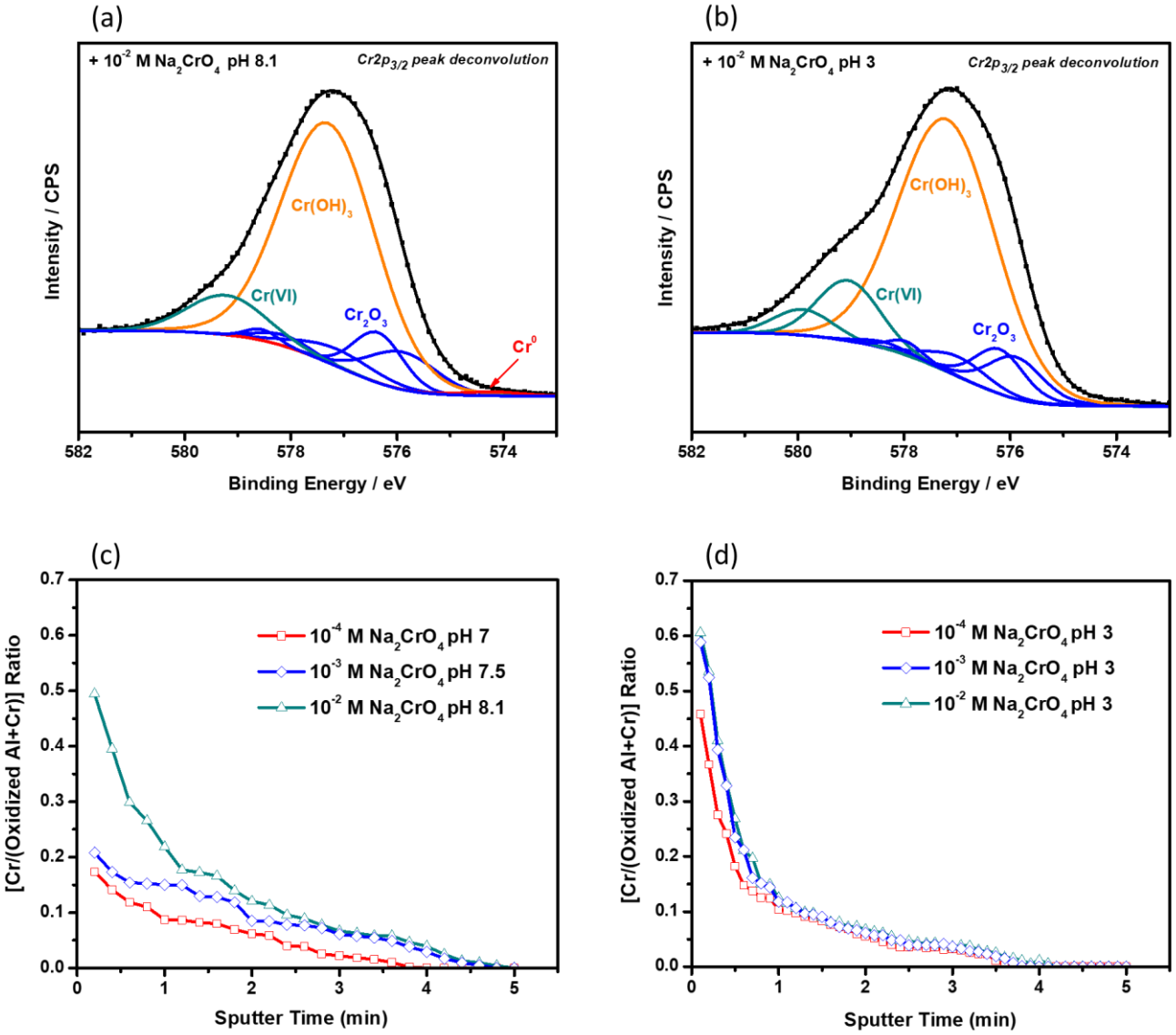

Figure 4.13. High-resolution XPS $Cr2p_{3/2}$ spectrum analysis on AA7050 surface coupled to 316SS after 24 h ZRA exposure in 0.001 M NaCl + 10^{-2} M Na_2CrO_4 at (a) natural pH and (b) pH 3 conditions. Total amount of Cr species in the surface film formed on AA7050 surface coupled to 316SS after 24 h ZRA exposure in 0.001 M NaCl as a function of chromate concentration under (c) natural pH and (d) pH 3 conditions.

4.4.5 Performance of Mg(II) in Relation to Chromate in Inhibiting Galvanic Corrosion of AA7050 Coupled to 316SS

The purpose of this investigation was to assess the inhibitive effect of Mg(II) on an actual AA-316SS galvanic couple in comparison to chromate. Previous studies have focused on the effect of Mg(II) on base AAs.[33–38] Although Mg(II) can be introduced into solution from a Mg-rich coating applied over the substrate, it is noted that in the case of AA7050 for instance, Mg(II) can also be released into solution as a result of dealloying of a Cu-rich IMP (i.e., Al_2CuMg), dissolution of Mg_2Si IMP, and conceivably dissolution of the strengthening precipitate, $MgZn_2$. Therefore, Mg(II) would be expected to be present in solution once corrosion of AA7050 initiates, albeit in concentrations that may be too low to have any significant beneficial effect.

SVET experiments were carried out in 0.001 M NaCl with the addition of either 10^{-4} M Mg(II) or 10^{-2} M Mg(II) to maintain the same inhibitor ion concentration as chromate in both natural pH and pH 3 conditions. Care was taken to ensure the $[Cl^-]$ remained constant at 0.001 M; 10^{-4} $MgCl_2$ was added to 8 x 10^{-4} M NaCl for the low concentration case, and 10^{-2} M $MgSO_4$ was added to 0.001 M NaCl for the high concentration case. In addition, since the sulfate ion SO_4^{2-} is known to have inherent inhibitive properties, a test experiment was conducted with the addition of 10^{-2} M Na_2SO_4 to base solution to assess its baseline inhibitive effect.

Figure 4.14 compares the SVET maps on AA7050-316SS fastener couple in inhibitor-free, 10^{-4} M chromate- and Mg(II)-containing 0.001 M Cl^- at the natural pH values that occurred for each solution. It was observed that in the Mg(II)-containing solution, j_z distributions over the fastener couple were at least one magnitude higher than in the chromate-containing solution. In addition, a distinct pitting corrosion morphology was observed across the AA7050 surface that appeared to intensify as j_z distributions over the 316SS increased over the course of 24 h. This observation was in contrast to that made in the corresponding environment containing a higher concentration of 10^{-2} M Mg(II) (Figure 4.15). Although still inferior compared to the activity of chromate by approximately five times, there appeared to be an appreciable degree of inhibition with the addition of 10^{-2} M Mg(II). Cathodic current density over the 316SS was decreased by over four times compared to the inhibitor-free case, and at longer times (> 10 h), there was barely

any indication of galvanic coupling or distinction in the cathodic activity between the 316SS and majority of the exposed AA7050 surface in supporting attack of a small anodically activated region. It is noted that despite the fact that the addition of 10^{-2} M Na_2SO_4 to the base solution provided some degree of inhibition somewhat comparable to that of 10^{-2} M $MgSO_4$, the current density distributions over the 316SS were approximately two times higher than observed with $MgSO_4$ after 24 h and there was still evidence of galvanic coupling. Thus, the inhibitive effect achieved with $MgSO_4$ was attributed predominantly to the activity of Mg(II).

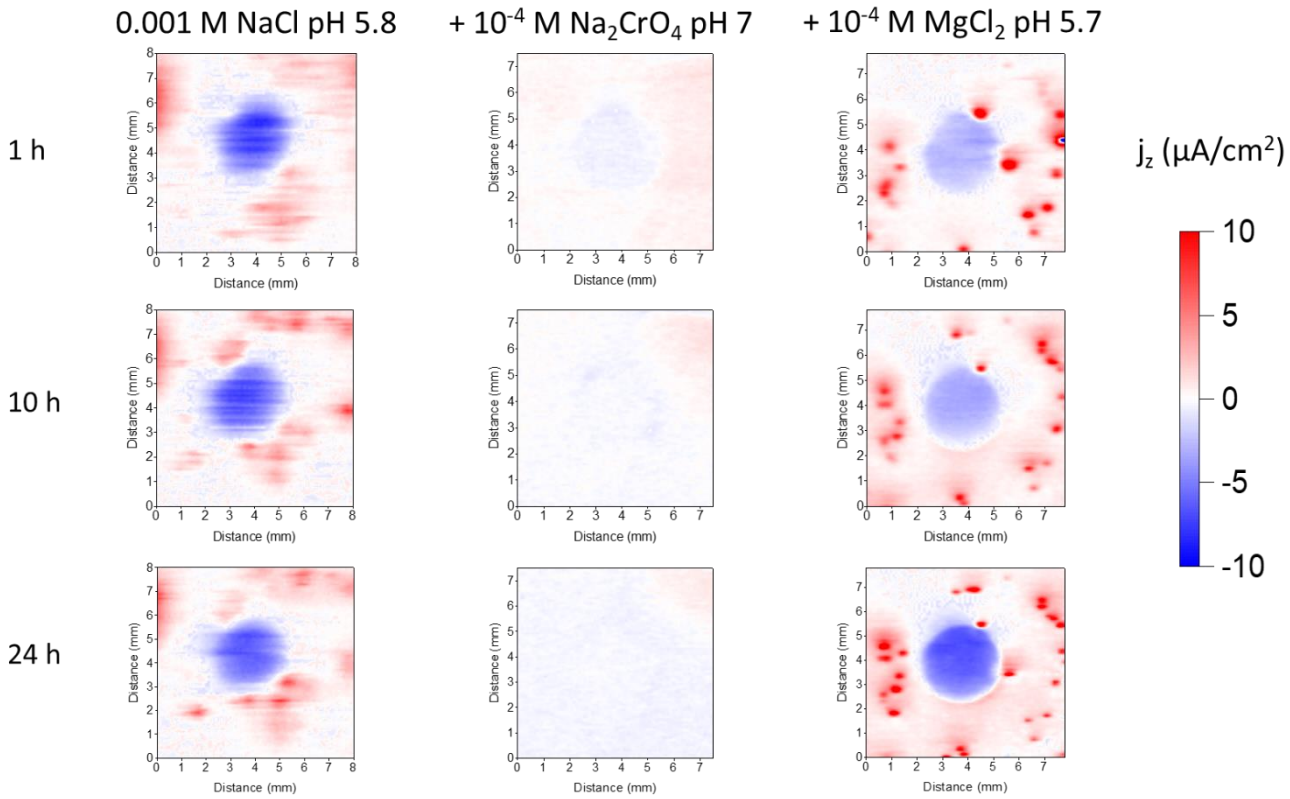

Figure 4.14. SVET-derived surface maps showing j_z distributions above a freely-corroding AA7050-316SS couple sample immersed in 0.001 M NaCl and with additions of 10^{-4} M chromate and 10^{-4} M Mg(II) at different times. The pH of the solutions was not adjusted.

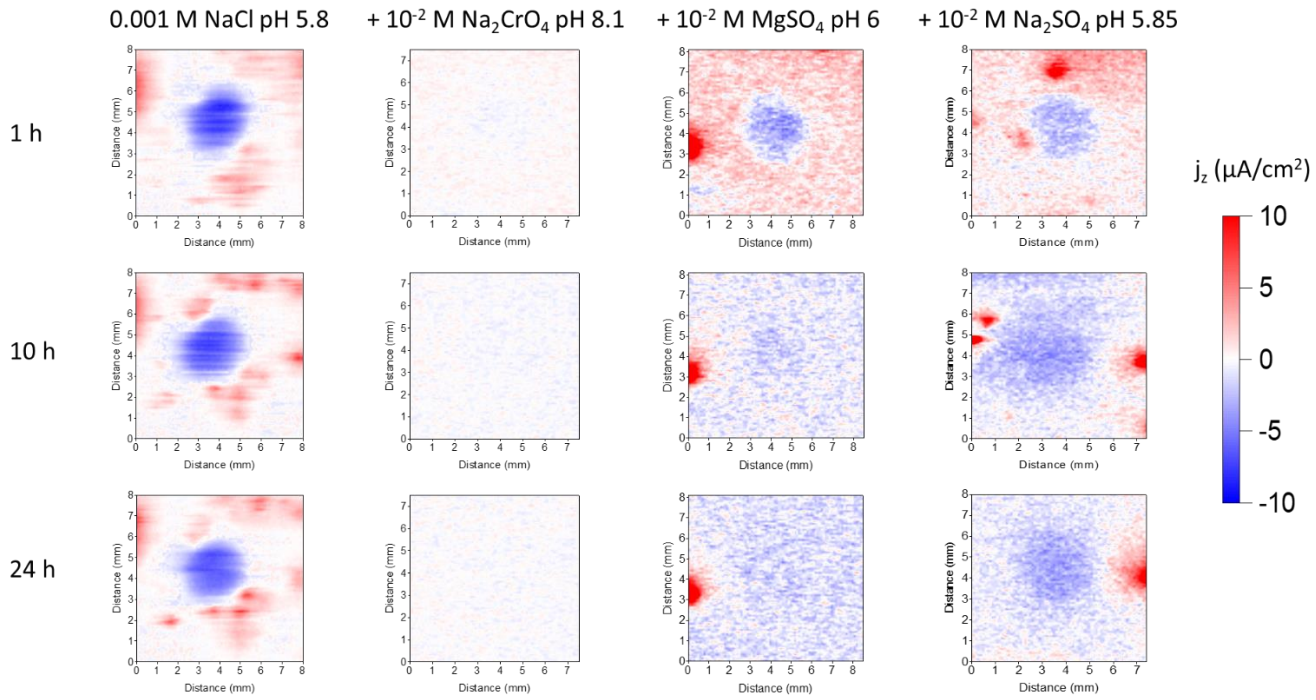

Figure 4.15. SVET-derived surface maps showing j_z distributions above a freely-corroding AA7050-316SS couple sample immersed in 0.001 M NaCl and with additions of 10^{-2} M chromate and 10^{-2} M Mg(II) at different times. The pH of the solutions was not adjusted.

In the acidic environment, the addition of 10^{-4} M Mg(II) suppressed j_z distributions over the fastener couple by up to five times compared to the inhibitor-free case, in contrast to over one order of magnitude with the addition of 10^{-4} M chromate (Figure 4.16). Another important observation was the emergence of pits within the vicinity of the AA7050-316SS galvanic couple interface. This observation was not apparent in either the inhibitor-free or chromate case. Interestingly, this behavior became more eminent when the Mg(II) concentration was increased to 10^{-2} M (Figure 4.17). Over the course of 24 h, the number of pits surrounding the 316SS fastener increased, with anodic j_z maximum of ~ 30 μA/cm^2. The proliferation of these pits was supported by the cathodic currents supplied by the 316SS and the vast unattacked area of the AA7050 surface. It is noted that in this environment, the addition of 10^{-2} M chromate shut down the galvanic coupling after very short times (≤ 1 h), with j_z distributions that were found to be comparable to those observed over uncoupled AA7050 surface in the same solution (Figure 4.6).

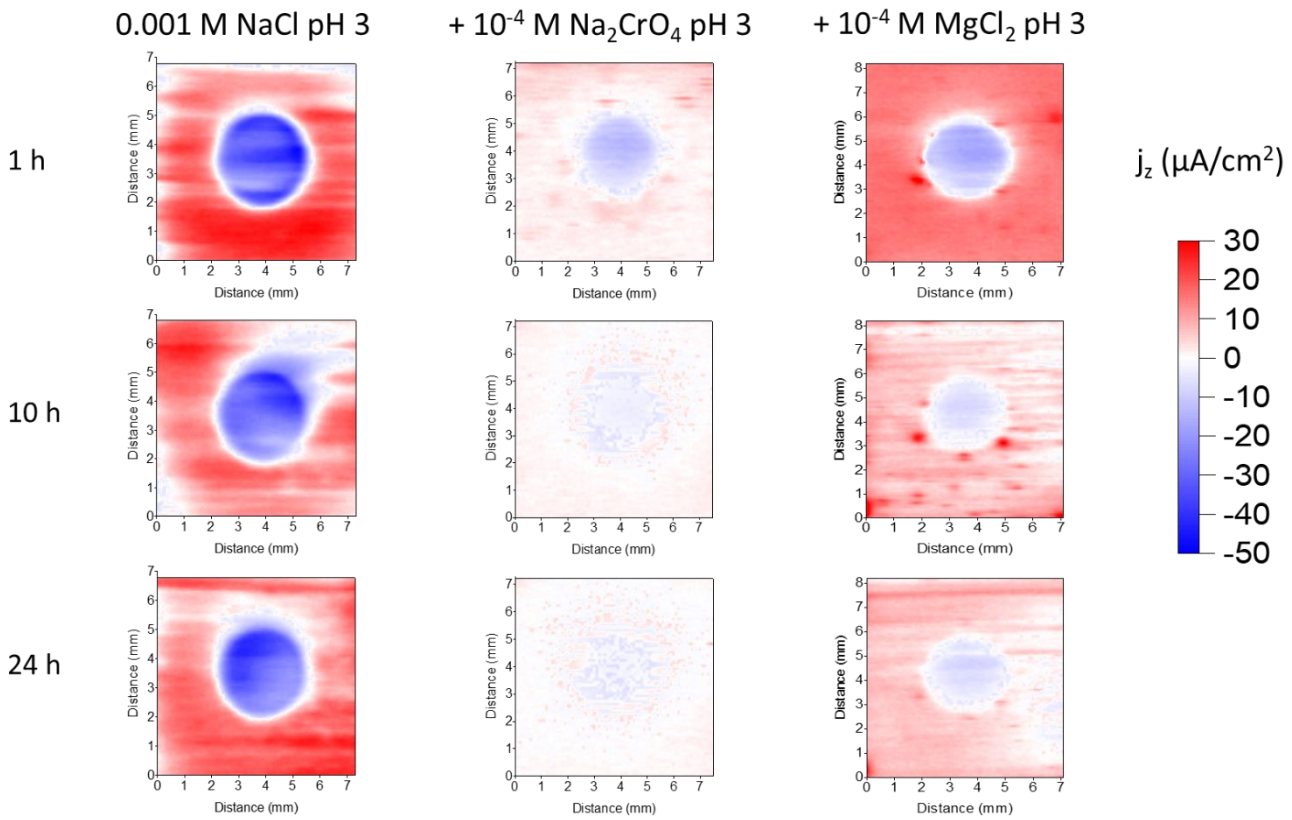

Figure 4.16. SVET-derived surface maps showing j_z distributions above a freely-corroding AA7050-316SS couple sample immersed in 0.001 M NaCl and with additions of 10^{-4} M chromate and 10^{-4} M Mg(II) at different times. The pH of each solution was adjusted to 3 using HCl.

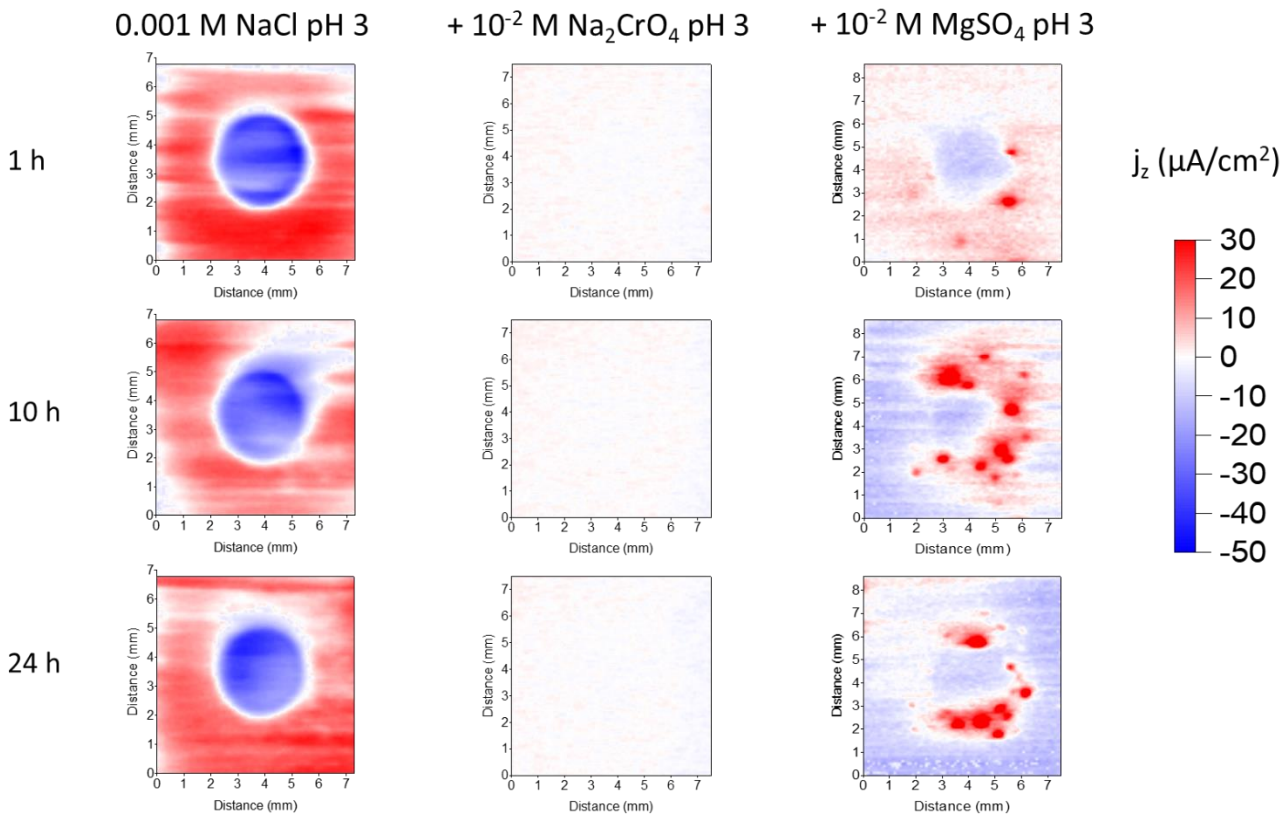

Figure 4.17. SVET-derived surface maps showing j_z distributions above a freely-corroding AA7050-316SS couple sample immersed in 0.001 M NaCl and with additions of 10^{-2} M chromate and 10^{-2} M Mg(II) at different times. The pH of each solution was adjusted to 3 using HCl.

4.4.6 Galvanic Corrosion Behavior of AA7050 Coupled to 316SS vs. High-Purity Cu with the Addition of Al^{3+}

In an attempt to simulate the more aggressive environments – i.e., high [Cl^-], low dissolved O_2, low pH, Al^{3+} – that would be characteristic of the damage propagation stage in a deep fastener crevice, experiments were conducted in deaerated 4.7 M NaCl + 0.1 M $AlCl_3$ and with additions of chromate. This set of experiments was carried out in order to assess the ability of chromate to suppress active corrosion of AA7050 as opposed to mitigating damage initiation. In this set of experiments, the pH of the solutions was not adjusted. It is important to note that the addition of chromate to this base solution had a negligible effect on the pH. As mentioned previously, Cu was introduced in this part of the study to represent Cu replating on AA7050 which would be probable under these simulated aggressive conditions, and would be expected to play

an important role in contributing to the total cathodic current available to sustain anodic dissolution.[3] Figure 4.18 compares the galvanic couple potentials and couple current densities obtained from ZRA experiments performed on AA7050 coupled to 316SS (Figures 4.18a and 4.18b) and to high-purity Cu (Figures 4.18c and 4.18d) in inhibitor-free and chromate-containing 4.7 M NaCl + 0.1 M $AlCl_3$. With 316SS, the galvanic couple potential appeared to ennoble with increasing chromate concentration, but a different and interesting trend was observed with the couple current density. In inhibitor-free solution, the initial current density was as high as ~ 3000 $\mu A/cm^2$ and quickly fell to ~ 750 $\mu A/cm^2$ within the first 2 h before steadily decreasing to ~ 300 $\mu A/cm^2$ at the end of the 24 h duration of experiment. Upon addition of 10^{-3} M chromate, the couple current density remained constant at ~ 680 $\mu A/cm^2$ throughout the duration of experiment. Increasing the chromate concentration to 10^{-2} M barely suppressed the couple current density to ~ 620 $\mu A/cm^2$. However, a more significant suppression of couple current density was achieved with the addition of 10^{-1} M chromate, for which the value remained constant at ~ 350 $\mu A/cm^2$.

In experiments where AA7050 was coupled to high-purity Cu, there was no clear trend in the evolution of the galvanic couple potential with increasing chromate concentration. However, the range of galvanic couple potentials was similar to that observed with AA7050 coupled to 316SS. Interestingly, the couple current densities for the AA7050-high purity Cu couple were generally lower than observed with the AA7050-316SS couple by at least one order of magnitude. In inhibitor-free solution, the initial current density of ~ 85 $\mu A/cm^2$ quickly fell and stayed constant at ~ 27 $\mu A/cm^2$ throughout the duration of experiment. Upon addition of various concentrations of chromate, the initial couple current densities were noticeably higher than those observed in inhibitor-free conditions, particularly with the addition of 10^{-2} M chromate (~ 2200 $\mu A/cm^2$). Furthermore, the couple current densities stabilized at higher values than in inhibitor-free conditions, with the exception of the highest concentration of 10^{-1} M chromate which remained constant at ~ 13 $\mu A/cm^2$.

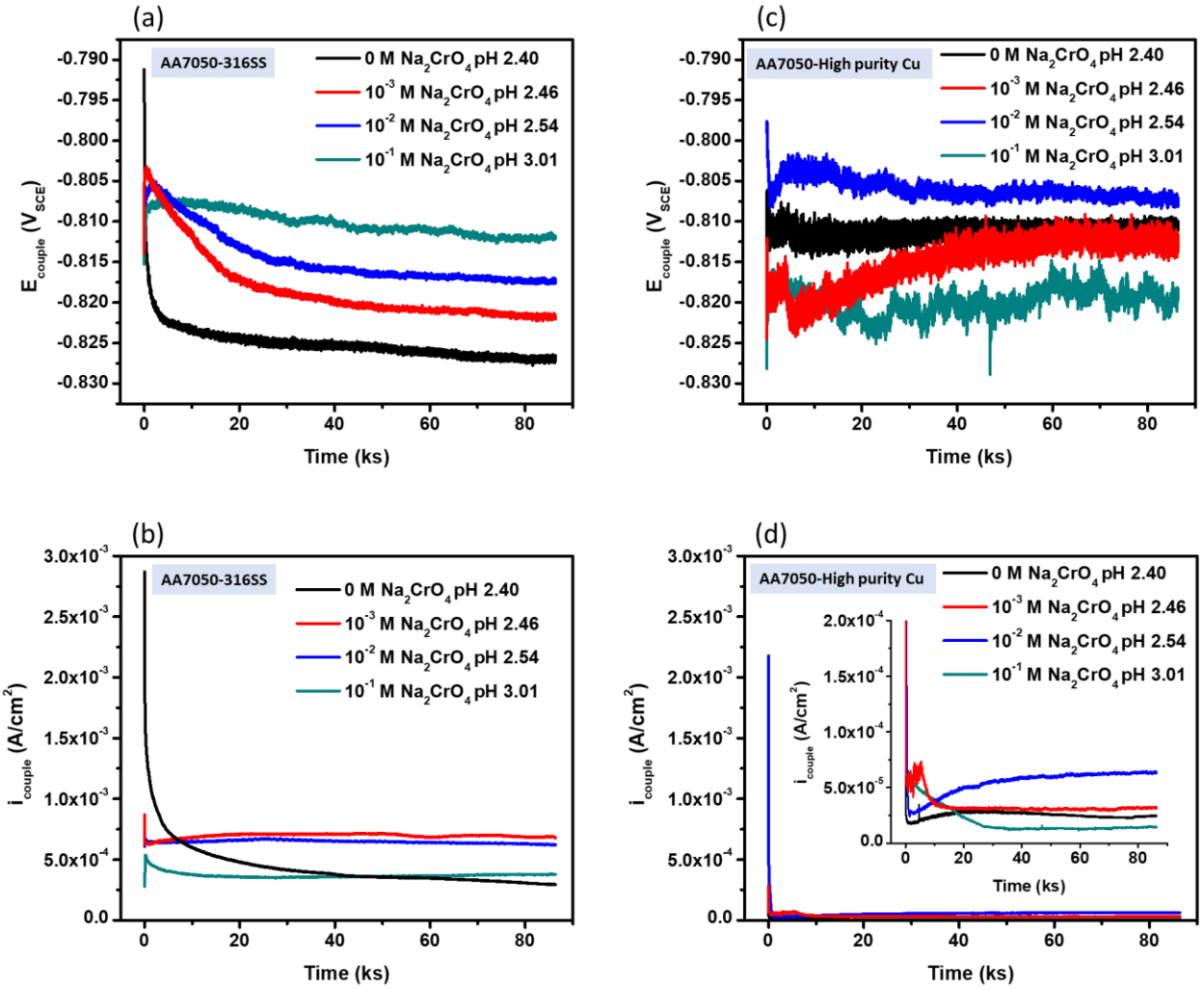

Figure 4.18. Galvanic couple potentials (a) and (c), couple current densities (b) and (d) as a function of time on AA7050-316SS and AA7050-high purity Cu planar couples, respectively, immersed in deaerated 4.7 M NaCl + 0.1 M $AlCl_3$ and with additions of chromate. The pH of the solutions was not adjusted.

On examination of the AA7050 sample surfaces and cross-sections, post experiments (Figures 4.19 and 4.20), the damage observed on AA7050 samples coupled to 316SS was greater both in terms of fissure density and depth when compared to AA7050 samples coupled to high-purity Cu. With both couples, the inhibitor-free samples were entirely covered with a distribution of both shallow and deep fissures. In contrast, the chromate-exposed samples were characterized by sparsely-distributed, but deep, fissures, with a reduction in the maximum fissure depth as chromate concentration increased.

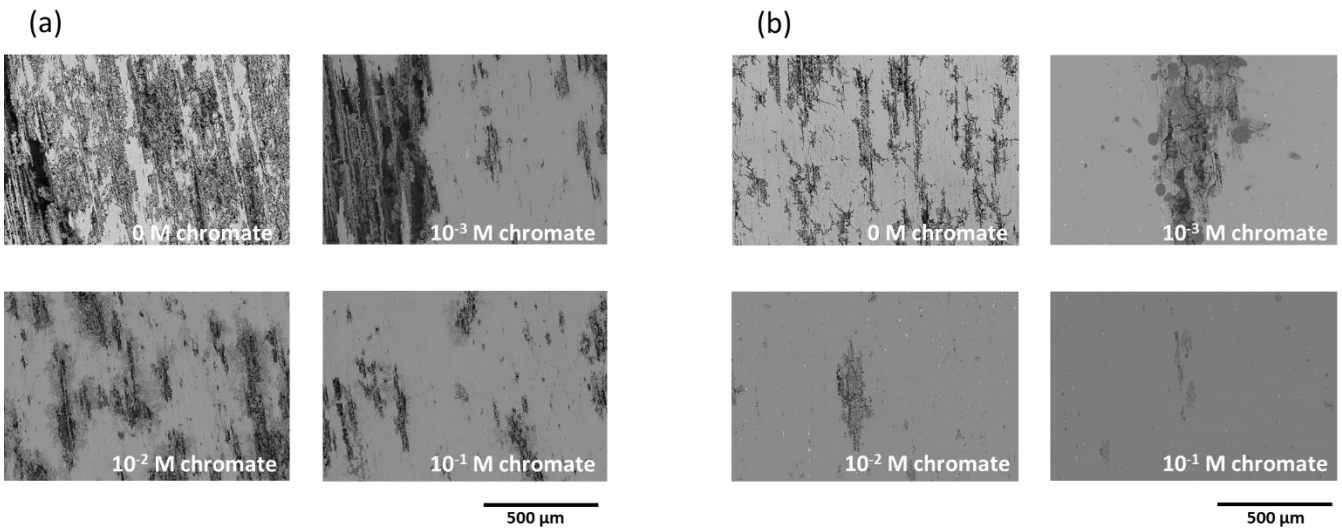

Figure 4.19. Surface SEM-CBS micrographs of AA7050 coupled to (a) 316SS and (b) high-purity Cu after 24 h ZRA exposure in deaerated 4.7 M NaCl + 0.1 M $AlCl_3$ and with additions of chromate.

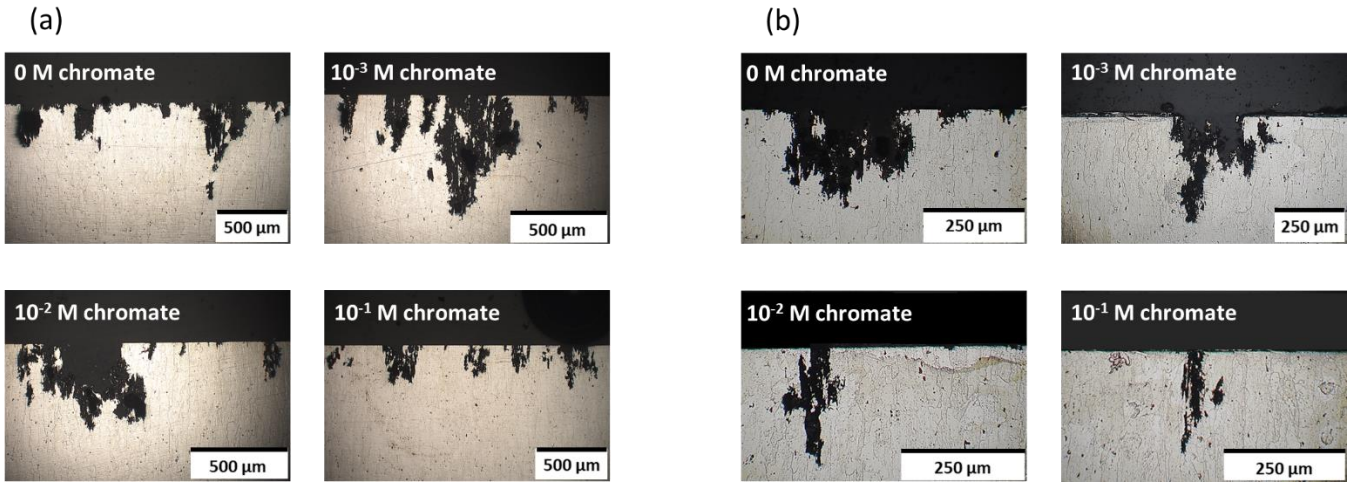

Figure 4.20. Optical cross-sectional images of AA7050 coupled to (a) 316SS and (b) high-purity Cu after 24 h ZRA exposure in deaerated 4.7 M NaCl + 0.1 M $AlCl_3$ and with additions of chromate.

Anodic and cathodic polarization curves were generated on AA7050 and 316SS/high-purity Cu, respectively, in deaerated 4.7 M NaCl + 0.1 M $AlCl_3$ and with additions of chromate (Figure 4.21) to aid rationalization of the results obtained during the ZRA experiments. Figure 4.21a compares the cathodic kinetics on 316SS and high-purity Cu as a function of chromate

concentration. Within the range of galvanic couple potentials obtained in the ZRA experiments (-0.79 to -0.83 V_{SCE}), minimal cathodic inhibition was observed on 316SS and none at all on Cu, regardless of chromate concentration. The HER kinetics were generally slower on Cu than on 316SS by at least one order of magnitude - in line with the observation made with the ZRA couple current densities. This result suggests that 316SS may likely be the dominant cathode under these conditions, especially if cathode size in a real fastener geometry is taken into consideration. Although anodic kinetics on AA7050 (Figure 4.21b) appeared to decrease on addition of chromate, passivation did not occur in these solutions.

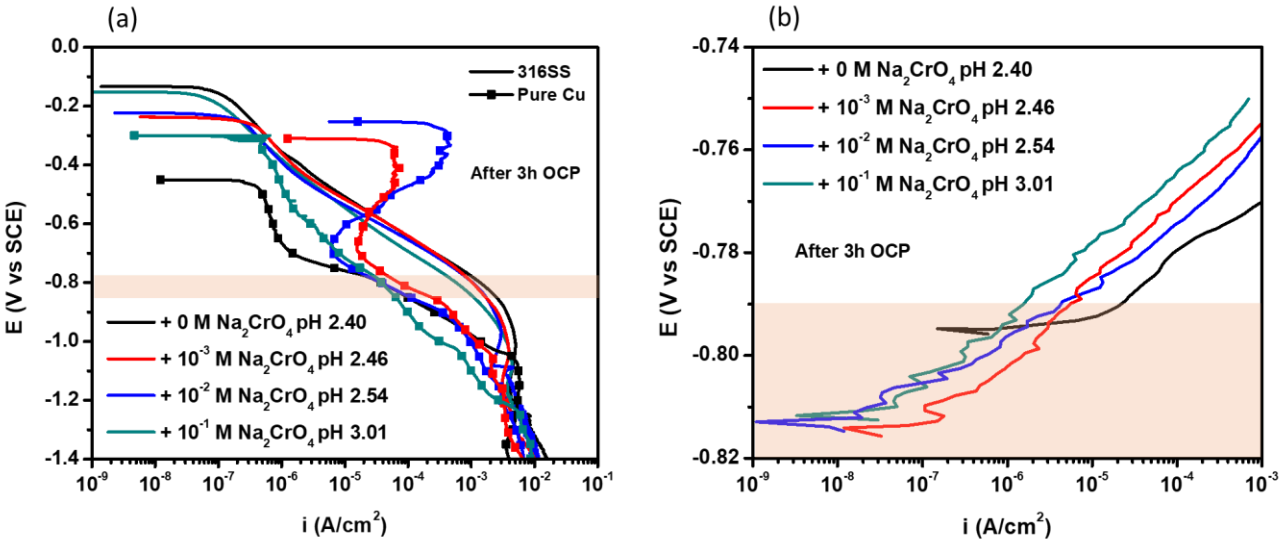

Figure 4.21. Polarization curves generated on (a) 316SS & high-purity Cu and (b) AA7050 in deaerated 4.7 M NaCl + 0.1 M $AlCl_3$ as a function of chromate concentration. The pH of the solutions was not adjusted. Orange boxes highlight the range of galvanic couple potentials obtained in the ZRA exposures.

4.4.7 Galvanic Corrosion Behavior of AA7050 Coupled to 316SS vs. High-Purity Cu without the Addition of Al^{3+}

In order to decouple the influence of Al^{3+} on chromate inhibition from that of low pH, similar experiments were also carried out in deaerated, acidified 5 M NaCl (i.e., without the deliberate addition of Al^{3+}) and with additions of chromate. The pH of the base 5 M NaCl solution was adjusted to 2.4 with sulfuric acid to match the natural pH of 4.7 M NaCl + 0.1 M $AlCl_3$ and to

keep the total [Cl^-] constant in order to permit a direct comparison. Although the inhibitive effect of the sulfate ion is acknowledged, the concentration of H_2SO_4 added to adjust solution pH in this work, 4.5 x 10^{-5} M, was considered too small to have any meaningful effect on corrosion inhibition in the acidified 5 M NaCl base solution. It is noted that the pH of the solution following the additions of chromate was not re-adjusted. It was observed that the additions of chromate to the acidified base solution significantly shifted the pH values in the alkaline direction with the shift becoming larger as chromate concentration increased. This observation is in contrast with that made in 4.7 M NaCl + 0.1 M $AlCl_3$ where the addition of the same amounts of chromate barely affected the base solution pH. Figure 4.22 displays the galvanic couple potentials and couple current densities as a function of time obtained from ZRA experiments performed on AA7050 coupled to 316SS (Figures 4.22a and 4.22b) and to high-purity Cu (Figures 4.22c and 4.22d) in inhibitor-free and chromate-containing 5 M NaCl pH 2.4. There were no obvious changes in the galvanic couple potential on both couples upon the addition of chromate, with the values fairly constant at ~ -0.82 V_{SCE}. In both cases, the couple current density was lower than in the presence of 0.1 M Al^{3+} and was observed to fall with increasing chromate concentration. However, chromate appeared to be more effective on 316SS than on high-purity Cu. With 316SS, the initial couple current density in inhibitor-free solution was ~ 30 μA/cm^2 – two orders of magnitude lower than with 0.1 M Al^{3+} – and steadily fell to ~ 6 μA/cm^2 within the first 3 h and then stayed constant at ~ 5 μA/cm^2 for the remaining duration of the experiment. Upon addition of 10^{-3} M chromate, the couple current density decreased to ~ 1.5 μA/cm^2, and increasing the concentration to 10^{-2} M further suppressed the couple current density to ~ 0.65 μA/cm^2. It is noted that the corresponding current density value with 0.1 M Al^{3+} was three orders of magnitude higher at ~ 620 μA/cm^2.

With high-purity Cu, the initial couple current density in inhibitor-free solution was ~ 100 μA/cm^2 - three times higher than measured for 316SS - and fluctuated for the duration of the experiment before settling at ~ 5 μA/cm^2 towards the end. Upon addition of 10^{-3} M chromate, the couple current density slightly decreased to ~ 4.5 μA/cm^2 and increasing the concentration to 10^{-2} M further suppressed the couple current density to ~ 2.1 μA/cm^2. The corresponding current density value with 0.1 M Al^{3+} was thirty times higher at ~ 64 μA/cm^2. It is noted that the

calculated maximum concentration of naturally present Al^{3+} stemming from corrosion of AA7050 in the acidified 5 M NaCl solutions after the 24-h ZRA experiments was ~ 10^{-4} M – three orders of magnitude lower than the intentional addition of 0.1 M.

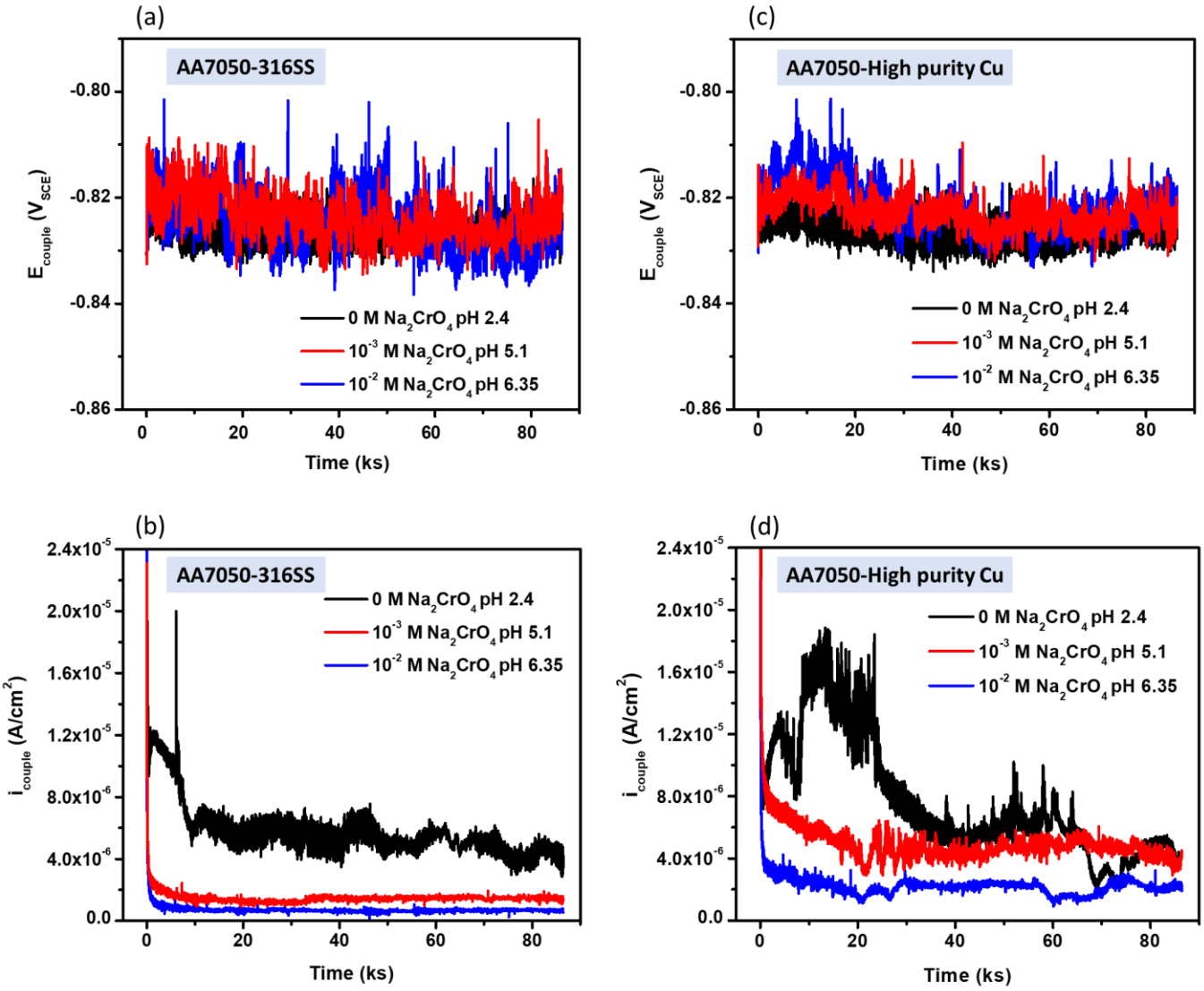

Figure 4.22. Galvanic couple potentials (a) and (c), couple current densities (b) and (d) as a function of time on AA7050-316SS and AA7050-high purity Cu planar couples, respectively, immersed in deaerated 5 M NaCl pH 2.4 and with additions of chromate. The pH of the base 5 M NaCl solution was adjusted with H_2SO_4, but was not re-adjusted on addition of chromate.

Upon examination of the AA7050 sample surfaces and cross-sections after the experiments (Figures 4.23 and 4.24), the damage was greater on coupling to high-purity Cu than

to 316SS with and without the additions of chromate. When coupled to 316SS, minimal damage was observed on AA7050 in the presence of 10^{-3} M chromate, and no damage was observed upon increasing the chromate concentration to 10^{-2} M.

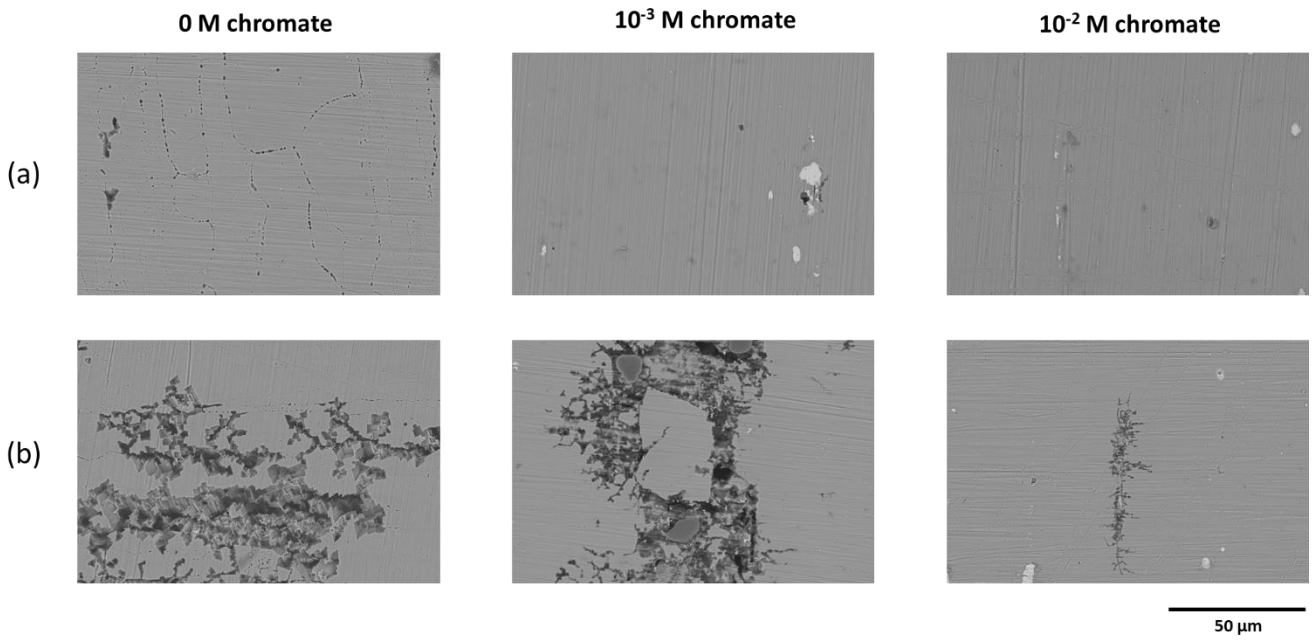

Figure 4.23. Surface SEM-CBS micrographs of AA7050 coupled to (a) 316SS and (b) high-purity Cu after 24 h ZRA exposure in deaerated 5 M NaCl pH 2.4 (with Al^{3+} only naturally present from AA7050 corrosion) and with additions of chromate.

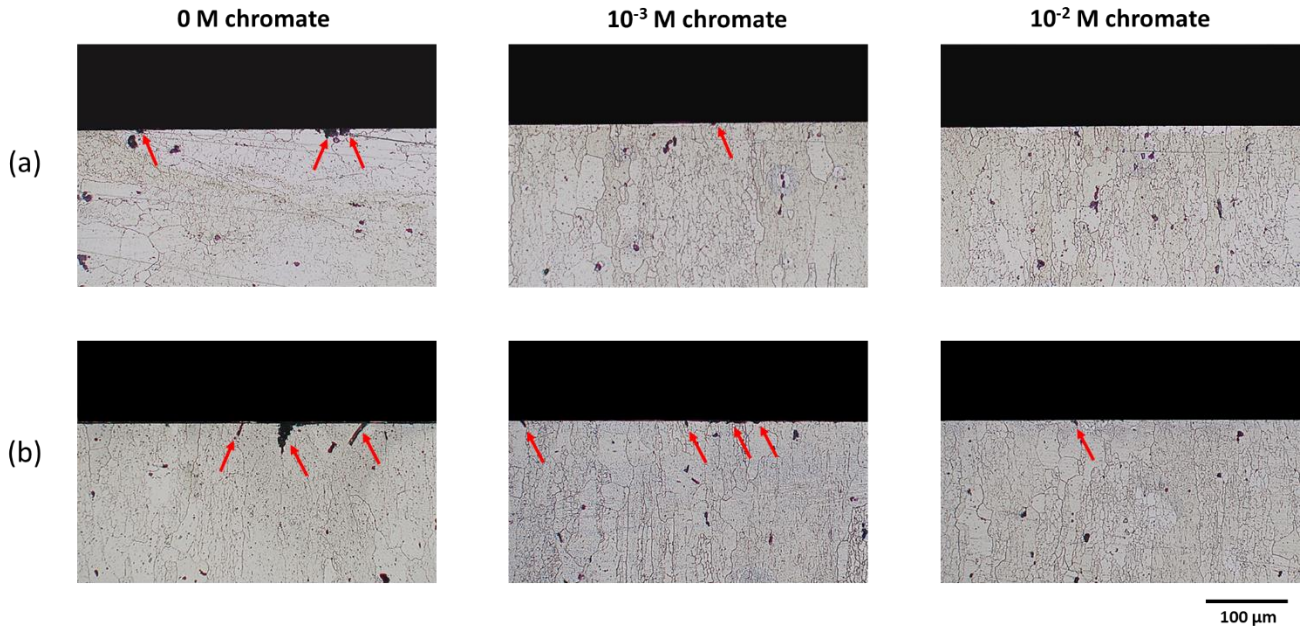

Figure 4.24. Optical cross-sectional images of AA7050 coupled to (a) 316SS and (b) high-purity Cu after 24 h ZRA exposure in deaerated 5 M NaCl pH 2.4 (with Al^{3+} only naturally present from AA7050 corrosion) and with additions of chromate.

Figure 4.25 presents the anodic and cathodic polarization curves generated on AA7050 and 316SS/high-purity Cu, respectively, in deaerated 5 M NaCl pH 2.4 and with additions of chromate. Within the range of galvanic couple potentials obtained in the ZRA experiments (-0.80 to -0.84 V_{SCE}), there was a four-fold decrease in cathodic kinetics on 316SS compared to a two-fold decrease in the kinetics on Cu, further providing evidence that chromate performs better on 316SS than on high-purity Cu in the absence of Al^{3+}. For AA7050, the passive current density appeared to decrease as chromate concentration increased. At the highest concentration of 10^{-2} M, the open circuit potential was at or above the pitting potential.

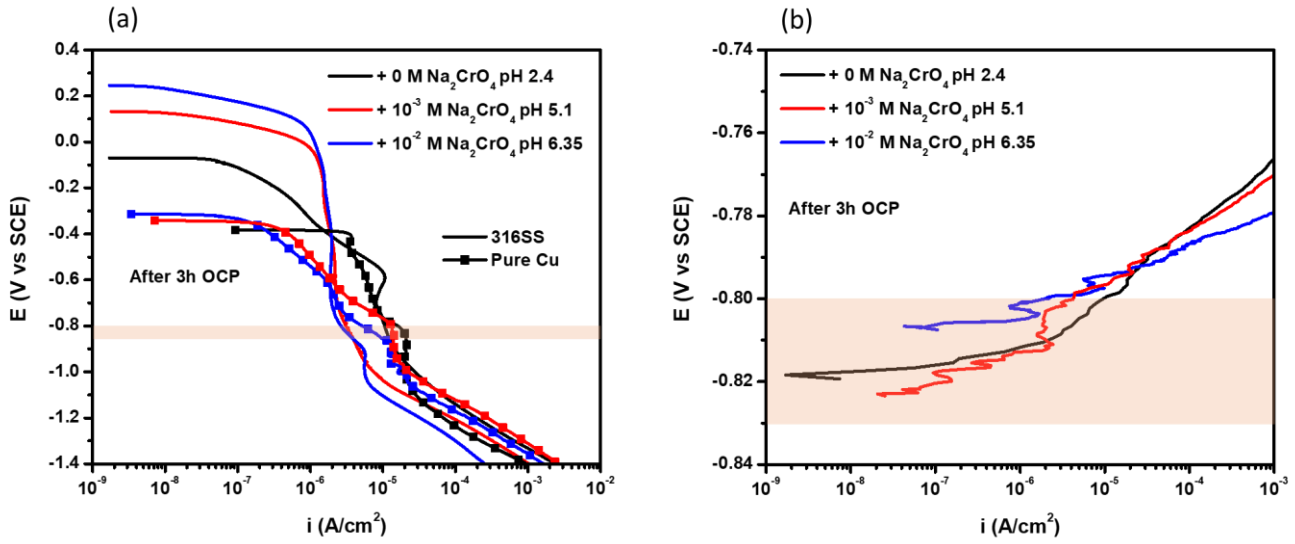

Figure 4.25. Polarization curves generated on (a) 316SS & high-purity Cu and (b) AA7050 in deaerated 5 M NaCl pH 2.4 and with additions of chromate. The pH of the base 5 M NaCl solution was adjusted with H_2SO_4, but was not re-adjusted after the addition of chromate. Orange boxes highlight the range of galvanic couple potentials obtained in the ZRA exposures.

4.4.8 Effect of Al^{3+} on Galvanic-Induced Damage on AA7050 Coupled to 316SS vs. High-Purity Cu

Figure 4.26 summarizes the calculated ZRA charge densities on AA7050 coupled to 316SS and AA7050 coupled to high-purity Cu in deaerated 5 M Cl^- with and without the deliberate addition of Al^{3+}. The total charge density associated with anodic dissolution of AA7050 coupled to either 316SS or high-purity Cu is described by Equation 4:

$$Q_{\Delta m-couple} = Q_{\Delta m-AA7050\ OCP} + Q_{net-couple} + Q_{H_2} \quad (4.4)$$

$Q_{\Delta m\text{-}AA7050\ OCP}$ and $Q_{\Delta m\text{-}couple}$ were determined from mass loss of AA7050 after exposure at OCP and after being coupled to 316SS/high-purity Cu, respectively, using Equation 4.1. $Q_{\Delta m\text{-}AA7050\ OCP}$ accounts for both the ORR and HER occurring on AA7050 at OCP. $Q_{net\text{-}couple}$ was calculated by integrating the couple current density over the time of exposure, and accounts for the total cathodic currents (ORR + HER) on 316SS/high purity Cu. Q_{H2} is the cathodic charge density associated with the HER on AA7050 on coupling to 316SS/high-purity Cu that is not reflected in $Q_{net\text{-}couple}$. The rate of the ORR occurring on AA7050 on coupling to 316SS/high-purity Cu is

assumed to be equal to that occurring on AA7050 at OCP. Overall, the charge densities in the 0.1 M Al^{3+}-containing solutions were up to two orders of magnitude higher with 316SS and one order of magnitude higher with high-purity Cu than the values observed in the respective solutions without the addition of 0.1 M Al^{3+}. Although Q_{H2} was not directly measured, it could be inferred from Equation 4.4 that Al^{3+} enhanced HER kinetics on AA7050, particularly on coupling to 316SS. It is noted that there was no measurable mass loss of AA7050 associated with OCP exposure in chromate-containing 5 M NaCl solutions.

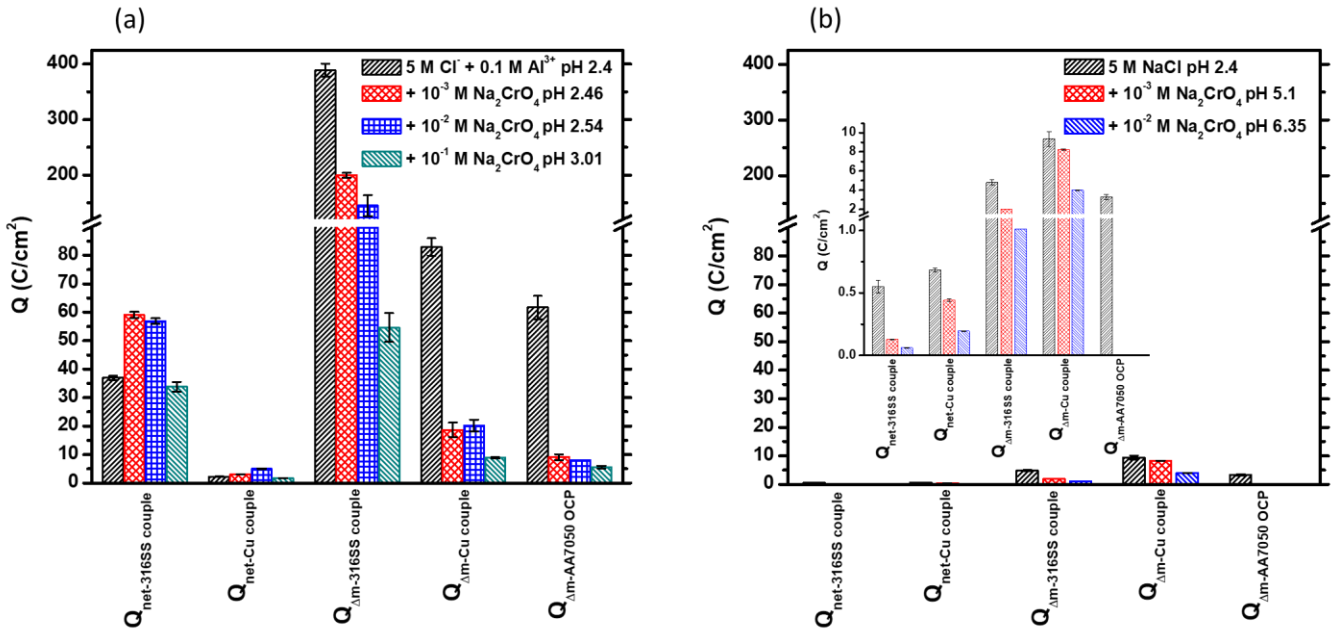

Figure 4.26. Comparison of ZRA charge densities on AA7050-316SS and AA7050-high purity Cu planar couples immersed in deaerated (a) 4.7 M NaCl + 0.1 M $AlCl_3$ and (b) 5 M NaCl pH 2.4 (with Al^{3+} only naturally present), and with additions of chromate. $Q_{net\text{-}couple}$ is the charge calculated by integrating the couple current density over the time of exposure, $Q_{\Delta m-couple}$ is the charge calculated from mass loss of AA7050 after being coupled to 316SS/high-purity Cu, and $Q_{\Delta m-AA7050\ OCP}$ is the charge calculated from mass loss of AA7050 after exposure at OCP.

Table 4.4 provides estimates for the maximum damage fissure depth as well as the area lost to corrosion from the optical cross-sectional images shown in Figures 4.20 and 4.24. It is important to note that area loss calculations were based solely on the full cross-sections of the areas shown and not the entire surface; it does not necessarily follow that the total area lost on coupling to 316SS in inhibitor-free 4.7 M NaCl + 0.1 M $AlCl_3$ was less than the area lost on addition of 10^{-3} M and 10^{-2} M chromate. That said, though sparsely-distributed, fissures were on average deeper in chromate-containing 4.7 M NaCl + 0.1 M $AlCl_3$ solutions. Maximum fissure depth in the 0.1 M Al^{3+}-containing solutions decreased with increasing chromate concentration. It is worth pointing out that with 316SS, even with addition of the highest chromate concentration of 10^{-1} M, the damage area in the 0.1 M Al^{3+}-containing environment remained at least two orders of magnitude higher than in inhibitor-free 5 M NaCl environment, compared to ~ eight times higher in the case of high-purity Cu. As noted previously, the analysis confirmed that the addition of 10^{-2} M chromate to 5 M NaCl completely stopped damage initiation on AA7050 coupled to 316SS, in contrast to AA7050 coupled to high-purity Cu.

Table 4.4. Fissure depth and total corrosion damage for the optical cross-sectional images shown in Figures 4.20 and 4.24.

Test solution	pH	Max fissure depth (μm)		Mean fissure depth (μm)		Area corroded (μm^2)	
		316SS	High-purity Cu	316SS	High-purity Cu	316SS	High-purity Cu
Deaerated 4.7 M NaCl + 0.1 M $AlCl_3$	Natural, 2.4	672.3	251.0	94.7	31.7	5.84×10^5	2.47×10^5
Deaerated 4.7 M NaCl + 0.1 M $AlCl_3$ + 0.001 M Na_2CrO_4	Natural, 2.46	612.5	503.0	135.1	55.7	8.40×10^5	1.62×10^5
Deaerated 4.7 M NaCl + 0.1 M $AlCl_3$ + 0.01 M Na_2CrO_4	Natural, 2.54	435.4	239.1	97.6	28.2	6.56×10^5	1.23×10^5
Deaerated 4.7 M NaCl + 0.1 M $AlCl_3$ + 0.1 M Na_2CrO_4	Natural, 3.01	288.5	219.2	44.2	51.0	2.83×10^5	8.51×10^3
Deaerated 5 M NaCl	Adjusted, 2.4	17.6	39.6	3.4	6.9	5.86×10^2	1.09×10^3
Deaerated 5 M NaCl pH 2.4 + 0.001 M Na_2CrO_4	Natural, 5.1	2.8	14.4	2.1	2.3	1.17×10^1	3.75×10^2
Deaerated 5 M NaCl pH 2.4 + 0.01 M Na_2CrO_4	Natural, 6.35	-	5.6	-	1.9	-	9.36×10^1

Table 4.5 highlights the effect of Al^{3+} on cathodic kinetics on 316SS and high-purity Cu. Data were taken within the galvanic couple potential range at -0.815 V_{SCE} from polarization curves in the respective environment in order to provide a snapshot of the differences in kinetics. This analysis enabled the determination of the likely dominant cathode during damage initiation vs. damage propagation stage in a typical AA7050-316SS fastener crevice environment. It can be seen clearly that the addition of 0.1 M Al^{3+} enhanced kinetics on 316SS compared to high-purity Cu. However, in the absence of 0.1 M Al^{3+}, kinetics were enhanced slightly on high-purity Cu, and chromate was observed to be less effective in suppressing kinetics on high-purity Cu compared to 316SS.

Table 4.5. Cathodic current densities on 316SS and high-purity Cu obtained from polarization curves in the respective test solution with data taken at -0.815 V_{SCE} (within the range of galvanic couple potentials).

Test solution	pH	Kinetics on 316SS (A/cm^2)	Kinetics on high-purity Cu (A/cm^2)
Deaerated 4.7 M NaCl + 0.1 M $AlCl_3$	Natural, 2.4	1.69×10^{-3}	5.17×10^{-5}
Deaerated 4.7 M NaCl + 0.1 M $AlCl_3$ + 0.001 M Na_2CrO_4	Natural, 2.46	1.21×10^{-3}	9.78×10^{-5}
Deaerated 4.7 M NaCl + 0.1 M $AlCl_3$ + 0.01 M Na_2CrO_4	Natural, 2.54	1.26×10^{-3}	5.22×10^{-5}
Deaerated 4.7 M NaCl + 0.1 M $AlCl_3$ + 0.1 M Na_2CrO_4	Natural, 3.01	7.10×10^{-4}	4.47×10^{-5}
Deaerated 5 M NaCl	Adjusted, 2.4	1.10×10^{-5}	1.83×10^{-5}
Deaerated 5 M NaCl pH 2.4 + 0.001 M Na_2CrO_4	Natural, 5.1	3.31×10^{-6}	1.34×10^{-5}
Deaerated 5 M NaCl pH 2.4 + 0.01 M Na_2CrO_4	Natural, 6.35	2.88×10^{-6}	6.38×10^{-6}

4.5 Discussion

The findings in this work are related to previous investigations in the literature to advance the understanding of chromate activity in occluded environments compared to external conditions. First, the effect of pH on the electrochemical behavior of AA7050-316SS galvanic couple under conditions designed to simulate boldly exposed surfaces is discussed in light of chromate activity. Next, the effect of Al^{3+} on the efficacy of chromate is discussed in the context of damage evolution in a fastener crevice, with an explanation as to why chromate appears to be less effective at suppressing active corrosion vs. initiation of corrosion on Al alloys coupled to SS fasteners as reported in the literature.[2,17,28–30] Lastly, the implications of our findings to real service structures are discussed.

4.5.1 Degree of Chromate Inhibition Falls with Decreasing pH

The significant increase in SVET baseline j_z distributions on uncoupled AA7050 in as low $[Cl^-]$ as 0.001 M at pH 3 (Figure 4.6), compared to those at natural pH (Figure 4.2), provides evidence of the exacerbating effect of pH alone on self-dissolution of AA7050. Although coupling with 316SS increased the cathodic area available for increased cathodic kinetics, which in turn increased the area-integrated total anodic current density, the anodic j_z maximum (~ 30 $\mu A/cm^2$) from the galvanic coupling (Figure 4.7) was only slightly higher than that observed without macro-coupling with 316SS (~ 25 $\mu A/cm^2$). This observation implies that in acidic environments, micro-galvanic (or self) corrosion of AA7050 may be as important as macro-galvanic-induced corrosion when AA7050 is coupled with 316SS. This adverse effect of acidic pH on corrosion of other Al alloys in chloride-containing environments has been reported and is attributed to the more rapid global dissolution of the oxide film in acidic conditions compared to the more localized attack of the protective oxide film in neutral conditions.[53–55] That said, the addition of chromate suppressed j_z distributions on both AA7050 and 316SS at pH 3 by at least an order of magnitude, although not to the levels attained at natural pH conditions (Figures 4.10 and 4.11).

The differences in the activity of chromate on the galvanic couple as a function of environmental pH can be further explored with the use of Mixed Potential Theory (MPT) to explain the ZRA results. The utilization of actual polarization curves to describe the time-

dependence of the couple behavior would require polarization curves at a series of times. However, since the goal of this work was not a quantitative analysis, the interpretation of the $E_{couple}(t)$ and $i_{couple}(t)$ in terms of MPT was carried out qualitatively with the schematics shown in Figures 4.4c and 4.8c. As presented in Figure 4.4c, the electrochemical kinetics of the AA7050-316SS couple in inhibitor-free conditions at natural pH is represented by point 1. Upon the addition of 10^{-4} M chromate, the system has little change in potential, but a large decrease in current, represented by point 2. This set of changes in E_{couple} and i_{couple} implies that there is a comparable reduction in anodic and cathodic kinetics on AA7050 and 316SS indicative of mixed inhibition by chromate. With further additions of chromate, at very short times, E_{couple} decreases with a corresponding decrease in current density, which is only possible if the cathodic kinetics slow substantially more than the anodic kinetics, as shown for point 3. At longer times, with cathodic reactions on 316SS stifled, the anodic kinetics continue to slow, causing E_{couple} to increase with a corresponding further decrease in current density labeled as point 4. This slowing of anodic kinetics indicates stabilization of the native oxide film on AA7050. Following the same logic at pH 3 conditions (Figure 4.8c), we speculate that inhibition is largely mixed except at the highest chromate concentration of 10^{-2} M where inhibition appears to be predominantly cathodic (Figures 4.8 and 4.9). Nonetheless, the degree of inhibition at pH 3 was generally lower than that observed at natural pH, with a best-case difference of about an order of magnitude.

The results explained above indicated that pH plays an important role in the effectiveness of chromate in aqueous chloride solutions. It is speculated that one possible effect of pH on chromate inhibition may be related to the speciation of Cr(VI) in solution.[56] To investigate this theory, XPS analyses of the chromate-induced layer formed on AA7050 after ZRA exposures in chromate-containing 0.001 M NaCl solutions were carried out. The results indicated a lower extent of chromate reduction in low pH conditions compared to higher pH conditions, evident from the larger unreduced Cr(VI) peak area and higher percentage of total Cr species in the surface film observed in pH 3 environments compared to natural pH environments (Figure 4.13). This observation is consistent with findings reported in previous studies on other substrates[25,57,58], and may be related to the variations in oxidizing strength of the different Cr(VI) species present in solution, which depends on the solution pH and total [Cr(VI)]. Chromate may

speciate predominantly as the bichromate ion ($HCrO_4^-$), dichromate ion ($Cr_2O_7^{2-}$) or chromate ion (CrO_4^{2-}) depending on the pH and total [Cr(VI)].[56,59–61] In low pH media (< 6), Cr(VI) exists as a distribution of $HCrO_4^-$ and $Cr_2O_7^{2-}$ with the former favored for total [Cr(VI)] < 10^{-2} M. In contrast, Cr(VI) speciates entirely as CrO_4^{2-} at higher pH (> 7) regardless of concentration.[56] $HCrO_4^-$ is thought to be less potent than $Cr_2O_7^{2-}$ and CrO_4^{2-} due to protonation which dehydrates the anion and partially neutralizes the ionic charge, consequently rendering the anion a weaker oxidizing species and less prone to reduction following adsorption on the substrate.[59,61] It can be inferred from our results that in pH 3 solutions, the predominance of $HCrO_4^-$ was at least partially responsible for the lower level of corrosion inhibition. As total [Cr(VI)] increased, the degree of inhibition improved because [$Cr_2O_7^{2-}$] increased relative to [$HCrO_4^-$], albeit still lower than the degree of inhibition attained at natural pH conditions with predominantly CrO_4^{2-} species. For instance, with total [Cr(VI)] = 10^{-4} M, chromate speciates entirely as $HCrO_4^-$ at pH 3, whereas at its natural pH of 7, it speciates as 25% $HCrO_4^-$ and 75% CrO_4^{2-}. With a higher total [Cr(VI)] = 10^{-2} M, chromate speciates as 66% $HCrO_4^-$ and 34% $Cr_2O_7^{2-}$ at pH 3, and as 3% $HCrO_4^-$ and 97% CrO_4^{2-} at its natural pH of 8.1. Calculations were made with Medusa™ software.

4.5.2 Chromate Inhibits Damage Initiation but Not Damage Propagation in Simulated AA7050-316SS Fastener Crevice Environments

Generally, crevice environments are part of differential aeration cells where dissolved oxygen is plentiful at the external surface, and depleted inside the crevice. As a result, the ORR cannot be sustained inside the crevice. Coupled with the hydrolysis of dissolved metal ions which lowers the pH, and migration of aggressive anions (e.g., Cl^-) to maintain electroneutrality, this situation creates a highly corrosive environment inside the crevice.[62] In the case of AA7050-316SS galvanic couples, the presence of the wetted external 316SS cathode renders the situation more dire. The 316SS provides larger cathodic currents from the ORR on its surface to sustain higher rates of anodic Al dissolution inside the crevice than would AA7050 if it were the only external cathode. In addition, any replated Cu (due to the release of Cu ions from Cu-bearing particles)[63] inside the crevice would aggravate the situation, providing sites for the HER. In this context, experiments were carried out in deaerated acidified 5 M Cl^- and with the addition of 0.1 M Al^{3+} to represent early stage low-rate and late stage high-rate damage propagation, respectively, in a

fastener crevice environment. Varying concentrations of chromate were added to assess the effectiveness of the inhibitor in both stages of damage evolution in a fastener crevice.

It is noted that within the range of the galvanic couple potentials in the inhibitor-free conditions at pH 2.4, the ORR was the main cathodic reaction in the 0.1 M Al^{3+}-free environment and the HER was the dominant cathodic reaction in the 0.1 M Al^{3+}-containing solution as evident from the respective cathodic polarization curves generated on 316SS and high-purity Cu (Figures 4.21a and 4.25a). As summarized in Table 4.5, the addition of chromate to the 0.1 M Al^{3+}-containing solution barely raised the pH from that of the base solution and had little or no inhibitive effect on HER on both 316SS and high-purity Cu, regardless of concentration. The resultant effect on the AA7050 anode was deep, isolated fissures where damage initiation was successful. We note that the depth and density of the fissures decreased with increasing chromate concentration. This result suggests that chromate acted to mitigate and/or delay damage initiation to the extent possible – via anodic inhibition – so that when damage eventually initiated, large cathodic currents from the 316SS and Cu-rich sites on AA7050 were supplied to the relatively small anodic sites resulting in fissures that propagated to depths that were on average larger than those without chromate in solution, with the exception of the highest chromate concentration of 10^{-1} M (Figure 4.20a). In inhibitor-free 0.1 M Al^{3+}-containing solution, the average fissure depth was much smaller because the large cathodic currents were supplied to a much larger active anodic area and at longer times, precipitation of corrosion products on the surface provided a barrier that impeded further propagation of damage. It is speculated that the predominance of the more potent $Cr_2O_7^{2-}$ in the environment containing 10^{-1} M chromate (as opposed to the predominance of the less potent $HCrO_4^-$ at lower chromate concentrations) led to improved inhibition of damage initiation and shallower fissure penetration.

On the other hand, in the absence of 0.1 M Al^{3+}, the damage on AA7050 was less severe (Figure 4.24) because the HER kinetics on 316SS and high-purity Cu were reduced by at least two orders of magnitude and half, respectively, compared to kinetics in the presence of 0.1 M Al^{3+} (Table 4.5). This result indicates that Al^{3+} facilitates both the production of H^+ in solution as well as HER kinetics, particularly on 316SS which can be related to the mechanism proposed by Liu et

al.[64] Liu proposed a mechanism based on the Grotthuss Theory where Al^{3+} coordinates with O bonds in water, thereby weakening the bond energy between O and H, and making it easier for H^+ to diffuse from the bulk solution to the electrode surface to undergo reduction. The apparent relatively sluggish HER kinetics on Cu may be attributed to the very slow step of H adsorption on the surface.[65,66]

The addition of chromate to deaerated acidified 5 M Cl^- in the absence of 0.1 M Al^{3+} shifted the pH in the alkaline direction where proton reduction would be more sluggish, making the environment more favorable for chromate reduction on AA7050 and subsequent inhibition of damage initiation. This spontaneous rise in pH in the absence of Al^{3+} indicated that an important effect of Al^{3+}, in addition to enhancing HER kinetics, was to act as a powerful buffer such that the addition of chromate did not raise the pH as would be the case in a metal-ion-free acidic solution. The addition of 10^{-3} M chromate to acidified Al^{3+}-free 5 M Cl^- shifted the pH of the base solution from 2.4 to 5.1 and was sufficient in concentration to mitigate damage initiation (Figure 4.24). This result provides more support for the tendency of chromate to suppress damage initiation[18] rather than active corrosion of AA7050 coupled to 316SS. It can be concluded that in a strongly acidic crevice environment complicated by the presence of Al^{3+} with a large buffer capacity, chromate has negligible effect on HER kinetics; the most chromate can do is adsorb on the surface in an effort to neutralize the positive surface charge[67] and possibly slow damage initiation.

From inspection of Equation 4.4 and Figure 4.26, the mass loss of AA7050 in the 0.1 M Al^{3+}-containing environments implies that most of the cathodic reaction was from the local HER. The paradox of this situation is that if the HER is catalyzed on these cathodic surfaces in the presence of Al^{3+}, to the point that the HER in the crevice becomes an important, if not dominant, cathodic reaction, it would be expected that copious OH^- production from the HER causes a rise in the crevice pH, which should lead to passivation. The ability of Al^{3+} to prevent that rise in pH, as indicated by the lack of pH change upon addition of chromate to the base 0.1 M Al^{3+}-containing solution, indicates that a similar large buffering effect of metal ions may be important in bimetallic crevices.

4.5.3 Importance of Cathodes in an AA7050-316SS Crevice: Role of Cu-rich IMPs/Replated Cu Vs. 316SS

At the onset of localized corrosion, it is conceivable that both Cu-rich IMPs and 316SS would be active in the crevice as cathodes catalyzing the ORR. As corrosion progresses and O_2 depletes, the probable release of Cu ions from Cu-rich IMPs[63] – enhanced by cathodic currents on the 316SS – could result in Cu replating on the AA7050 surface and conceivably on the 316SS, consequently increasing the total surface area of active Cu.[17] Based on Table 4.5, it is speculated that the replated Cu, in addition to the Cu-rich IMPs, may become the more significant cathode that drives damage initiation and/or low rate early stage damage propagation on AA7050 whether or not chromate were to be present. However, in the event where chromate was unavailable or insufficient to adequately inhibit cathodic reactions on the replated Cu/Cu-rich IMPs (and possibly 316SS) leading to the accumulation of a substantial amount of Al^{3+} in the crevice, the dominant cathode would be expected to switch to 316SS with attendant substantial increase in the supply of cathodic HER currents available to support extensive damage propagation on AA7050.

4.5.4 Ramifications for Localized Corrosion Damage and Inhibition of Actual Complex Al-Based Structures with Micro- and Macro-Galvanic Couples

In field applications, chromate is stored in protective coating systems applied over Al-based structures. Upon the creation of a defect in the coating, chromate is released, in a controlled fashion, to the exposed area in order to mitigate dissolution of the corroding Al substrate. If the defect occurs within the vicinity of the 316SS fastener, it is reasonable to assume that the leaching phase and transport of chromate from the surface into the fastener crevice would take some time, during which damage would have initiated and progressed within the crevice. This situation would then likely require chromate to be able to suppress active corrosion of AA7050, as opposed to chromate acting to prevent corrosion from initiating if it were present in the crevice solution at time t = 0. The results of the current work suggest that the presence of chromate - even at concentrations much higher than would be attainable in the field[56,68] - may not be effective at suppressing high-rate damage propagation, with an accumulation of Al^{3+} occurring over a localized area on AA7050 within a deep fastener crevice. The conclusions made

from this work may be extended to explain the results reported by Rafla and Scully[17] in which chromate was present throughout the crevice at the start of the test. It is conceivable that chromate was effective at suppressing damage initiation at/near the surface via cathodic inhibition on the 316SS and Cu-rich IMPs, where the ORR was occurring and the pH was high. However, such cathodic inhibition could not be achieved towards the bottom of the crevice where either chromate was depleted or [Al^{3+}] and [H^{+}] were likely high. In real service conditions, such deep fissures could act as susceptible sites for fatigue crack nucleation with the potential for accelerated crack propagation rates, which would be detrimental to the service life of the Al-based structures.[9] It is imperative that candidates for chromate replacement systems be effective in mitigating enhanced acidic HER rates in a fastener crevice.

4.6 Conclusions

The work presented herein experimentally assessed the efficacy of chromate in protecting AA7050 against macro-galvanic induced attack when coupled to 316SS in simulated crevice environments, compared to conditions representative of the external surface. Based on the results, the following conclusions were made:

- Chromate suppressed initiation of damage on AA7050 by suppressing cathodic kinetics on 316SS and anodic kinetics on AA7050, however, the degree of inhibition decreased with decreasing pH.
- The decreased level of chromate inhibition in acidic solutions was attributed to the predominance of the bichromate ion ($HCrO_4^-$) which is more difficult to reduce compared to either the dichromate ion ($Cr_2O_7^{2-}$) or the chromate ion (CrO_4^{2-}).
- Chromate exhibited a diminished ability to inhibit the HER compared to the ORR. However, low solution pH by itself was not considered to be the main damage driver in an AA7050-316SS fastener crevice.
- The presence of 0.1 M Al^{3+} inside the crevice enhanced HER kinetics and acted as a strong buffer such that chromate became ineffective at providing cathodic inhibition on the 316SS/high-purity Cu or raising the pH of the environment. Minimal anodic inhibition,

realized via electrostatic adsorption, was insufficient to mitigate damage initiation and/or propagation on AA7050.

- With no Al^{3+} added to the environment, high-purity Cu was determined to be the more significant cathode, whereas 316SS became the more significant cathode in the presence of 0.1 M Al^{3+}.
- Chromate was assessed to have a superior inhibiting effect over Mg(II) on the AA7050-316SS fastener. Although Mg(II) provided some degree of inhibition in certain environments via possible formation of a $Mg(OH)_2$ film over the couple surface, it is speculated that the $Mg(OH)_2$ film was less impervious than $Cr(OH)_3$ in impeding the ORR occurring over 316SS.

4.7 References

1. C. A. Matzdorf et al., *Corrosion*, **69**, 1240–1246 (2013).
2. Z. Feng and G. S. Frankel, *Corrosion*, **70**, 95 (2014).
3. V. N. Rafla, A. D. King, S. Glanvill, A. Davenport, and J. R. Scully, *Corrosion*, **74**, 5–23 (2018).
4. R. S. Marshall, R. G. Kelly, A. Goff, and C. Sprinkle, *Corrosion*, **75**, 1461–1473 (2019).
5. V. Rafla et al., *Corrosion*, **71**, 1171–1176 (2015).
6. V. N. Rafla and J. R. Scully, *Corrosion*, **75**, 12–28 (2019).
7. A. Moran et al., *Corrosion*, **75**, 484–498 (2019).
8. R. S. Marshall, A. Goff, C. Sprinkle, A. Britos, and R. G. Kelly, *Corrosion*, **76**, 476–484 (2020).
9. N. E. C. Co and J. T. Burns, *Int. J. Fatigue*, **103**, 234–247 (2017).
10. J. Zhao, G. S. Frankel, and R. L. Mccreery, *J. Electrochem. Soc.*, **145**, 2258–2264 (1998).
11. J. D. Ramsey and R. L. Mccreery, *J. Electrochem. Soc.*, **146**, 4076–4081 (1999).
12. D. Chidambaram, C. R. Clayton, and G. P. Halada, *J. Electrochem. Soc.*, **150**, B224 (2003).
13. D. Chidambaram, C. R. Clayton, and G. P. Halada, *J. Electrochem. Soc.*, **151**, B151–B159 (2004).
14. Q. Meng and G. S. Frankel, *Corrosion*, **60**, 897–905 (2004).
15. S. C. Morton and G. S. Frankel, *Mater. Corros.*, **65**, 351–361 (2014).
16. R. K. Gupta, B. R. W. Hinton, and N. Birbilis, *Corros. Sci.*, **82**, 197–207 (2014).
17. V. N. Rafla and J. R. Scully, *Corrosion*, **75**, 587–603 (2019).

18. S. T. Pride, J. R. Scully, and J. L. Hudson, *J. Electrochem. Soc*, **141**, 3028–3040 (1994).

19. U.-E. Charles-Granville, C. Liu, J. R. Scully, and R. G. Kelly, *J. Electrochem. Soc.*, **167**, 111507 (2020).

20. J. Zhao et al., *Surf. Coatings Technol.*, **140**, 51–57 (2001).

21. G. O. Ilevbare and J. R. Scully, *J. Electrochem. Soc.*, **148**, 196–207 (2001).

22. G. O. Ilevbare, J. R. Scully, J. Yuan, and R. G. Kelly, *Corrosion*, **56**, 227–242 (2000).

23. G. O. Ilevbare and J. R. Scully, *Corrosion*, **57**, 134–152 (2001).

24. A. Sehgal, G. S. Frankel, B. Zoofan, and S. Rokhlin, *J. Electrochem. Soc.*, **147**, 140–148 (2000).

25. A. Kolics, A. S. Besing, and A. Wieckowski, *J. Electrochem. Soc.*, **148**, 322–331 (2001).

26. W. J. Clark, J. D. Ramsey, R. L. McCreery, and G. S. Frankel, *J. Electrochem. Soc.*, **149**, B179–B185 (2002).

27. Y. Baek and G. S. Frankel, *J. Electrochem. Soc.*, **150**, B1–B9 (2003).

28. Z. Feng, J. Boerstler, G. S. Frankel, and C. A. Matzdorf, *Corrosion*, **71**, 771–783 (2015).

29. Z. Feng, G. S. Frankel, and C. A. Matzdorf, *J. Electrochem. Soc.*, **161**, C42–C49 (2014).

30. Z. Feng, G. S. Frankel, W. H. Abbott, and C. A. Matzdorf, *Corrosion*, **72**, 342–355 (2016).

31. G. Williams and H. Neil McMurray, *J. Electrochem. Soc.*, **155**, C340 (2008).

32. R. Akid and M. Garma, *Electrochim. Acta*, **49**, 2871–2879 (2004).

33. A. D. King, B. Kannan, and J. R. Scully, *Corrosion*, **70**, 512–535 (2014).

34. B. Kannan and J. R. Scully, *Corrosion*, **72**, 1363–1384 (2016).

35. B. Kannan, C. F. Glover, H. N. McMurray, G. Williams, and J. R. Scully, *J. Electrochem. Soc.*, **165**, C27–C41 (2018).

36. R. J. Santucci, B. Kannan, W. Abbott, and J. R. Scully, *Corrosion*, **75**, 440–456 (2019).

37. R. J. Santucci, M. D. Holleman, and J. R. Scully, *Surf. Coatings Technol.*, **383**, 125245 (2020).

38. C. Liu, V. A. Yang, and R. G. Kelly, *J. Electrochem. Soc.*, **166**, C134–C146 (2019).

39. A. C. Bastos, M. C. Quevedo, O. V. Karavai, and M. G. S. Ferreira, *J. Electrochem. Soc.*, **164**, C973–C990 (2017).

40. Á. Keresztesi et al., *Environ. Res.*, **188**, 109872 (2020).

41. D. Möller, *Tellus B*, **42**, 254–262 (1990).

42. C. Neal and J. W. Kirchner, *Hydrol. Earth Syst. Sci.*, **4**, 295–310 (2000).

43. H. S. Isaacs, *Corros. Sci.*, **28**, 547–558 (1988).

44. S. Böhm, H. N. McMurray, S. M. Powell, and D. A. Worsley, *Electrochim. Acta*, **45**, 2165–2174 (2000).

45. G. Williams, A. J. Coleman, and H. N. McMurray, *Electrochim. Acta*, **55**, 5947–5958 (2010).

46. D. Chidambaram, G. P. Halada, and C. R. Clayton, *Appl. Surf. Sci.*, **181**, 283–295 (2001).

47. M. C. Biesinger et al., *Appl. Surf. Sci.*, **257**, 2717–2730 (2011).

48. T. H. Nguyen, B. F. Brown, and R. T. Foley, *Corrosion*, **38**, 319 (1982).

49. K. R. Cooper and R. G. Kelly, *Corros. Sci.*, **49**, 2636–2662 (2007).

50. K. R. Cooper, *Chemistry and electrochemistry of environment-assisted cracking of an aluminum-zinc-magnesium-copper alloy*, PhD dissertation, University of Virginia, (2001).

51. H. N. McMurray, D. Williams, and D. A. Worsley, *J. Electrochem. Soc.*, **150**, B567 (2003).

52. A. C. Bastos, M. C. Quevedo, and M. G. S. Ferreira, *Corros. Sci.*, **92**, 309–314 (2015).

53. B. Zaid, D. Saidi, A. Benzaid, and S. Hadji, *Corros. Sci.*, **50**, 1841–1847 (2008).

54. I. W. Huang, B. L. Hurley, F. Yang, and R. G. Buchheit, *Electrochim. Acta*, **199**, 242–253 (2016).

55. L. Yin, Y. Jin, C. Leygraf, and J. Pan, *J. Electrochem. Soc.*, **164**, C768–C778 (2017).

56. J. D. Ramsey, L. Xia, M. W. Kendig, and R. L. McCreery, *Corros. Sci.*, **43**, 1557–1572 (2001).

57. L. Gáncs et al., *Electrochem. Solid-State Lett.*, **5**, B16 (2002).

58. A. Dzieniszewska, J. Kyziol-Komosinska, and M. Pająk, *PeerJ*, **8** (2020).

59. F. Brito et al., *Polyhedron*, **16**, 3835–3846 (1997).

60. M. M. Hoffmann, J. G. Darab, and J. L. Fulton, *J. Phys. Chem. A*, **105**, 1772–1782 (2001).

61. M. W. Kendig and R. G. Buchheit, *Corrosion*, **59**, 379–400 (2003).

62. P. R. Roberge, *Handbook of Corrosion Engineering*, McGraw-Hill, New York, (1999).

63. Y. Yoon and R. G. Buchheit, *J. Electrochem. Soc.*, **153**, B151 (2006).

64. C. Liu, P. Khullar, and R. G. Kelly, *J. Electrochem. Soc.*, **166**, C153–C161 (2019).

65. S. Trasatti, *Electroanal. Chem. Interfacial Electrochem.*, **39**, 163–184 (1972).

66. B. E. Conway and G. Jerkiewicz, *Solid State Ionics*, **150**, 93–103 (2002).

67. M. Kendig, S. Jeanjaquet, R. Addison, and J. Waldrop, *Surf. Coatings Technol.*, **140**, 58–66 (2001).

68. L. Xia, E. Akiyama, G. Frankel, and R. Mccreery, *J. Electrochem. Soc.*, **147**, 2556–2562 (2000).

5. Application of Finite Element Modeling (FEM)-based Laplacian Equation to predict Macro-Galvanic Current Distributions on AA7050-316SS Couple

The work presented in this chapter has been reported in the following publication:

U.-E. Charles-Granville*, R. S. Marshall*, C. V. Moraes*, C. F. Glover, J. R. Scully, R. G. Kelly, "Application of Finite Element Modeling to Macro-Galvanic Coupling of AA7050 and SS316: Validation Using the Scanning Vibrating Electrode Technique", *J. Electrochem. Soc.*, **169**, 031502 (2022). * Equal contribution

5.1 Abstract

The scanning vibrating electrode technique (SVET) was utilized to experimentally validate the applicability of finite element modeling (FEM) in simulating macro-galvanic-induced corrosion of AA7050 coupled to SS316, in environments representative of the boldly exposed surface of an actual fastener couple. The FEM boundary conditions were modified from the SVET environments in which the AA7050-SS316 couple sample was initially exposed, in order to better represent the steady-state corroding surface of the localized corrosion-prone AA7050. Better agreements between the SVET-derived data and the model in the case of macro-galvanic coupling behavior were achieved for near-neutral conditions, compared to acidic conditions. The current density at the electrode/electrolyte interface was determined with the validated model. In addition, the percent difference between the measured current density at the SVET probe height and that at the electrode surface was observed to scale with the magnitude of current density at the electrode surface, with the largest discrepancy seen at the galvanic couple interface. Plausible reasons for the deviation of the model predictions from the SVET-derived data are discussed.

5.2 Introduction

Precipitation-strengthened Al alloys such as those belonging to the 2XXX and 7XXX series are the preferred materials for the construction of light-weight aerospace vehicles.[1] Despite their superior mechanical properties, these high-strength Al alloys pose a huge challenge in weldability. Because they are precipitation-strengthened, the use of traditional welding

techniques to join them often leaves undesirable weld joints with deteriorated properties due to weld porosity and weld cracking during solidification.[2] As an alternative, high-strength, noble fasteners such as stainless steels (SS) are often used in joining the Al alloy (AA) parts in aerospace structures. In natural corrosive environments, macro-galvanic interactions between the more noble fastener and the AA, in addition to the micro-galvanic coupling within the base AA microstructure,[3] can exacerbate localized corrosion of the Al-based structures.[4–11]

Many studies of galvanic corrosion processes on Al alloys have utilized a number of experimental techniques, including the zero resistance ammeter (ZRA) technique, the coupled microelectrode array (CMEA), and the scanning vibrating electrode technique (SVET).[11–20] The ZRA technique conducted on planar coupled electrodes enables the simultaneous measurements of global galvanic potentials and coupling currents. In this configuration, spatial resolution of localized corrosion processes occurring on the AA cannot be captured; only global current measurements are possible. In this context, the CMEA coupled with the ZRA allows the interrogation of in-situ local electrochemical processes occurring on individual microelectrodes by mapping the local current density distributions as a function of spatial location and time. In the case of AA7XXX, one can monitor the transition of initial anodes to cathodes which could signify dealloying of Al_2CuMg and/or Cu replating.[11,15] That said, some of the limitations of the CMEA are the intricacy of constructing the arrays, the use of surrogate materials as opposed to plate or sheet products used in aerospace construction, as well as the need for controlling specific geometric parameters such as anode-to-cathode ratio and electrode spacing.

The primary benefit of using the SVET to investigate galvanically-induced corrosion is that it enables the spatial and temporal resolution of the electrochemical behavior from the macro-galvanic couple (between SS and AA, in this instance) and localized behavior as a result of the micro-galvanic coupling on the same surface. The evolution of local net anodic and cathodic activity can be mapped, enabling the magnitude of currents to be monitored as a function of time. This distinction between the two types of corrosion occurring in this system cannot be achieved with bulk electrochemical techniques. Although the SVET provides a good representation of the localized corrosion processes occurring *in-situ* on an electrode surface with

no perturbation from the test itself, the results should be used with caution.[21] The SVET measures the dominant reaction or net current and detects current based on the potential gradient. It also does not account for local variations in conductivity that may occur at the electrode surface as a result of corrosion processes, and is disrupted by hydrogen bubbles.[22] The SVET measurements are not taken at the electrode surface but at a specific height above the electrode surface, typically ~ 50-150 µm.[17,20,23–25] As such, the calculated currents are typically an underestimation of the actual values at the electrode surface.[21] One way to bridge this gap is to utilize finite element modeling (FEM) in conjunction with the SVET. If the FEM simulations can be reasonably validated by the SVET at a specified probe height, then one can utilize the FEM to predict current density distributions at the electrode surface as well as quantify the underestimation of the electrode surface current density as a function of SVET probe height.

A number of studies have employed the SVET to validate FEM simulations using the Laplace,[26–28] Laplace and Fick's second law,[24,29,30] and Nernst-Planck[26,29,31,32] as governing equations. The Laplace equation assumes that the solution is homogeneously mixed such that the diffusive and convective transport of species can be ignored, allowing the solution to be treated as an ohmic resistor, which makes the model less complex.[33] The Laplace approach can be supplemented with transport equations for cases in which kinetics of the electrodes are dependent on the concentration of species present in the electrolyte, that either do not considerably carry the current (minor species) or that do not have charge (e.g., O_2). This approach has been widely used to model the mixed charge-transfer and diffusion-controlled kinetics of the oxygen reduction reaction (ORR).[24,29,30]

The Nernst-Planck equation is more robust in considering concentration gradients of all ionic species in the electrolyte, yet computationally demanding in terms of complexity and execution time.[33] Thébault et al.[29] demonstrated that the locally-induced convection from the vibrating probe tip during SVET measurements homogenizes the electrolyte, thus, eliminating any concentration and conductivity gradients. This natural outcome makes the SVET an ideal experimental technique to compare with a Laplacian model.

When solving for the variables that describe corrosion phenomena in FEM with any of the governing equations above, it is common to use a scaffolding approach to determine the correct boundary conditions by starting with simplifying assumptions and working towards a more realistic scenario.[27,34–36] As noted previously, computational results depend highly on the choice of boundary conditions, which are also dependent on a variety of environmental factors.[33]

The aforementioned studies demonstrate the viability of the SVET for modeling galvanic corrosion processes and, to the best of the authors' knowledge, no studies in the available literature have combined these techniques with a focus on AA-SS galvanically-coupled systems.

The objective of this work is to utilize the SVET to validate the FEM-based Laplacian model in predicting macro-galvanic current distributions on an AA7050-SS316 couple in simulated environments representative of near-neutral and acidic corrosive conditions. The geometry of the AA7050-SS316 couple mimics the boldly exposed surface of an actual fastener couple.

As with all models, the choice of the input boundary conditions is crucial to the accuracy and reliability of the model as a predictive tool, especially for conditions that are experimentally difficult or impractical to investigate. Emphasis is made on the choice of boundary conditions as well as the adjustments made in an attempt to correctly represent the conditions being simulated. The sources of the discrepancies observed between the SVET and modeling results are discussed. The results of this study are intended to add to the knowledge base of the applicability of FEM to the simulation of galvanic corrosion phenomena.

5.3 Methods

5.3.1 SVET Measurements

The AA7050-SS316 couple was constructed by inserting a short rod of SS316 onto an AA7050 plate with the dimensions as shown in Figure 5.1a. The SS316 rod was flush-mounted so that the transverse cross-section produces a circular disk in the plane of the plate. The anode-to-cathode area ratio was ~ 7:1. No intentional crevice gap was created. The structure was encapsulated in epoxy with an internal Ni wire electrical connection. Immediately preceding each experiment, the sample was wet-ground successively from 400 grit to a surface finish of 1200 grit

with SiC paper, rinsed with deionized water, and dried with clean compressed air. A Biologic SP™ instrument was utilized for the SVET measurements. The scans were conducted on an area of ~ 7.5 mm x 7.5 mm within the exposed bare area of the couple surface in each case, under freely corroding conditions. For each experiment, the exposed couple surface was fully immersed (i.e., water layer thickness ≥ 1000 µm) in an electrolyte bath containing aqueous 1 mM NaCl electrolyte at the relevant pH. The choice of 1 mM NaCl was made based on the resolution limitations of the SVET as signal-to-noise ratios decrease with increasing solution conductivity.[21] Experiments were conducted at the electrolyte's natural pH of 5.8 and at pH 3 (adjusted with HCl) to simulate normal rainy conditions and acid rain conditions, respectively.

An additional experiment was conducted on a 200 µm Au point current source that was used to determine the change in the SVET-derived current density as a function of the SVET probe height from the electrode surface. Two current values of 5 µA and 25 µA were applied separately to the Au point current source. The experiments were conducted in 1 mM NaCl at its natural pH of 5.8, for consistency with the galvanic coupling experiment.

The vibrating SVET probe consisted of a platinum probe with a diameter specified by the manufacturer as between 5 and 50 µm. The probe was positioned vertically and scanned at a constant height of 100 µm above the experimental area with a peak-to-peak amplitude of 30 µm and a frequency of 80 Hz. The peak-to-peak SVET voltage signal (V_{pp}) is related to the current flux density along the axis of probe vibration (j_z) by:

$$V_{pp} = j_z \left(\frac{A_{pp}}{\kappa}\right) \tag{5.1}$$

where κ is solution conductivity and A_{pp} is the peak-to-peak amplitude of vibration of the SVET probe, such that a quantity $G = \kappa/A_{pp}$ may be defined as the SVET calibration factor.

SVET calibration was carried out galvanostatically using the point current source technique described above, where a graphite counter electrode was held ~ 8 cm away from the Au point current source, and the setup can be found elsewhere.[37,38] Samples were scanned immediately following immersion and continuously thereafter for a period of 24 h. The total number of measurement points in each scan was ~ 5776, and the time taken for each

measurement was ~ 0.12 s, for a full scan duration of ~ 12 min. There was no wait time between measurements. SVET j_z distributions were plotted using Surfer 8™ by Golden Software.

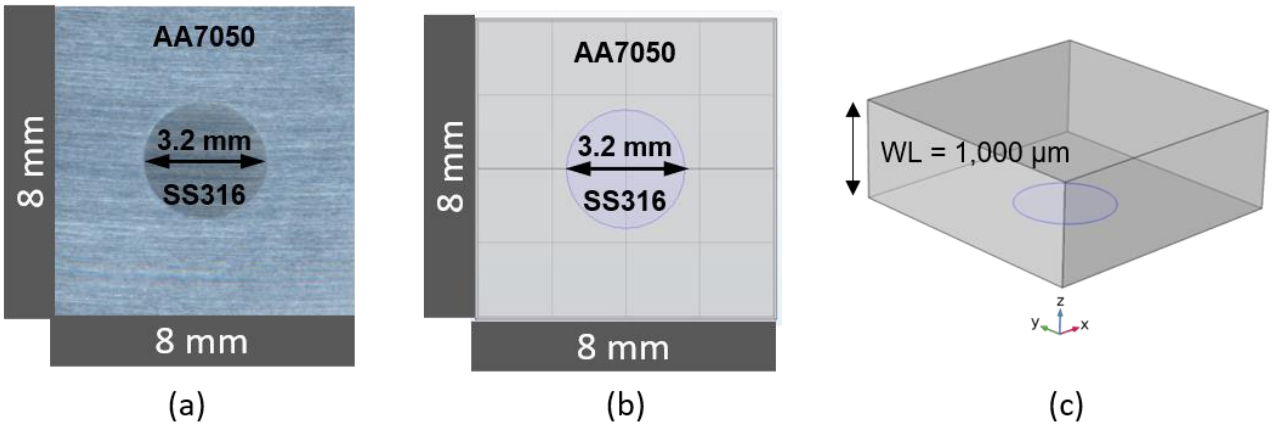

Figure 5.1. Geometry of the AA7050-SS316 couple used for (a) SVET experiments and (b) FEM; (c) xy, yz, and xz boundaries representing the air/solution interface in (b) with z = water layer thickness of 1000 µm.

5.3.2 Electrochemical Measurements

Cathodic and anodic potentiodynamic polarization curves were generated on SS316 and AA7050, respectively, to serve as input boundary conditions for the model. Experiments were conducted on separate SS316 and AA7050 specimens in a standard three-electrode flat cell configuration, in the same environments used for the SVET measurements, under quiescent conditions. HCl was used to adjust the pH. Two concentrations of $AlCl_3$, 0.003 mM and 0.3 mM, were added to the cathodic scans while maintaining the total chloride concentration of 1 mM. The pH in both $AlCl_3$ containing solutions was not controlled but was measured to be 5 and 3.6 for the low and high concentrations, respectively. The scans were conducted after a 30-min full immersion exposure at open circuit and at a scan rate of 0.5 mV/s.

5.3.3 Model Description

5.3.3.1 Governing Equation

COMSOL Multiphysics® software (v. 5.6) was used to solve the partial differential equations by the finite element method. Laplace equation (Equation 5.2) was used to solve for the potential distribution in the electrolyte domain:

$$\nabla^2 \varphi = 0 \tag{5.2}$$

where φ is the electrolyte potential. By using Laplace as the governing equation, the electrolyte is assumed to be well-mixed (i.e., there is a negligible concentration gradient of the ionic species); hence, electrolyte is assumed to behave as a homogeneous ohmic conductor with a constant conductivity. Thus, the electrolyte current density could be solved using Ohm's law:

$$i = \kappa_i \nabla \varphi \tag{5.3}$$

where κ_i corresponds to the conductivity of the solution i. For each case investigated, the conductivities were adjusted according to the solution in which the measurements were performed. Table 5.1 shows the conductivity of the solutions considered in this work, which were calculated using OLI™ Studio Analyzer 10.1 (from OLI Systems, NJ). In all scenarios tested, the conservation of charge (i.e., $I_a = I_c$, with I_a being the total anodic current and I_c being the total cathodic current) was verified.

The assumption of a well-mixed electrolyte to model SVET measurements is reasonable, as the convection induced by the microelectrode vibrations homogenizes the electrolyte, reducing any concentration gradients.[29]

In an additional model, Al^{3+} production and transport were calculated. Fick's second law was used to solve for the concentration distribution through space and time:

$$\nabla^2 c_{Al^{3+}} = 0 \tag{5.4}$$

Note that, even though Al^{3+} is a charged species that can carry current, it was assumed that Na^+, Cl^-, and H^+ were the main species that carried current.

The model was built using a 3D geometry. The dimensions of the sample on which the SVET was performed were used to build the geometry, as shown in Figure 5.1b.

Table 5.1. Parameters used in the FEM.

Parameter	Description	Value
$\mathbf{i_{0,5.8}}$	Pseudo-exchange current density for ORR kinetics in pH 5.8	4 x 10^{-11} (A/cm^2)
$\boldsymbol{b_{c,5.8}}$	Fitted cathodic Tafel slope in pH 5.8	-0.193 (V) 95%CI (-0.194, -0.191)
$\mathbf{E_{eq,5.8}}$	Equilibrium potential of the cathode in pH 5.8	0.573 (V)
$\mathbf{i_{lim,5.8}}$	Diffusion limited current density in pH 5.8	1.2 x 10^{-5} (A/cm^2)
$\boldsymbol{\kappa_{5.8}}$	Conductivity in 0.001M NaCl, pH 5.8	0.0188 (S/m)
$\mathbf{i_{0,3}}$	Pseudo-exchange current density for ORR kinetics in pH 3	5 x 10^{-13} (A/cm^2)
$\boldsymbol{b_{c,3}}$	Fitted cathodic Tafel slope in pH 3	-0.181 (V) 95%CI (-0.182, -0.180)
$\mathbf{E_{eq,3}}$	Equilibrium potential of the cathode in pH 3	0.809 (V)
$\mathbf{i_{lim,3}}$	Diffusion limited current density in pH 3	3 x 10^{-5} (A/cm^2)
$\boldsymbol{\kappa_3}$	Conductivity in 0.001M NaCl, pH 3	0.0767 (S/m)

5.3.3.2 Boundary Conditions

As illustrated by Figure 5.1c, at the upper (xy), left (yz), and right (xz) boundaries, which represent the air/solution interface (z = water layer thickness), Neumann boundary conditions were applied (i.e., no current flux). At the lower boundary, the electrochemical kinetics of SS316 and AA7050 were defined using different approaches. In the first approach, piecewise interpolations of the full immersion potentiodynamic polarization scans were used as boundary conditions. In a second approach, a limiting current density corresponding to the diffusion-

limited oxygen reduction reaction (ORR) current density was imposed. In a third approach, the cathodic kinetics of SS316 were defined using an analytical expression:

$$i = \frac{i_{ct}}{1 + \left|\frac{i_{ct}}{i_{lim}}\right|} \tag{5.5}$$

$$i_{ct} = i_0 \cdot 10^{\frac{E-E_0}{b}} \tag{5.6}$$

where i_{ct} is the charge transfer-controlled portion of the current density, i_{lim} is the ORR limiting current density extracted from the cathodic polarization scans, i_0 is a pseudo-exchange current density, E is the applied potential, E_0 is the reversible potential, and b is a fitted Tafel slope. The pseudo-Tafel parameters were obtained by fitting Equation 5.6 to the cathodic polarization scans. The values of the parameters are displayed in Table 5.1.

Note that the edges of the sample (x = 0 and 8 mm) were the boundaries of the simulation, which simulates a condition in which the walls of the container in which the SVET was performed were exactly at the edges of the sample (Figures 5.1b and 5.1c). This modeling approach is common in the literature, even if the sample is exposed to large volumes of solution such as occurs during SVET.[24,26,28,31] However, the dimensions of the container in which the SVET was performed were much larger than the sample's dimensions.

For the case in which Al^{3+} concentration was calculated, Faraday's law was used to calculate the local flux of the Al^{3+} species being produced at the AA7050 electrode ($J_{Al^{3+}}$), with the assumption that the dissolution of the other alloying elements present in AA7050 (e.g., Zn, Mg) are negligible:

$$J_{Al^{3+}} = \frac{i_{local,AA7050}}{nF} \tag{5.7}$$

where n is the number of electrons transferred during the reaction, and F is Faraday's constant. Additionally, for the case in which Al^{3+} was considered, the geometry of the model was altered to match the total volume of the solution in which the SVET measurements were performed. Zero flux boundary conditions were imposed at the interfaces between electrolyte/air and at the walls of the container. Effects of natural convection were not taken into consideration.

5.3.3.3 Error Calculations

When comparing experimental results against each other, such as calculating the conservation of electroneutrality between the experimentally-derived anodic and cathodic currents, or to quantify the difference between computational results, the percent difference was used (Equation 5.8).

$$\frac{ABS(x_1 - x_2)}{ABS\left(\frac{(x_1 + x_2)}{2}\right)} \times 100 \tag{5.8}$$

where ABS represents the absolute value, x_1 represents one experimental/computational datapoint, and x_2 represents another experimental/computational datapoint, respectively. However, when the computational and experimental current densities (or currents) were compared, the percent error was utilized (Equation 5.9).

$$\frac{ABS(i_{experiment} - i_{computational})}{ABS(i_{experiment})} \times 100 \tag{5.9}$$

In this way, the experimental results acted as a "baseline" with which to compare the computational data.

5.4 Results

5.4.1 Potentiodynamic Scans

Cathodic and anodic potentiodynamic scans (PDS) were plotted separately for clarity in Figures 5.2a and 5.2b, respectively. Note that only cathodic reactions on the SS316 surface were considered in this work. The anodic passive current density of SS316 was calculated to be

approximately three orders of magnitude lower than the cathodic behavior of SS316 within the potential range of interest. This result justifies the assumption that anodic reactions occurring on the SS316 surface in the present system would be negligible.

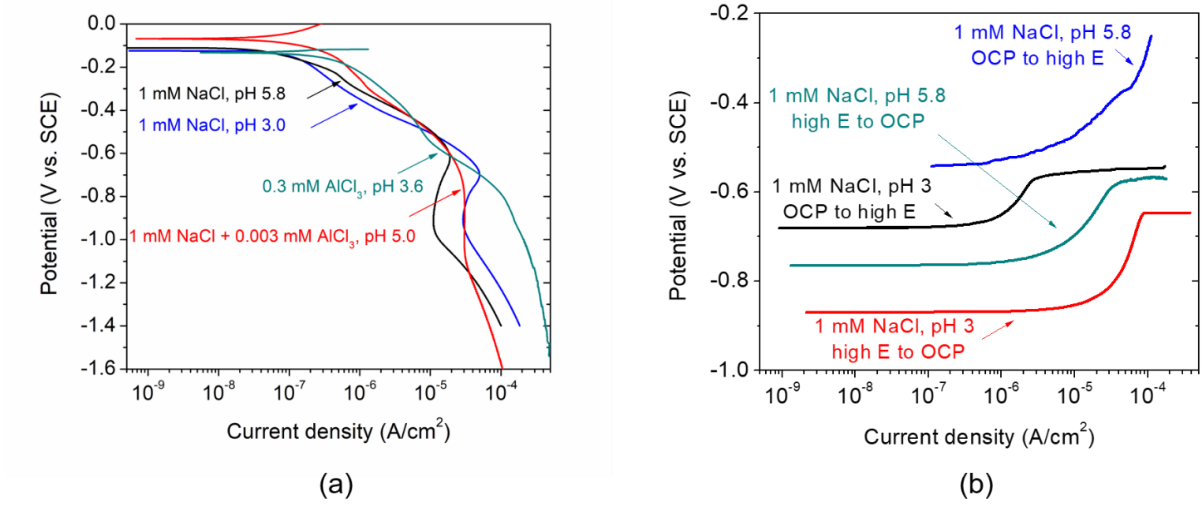

Figure 5.2. Potentiodynamic polarization scans used as input boundary conditions for the model; (a) cathodic scans on SS316, and (b) anodic scans on AA7050, corrected for ohmic drop.

In the pH 3 environment, cathodic kinetics on SS316 increased by at least two-fold compared to that at pH 5.8, which is consistent with what has been reported in the literature.[39,40] Additionally, it was observed that the cathodic kinetics increased with increasing Al^{3+} concentration while keeping the chloride concentration constant. Decreased amounts of Al^{3+} in solution exhibited a smaller effect, with a diffusion limiting current density visible and approximately equal to that observed in the pH 3 solution, where no additions of $AlCl_3$ were made. Both the change in pH and the addition of Al^{3+} had minimal impact on the open circuit potential (OCP) of the SS316. Concerning the cathodic scans on SS316 without the addition of Al^{3+}, there was a current wave at potentials between the charge-transfer regime and the diffusion limiting regime (Figure 5.2a). This cathodic peak was determined to be a transient and will be discussed in a later section.

All anodic curves were manually post-processed to correct for ohmic drop by first calculating the slope of the linear E vs. i plot to determine the ohmic (solution) resistance. The true potential was determined by subtracting the product of the current density and ohmic resistance, that is, the potential due to ohmic drop. To confirm the calculated solution resistance from post-processing, EIS was used to measure the actual resistance between the reference and working electrodes. Impedance at high frequencies performed in the same cell, assuming a Randles circuit, resulted in ohmic resistance values consistent with the manually calculated values as displayed in Table 5.2.

Table 5.2. Ohmic resistance values used for iR correction of anodic polarization curves.

Description of Technique	Description of Solution	R_{ohmic} ($\Omega \cdot cm^2$)
EIS	1 mM NaCl, pH 5.8	5750
Manual correction	1 mM NaCl, pH 5.8, OCP to high E positive scan	7221
Manual correction	1 mM NaCl, pH 5.8, high E to OCP negative scan	5246
EIS	1 mM NaCl, pH 3	3541
Manual correction	1 mM NaCl, pH 3, OCP to high E positive scan	3368
Manual correction	1 mM NaCl, pH 3, high E to OCP negative scan	2467

Conventional anodic polarization of AA7050 typically starts either at, or slightly below, the measured OCP before scanning to more positive potentials. In this study, scans were also conducted starting at a high potential and sweeping towards the OCP. This method captures the anodic kinetics and OCP while the surface is undergoing active localized corrosion, and is evident in the data presented in Figure 5.2b, where increased anodic kinetics and a suppressed OCP are observed in the 'high E to OCP' negative scans, relative to those observed for the positive 'OCP to high E' scans. Additionally, independent of scan direction, the OCP of the AA7050 in the pH 3 solution was found to be more negative than that observed in pH 5.8. When considering a steady-state model, the boundary conditions should also reflect steady-state corrosion while neglecting any passive breakdown initiation period that may occur during the initial immersion. Selecting a polarization curve that best describes the steady-state corroding surface requires careful consideration. This aspect of modeling will be discussed later.

5.4.2 SVET Current Density Distributions

Figures 5.3a and 5.3b show the SVET-derived current density distribution maps obtained on the AA7050-SS316 couple in 1 mM NaCl at pH 5.8 and pH 3, respectively, after 24 h of immersion. Under pH 5.8 conditions (Figure 5.3a), localized anodic activity was observed in multiple locations on the AA7050 surface, indicative of pitting corrosion. It is noteworthy that these anodically activated regions on the AA7050 surface were not necessarily found to be adjacent to the SS316 cathode. Peak anodic and cathodic j_z values over the couple surface were ~ $\pm$ 10 μA/cm^2. Under pH 3 conditions (Figure 5.3b), increased cathodic current density over the SS316 (up to 50 μA/cm^2) facilitated the anodic activation of nearly the entire exposed surface of AA7050, with an anodic j_z maximum of ~ 30 μA/cm^2. The j_z distributions measured above the SS316 were up to five times greater than the values observed over SS316 under pH 5.8 conditions.

5.4.3 Comparison of the Global Current Density Distribution

Two steady-state finite element models were created, with input from PDS providing the boundary conditions. Each PDS was performed in an identical solution as that used for the SVET measurements. The global current density was calculated for each pH condition and compared with results measured from the SVET (Figures 5.3c and 5.3d). At a distance of 100 μm above the surface, the SVET tip measures the electrolyte current density in the normal z-direction by oscillating $\pm$ 15 μm to calculate the potential difference. The resulting current density is important to distinguish from that on the electrode surface. Therefore, the z-component of the current density vector 100 μm above the surface was calculated computationally, unless otherwise specified.

To best compare the dynamic experimental data with the steady-state computational results, SVET experiments were conducted for 24 h. Area-averaged integrated current density vs. time plots were used to confirm that the system reached steady-state. Note that the bounds of the color-scale bar from the computational plots are consistent with that of the SVET data and that the pH 3 scenario bounds are not symmetric. Qualitatively, the models at both pH conditions capture the interface between the AA7050 panel and SS316 disk, with the same order of

magnitude as was measured via SVET (Figures 5.3a to 5.3d). That is, the model also predicted an increase in current density as the solution was changed from pH 5.8 to pH 3.

Figures 5.3e and 5.3f show the simulated potential distributions for the pH 5.8 and pH 3 conditions, respectively. For both pH cases, there was a small ohmic drop across the electrodes (6 mV for the pH 5.8 case, and 12 mV for the pH 3 case), and the couple potentials were closer to the non-polarizable AA7050 anode.

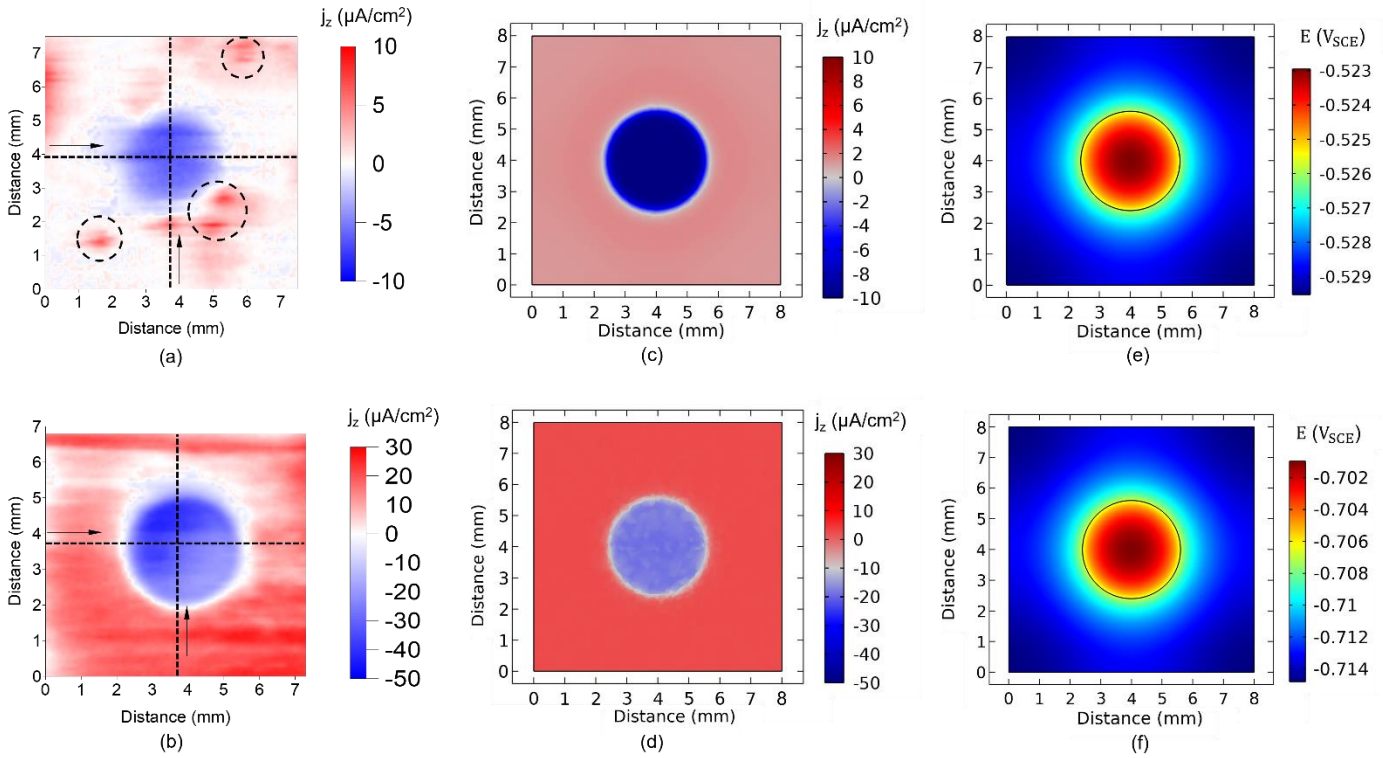

Figure 5.3. SVET-derived 24 h surface maps (a) and (b), corresponding FEM results (c) and (d) showing current density distributions above a freely-corroding AA7050-SS316 couple immersed in 1 mM NaCl at pH 5.8 and pH 3, respectively. Note that the color bar in each pH scenario is consistent. Current density distributions were taken at a distance of 100 μm above the electrode surface, in each case. Dashed lines in (a) and (b) show the location of vertical and horizontal line profiles taken. Dashed circles in (a) show some regions with localized corrosion activity. Potential distributions (e) and (f) corresponding to FEM current density maps (c) and (d), respectively.

5.4.4 Comparison of the Current Density Line Profiles under pH 5.8 Conditions

Line scans taken across the center of the sample, as indicated by the black dashed lines in Figures 5.3a and 5.3b, were compared between the SVET data and modeled results to facilitate a more rigorous interrogation of the current density distributions across the galvanic interface. Note that the SVET line scans contain small fluctuations rather than a completely smooth line, indicative of the local reaction transients taking place at the time of the scan or noise due to hydrogen bubbles, as seen in the 2D maps presented in Figures 5.3a and 5.3b.

To compare the model with the SVET line scans, three boundary condition scenarios (as displayed in Figure 5.4a) were tested in 1 mM NaCl at its natural pH of 5.8:

1. Cathodic SS316 PDS and anodic AA7050 PDS (full PDS)
2. Cathodic SS316 PDS with i_{lim} imposed and anodic AA7050 PDS (PDS + i_{lim})
3. Cathodic SS316 i_{ct} fitting with i_{lim} imposed and anodic AA7050 PDS (i_{ct} + i_{lim})

In all scenarios, the modeled results show the electrolyte current density calculated at a height of 100 µm from the surface for consistency with the SVET-derived data.

For scenario 1 (full PDS), the evaluation largely overestimated both the anodic and cathodic currents when compared to those measured with the SVET (Figure 5.4b). Speculating that the overestimation may be due to the current wave between the charge-transfer and diffusion limiting current regime, a new model was created (scenario 2), strictly enforcing that the maximum current density was not greater than the diffusion limiting current density ($i_{lim,\ 5.8}$) reported in Table 5.1 (Figure 5.4a). Although neglecting current densities greater than $i_{lim,5.8}$ neglected the HER as well as the cathodic current wave, the couple potential was positive enough such that the HER would not contribute in any way. Utilizing the new cathodic boundary condition (PDS + i_{lim}), the computational line scan of current density decreased to values closer to what was measured with the SVET (Figure 5.4b).

An additional method of selecting model boundary conditions involves the use of charge transfer-controlled kinetic parameters (scenario 3), which were extracted from the measured

cathodic PDS (Figure 5.4a), and are documented in Table 5.1. These E-log(i) parameters generalize the cathodic behavior in the given environment, increasing the reproducibility of FEM, and were input as new cathodic boundary conditions ($i_{ct} + i_{lim}$) while the AA7050 anodic boundary condition remained the same. The resulting cathodic current density was increased slightly, while the anodic current remained nearly constant due to the much larger anodic surface area. Both boundary conditions including i_{lim} appeared to accurately capture the peak anodic behavior in the horizontal line scan, as well as the overall cathodic behavior seen in both horizontal and vertical line scans (Figure 5.4b).

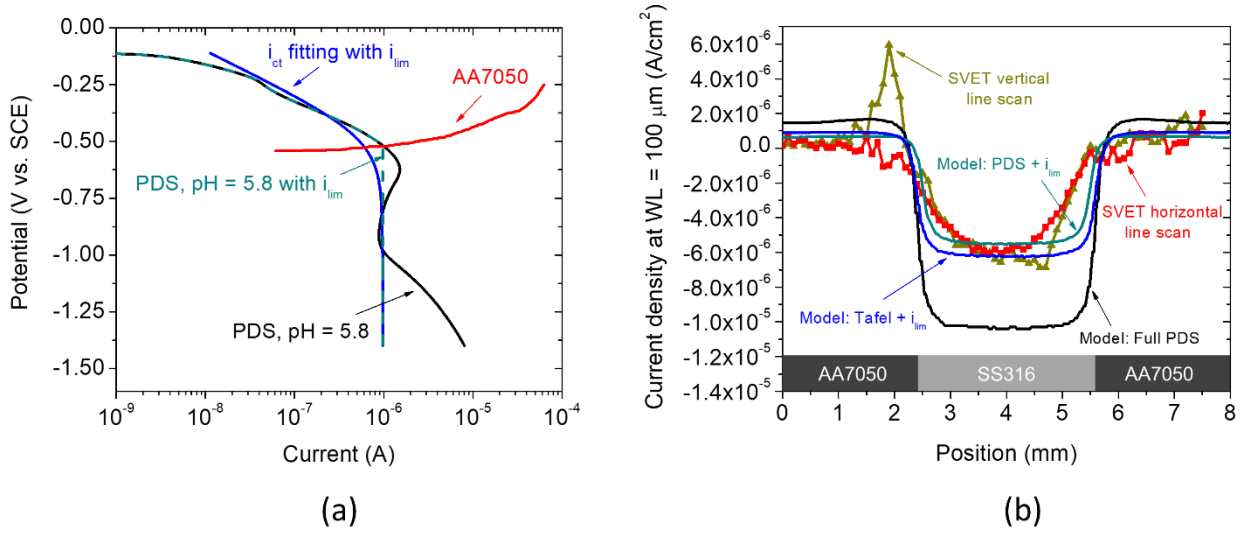

Figure 5.4. (a) Anodic and cathodic boundary conditions used within the model, scaled to correct for cathode:anode area differences; (b) comparison of the SVET current density line profiles with three computational models for pH 5.8 conditions. The current density line profiles were taken at a distance of 100 μm above the electrode surface, in each case. The notation "full PDS" in (b) indicates the black and red curves in (a) were used as boundary conditions. Correspondingly, "PDS + i_{lim}" in (b) indicates the dashed teal and red curves in (a) were used. Lastly, "$i_{ct} + i_{lim}$" in (b) indicates the blue and red curves in (a) were used as boundary conditions.

To determine whether the observed cathodic current wave was a complexation of species, or a transient reaction, a potentiostatic hold was applied to SS316 at a value of -0.62 V vs. SCE for 24 h (Figure 5.5). During the hold, the current density decreased sharply before quickly stabilizing, indicating that a transient reaction may have occurred but would not be sustained nor

representative of the long-term cathodic behavior of the SS316. The transient reaction was speculated to be the reduction of the native Fe^{3+} oxide to Fe^{2+}, which is consistent with the system E-pH region on the iron E-pH diagram, calculated using Medusa™ software. It is noted that the native oxide film on the SS316 was not reduced prior to performing the PDS.

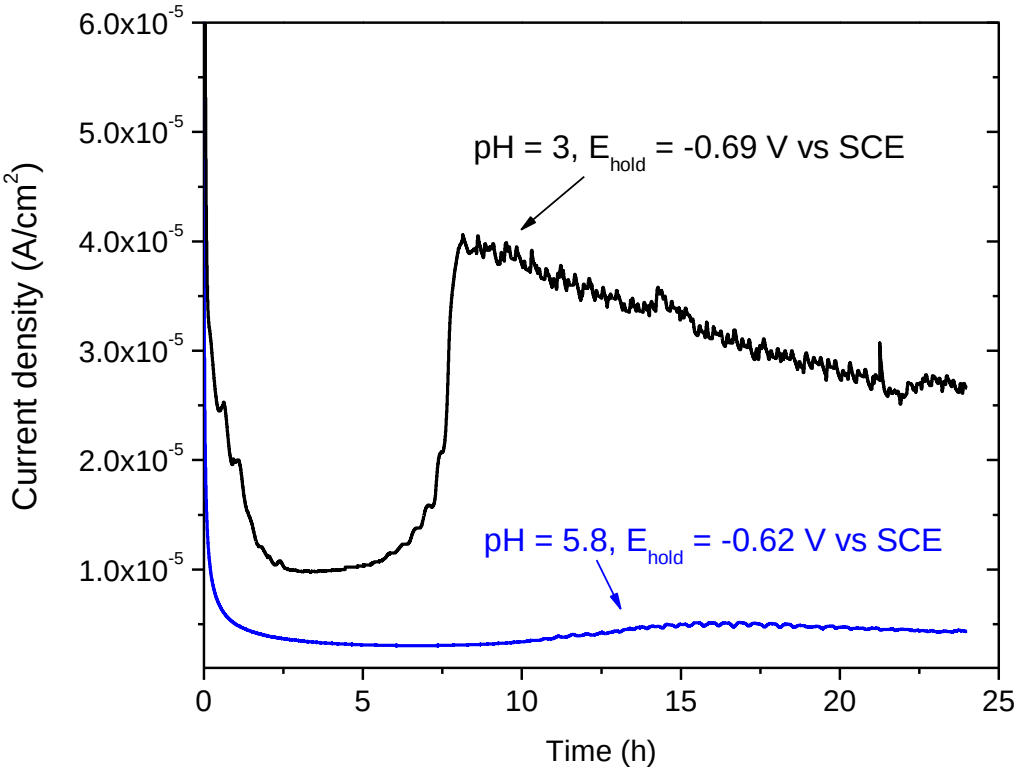

Figure 5.5. 24-h potentiostatic tests on SS316 in 1 mM NaCl at pH 5.8 and pH 3. Potentials were held at the values corresponding to the peak current waves observed on the respective cathodic polarization curves displayed in Figure 5.2a.

5.4.5 Comparison of the Current Density Line Scans under pH 3 Conditions

A similar approach was employed to model the galvanic coupling between AA7050 and SS316 in the pH 3 solution, with the following boundary conditions tested, as displayed in Figures 5.6a and 5.6c:

1. Cathodic SS316 i_{ct} fitting with i_{lim} imposed (1) and anodic AA7050 positive PDS, OCP to high E (2)
2. Cathodic SS316 with 0.003 mM $AlCl_3$ PDS (3) and anodic AA7050 positive PDS, OCP to high E (2)
3. Cathodic SS316 with 0.003 mM $AlCl_3$ PDS (3) and anodic AA7050 negative PDS, high E to OCP (4)
4. Cathodic SS316 with 0.3 mM $AlCl_3$ PDS (5) and anodic AA7050 negative PDS, high E to OCP (4)

Figure 5.6b shows current density line profiles calculated by the models and measured by the SVET, both at a distance of 100 µm above the electrode surface. The SVET-derived data were extracted from both the horizontal and vertical centerlines of the sample surface. Additionally, the plot shows an SVET-derived current density line profile where an average value has been applied for the cathodic portion. This corrects the asymmetry observed in the cathodic region and entailed averaging all cathodic current density data points except the first and last three, as they were approximately symmetric. The averaged value was plotted between the original, unaveraged cathodic data points.

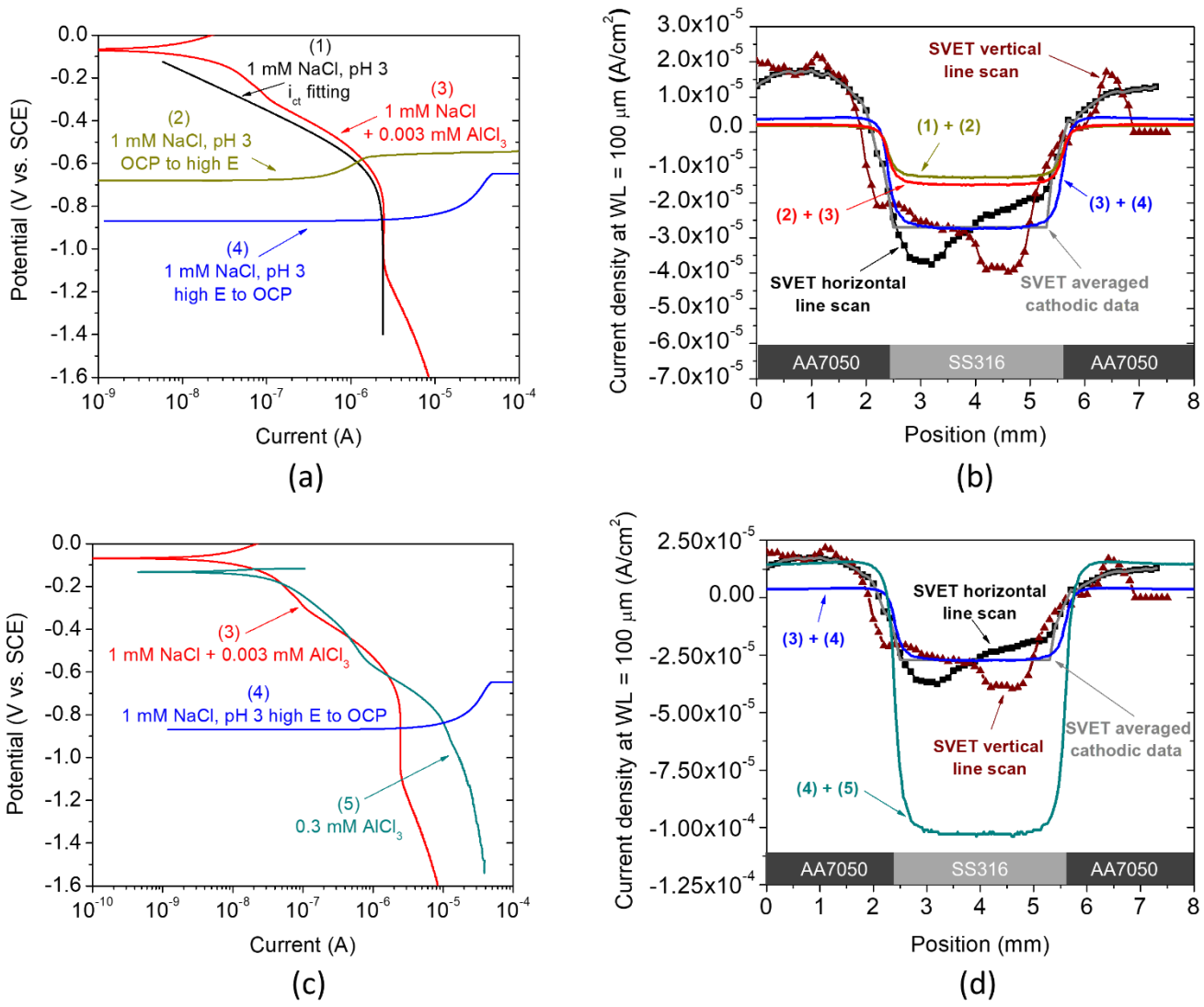

Figure 5.6. (a) and (c) Anodic and cathodic boundary conditions used within the model, scaled to correct for cathode:anode area differences, and (b) and (d) comparison of the SVET current density line profiles with 4 computational models, for pH 3 conditions. The current density line profiles were taken at a distance of 100 µm above the electrode surface, in each case. Numerical values in (b) and (d) represent the solutions in (a) and (c), with (1) = cathodic analytically-fitted charge transfer-controlled PDS on SS316 in 1 mM NaCl at pH 3, (2) = anodic PDS on AA7050 in 1 mM NaCl at pH 3 scanned in the positive direction from the OCP to high E, (3) = cathodic PDS on SS316 in 1 mM NaCl + 0.003 mM $AlCl_3$, (4) = anodic PDS on AA7050 in 1 mM NaCl at pH 3 scanned in the negative direction from high E to the OCP, (5) = cathodic PDS on SS316 in 0.3 mM $AlCl_3$.

In the first model scenario tested ((1) and (2) in Figure 5.6a), the cathodic kinetics on SS316 were implemented using fitted charge transfer-controlled kinetics with a limiting current density ($i_{lim,3}$ = 30 μA/cm^2), as this approach provided better agreement with the SVET-derived data from the experiments performed in the pH 5.8 solution. That is, the coupled SS316 cathode and AA7050 anode within the SVET were assumed to behave exactly as described by the polarization of the individual materials in the same solution and pH but with an imposed limiting current density. The model underestimated both anodic and cathodic current densities (line (1) + (2) in Figure 5.6b). The anodic current densities were underestimated by almost one order of magnitude, whereas the cathodic current densities were ca. 30% lower than the averaged cathodic current density. The strikingly different results obtained from the calculations indicated that the boundary conditions implemented at the SS316 and AA7050 surfaces did not represent the kinetics of the coupled alloys after 24 h of exposure in the pH 3 solution. It was rationalized that the electrolyte chemistry after 24 h of exposure evolved due to the higher currents observed in the acidic solution; thus, the behavior of the alloys in the solution in which the SVET sample was initially exposed would not represent the kinetics after the 24 h exposure.

In an attempt to simulate a more representative electrolyte chemistry of the galvanic couple, new cathodic boundary conditions (scenario 2) were generated with a low concentration of Al^{3+} ((3) in Figure 5.6a). This modification was incorporated because the presence of Al^{3+} in the electrolyte (stemming from the oxidation of the AA7050 anode) could influence the electrochemical behavior of the SS316 cathode. However, the kinetics of the AA7050 anode were still assumed to behave as the conventional positive polarization of OCP to high E would predict (i.e., with a passive film present). Line (2) + (3) in Figure 5.6b shows the current density profile obtained when using this boundary condition, in comparison with the SVET-derived data. Utilizing faster cathodic kinetics in this modified model slightly increased the cathodic current densities; however, it still largely underestimated both the SVET-derived anodic and cathodic current densities.

Scenario 3 simulated a condition in which AA7050 was actively corroding, i.e., little to no passive film present. New anodic polarization scans were performed by starting the scan at a high

E and sweeping down to the OCP, as described previously ((4) in Figure 5.6a). The results are shown in Figure 5.6b (line (3) + (4)). The cathodic current densities calculated from the model correlated well to the averaged SVET-derived cathodic current densities. However, the anodic current densities were still underestimated. The total current density increased by a factor of 1.55, which is consistent with Mixed Potential Theory predictions (Figure 5.6a). Due to the smaller area, the current density on the SS316 is higher, so the 55% increase in the cathodic current density results in a higher increase than the anodic current density increase.

One last scenario was tested (scenario 4), in which the anodic kinetics were kept the same as the previous model in scenario 3 (i.e., where negative PDS were conducted from high E to the OCP), but the Al^{3+} concentration was increased on the cathodic boundaries from 0.003 mM $AlCl_3$ to 0.3 mM $AlCl_3$ ((5) in Figure 5.6c), to account for the increased dissolution of the AA7050 anode.

Evaluating the PDS data with both Al^{3+} concentrations, the higher Al^{3+} concentration resulted in faster cathodic kinetics (Figure 5.6c). This observation also translated to the model. Figure 5.6d shows line scans from the models using the two Al^{3+} concentrations as cathodic boundary conditions, in comparison to the SVET-derived data. The high Al^{3+} concentration resulted in anodic current densities that were in agreement with those measured with the SVET. However, the cathodic current densities were largely overestimated by approximately one order of magnitude.

5.4.6 Total Current Comparisons in pH 5.8 and pH 3 Environments

Although it was not possible to simulate the pitting events that occurred under pH 5.8 conditions with the modeling approach used in this work (Figure 5.4b), good comparisons were achieved when total currents were considered. Figure 5.7a compares the SVET-derived total currents with FEM results for pH 5.8 conditions assuming the horizontal line scan (with no apparent pitting events) was representative of the current distributions over the entire sample. The $i_{ct} + i_{lim}$ fitted kinetics slightly overestimated the total anodic and cathodic currents by 0.13 µA. However, the same boundary conditions largely underpredicted the experimental data when the total currents derived from the global sample were analyzed (Figure 5.7c).

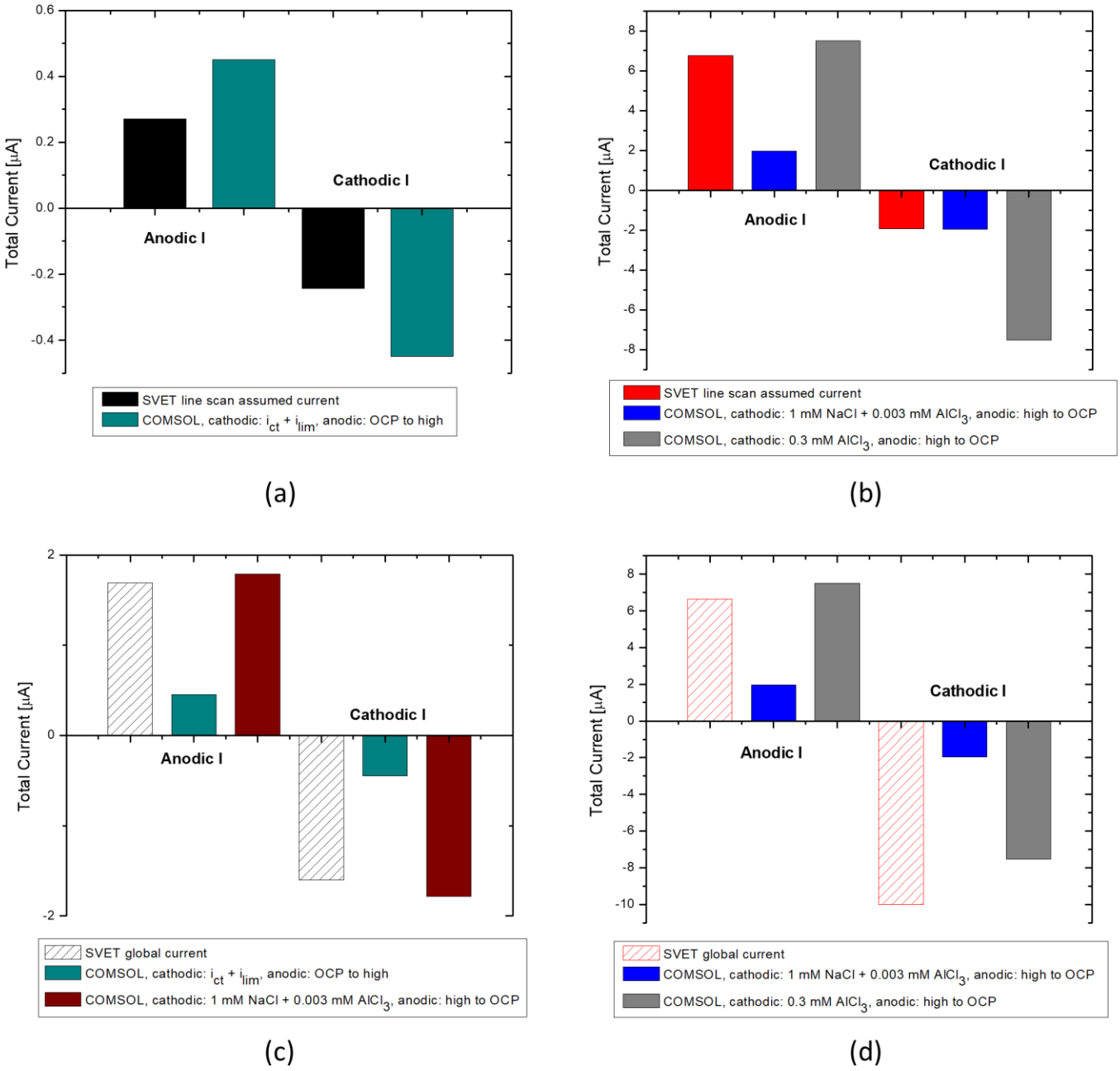

Figure 5.7. Computational and SVET-derived total currents assumed only from the line profiles under (a) pH 5.8 and (b) pH 3 conditions; area-averaged integrated total currents calculated over the entire AA7050-SS316 couple surface under (c) pH 5.8 and (d) pH 3 conditions. Both the computational and SVET-derived total currents in each pH case, were calculated from the current density distributions taken at a distance of 100 μm above the electrode surface.

To better represent the high currents from the localized corrosion, the boundary conditions simulating an actively pitting surface over the entire AA7050 surface (i.e., negative anodic PDS from high E to OCP) with release and transport of a low concentration of Al^{3+} to the bulk solution, including over the SS316 (cathodic scan with the addition of 0.003 mM Al^{3+}) were utilized. A better agreement was attained for total currents, with 3% error between the computational and total anodic currents and 8.5% error between the computational and total cathodic currents (Figure 5.7c). Note that the percent difference between the global anodic and cathodic currents from the SVET was 5.5%.

For the pH 3 environment line profiles, the experimental anodic and cathodic current densities could only be replicated with separate models taking into account the two concentrations of Al^{3+} as cathodic boundary conditions (Figure 5.6d). When the total current was calculated, assuming that the line scan was representative of the entire system, a similar trend was observed (Figure 5.7b). When the low Al^{3+} concentration boundary conditions were used, the *cathodic* currents from the computational results had 7% error relative to the SVET measurements, while the *anodic* current was underestimated by 71%. However, when the higher Al^{3+} concentration boundary conditions were used, the computational *anodic* current had only 11% error when compared with the SVET-derived data, while the computational *cathodic* currents largely overestimated the experimental work by 291% (Figure 5.7b).

However, looking instead at the globally calculated SVET currents, there was a reasonable agreement with the high Al^{3+} concentration model (Figure 5.7d). That is, the model simulated with the boundary conditions of scenario 4 presented a better agreement with the global SVET currents. The computational anodic currents had 13% error in comparison to the SVET global anodic currents, whereas the computational cathodic currents had 26% error.

5.5 Discussion

5.5.1 Macro-Galvanically-Driven Corrosion of AA7050 is Exacerbated in Acidic Conditions

The significant increase in SVET-derived j_z distributions over the surface of the AA7050-SS316 couple when fully immersed in pH 3 solution compared to those observed at pH 5.8 conditions was expected due to the detrimental effect of acidic pH on galvanic corrosion of Al alloys. On the uncoupled AA7050, pH 3 is shown to increase anodic kinetics relative to the case at pH 5.8 (Figure 5.2b). This adverse effect of low pH is attributed to the uniform dissolution of the native oxide film in acidic conditions compared to the more localized attack of the protective oxide film in (near) neutral conditions.[41–43] Coupling with SS316 exacerbates the attack on AA7050 because of the increased cathodic current available to sustain higher rates of Al dissolution (Figure 5.2a). The released Al^{3+} could transport from local anodic sites into the bulk solution, including over the SS316, leading to further increases in cathodic currents (Figure 5.2a). This phenomenon of Al^{3+} increasing cathodic kinetics on SS316 has been reported previously, and was determined to mainly impact the HER diffusion kinetics.[39,44] In the present work, this impact on the HER kinetics was evident on the cathodic scan carried out in 0.3 mM $AlCl_3$ (Figure 5.2a).

5.5.2 Choice of Computational Boundary Conditions to Best Represent Different Environments

Choosing boundary conditions within the model may seem as straightforward as conducting PDS in a replicate solution of the system of interest. However, this work has shown that there are two potential pitfalls that must be appreciated, 1) the time dependence of the PDS and 2) the effects of localized corrosion.

The PDS time-dependence was apparent during the cathodic scans. Although the model assumed steady-state, the PDS samples were exposed to the solution for 30 min at OCP with an additional 30 min of exposure during the scan, resulting in only 1 h of total exposure time. Therefore, the transient current wave was still observed (Figure 5.2a). The decay in current density during the potentiostatic hold (Figure 5.5) confirms that the cathodic current wave was a transient reaction that would not be present during longer times of exposure, such as with the 24 h SVET scan. Neglecting the cathodic current transient (i.e., using PDS + i_{lim}, and i_{ct} + i_{lim}

boundary conditions) led to a better comparison between the model and SVET line scans in the pH 5.8 environment (Figure 5.4b). Transient reactions may be present during a fast-scan polarization experiment; however, if the goal is to represent a steady-state system such as the SVET after 24 h, then careful evaluation of the PDS must be conducted to determine that no transient reactions are present.

In aggressive environments, such as acidic conditions, it is necessary to ensure that the computational boundary conditions for a steady-state model represent an actively corroding system. In the current system, this was accomplished by modifying both the anodic and cathodic boundary conditions.

As stated previously, an acidic environment breaks down the native passive film on Al alloys. However, the anodic PDS in pH 3 solution that was scanned conventionally from OCP to high E was not able to capture the kinetics of the active system measured with the SVET (Figure 5.6b). The reason could either be due to the short exposure time of the PDS when immersed in the acidic condition, thereby not allowing enough time for the passive film to dissolve, or due to the lack of extra polarization provided by the SS316 in the SVET galvanic couple. The latter is justified by the fact that the anodic polarization of AA7050, provided by galvanically coupling with the SS316, is greater in acidic conditions than in near-neutral conditions, as evident by the potential difference between the alloys (i.e., the driving force for galvanic coupling) in Figures 5.3e and 5.3f. Performing the anodic polarization scan starting at a high E to OCP artificially ensured that the entire surface was active and uninhibited corrosion could occur (Figure 5.2b).

Concerning the cathodic kinetics, it is expected that there would be an increase in the concentration of Al^{3+} due to the relatively high anodic kinetics and the stability of the Al^{3+} species at pH 3.[45] Because it has been observed that Al^{3+} increases the cathodic kinetics on SS316,[39,44] two new cathodic PDS were conducted on SS316 (Figure 5.6c). The low Al^{3+} concentration, containing 1 mM NaCl + 0.003 mM $AlCl_3$, was estimated by calculating the total anodic charge from the SVET-derived current density measurements after 24 h, and then using Faraday's law to calculate the total amount of Al^{3+} produced, assuming that the dissolution of the other alloying elements present in AA7050 (e.g., Zn, Mg) to be negligible. The higher concentration of Al^{3+}, 0.3

mM attained with only $AlCl_3$, was determined to be the maximum amount of Al^{3+} possible while keeping the chloride concentration consistent with the other scenarios.

In order to verify if the Al^{3+} concentrations chosen to perform the new boundary conditions were appropriate and to calculate the Al^{3+} concentration at the surface of SS316 and AA7050, the production and transport of Al^{3+} were calculated in the model that simulated the galvanic coupling in the pH 3 solution, using the activated AA7050 PDS. Figure 5.8 shows the simulated Al^{3+} concentration as a function of position and time. At the SS316 surface, the concentration ranged from 0.28 mM to 0.34 mM after 24 h. The method of calculating the Al^{3+} concentration by utilizing the total charge and dividing by the volume of the solution thereby underestimated the Al^{3+} concentration at the surface of SS316. It is noted that the model calculations were performed ignoring the convection caused by the vibration of the SVET probe. The forced convection decreases concentration gradients and homogenizes the solution. Thus, the concentration of the species at the electrode surface is also expected to change.

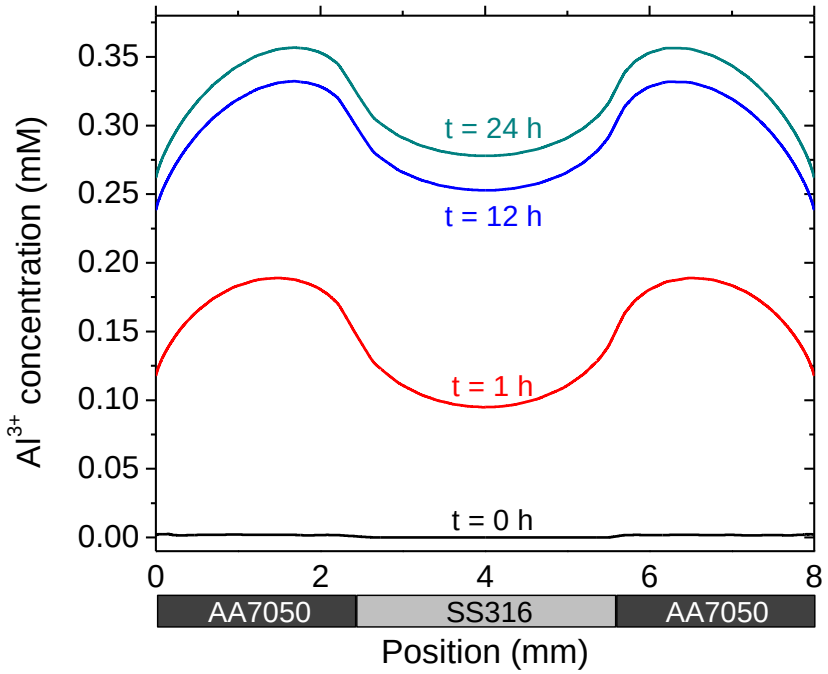

Figure 5.8. Simulated spatial distribution of the Al^{3+} concentration at different times at the centerline of the geometry.

It is also worth noting that the assumption that Na^+, Cl^-, and H^+ are the only species carrying current might not be valid after 24 h as the concentration of Al^{3+} increases to values of the same order of magnitude as Na^+, Cl^-, and H^+. Thus, under this condition, the Nernst-Planck equation approach must be invoked. To maintain electroneutrality, it is likely that an increase in the local Cl^- and OH^- concentration would occur to compensate for the additional positive charge originating from the Al^{3+} production. Additionally, if the supporting electrolyte assumption is no longer valid, then local changes in the conductivity of the solution should be taken into consideration.

5.5.3 Discrepancies Between Model Predictions and SVET Measurements

Both vertical and horizontal SVET-derived line profiles were compared with the model in order to capture a good representation of the localized processes occurring on the AA7050 surface. The simulated galvanic coupling under pH 3 conditions presented higher discrepancies compared to those simulated for pH 5.8 conditions, when using the $i_{ct} + i_{lim}$ boundary conditions (Figures 5.4b and 5.6b). Interestingly, the reverse situation was expected because the computational model, with the present homogenous assumptions, should better represent the case of pH 3 in which the oxide film was dissolved globally and more uniform corrosion was occurring, as opposed to the localized corrosion occurring in the pH 5.8 case. Furthermore, the SS316 cathodic current measured potentiostatically at pH 3 varied throughout the 24-h test, indicating that steady-state was not achieved (Figure 5.5), in contrast to the present assumption of a steady-state model. Considering the stability of the current measured by the potentiostatic hold at pH 5.8 and the relatively good comparison with computational results, it is conceivable that the system at pH 3 may not have reached steady-state within 24 h.

When quantifying the difference between the SVET and FEM calculated total currents, the percent error between the anodic and cathodic values was often asymmetric, which can be attributed to an asymmetry in the experimental anodic and cathodic currents. Within the model, the anodic and cathodic currents must be equal to preserve the conservation of charge. However, as visible in Figure 5.7b, the total anodic and cathodic currents obtained experimentally at pH 3 were not equal, with 111% difference (i.e., 4.8 μA). This situation would therefore be impossible

for a singular model to capture, because the computational currents *have to be equal*. Speculations as to possible causes of the lack of electroneutrality in the experimental measurements are discussed in a later section.

Comparing the globally calculated total current over the entire sample, the experimental difference between anodic and cathodic currents was much lower (41%, 3.5 μA). Using boundary conditions with the high Al^{3+} concentration resulted in the best comparison with the experimental values (Figure 5.7d). Notably, the high concentration of Al^{3+} was also predicted to occur based on local flux predictions of the model (Figure 5.8).

It is suggested that another source of the discrepancies observed between the model predictions and the SVET measurements is the inhomogeneities of the anodic and cathodic kinetics of AA7050 and SS316 due to surface heterogeneity and/or changes in local chemistry. Indeed, the analysis of the current density maps in Figures 5.3a and 5.3b shows that the distributions are non-uniform. Localized "hot spots" of current density can be seen from the SVET in pH 5.8, where pits grew while the remaining AA7050 surface was either passive or catalytic to cathodic reactions (Figure 5.3a). In the pH 3 case, there were regions with significantly decreased anodic activities over the top half of the sample surface (Figure 5.3b). These regions with lower current densities might correspond to locations with precipitated corrosion products. Such regions could include locations immediately adjacent to cathodic areas, where the local pH could be considerably higher. As a result, the bulk of the cathodic current that the SS316 supplies may support rapid dissolution of the remaining active areas on the AA7050.

Such localized distributions are not captured in the model, as the polarization scans performed on AA7050 represent averaged kinetics of the intermetallic particles and the matrix weight by their activity and area fractions. Thus, within the model, AA7050 was assumed to be homogeneous with the entire panel actively corroding. On a macroscale, this assumption is generally valid as the local cathodic and anodic regions average out, as noted when comparing the global total currents (Figure 5.7c and 5.7d). One method of manually accounting for the local variations was conducted in the pH 3 horizontal line scan, where the cathodic currents were averaged to provide a better comparison with the homogenous model (Figure 5.6b). The peak

cathodic current between the modeled scenario 3 and the averaged cathodic kinetics had 1% difference between them (Figure 5.6b).

The observations discussed above highlight the experimental complexities of non-steady-state, lack of charge conservation, and inhomogeneities in electrode surface conditions and/or chemistry. These complexities may shed light on the inability of the model to correctly estimate both the cathodic and anodic current densities with the same boundary conditions. This observation may be important, especially in systems in which the increased electrochemical activity leads to significant changes in the local electrolyte chemistry, which in turn can locally affect the electrochemical behavior of the electrode. That is, one portion of the sample in the pH 3 environment may be undergoing different rates than an adjacent portion, due to local changes in the electrolyte or at the electrode surface, making it difficult to predict computationally. For such cases, transient models that take into account the evolving electrolyte chemistry and its effect on the electrochemical behavior of the alloys can improve the predictability of the computational approach.[36]

5.5.4 Advantages of Combining the SVET and Computational Techniques

The advantages of combining SVET with FEM approaches have been discussed in the literature, and both techniques have been combined to investigate the galvanic coupling behavior between dissimilar alloys.[16,24,26,27,29–32,46] As stated previously, the SVET tip herein measured the potential difference at 85 μm and 115 μm over the entire surface. This potential difference allows for the calculation of the ionic current density (Equation 5.1), which is assumed to be at an average distance of 100 μm from the sample surface. One important aspect of modeling is the ability to calculate the current density at the electrode/electrolyte interface and also at any point within the electrolyte. Thus, once validated, the models can be used to predict the current density at the electrode/electrolyte interface and better interpret the results obtained with SVET.

Recently, Saeedikhani et al.[24] compared SVET and modeling results performed on a scratched zinc-based coating applied to a steel substrate. Although a good agreement of

electrolyte current density above the surface was observed between SVET and FEM, the current density at the electrode/electrolyte was underpredicted, especially within the scribed region. One of the major sources of the discrepancy was due to the geometry of the specimen, as the distance between the SVET probe and the electrode surface almost doubled (from 150 to 270 μm) as it moved from the Zn-coated steel surface to the scribed bare steel. In this work, however, a planar geometry was used to measure the galvanic current densities between AA7050 and SS316. Thus, the SVET probe height from the electrode surface was constant across the sample. Any local variation between the electrolyte current density and the interface current density could then be isolated and attributed to a non-geometric effect.

Figure 5.9a shows the calculated electrolyte current densities in the pH 5.8 environment at four heights: z = 0 (at the electrode/electrolyte interface), z = 85 μm, z = 100 μm, z = 115 μm. At the center of the SS316 electrode (x = 4 mm), a difference in current density of ca. 10% was observed between z = 0 and z = 100 μm. The difference in current density from 85 μm to 115 μm above the surface, which were the minimum and maximum distance of the SVET tip, respectively, was calculated. The value was negligible at 0.22 $\mu A/cm^2$, in the context of currents discussed in this work, with the peak cathodic current in pH 5.8 being 6 $\mu A/cm^2$ (Figure 5.4b).

Figure 5.9b shows the absolute and percent difference between the current density at the electrode surface and the electrolyte current density calculated at a distance of 100 μm above the surface as a function of position. Near the interface between AA7050 and SS316, there is a significant increase (200%) in the difference between the currents. Conversely, far from the coupled interface, the current densities difference is ca. 10%. The variation in the percent difference can be understood by Figure 5.9a, in which the current density at the electrode surface follows a step function, with the current densities immediately changing from anodic to cathodic. In contrast, the current density at 100 μm above the surface is a continuous function.

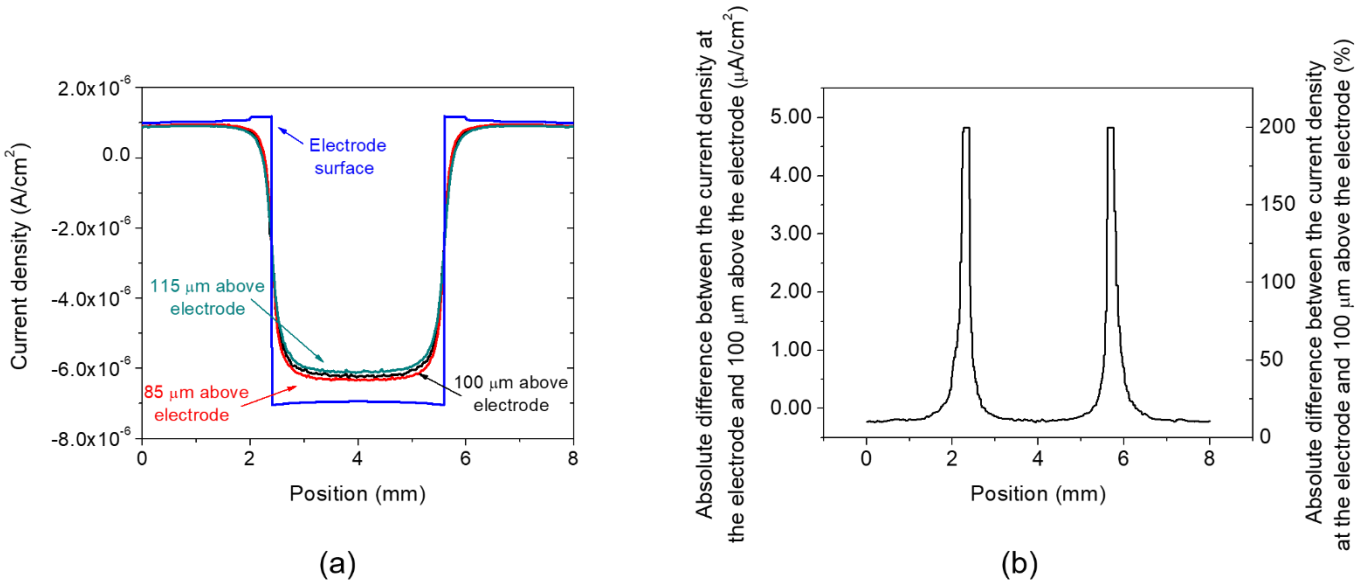

Figure 5.9. (a) Computationally-derived current densities along horizontal line scan at various distances from the electrode surface; (b) absolute and percent difference between current density at the electrode surface vs. at 100 μm above the electrode surface, as a function of the x-axis position.

Looking instead at the distance from the electrode surface in the z-direction, the current density magnitude was seen to decrease linearly with a slope of -70 A/m^3 (Figure 5.10a). At the position of x = 1 mm above the AA7050 surface, the slope was decreased to -10 A/m^3. The comparison of the two slopes above indicates that lower current densities, as observed above the anodic region, decrease the degree of variation of current density with position from the electrode surface, due to ohmic drop. Indeed, the ratio between the slopes is the same as the ratio between the current densities at the surface of the electrode. Practically, this result indicates that in systems with low overall current densities, the height of the SVET probe tip will not largely impact the results. However, in systems or locations with high current densities, the chosen height of the SVET probe tip can have a substantial effect on the measured results in comparison to the current densities occurring at the electrode surface.

This result is further demonstrated by the experimental data presented in Figure 5.10b, where the peak current was measured above a point current source with two applied current values over a range of SVET probe heights. The higher applied current ($i_{applied}$ = 25 μA) resulted in

a faster decrease in SVET-derived current density as a function of probe height, i.e., a steeper slope, in comparison to the lower applied current ($i_{applied}$ = 5 µA). These results validate what was observed computationally in Figure 10a. Furthermore, Murer et al.[26] and Demeter et al.[47] also observed this inverse correlation between current density magnitude and probe height, both experimentally and computationally. Therefore, it is recommended that the SVET be conducted at several probe heights, although it does not completely alleviate issues seen at the galvanic couple interface.

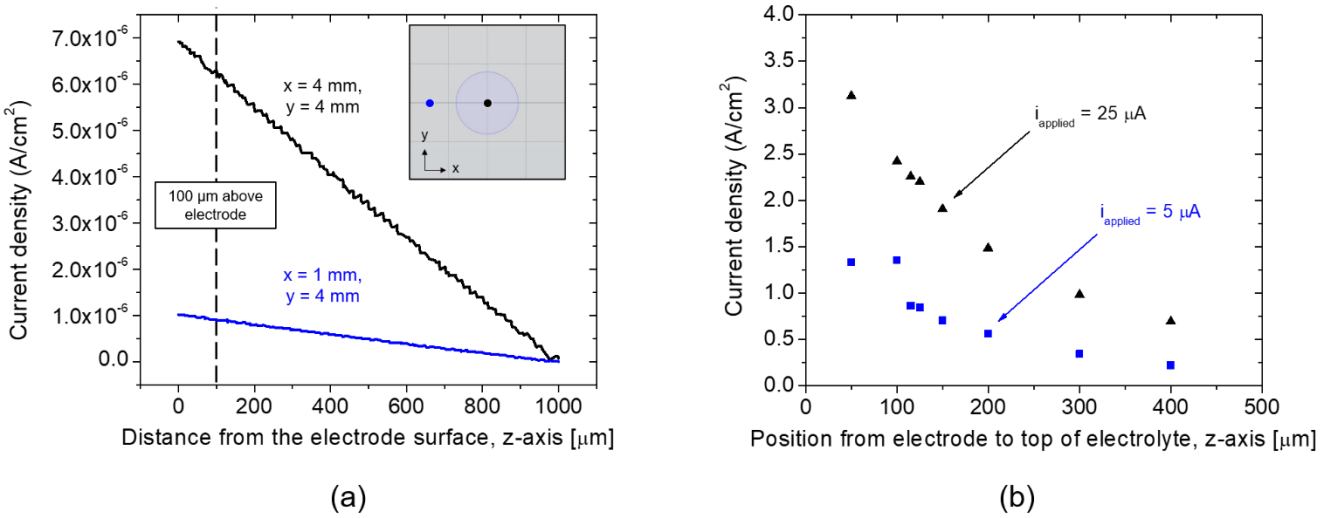

Figure 5.10. (a) Computationally-derived linear relationship of current density with distance from the electrode surface to the top of the electrolyte, along the z-axis; (b) SVET-derived point source data, with measured current density as a function of SVET probe height, with two applied current values. Inset in (a) represents the x-y view of sample surface, and the points chosen to measure current density along the z-axis.

Visualization of the current density vectors in a planar view can improve the understanding of the variations observed between the current density at the electrode surface and at a specified distance within the electrolyte above the anode/cathode interface. Figure 5.11a shows the electrolyte current density lines and the magnitude of the electrolyte current density in the z-direction, represented by a color gradient from a "slice" of the geometry in the x-z plane at the center of the geometry, and Figure 5.11b shows the ratio between the z-

component of the electrolyte current density and the magnitude of the electrolyte current density vector.

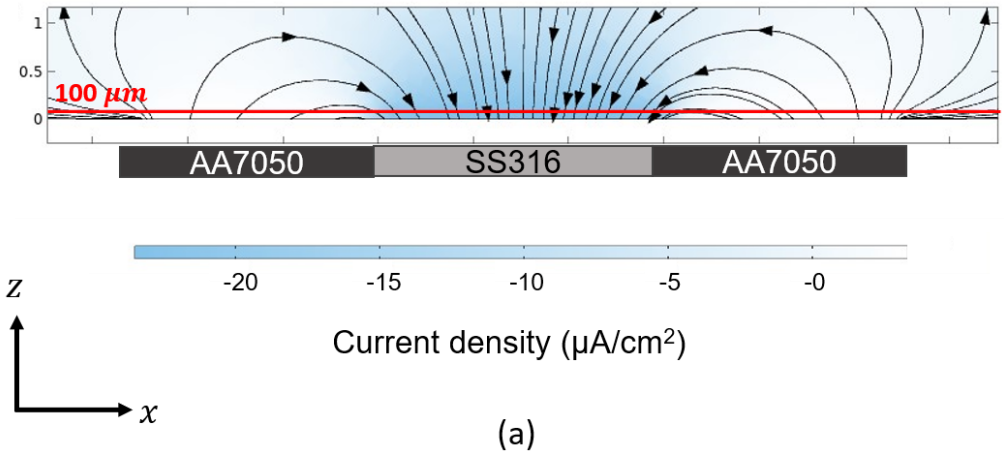

(a)

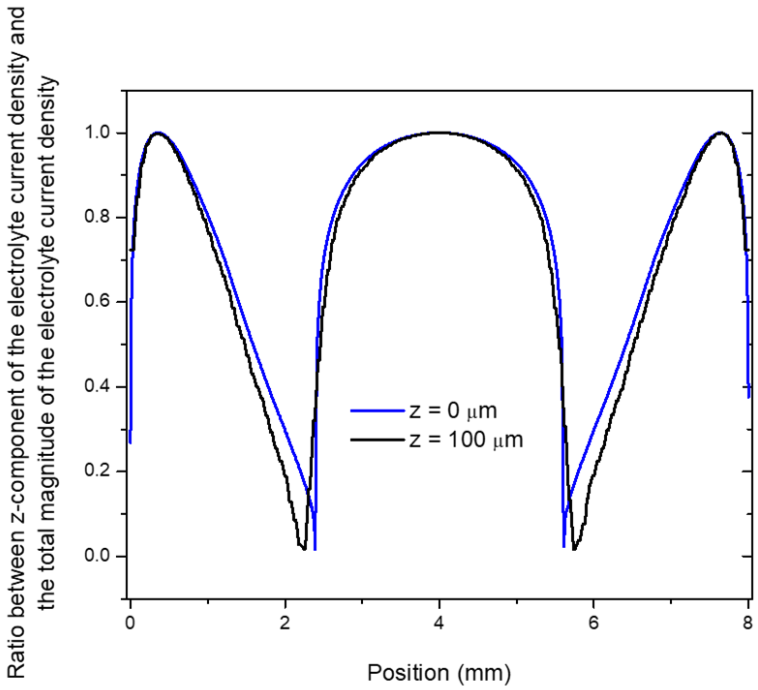

(b)

Figure 5.11. (a) Electrolyte current density lines and the magnitude of the electrolyte current density in the z-direction represented by a color gradient at the x-z plane at the center of the geometry. The red line indicates the distance between the SVET probe and the electrode used in this work; (b) ratio between the z-component of the current density and the magnitude of the current density vector at different electrolyte heights (0 and 100 μm).

Note that the simulation used to determine the current density vectors in Figure 5.11 was conducted in a geometry whose volume was equivalent to the volume of electrolyte used for the SVET experiments. Conventionally, computational works have kept the electrolyte *height* consistent with experimental conditions, but have not considered the effects of keeping the electrolyte *volume* the same.[24,26,28,31] This assumption does not affect the interface current densities, and it is computationally less expensive to mesh a smaller volumed domain. However, when considering current density in the electrolyte (i.e., above the electrode surface) or the concentration of ions, the volume of the electrolyte becomes more important. This distinguishing feature of the large-volume model can be seen by the current density vectors in Figure 5.11a, in that they continue past the edges of the galvanic couple.

As the SVET probe measures the potential difference between two points by oscillating in the z-direction, it is only able to "sense" the z-component of the electrolyte current density. As Figure 5.11a indicates, at regions further away from the boundary between the two electrodes (SS316 and AA7050) and from the edges of the AA7050 electrode, most of the magnitude of the current density vectors are composed by the z-component. However, near the boundary between the two electrodes and near the edges of the sample, the magnitude of the z-component of the electrolyte current density vector decreases significantly. As the probe moves closer to the surface, the z-component of the current density vector increases, consistent with the negative slope observation in Figure 5.10. Interestingly, as Figure 5.11b shows, the z-component of the current density is small near the edge of the galvanic couple and at the edge of the sample, even at z = 0 μm, indicating an intrinsic limitation of the SVET technique in capturing the current densities at such locations by measuring the potential difference only in the z-direction.

Two important conclusions can be drawn from this analysis. First, increasing the spatial resolution of the SVET by decreasing the step-size in the x- and y-directions would not improve the underestimation of the current density at the electrode surface, as the current density measurement losses are purely based on the limitation of the distance between the probe and the electrode surface and the assumption that all current is in the z-direction. Second, even at

locations very close to the surface, part of the current density would not be sensed, because of the direction of the current density vector near the galvanic couple and near the edges of the sample.

5.6 Limitations

5.6.1 Experimental Limitations

As mentioned previously, the choice of 1 mM NaCl used in this work was made based on the resolution limitations of the SVET. In real atmospheric environments, the NaCl concentration would be expected to equilibrate at ~ 600 mM at 98% relative humidity.[11] However, because the SVET signal-to-noise ratios decrease with increasing solution conductivity,[21] experiments conducted in 600 mM NaCl would be too noisy to allow extraction of any meaningful information. Therefore, with reasonable model validation with the SVET at low Cl^- concentrations, predictions could be made with the model for higher Cl^- concentration scenarios.

Another limitation with the SVET is the frequent mismatch of the area-averaged integrated total anodic and cathodic currents, especially in non-steady state systems, which drift and exhibit transient reactions.[18,23,48] At any instant in time, the total anodic and cathodic currents in reality are equal in magnitude, so that the net current equals zero. A general rule of thumb for the SVET to be able to avoid this situation is that the measurement time be much less than the periodicity of transients or the time frame of drifts. The error depends on the magnitude and area of the current transient relative to the steady-state current and area. Regarding another issue, for the couple geometry utilized in this work, there was a slight overestimation of the total cathodic current, particularly for the pH 3 case, most likely due to edge effects. That is, the SVET misses the anodic activity in the vicinity of the edges of the AA7050 surface but captures the cathodic activity occurring over the entire SS316 surface located at the center of the structure.

5.6.2 Computational Limitations

One shortcoming of the model is readily apparent through its prediction of homogenous current density distributions in Figures 5.3c and 5.3d, as opposed to the non-uniform distribution (with distance and time), which occurs experimentally (Figures 5.3a and 5.3b). Additionally,

because of the macroscale geometry in this work, the model cannot account for localized corrosion. Localized corrosion is an important form of corrosion that occurs on AA, especially when galvanically coupled with more noble alloys, such as SS, that can polarize the AA to potentials above critical potential thresholds for localized corrosion (e.g., pitting and repassivation potentials). It is acknowledged that in real service conditions, such localized hotspots as observed on the SVET-derived surface map for the pH 5.8 case may be important, as they could act as susceptible sites for fatigue crack nucleation.[49] Furthermore, the model is not able to capture the precipitation of any corrosion products, which may stifle the local anodic and cathodic reactions in some areas and cause a shift of those currents elsewhere. Notice that the white "halo" in the global current distributions is larger in the experimental maps than the computational model would predict (Figures 5.3b and 5.3d). As the locations closest to the anode/cathode interface should have the highest currents, it follows that the precipitation of corrosion products would also be greatest in this area, leading to a corresponding decrease in current at longer times. As the present model cannot yet account for the corrosion product formation, the white "halo" is underpredicted. Recent work in the literature have utilized FEM to investigate the effects of corrosion products on micro- and macro-galvanic corrosion.[36,50–52] Understanding the complex precipitation reactions and how they may contribute in stifling localized corrosion, is an area of future work. In addition, sites with copper replating could switch their behavior from anodic to cathodic, which was not accounted for in the present model.

5.7 Conclusions

The scanning vibrating electrode technique (SVET) was utilized to experimentally validate the applicability of finite element modeling (FEM) in simulating macro-galvanic-induced corrosion of AA7050 coupled to SS316. The SVET and FEM both provided local current density distributions, which were then compared. The discrepancy between the two techniques was traced to several sources. However, once the correct boundary conditions were used to validate the model, both techniques were able to enhance each other, thereby providing valuable information otherwise unachievable. In summary, the following findings are highlighted:

- Methods are proposed to generate anodic and cathodic boundary conditions to represent a macro-scaled galvanic couple between AA7050 and SS316, with localized corrosion present. One method of including the accelerated kinetics present during localized corrosion while still assuming a homogenous surface condition was based on performing the anodic scans starting at a high potential and decreasing it to OCP, in order to capture the behavior of a surface without the native oxide present. Furthermore, the addition of Al^{3+} in the cathodic polarization scans led to better agreement between the total currents calculated with the model and measured with SVET.
- Although the computational model was not able to capture the localized corrosion events (as seen especially in the less aggressive pH 5.8 scenario), the *total anodic currents* in the overall macro-scale geometry, through using boundary conditions generated with the methods above, were found to have less than 13% error when compared with the global SVET currents, in both pH environments.
- The AA7050-SS316 galvanic couple in near-neutral solutions reached steady-state within 24 h, making computational validation through SVET less complicated. Better agreements regarding macro-galvanic couple behavior were achieved in pH 5.8 environment compared to pH 3 environment. However, the FEM method was not able to address corrosion at specific locations on the AA7050 in the pH 5.8 scenario where corrosion was localized.
- Electrolyte current densities measured by vibrating probe methods at a distance of 100 µm from the electrode surface can be significantly different from the actual current density at the electrode surface, and the difference depends on the position above the galvanic coupled surface. It was predicted that there was a 10% difference at locations far away from the galvanic couple interface. At the vicinity between the two electrodes, the difference was as high as 200%, corresponding to ca. 5 $\mu A/cm^2$.
- The linear dependence of current density on the SVET probe height from the electrode surface was found to scale directly with the current density magnitude. This result indicated that the underestimation of the SVET-derived data from the current density at the electrode surface is dependent on both the z-position and the spatial location on the

galvanic couple and current density magnitude. That is, in systems or positions with high current densities or galvanic coupling currents, choosing the SVET probe tip height from the electrode surface can have a more significant impact on the results as opposed to lower current density systems, due to ohmic drop and the inability of the probe oscillation to capture components of the current that are parallel to the surface.

5.8 References

1. J. R. Davis, *Corrosion of Aluminum and Aluminum Alloys*, (1999).

2. D. Olson, T. Siewert, S. Liu, and G. Edwards, *ASM Handbook Vol 6: Welding, Brazing, and Soldering*, ASM International, New York, (1993).

3. U.-E. Charles-Granville, C. Liu, J. R. Scully, and R. G. Kelly, *J. Electrochem. Soc.*, **167**, 111507 (2020).

4. C. A. Matzdorf, W. C. Nickerson, B. C. Rincon Troconis, G. S. Frankel, L. Li, and R. G. Buchheit, *Corrosion*, **69**, 1240 (2013).

5. Z. Feng and G. S. Frankel, *Corrosion*, **70**, 95 (2014).

6. R. S. Marshall, R. Kelly, A. Goff, and C. Sprinkle, *Corrosion*, **75**, 1461 (2019).

7. R. S. Marshall, A. Goff, C. Sprinkle, A. Britos, and R. Kelly, *Corrosion*, **76**, 476 (2020).

8. A. Moran, J. Jennings, H. Nee, S. Pearson, B. Clark, and R. S. Lillard, *Corrosion*, **75**, 484 (2019).

9. V. Rafla, A. Davenport, and J. R. Scully, *Corrosion*, **71**, 1300 (2015).

10. V. N. Rafla, A. D. King, S. Glanvill, A. Davenport, and J. R. Scully, *Corrosion*, **74**, 5 (2018).

11. V. N. Rafla and J. R. Scully, *Corrosion*, **75**, 12 (2019).

12. W. J. Clark, J. D. Ramsey, R. L. McCreery, and G. S. Frankel, *J. Electrochem. Soc.*, **149**, B179 (2002).

13. Z. Feng, G. S. Frankel, W. H. Abbott, and C. A. Matzdorf, *Corrosion*, **72**, 342 (2016).

14. L. Shi, X. Yang, Y. Song, D. Liu, K. Dong, D. Shan, and E.-H. Han, *J. Mater. Sci. Technol.*, **35**, 1886 (2019).

15. V. N. Rafla, P. Khullar, R. G. Kelly, and J. R. Scully, *J. Electrochem. Soc.*, **165**, C562 (2018).

16. K. B. Deshpande, *Corros. Sci.*, **52**, 2819 (2010).

17. B. Kannan, C. F. Glover, H. N. McMurray, G. Williams, and J. R. Scully, *J. Electrochem. Soc.*,

165, C27 (2018).

18. L. B. Coelho and M. G. Olivier, *Corros. Sci.*, **136**, 292 (2018).

19. J. R. Kish, N. Birbilis, E. M. Mcnally, C. F. Glover, X. Zhang, J. R. Mcdermid, and G. Williams, *JOM*, **69**, 2335 (2017).

20. C. F. Glover, T. W. Cain, and J. R. Scully, *Corros. Sci.*, **149**, 195 (2019).

21. A. C. Bastos, M. C. Quevedo, O. V. Karavai, and M. G. S. Ferreira, *J. Electrochem. Soc.*, **164**, C973 (2017).

22. S. Fajardo, C. F. Glover, G. Williams, and G. S. Frankel, *Electrochim. Acta*, **212**, 510 (2016).

23. G. Williams and H. Neil McMurray, *J. Electrochem. Soc.*, **155**, C340 (2008).

24. M. Saeedikhani, K. X. Kuah, S. Wijesinghe, S. Vafakhah, and D. J. Blackwood, *J. Electrochem. Soc.*, **168**, 081505 (2021).

25. P. Atz Dick, G. H. Knörnschild, and L. F. P. Dick, *Corros. Sci.*, **114**, 28 (2017).

26. N. Murer, R. Oltra, B. Vuillemin, and O. Néel, *Corros. Sci.*, **52**, 130 (2010).

27. Z. Haque, B. A. Clark, and R. S. Lillard, *Corrosion*, **74**, 903 (2018).

28. K. B. Deshpande, *Corros. Sci.*, **52**, 3514 (2010).

29. F. Thébault, B. Vuillemin, R. Oltra, C. Allely, and K. Ogle, *Electrochim. Acta*, **82**, 349 (2012).

30. F. Thébault, B. Vuillemin, R. Oltra, C. Allely, and K. Ogle, *Corros. Sci.*, **53**, 201 (2011).

31. D. Snihirova, D. Höche, S. Lamaka, Z. Mir, T. Hack, and M. Zheludkevich, *Corros. Sci.*, **157**, 70 (2019).

32. O. Dolgikh, A.-S. Demeter, S. V. Lamaka, M. Taryba, A. C. Bastos, M. C. Quevedo, and J. Deconinck, *Electrochim. Acta*, **203**, 379 (2016).

33. C. Liu and R. G. Kelly, *Corrosion*, **75**, 1285 (2019).

34. N. Murer, N. A. Missert, and R. G. Buchheit, *J. Electrochem. Soc.*, **159**, C265 (2012).

35. H. Wang, F. Presuel, and R. G. Kelly, *Electrochim. Acta*, **49**, 239 (2004).

36. C. V. Moraes, R. J. Santucci, J. R. Scully, and R. G. Kelly, *J. Electrochem. Soc.*, **168**, 051505 (2021).

37. H. S. Isaacs, *Corros. Sci.*, **28**, 547 (1988).

38. S. Böhm, H. N. McMurray, S. M. Powell, and D. A. Worsley, *Electrochim. Acta*, **45**, 2165 (2000).

39. C. Liu, P. Khullar, and R. G. Kelly, *J. Electrochem. Soc.*, **166**, C153 (2019).

40. Z. Duan, C. Man, C. Dong, Z. Cui, D. Kong, L. Wang, and X. Wang, *Corros. Sci.*, **167**, 108520 (2020).

41. B. Zaid, D. Saidi, A. Benzaid, and S. Hadji, *Corros. Sci.*, **50**, 1841 (2008).

42. I. W. Huang, B. L. Hurley, F. Yang, and R. G. Buchheit, *Electrochim. Acta*, **199**, 242 (2016).

43. L. Yin, Y. Jin, C. Leygraf, and J. Pan, *J. Electrochem. Soc.*, **164**, C768 (2017).

44. U.-E. Charles-Granville, C. Glover, J. R. Scully, and R. Kelly, *J. Electrochem. Soc.* **168**, 121509 (2021).

45. E. Deltombe and M. Pourbaix, *Corrosion*, **14**, 16 (1958).

46. M. Saeedikhani and D. J. Blackwood, *Corros. Mater. Degrad.*, **1**, 273 (2020).

47. A. S. Demeter, O. Dolgikh, A. C. Bastos, D. Deconinck, S. Lamaka, V. Topa, and J. Deconinck, *Electrochim. Acta*, **127**, 45 (2014).

48. A. C. Bastos, M. C. Quevedo, and M. G. S. Ferreira, *Corros. Sci.*, **92**, 309 (2015).

49. N. E. C. Co and J. T. Burns, *Int. J. Fatigue*, **103**, 234 (2017).

50. T. Q. Ansari, J.-L. Luo, and S.-Q. Shi, *npj Mater. Degrad.*, **3**, 1 (2019).

51. M. Saeedikhani, N. V. Steen, S. Wijesinghe, S. Vafakhah, H. Terryn, and D. J. Blackwood, *J. Electrochem. Soc.*, **167**, 041503 (2020).

52. L. Yin, Y. Jin, C. Leygraf, and J. Pan, *Electrochim. Acta*, **192**, 310 (2016).

6. Galvanic Couple Behavior Between AA7050-T7451 and 316SS in Chromate-Containing NaCl Solutions Assessed with a Coupled Micro-Electrode Array Under Thick Electrolyte Film and Cyclic Wet-Dry Conditions

6.1 Abstract

The electrochemical behavior of an AA7050-316SS galvanic couple in chromate-containing NaCl environments under relatively constant thick films and wet-dry cycling was investigated utilizing the coupled micro-electrode array (CMEA) approach. The CMEA approach provided a means to analyze the in-situ electrochemical kinetics as a function of spatial location and time. In inhibitor-free environments, the total net anodic charge associated with galvanic current increased with increasing conductivity and aggressiveness of the environment, with AA7050 electrodes supplying more than half of the total net cathodic charge in relation to the 316SS electrodes in the more aggressive environments. Under thick films, chromate was less effective at suppressing cathodic kinetics on the 316SS and AA7050 net cathodes as chloride concentration increased. Under wet-dry cycling conditions, the effectiveness of chromate was diminished when compared to thick film conditions, due to the alternation in equilibrium chloride concentration as electrolyte thickness changed upon onset of drying and wetting. Furthermore, chromate exhibited a diminished ability to suppress cathodic currents on the AA7050 net cathodes in comparison to the 316SS electrodes. This study highlighted the importance of Cu-rich intermetallic particles and replated Cu on precipitation-strengthened Al alloys when considering the driving force of cathodes in sustaining anodic dissolution in typical Al alloy macro-galvanic systems exposed to atmospheric conditions.

6.2 Introduction

Precipitation-strengthened Al alloys (AA) such as AA7050-T7451 are commonly used in aerospace applications. AA7050-T7451 is particularly attractive because it retains its high strength, fracture and fatigue properties in larger and thicker sections, which offers the aerospace industry the advantage of minimizing the number of parts in new structures.[1] Unfortunately, these precipitation-strengthened AAs are susceptible to localized corrosion due

formation of micro-galvanic couples between the Al matrix and constituent (or intermetallic) particles as a result of their heterogeneous microstructure. These constituent particles can be anodic or cathodic to the Al matrix depending on their electrochemical characteristics relative to the Al matrix.[2,3] Reports in the literature have demonstrated that the Cu-rich intermetallic particles (IMPs) are the major facilitators of localized corrosion of precipitation-strengthened AAs in chloride-containing environments.[3-4] In the context of cathodic activity, these Cu-rich IMPs catalyze the fast oxygen reduction reaction (ORR) rates required to sustain anodic dissolution of the peripheral Al matrix and/or preferential dealloying of active elemental constituent(s) of the Cu-rich IMPs and subsequent electrodeposition of Cu on the surface.[3–6]

In aerospace applications, the AA structural components are commonly joined with high-strength noble fasteners, notably 316SS, as an alternative to welding due to challenges encountered during traditional welding of precipitation-strengthened AAs.[7] Although the structures are coated to mitigate galvanic-induced localized corrosion of the AA component, defects in these coating systems are inevitable during the operational and maintenance life cycles of the Al-based structures. When exposed to natural corrosive environments, including conditions of atmospheric exposure stemming from wet-dry cycling imposed by diurnal changes in temperature and relative humidity (RH), this situation would often create a macro-galvanic cell between the localized corrosion-susceptible base AA component and the 316SS, in which the AA component may be polarized above its pitting potential, resulting in greater localized corrosion than if there was no external 316SS cathode.[8–12] In this regard, inhibitor release, for instance chromate, from the coating system, and transport to the corroding site, would be crucial in mitigating the localized attack.

A number of studies have shown that macro-galvanic coupling can negatively impact chromate inhibition of these AAs.[9,10,13–15] It is noted that most of these studies were carried out on chromate-coated, scribed AA panels containing bare 316SS fasteners, where the 316SS fasteners were physically distant from any chromate that may have been released from the coating adjacent to the scribes. In addition, a measured concentration of chromate that might have leached out into the scribes was not reported. Recently (in Chapter 4), the scanning

vibrating electrode technique (SVET) was used to map and visualize the local current density distributions in-situ over the boldly exposed surface of an actual AA7050-316SS fastener couple, in comparison with uncoupled AA7050, where measured chromate concentrations were added to the test solutions, circumventing the leaching phase from a coating.[16] However, there were several limitations in this work that rendered the experimental conditions weakly relevant to the service conditions of aerospace structures. First, the resolution of the SVET, as regards the net reaction rate of the AA-SS system, restricted the choice of electrolyte to a low conductivity electrolyte (i.e., 0.001 M NaCl), because the signal-to-noise ratios decrease with increasing solution conductivity.[17] Experiments conducted on AA in higher conductivity electrolytes would be too noisy to allow extraction of any meaningful information. Second, the SVET setup is more favorable for conducting full immersion experiments, and so thin film measurements are difficult to achieve. Third, measurements are not taken at the electrode surface but at a specific height above the electrode surface, typically ~ 50-150 µm.[18–22] As such, the calculated currents are typically an underestimation of the actual values at the electrode surface.[17] Fourth, the use of a planar AA7050-316SS macro-couple configuration did not permit a clear discernment of the contributions of AA7050 and 316SS to the total cathodic currents, and there was a mismatch of the area-averaged integrated total anodic and cathodic currents.

The above-described limitations of the SVET can be surmounted with the use of coupled micro-electrode arrays (CMEAs). CMEAs permit access to real-service geometric configurations as well as the interrogation of in-situ local electrochemical processes occurring on individual micro-electrodes by mapping the local current density distributions as a function of spatial location and time. In the case of AA7050 for instance, one can monitor the transition of initial anodes to cathodes which would indicate dealloying of Cu-rich IMPs and/or Cu replating on the surface. Furthermore, in contrast to the SVET which is limited to full immersion studies, CMEAs offer an approach to assess thick and thin film measurements in more concentrated saline environments as well as wet-dry cycling in a controlled humidity and temperature chamber. In light of AA-SS systems, Rafla et al.[23,24] utilized the CMEA approach to investigate the galvanic current interactions on various AA7050-316SS fastener geometries under thick films and atmospheric conditions including wet-dry cycling. The present study will extend the work of Rafla

to investigate the ability of chromate to mitigate the adverse galvanic interactions on an AA7050-316SS macro-couple under thick films in comparison to conditions of wet-dry cycling in dilute and concentrated saline electrolytes. It is noted that the AA7050-316SS CMEA investigated in this work was constructed in a similar geometry to that used in the SVET experiments discussed in Chapter 4.

6.3 Experimental

6.3.1 Coupled Micro-Electrode Array Construction

The CMEA utilized in this work (as shown in Figure 6.1) was constructed using an AA7050 square panel (20 mm x 20 mm x 6.35 mm) with forty drilled holes of diameter 0.75 mm surrounding twenty-five drilled holes of diameter 0.375 mm. The aim was to simulate a galvanic couple with a flush mounted fastener mimicking the fastener in plate. The holes were spaced ~ 0.2 mm apart to ensure that electrical shorts were avoided. The holes were drilled in a square fashion covering an area of 6.45 mm x 6.45 mm in the center of the panel. The AA7050 wire (diameter 0.5 mm) drawing process was carried out by DOE Ames Laboratory. The AA7050 panel and wires were machined from 2" thick AA7050 plates obtained from ALCOA. The 316SS wires (diameter 0.25 mm, insulated with heavy polyamide) were obtained from California Fine Wire Company. The bare AA7050 wires were manually coated with insulating varnish prior to embedding the wires in the square panel using super glue. Care was taken to ensure that there were no electrical connections between the wires and the panel. The entire structure was thereafter encapsulated in epoxy. The area ratio of AA7050 to 316SS in the CMEA was ≈ 6:1. Immediately preceding each experiment, the CMEA was wet-ground successively from 120 grit to a surface finish of 1200 grit with SiC paper, rinsed with deionized water, and dried with clean compressed air. Table 6.1 shows the nominal composition of AA7050-T7451 and 316SS.

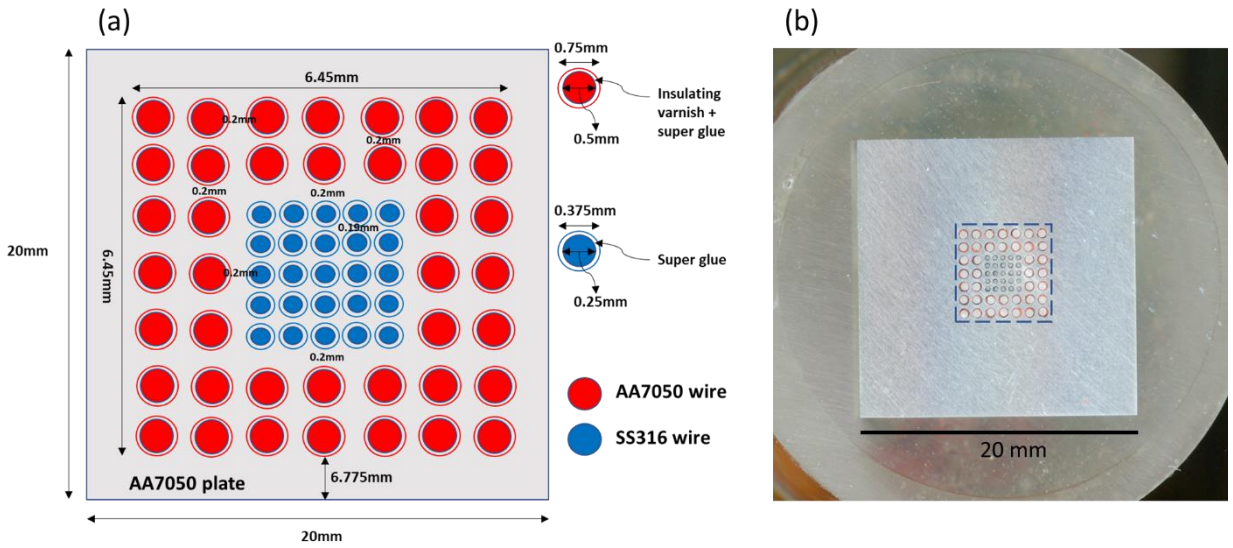

Figure 6.1. (a) Schematic and (b) scanned image of the AA7050-316SS CMEA utilized in this work. The area ratio of AA7050 to 316SS in the CMEA was ≈ 6:1. Blue dashed box indicates the area exposed to electrolyte during the experiments.

Table 6.1. Nominal Composition of AA7050-T7451 and 316SS (in wt%).

AA7050	**Zn**	**Mg**	**Cu**	**Fe**	**Si**	**Zr**	**Mn**	**Ti**	**Cr**	**Al**	
	6.7	2.6	2.6	0.15	0.12	0.15	0.1	0.06	0.04	balance	
316SS	**C**	**Mn**	**P**	**S**	**Si**	**Ni**	**Mo**	**Cu**	**Cr**	**N**	**Fe**
	0.019	1.75	0.039	0.028	0.46	10.16	2.05	0.44	17.03	0.071	balance

6.3.2 Electrochemical Measurements

Experiments were conducted in a controlled Microclimate Temperature and Relative Humidity (RH) Chamber Model MCB 1.2 supplied by Cincinnati Sub-Zero Products, Inc. The RH chamber recorded RH and temperature data for every experiment. The duration of all experiments was 24 h. For the thick film conditions, the RH chamber was set to 98% RH or 80% RH in order to maintain an equilibrium NaCl concentration of 0.6 M or 5 M, respectively, with temperature kept constant at 25° C. Wet-dry cycle conditions involved cycling at 98% RH for 1 h and 30 % RH for 3 h for a total of six cycles, with an initial (i.e., starting) NaCl concentration of 0.6 M. Temperature was kept constant at 35° C. The temperature was elevated for the wet-dry cycle

conditions in order to stay within the optimal operating range of the RH chamber when cycling. Where indicated, concentrations of Na_2CrO_4 ranging from 10^{-4} M to 10^{-2} M were added to the base NaCl solutions. Prior to each experiment, thick electrolyte films were placed on the CMEA using a 6 mm thick square plexiglass with a center cutout (~ 7 mm x 7 mm) glued and aligned to confine the electrolyte to the wires. Utilizing the plexiglass in this manner ensured that each wire electrode was exposed to approximately an equivalent electrolyte layer thickness with no edge effects. Select experiments were repeated to ensure reproducibility and the total net anodic charge had a percent error within ± 10%. It is noted that a smaller electrode may present more variability in results; in the case of AA7050, there is no control on which electrode may be an anode or cathode due to the heterogeneous distribution of constituent particles.[24]

The CMEA was connected via ribbon cables to a Scribner Associates Inc. model 910B multi-channel micro-electrode analyzer (MMA) used to collect data on the wires. The MMA galvanically couples each micro-electrode via a zero-resistance ammeter (ZRA) with a measurable current range of 3.3 nA to 100 µA per channel. The MMA software allows for a user-selective real-time color display of a matrix of electrode currents as a function of spatial position on a sample surface. In each current map, red indicates an anodic current (i.e., net positive) and blue indicates a cathodic current (i.e., net negative). A white color indicates freely corroding conditions (i.e., where anodic current equals cathodic current - under circumstances such as when anodes and cathodes are present on one electrode or when an electrode is too far away to galvanically couple and ohmic drop places electrode close to its open circuit potential) where the net current is zero. In this study, the data acquisition rate was one point per second.

6.4 Results

6.4.1 Galvanic Current Interactions Between AA7050 and 316SS in 0.6 M NaCl Under Thick Electrolyte Film Conditions

Figure 6.2 displays the real-time current maps of the AA7050-316SS CMEA exposed to a relatively constant thick film of inhibitor-free 0.6 M NaCl solution at 98% RH and 25° C. The schematic on the left shows the configuration and wire labels on the maps to guide the reader. For example, electrode A1 is the first AA7050 wire at the upper left and S1 is the first 316SS wire.

For the duration of the experiment, it was observed that while a few of the AA7050 electrodes maintained a certain polarity whether anodic or cathodic or even just freely corroding, most of the electrodes often switched polarity sporadically. For instance, electrode A4 persisted as a strong anode until the current decayed at the end of the experiment. In contrast, electrode A37 started out as a weak anode, then transitioned to a strong cathode after 10 h, and finally switched to the strongest anode at the end of the experiment. In addition, there were no clear correlations of local AA7050 net anodes or cathodes as a function of position from the 316SS electrodes. It is also important to note the decay of currents with time. Towards the end of the experiment, majority of the AA7050 electrodes were freely corroding (i.e., net current = 0) while A35, A37, and A38 net anodes were being supported by the cathodic currents from the 316SS electrodes, particularly S1.

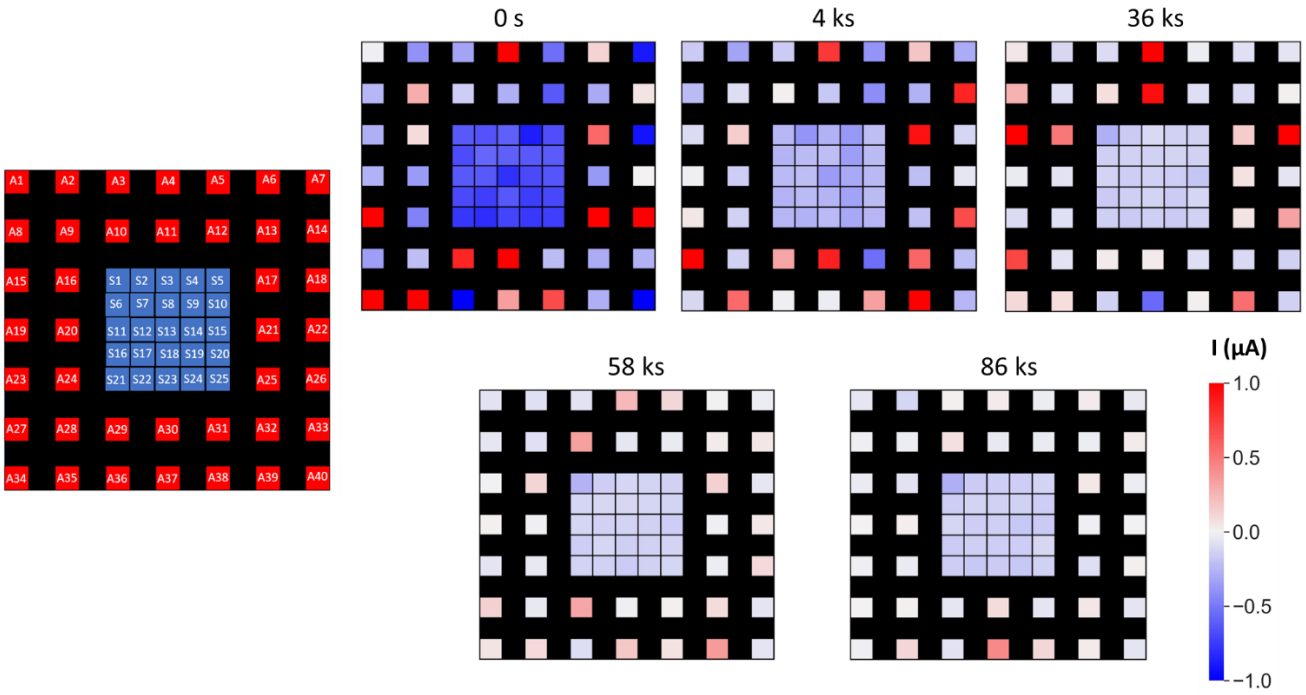

Figure 6.2. Current maps of the AA7050-316SS CMEA at various times over 24 h exposure under a thick film of 0.6 M NaCl solution at 98% RH and 25° C.

Figure 6.3 presents the corresponding ZRA net galvanic current density as a function of time on the individual electrodes. Transient events prevailed on the AA7050 electrodes as evident by the current spikes. The highest net anodic current density of 6.3 x 10^{-3} A/cm^2 was observed on A4 and the highest net cathodic current density of -1.12 x 10^{-2} A/cm^2 was observed on S13, both occurring at the beginning of the experiment. The total net anodic charge over the 24 h exposure was 0.523 C and the total net cathodic charge was -0.524 C. AA7050 electrodes contributed 33% of the total net cathodic charge.

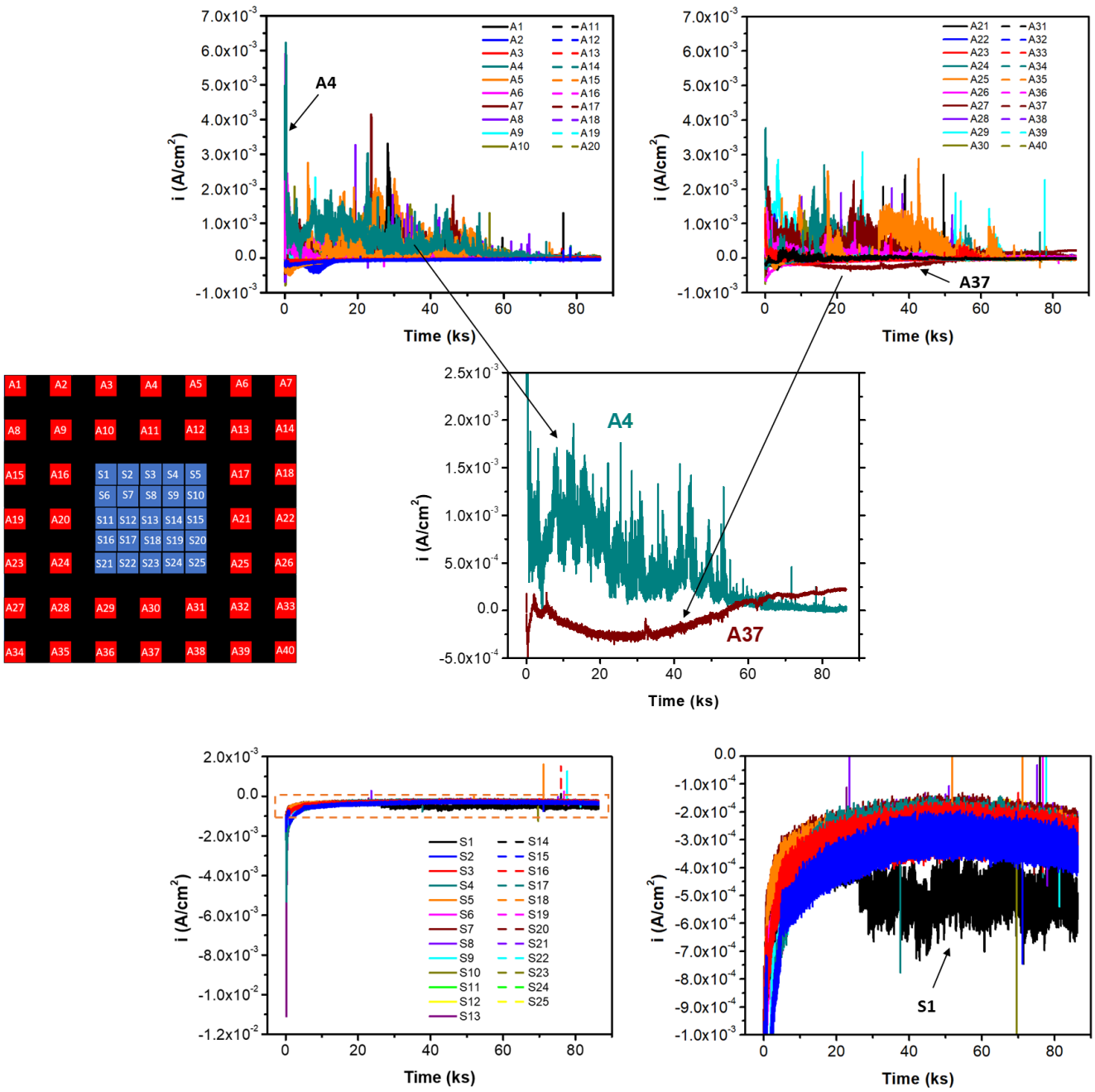

Figure 6.3. ZRA net galvanic current density as a function of time on the AA7050-316SS CMEA electrodes under a thick film of 0.6 M NaCl solution at 98% RH and 25° C. The bottom right plot zooms in the orange dashed region on the bottom left plot for the 316SS electrodes.

Figure 6.4 shows the optical micrographs of electrodes A3 and A4 after the 24 h ZRA exposure. As noted previously, A4 persisted as a net anode throughout the experiment while A3 was, for the most part, freely corroding for the duration of the experiment even though it initially started out as a weak cathode. The key point here was to showcase the difference in the surface morphology between a net anode and a freely corroding electrode. On inspection, it can be seen that the damage morphology on A4 was characterized by deep pits localized to the perimeter of the wire. On A3, there was barely any damage observed.

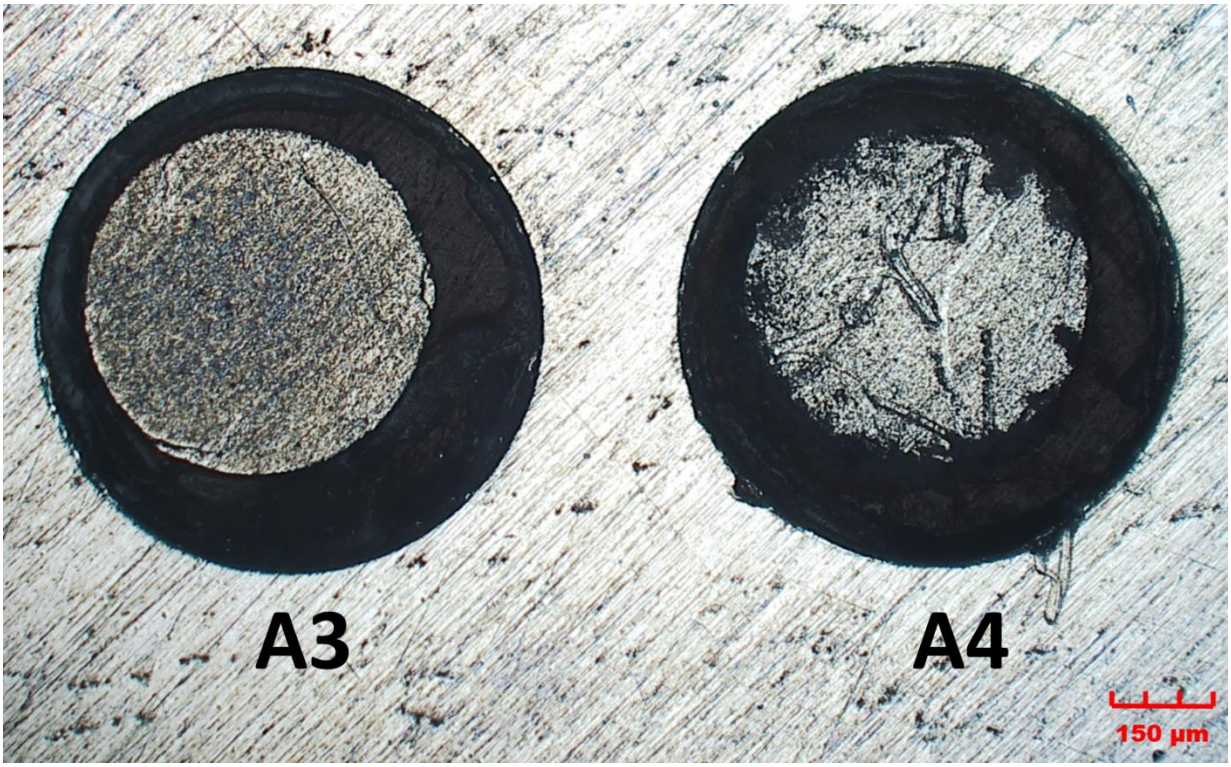

Figure 6.4. Optical micrographs of A3 and A4 electrodes after the ZRA exposure under a thick film of 0.6 M NaCl solution at 98% RH and 25° C.

Upon addition of 10^{-4} M chromate, currents were generally reduced on the electrodes (Figures 6.5 and 6.6). However, throughout the duration of the experiment, there appeared to be one dominant net anode, A37, and one dominant net 316SS cathode, S13. Electrode A37 accounted for about 60% of the total net anodic charge while S13 accounted for 10% of the total cathodic charge. The total net anodic and cathodic charges were 0.468 C and -0.469 C,

respectively, representing an overall 11% decrease in charge compared to the inhibitor-free case. In this 10^{-4} M chromate environment, AA7050 contributed 40% of the total net cathodic charge. It is noted that the magnitude of the cathodic charge contribution from AA7050 in this environment (i.e., -0.186 C) was higher than observed in the inhibitor-free case (i.e., -0.173 C). This result indicated that this low concentration of chromate had a minimal effect on AA7050 net cathodes. In contrast, the same concentration of chromate effected a 20% decrease in charge on the 316SS electrodes compared to the charge attained in inhibitor-free conditions.

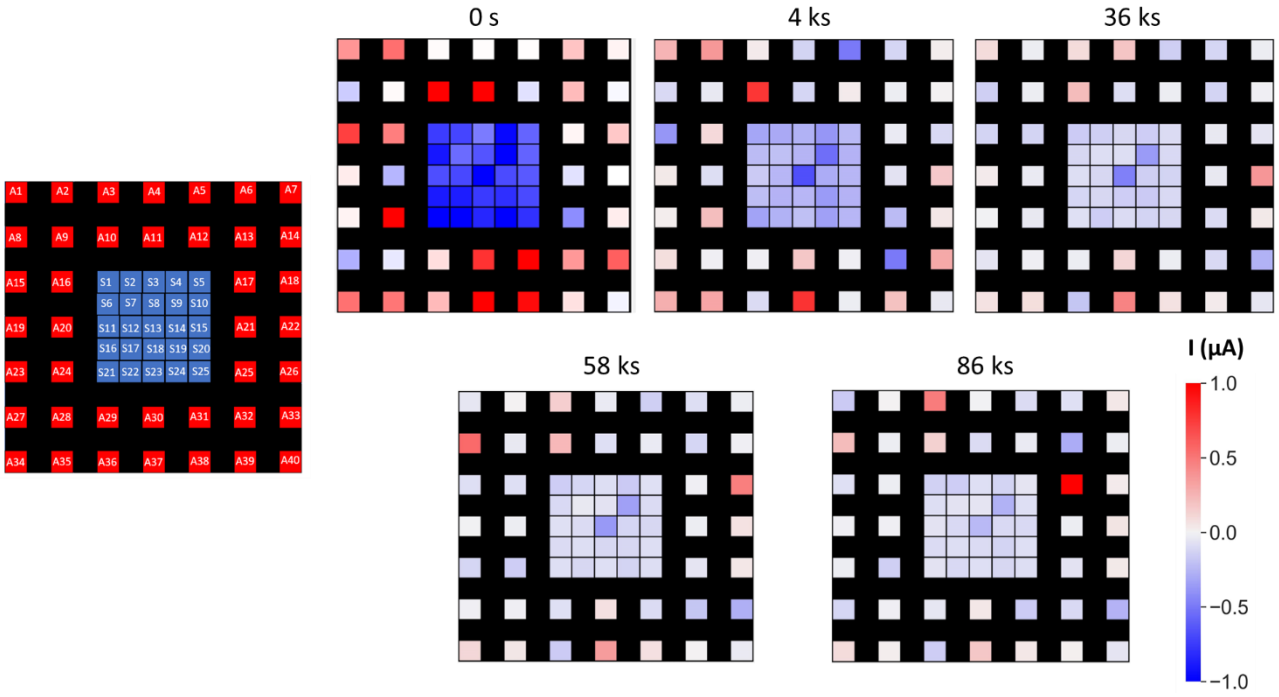

Figure 6.5. Current maps of the AA7050-316SS CMEA at various times over 24 h exposure under a thick film of 0.6 M NaCl solution with the addition of 10^{-4} M chromate at 98% RH and 25° C.

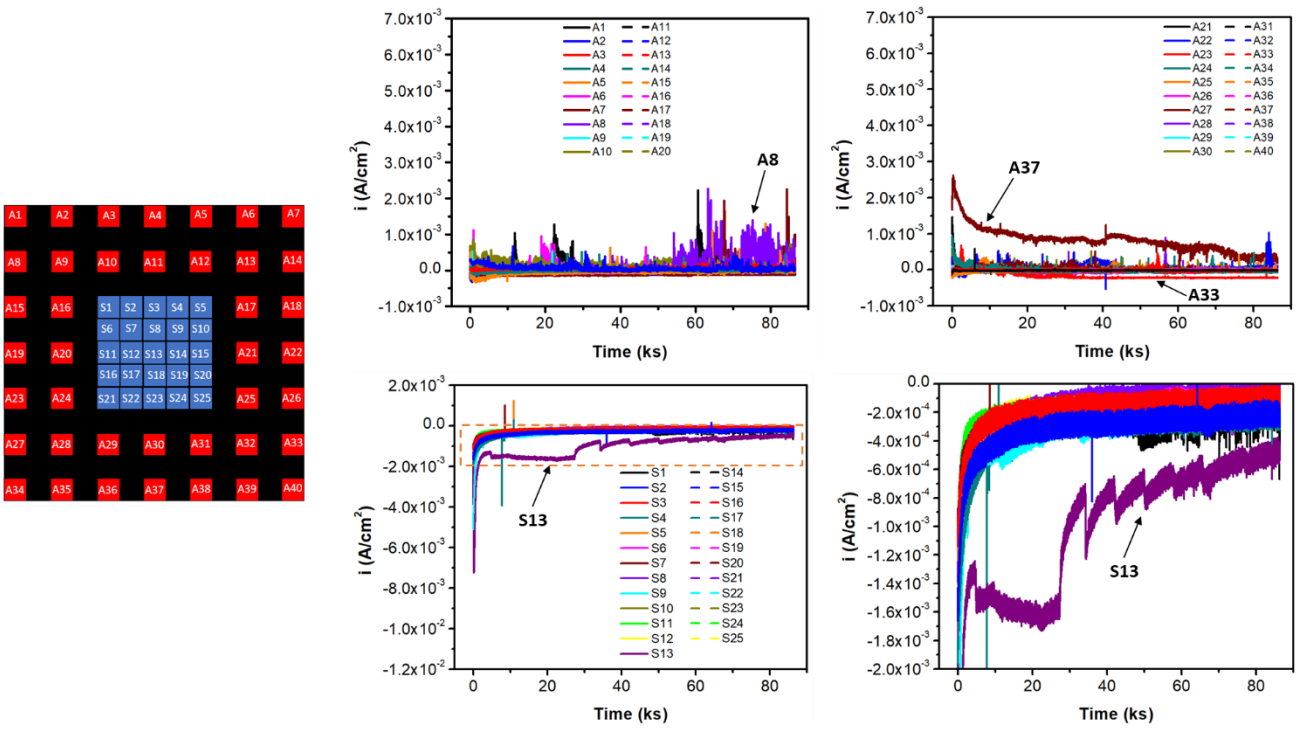

Figure 6.6. ZRA net galvanic current density as a function of time on the AA7050-316SS CMEA electrodes under a thick film of 0.6 M NaCl solution with the addition of 10^{-4} M chromate at 98% RH and 25° C. The bottom right plot zooms in the orange dashed region on the bottom left plot for the 316SS electrodes.

Upon increasing the chromate concentration to 10^{-2} M, currents were further reduced on the electrodes (Figures 6.7 and 6.8). Electrodes A12 and A34 persisted as dominant net anodes, albeit with lower current magnitude than observed on the net anodes in the environment containing a lower chromate concentration of 10^{-4} M. The total net anodic and cathodic charges were 0.316 C and -0.316 C, respectively, representing an overall 40% decrease in charge compared to the inhibitor-free case. In this 10^{-2} M chromate environment, AA7050 contributed 49% of the total net cathodic charge. That said, the magnitude of the charge was 10% and 16% lower than those observed in inhibitor-free and 10^{-4} M chromate environments, respectively. The cathodic charge contribution from the 316SS electrodes was reduced by 55% compared to the inhibitor-free case.

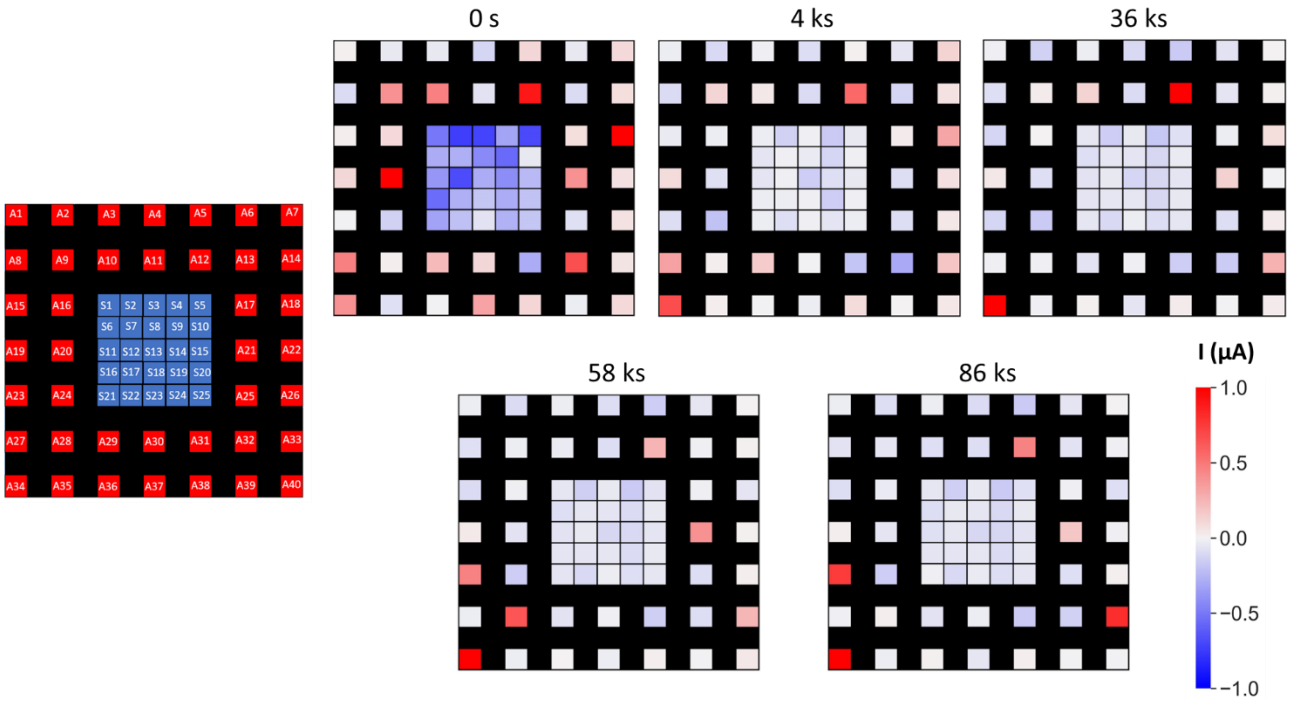

Figure 6.7. Current maps of the AA7050-316SS CMEA at various times over 24 h exposure under a thick film of 0.6 M NaCl solution with the addition of 10^{-2} M chromate at 98% RH and 25° C.

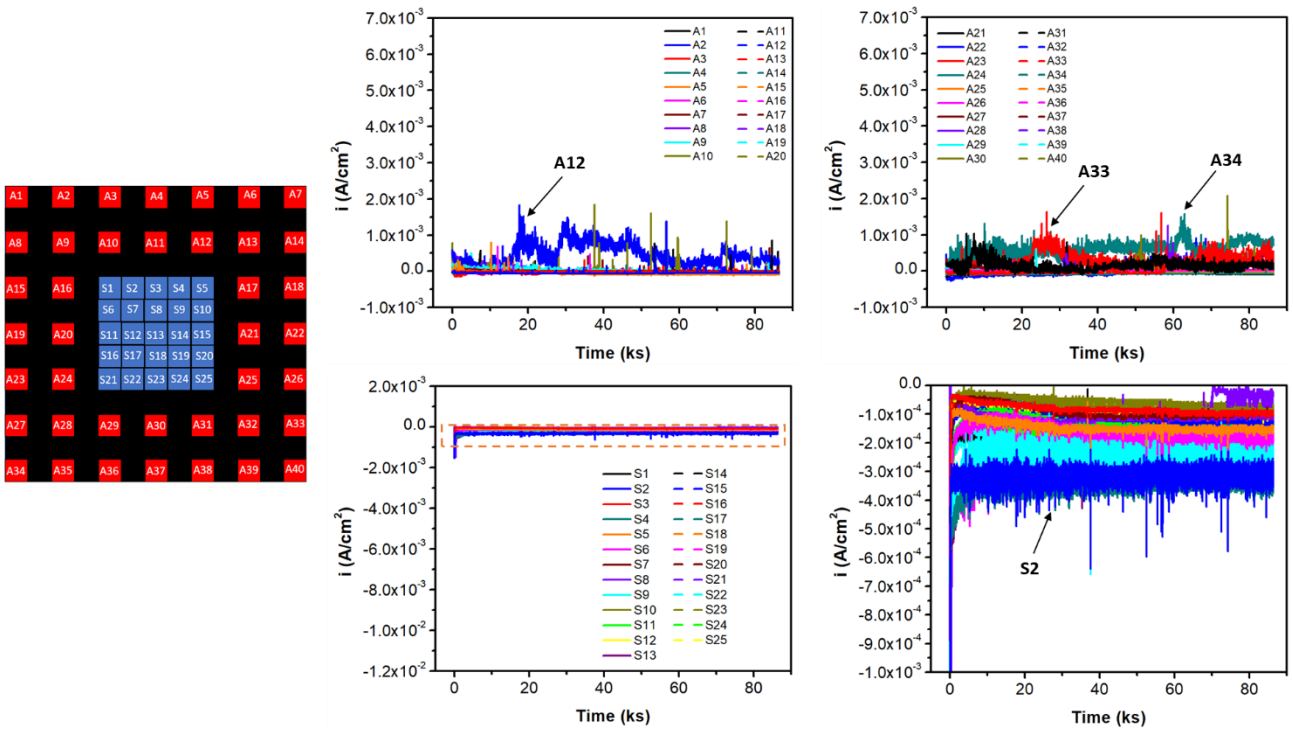

Figure 6.8. ZRA net galvanic current density as a function of time on the AA7050-316SS CMEA electrodes under a thick film of 0.6 M NaCl solution with the addition of 10^{-2} M chromate at 98% RH and 25° C. The bottom right plot zooms in the orange dashed region on the bottom left plot for the 316SS electrodes.

6.4.2 Galvanic Current Interactions Between AA7050 and 316SS in 5 M NaCl Under Thick Electrolyte Film Conditions

Figures 6.9 and 6.10 display the real-time current maps and the ZRA net galvanic current density as a function of time on individual electrodes, respectively, on the AA7050-316SS CMEA exposed to a relatively constant thick film of inhibitor-free 5 M NaCl solution at 80% RH and 25° C. On inspection of the current maps, as in 0.6 M NaCl, there were no clear correlations of local AA7050 net anodes or cathodes as a function of position from the 316SS electrodes. Instead, there were several AA7050 net cathodes, in addition to the 316SS electrodes, supporting a fewer number of AA7050 net anodes. In particular, A37 prevailed as a dominant cathode after 8 h, contributing 23% of the total net cathodic charge. The total net anodic charge over the 24 h exposure was 0.582 C and the total net cathodic charge was -0.583 C. This magnitude of charge in 5 M NaCl was 11% higher than observed in inhibitor-free 0.6 M NaCl. In addition, AA7050

electrodes contributed 56% of the total net cathodic charge. It is also important to note that in contrast to the 0.6 M NaCl environment, there was no apparent decay of currents with time in this case.

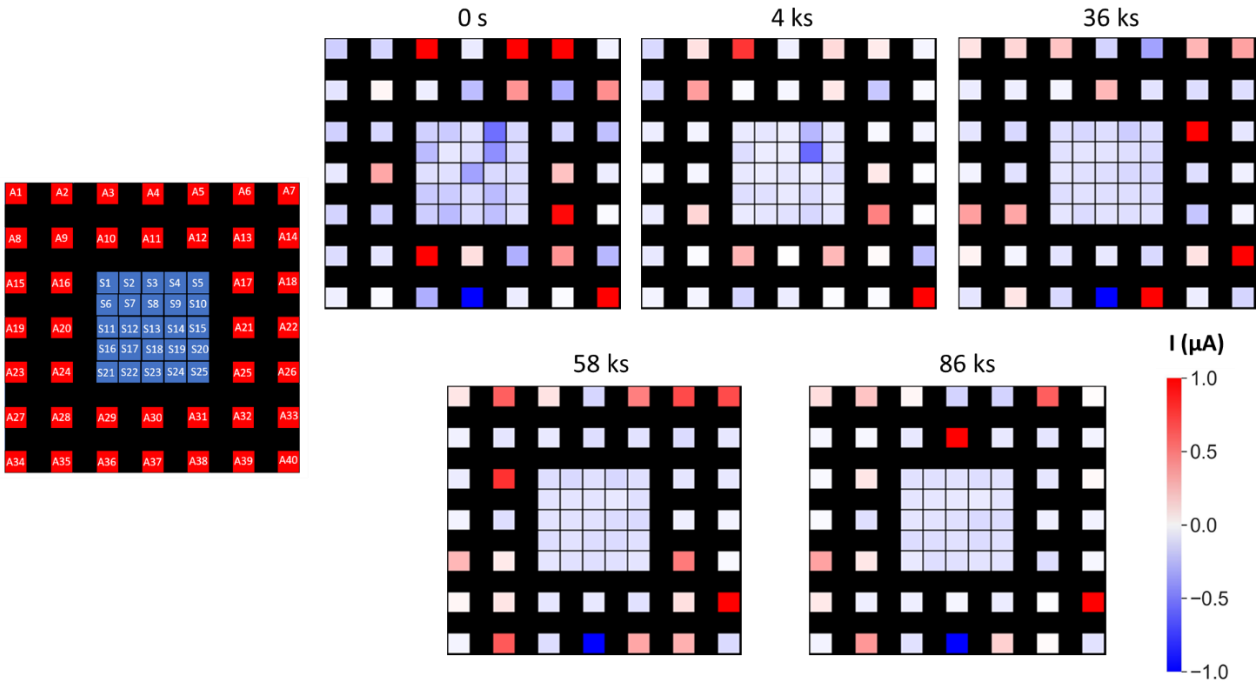

Figure 6.9. Current maps of the AA7050-316SS CMEA at various times over 24 h exposure under a thick film of 5 M NaCl solution at 80% RH and 25° C.

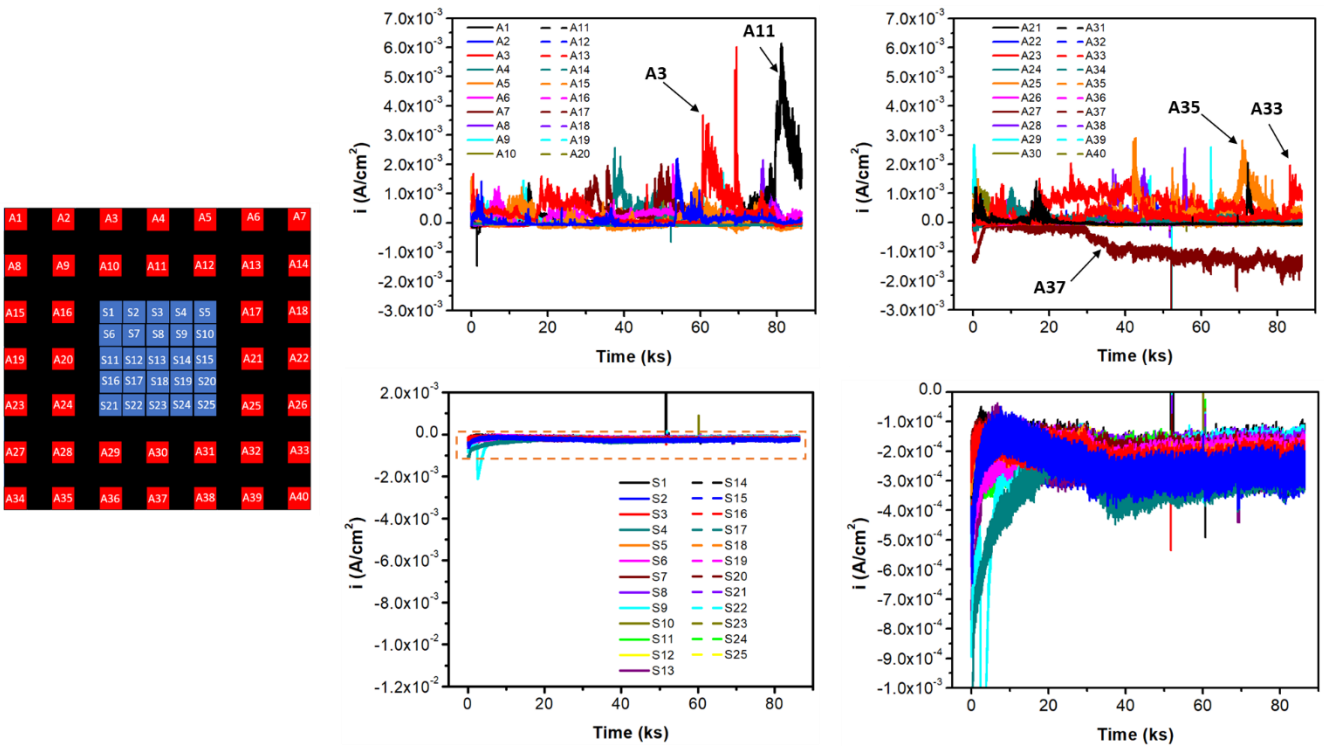

Figure 6.10. ZRA net galvanic current density as a function of time on the AA7050-316SS CMEA electrodes under a thick film of 5 M NaCl solution at 80% RH and 25° C. The bottom right plot zooms in the orange dashed region on the bottom left plot for the 316SS electrodes.

Upon addition of 10^{-4} M chromate, currents were generally suppressed on the electrodes (Figures 6.11 and 6.12). There were no significant dominant AA7050 net anodes or cathodes. The total net anodic and cathodic charges were 0.476 C and -0.476 C, respectively, representing an overall 18% decrease in charge compared to the inhibitor-free 5 M NaCl case. In this 10^{-4} M chromate environment, AA7050 contributed 55% of the total net cathodic charge. Interestingly, the magnitude of the AA7050 charge contribution was 19% lower than that observed in the inhibitor-free 5 M environment, in comparison to the case of 0.6 M NaCl where there was no suppression in AA7050 net cathodic charge upon addition of 10^{-4} M chromate. The cathodic charge contribution from the 316SS electrodes was reduced by 19% upon addition of 10^{-4} M chromate to 5 M NaCl compared to the inhibitor-free environment.

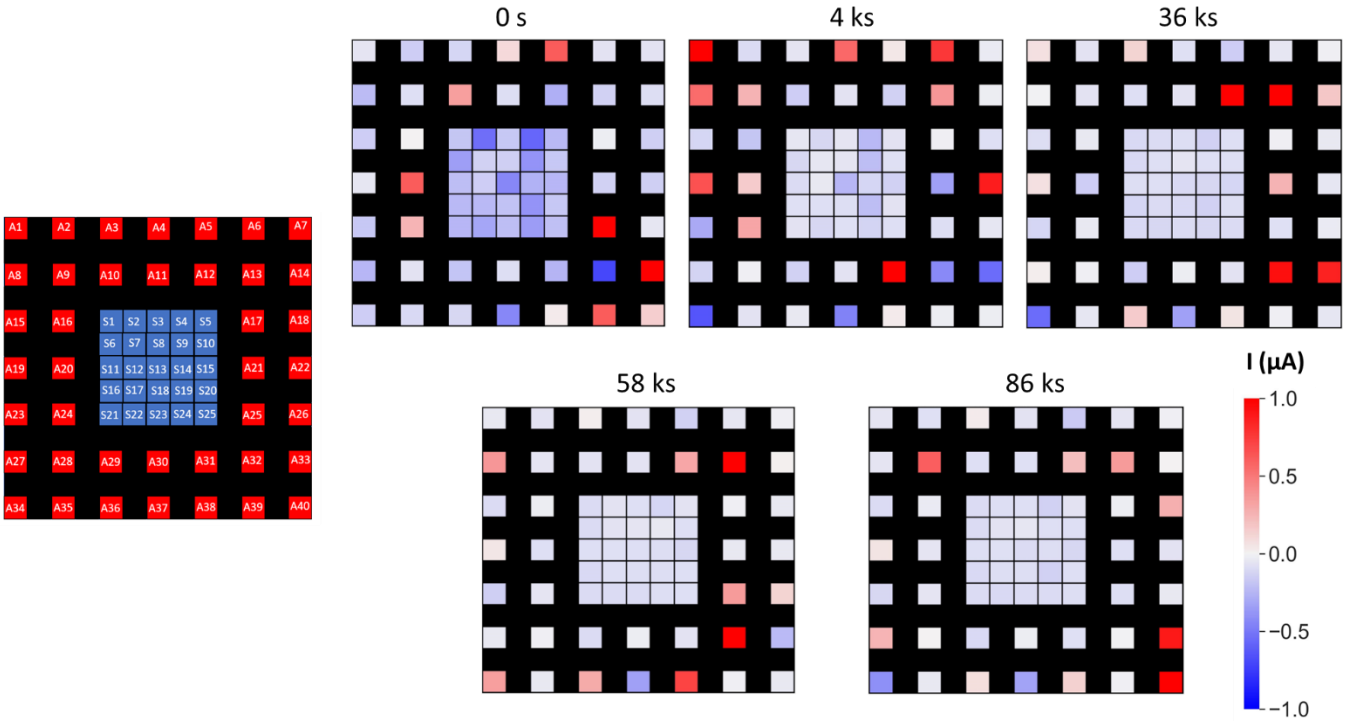

Figure 6.11. Current maps of the AA7050-316SS CMEA at various times over 24 h exposure under a thick film of 5 M NaCl solution with the addition of 10^{-4} M chromate at 80% RH and 25° C.

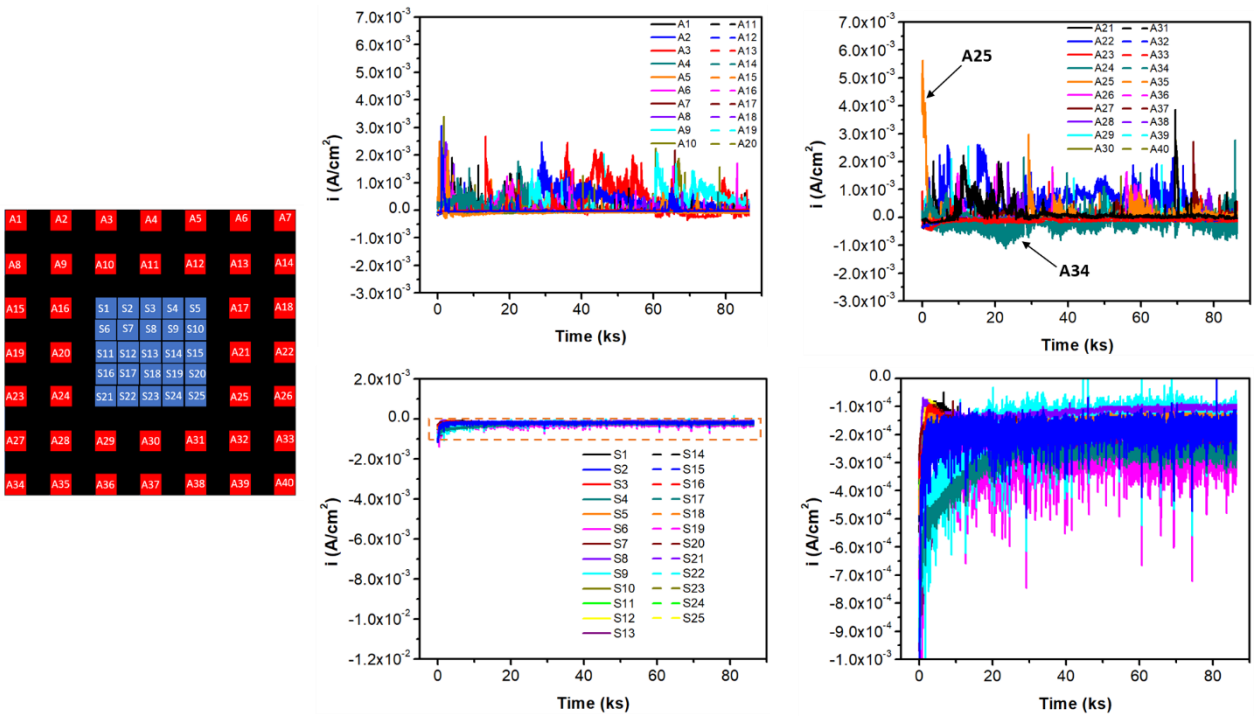

Figure 6.12. ZRA net galvanic current density as a function of time on the AA7050-316SS CMEA electrodes under a thick film of 5 M NaCl solution with the addition of 10^{-4} M chromate at 80% RH and 25° C. The bottom right plot zooms in the orange dashed region on the bottom left plot for the 316SS electrodes.

Currents were further suppressed upon increasing the chromate concentration to 10^{-2} M (Figures 6.13 and 6.14). Electrodes A29 and A34 persisted as dominant net anodes at different times during the exposure while A37 persisted as a net cathode throughout the duration of the experiment. A majority of the AA7050 electrodes appeared to be freely corroding at various time spans during the 24 h experimental period. The total net anodic and cathodic charges were 0.354 C and -0.353 C, respectively, representing an overall 39% decrease in charge compared to the inhibitor-free case. AA7050 contributed 52% of the total net cathodic charge. That said, the magnitude of the charge was 44% and 31% lower than those observed in the inhibitor-free and 10^{-4} M chromate environments, respectively. The cathodic charge contribution from the 316SS electrodes was reduced by 34% compared to the inhibitor-free case.

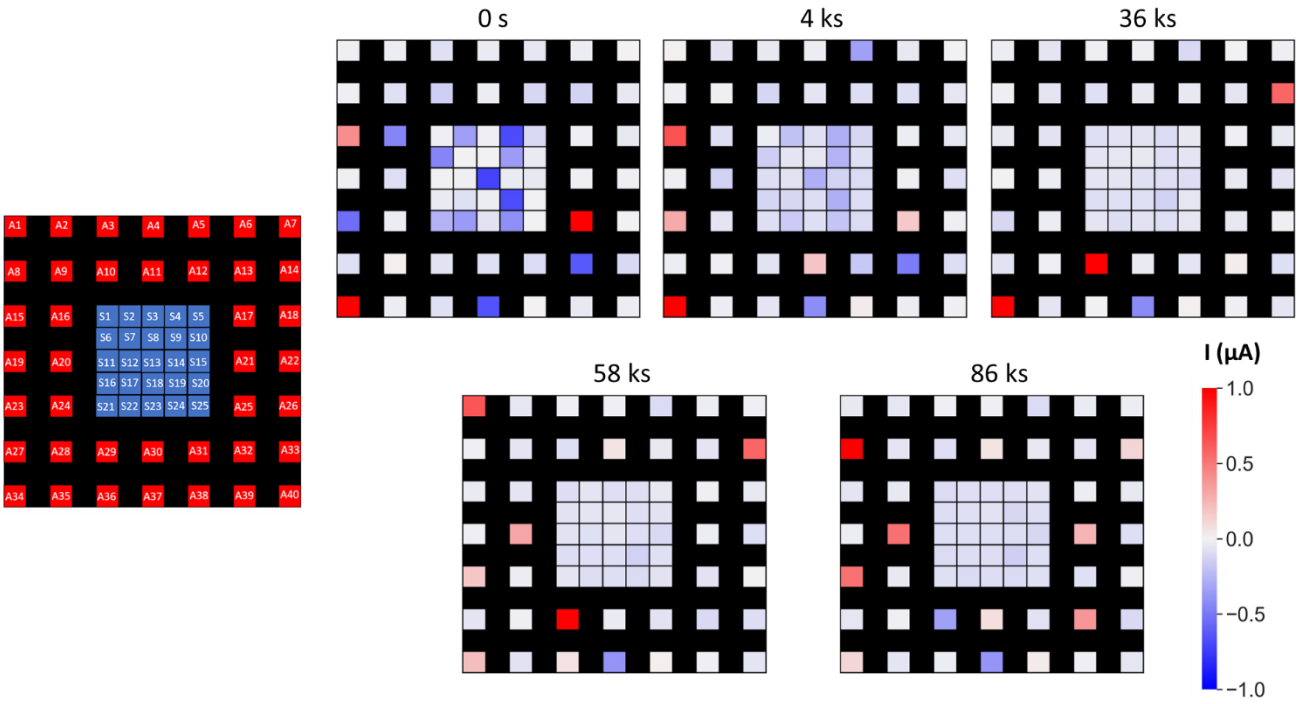

Figure 6.13. Current maps of the AA7050-316SS CMEA at various times over 24 h exposure under a thick film of 5 M NaCl solution with the addition of 10^{-2} M chromate at 80% RH and 25° C.

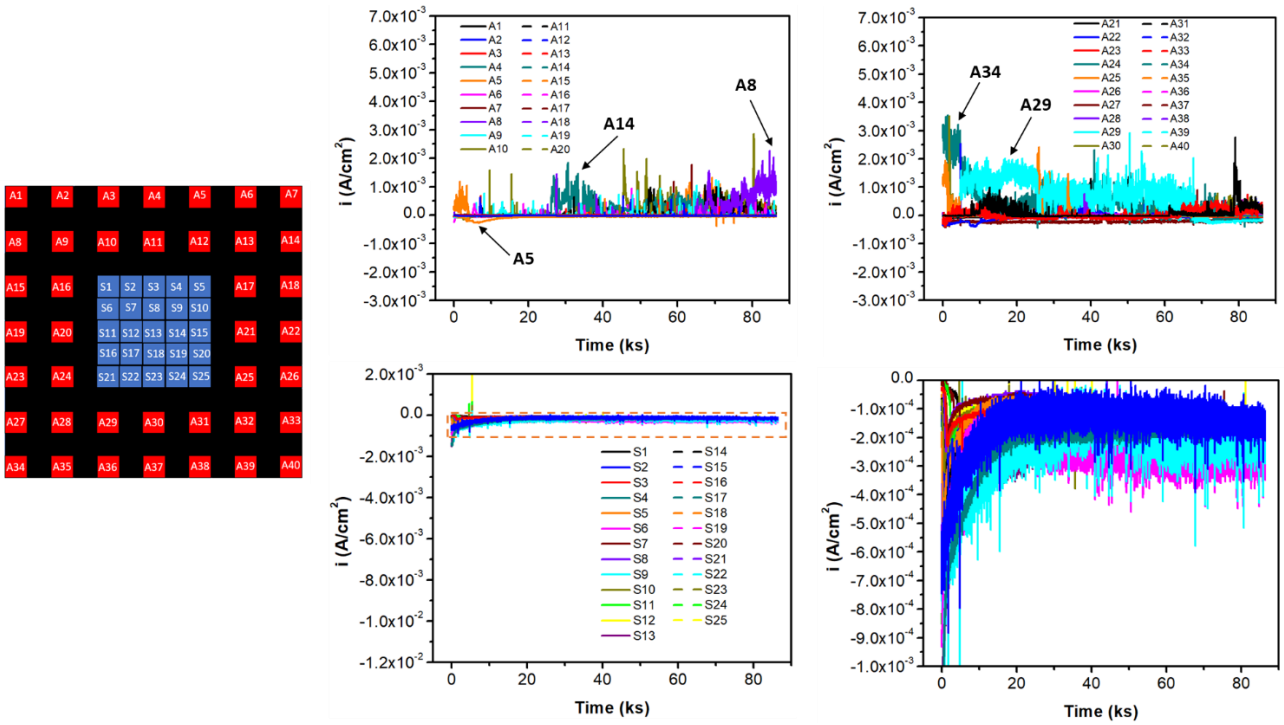

Figure 6.14. ZRA net galvanic current density as a function of time on the AA7050-316SS CMEA electrodes under a thick film of 5 M NaCl solution with the addition of 10^{-2} M chromate at 80% RH and 25° C. The bottom right plot zooms in the orange dashed region on the bottom left plot for the 316SS electrodes.

6.4.3 Galvanic Current Interactions Between AA7050 and 316SS in 0.6 M NaCl Under Wet-Dry Cycle Conditions

Figures 6.15 and 6.16 display the real-time current maps and the ZRA net galvanic current density as a function of time on individual electrodes, respectively, on the AA7050-316SS CMEA exposed to 24 h cyclic wet-dry conditions under a thick film of inhibitor-free 0.6 M NaCl solution at 35° C. Under cyclic wet-dry conditions, currents on the electrodes increased by up to an order of magnitude in comparison to those attained at constant thick film conditions. To put in context, wet periods include a completely wet period where the electrolyte layer is thick (i.e., at 98% RH), onset of drying where the electrolyte layer thins out (i.e., where the RH gradually ramps down from 98%), and onset of wetting where the electrolyte layer builds up (i.e., where the RH quickly ramps up to 98%). In this work, multiple test runs were carried out to determine the RH at which the surface was completely dry, and that value was determined to be ~ 40% RH. Current spikes

were prevalent during periods of onset of wetting and drying (Figure 6.16). The average net anodic charge per hour during a wet period was about 35% higher than observed during a dry period. The total net anodic and cathodic charges were 0.848 C and -0.847 C, respectively, representing an overall 62% increase in charge compared to the constant thick film case. AA7050 electrodes supplied 51% of the total net cathodic charge.

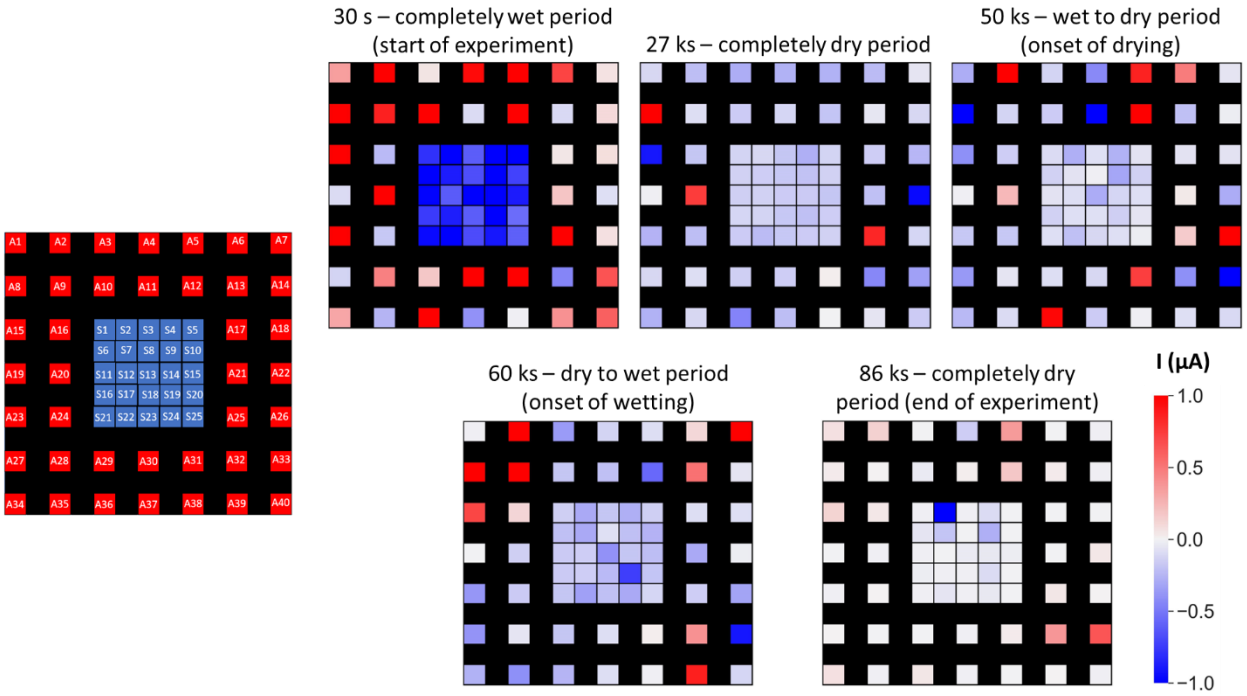

Figure 6.15. Current maps of the AA7050-316SS CMEA at various times over a 24-h wet-dry cyclic exposure under a thick film of 0.6 M NaCl solution. The cycle was for 1 h at 98% RH and 3 h at 30% RH for a total of 6 cycles. Temperature was kept constant at 35° C.

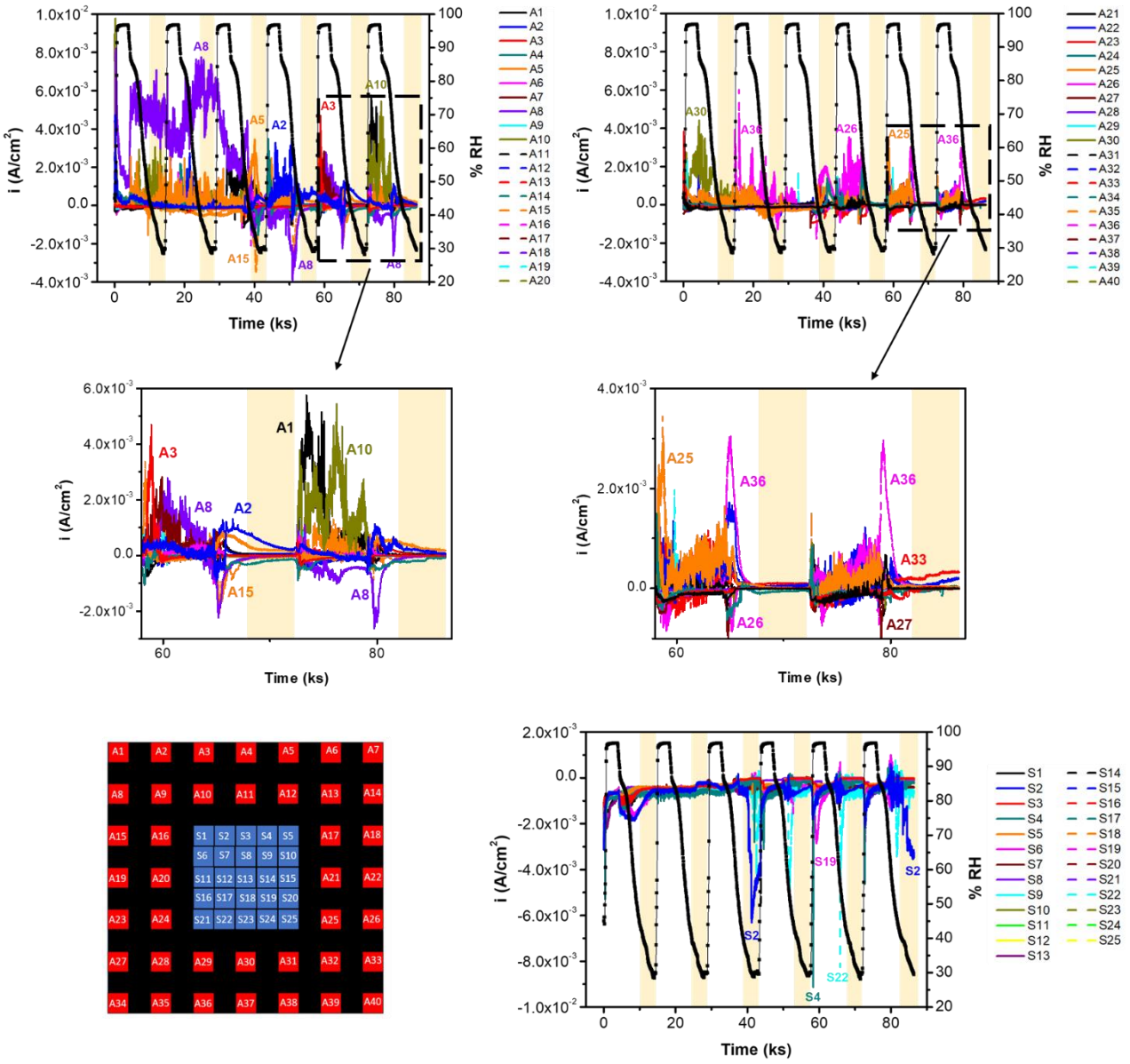

Figure 6.16. ZRA net galvanic current density as a function of time on the AA7050-316SS CMEA electrodes exposed to 24-h wet-dry cyclic conditions under a thick film of 0.6 M NaCl solution. The cycle was for 1 h at 98% RH and 3 h at 30% RH for a total of 6 cycles. Temperature was kept constant at 35° C. The RH data for the wet-dry cycle is shown on the right axis. Yellow bars indicate dry periods when the surface was deemed completely dry.

Interestingly, upon introduction of 10^{-4} M chromate to solution (Figures 6.17 and 6.18), there was only a 7% decrease in the total net anodic charge in comparison to the inhibitor-free case. Currents were not suppressed on the AA7050 net cathodes; the decrease in charge was attributed to a rather small charge suppression (~ 10%) on the 316SS electrodes. Furthermore, although the total net charge per wet period was higher than that during a dry period, the average net anodic charge per hour during a wet period was surprisingly approximately equal to that observed during a dry period at 0.034 C/hr. This observation was in contrast to the inhibitor-free case where the average net charge per hour during a wet period was about 35% higher than observed during a dry period. Another key observation was that with each progressive wet period, the total net anodic charge increased. The total net anodic and cathodic charges were 0.794 C and -0.793 C, respectively, representing an overall 70% increase in charge compared to the constant thick film case. AA7050 electrodes supplied 53% of the total net cathodic charge. As evident on the current maps (Figure 6.17), there was still considerable anodic and cathodic activity at the end of the experiment. The total net anodic charge at the final hour of the experiment (completely dry period) was 0.026 C. The corresponding value in the inhibitor-free case was only 0.008 C.

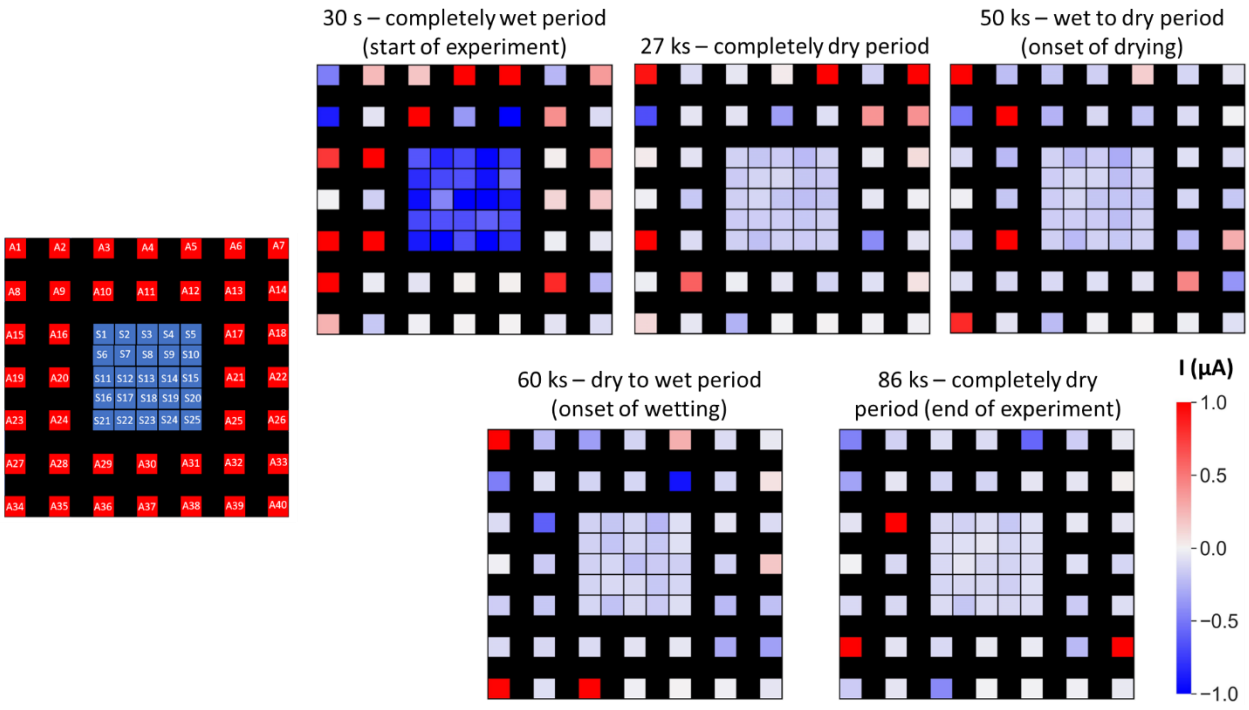

Figure 6.17. Current maps of the AA7050-316SS CMEA at various times over a 24-h wet-dry cyclic exposure under a thick film of 0.6 M NaCl solution with the addition of 10^{-4} M chromate. The cycle was for 1 h at 98% RH and 3 h at 30% RH for a total of 6 cycles. Temperature was kept constant at 35° C.

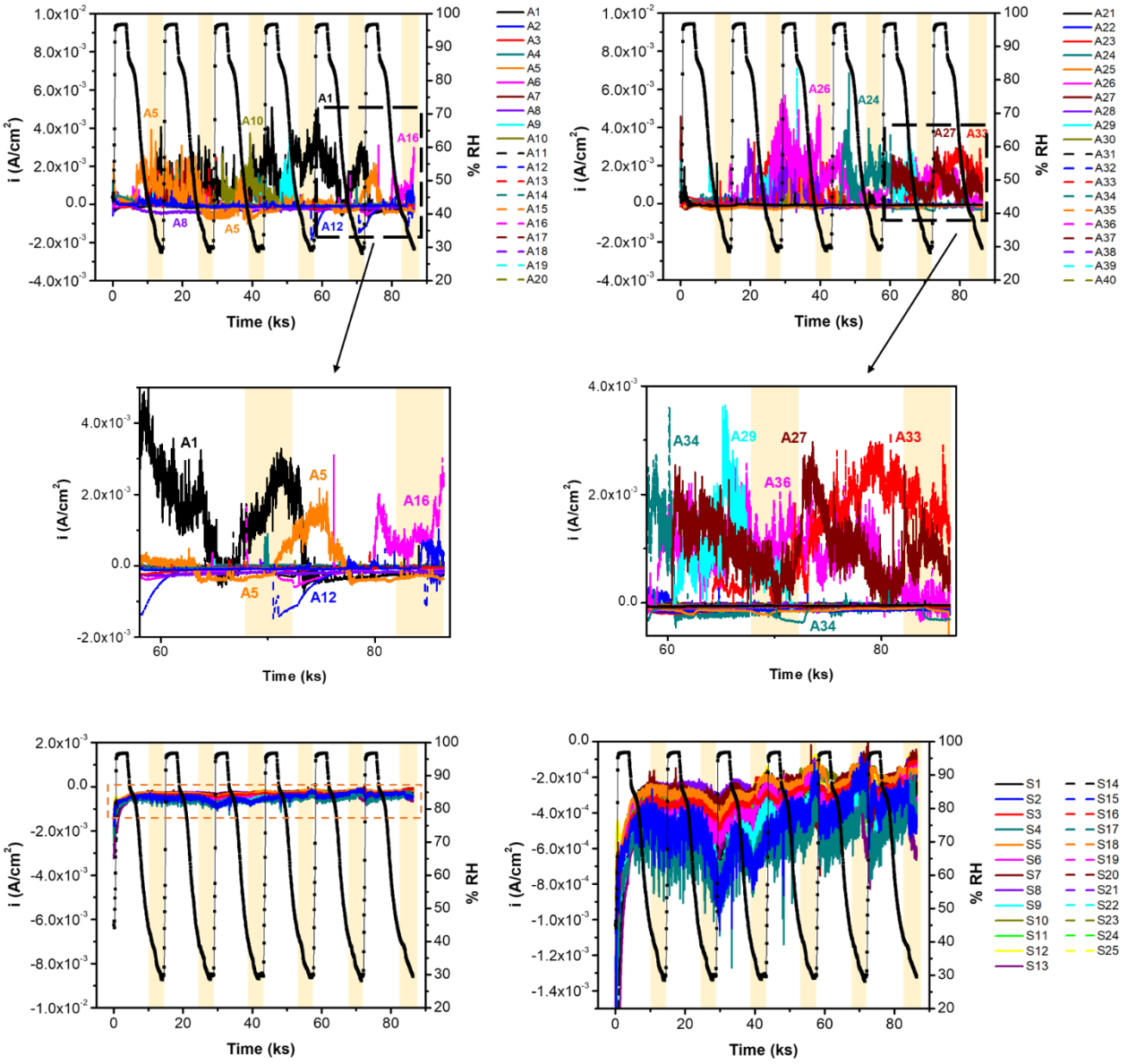

Figure 6.18. ZRA net galvanic current density as a function of time on the AA7050-316SS CMEA electrodes exposed to 24-h wet-dry cyclic conditions under a thick film of 0.6 M NaCl solution with the addition of 10^{-4} M chromate. The cycle was for 1 h at 98% RH and 3 h at 30% RH for a total of 6 cycles. Temperature was kept constant at 35° C. The RH data for the wet-dry cycle is shown on the right axis. Yellow bars indicate dry periods when the surface was deemed completely dry.

Upon increasing the chromate concentration to 10^{-2} M (Figures 6.19 and 6.20), currents were further reduced on the electrodes, albeit only marginally when compared to the lower chromate concentration values. There was only a 15% decrease in the total net anodic charge in comparison to the inhibitor-free case. In contrast to 10^{-4} M chromate, this higher concentration of chromate suppressed the currents on the AA7050 net cathodes, effecting a 15% suppression in total net cathodic charge. The average net anodic charge per hour during a wet period was about 11% higher than observed during a dry period. That said, the average net anodic charge per hour during a dry period in this environment was still higher (~ 7%) than attained in inhibitor-free conditions. The total net anodic and cathodic charges were 0.720 C and -0.720 C, respectively, corresponding to greater than a 100% increase in charge compared to the constant thick film case. AA7050 electrodes supplied 51% of the total net cathodic charge. As evident on the current maps (Figure 6.19), there was still considerable anodic and cathodic activity at the end of the experiment, though not as significant as observed in the 10^{-4} M chromate environment. The total net anodic charge at the final hour of the experiment (completely dry period) was 0.016 C which was twice higher than the corresponding value attained in inhibitor-free conditions.

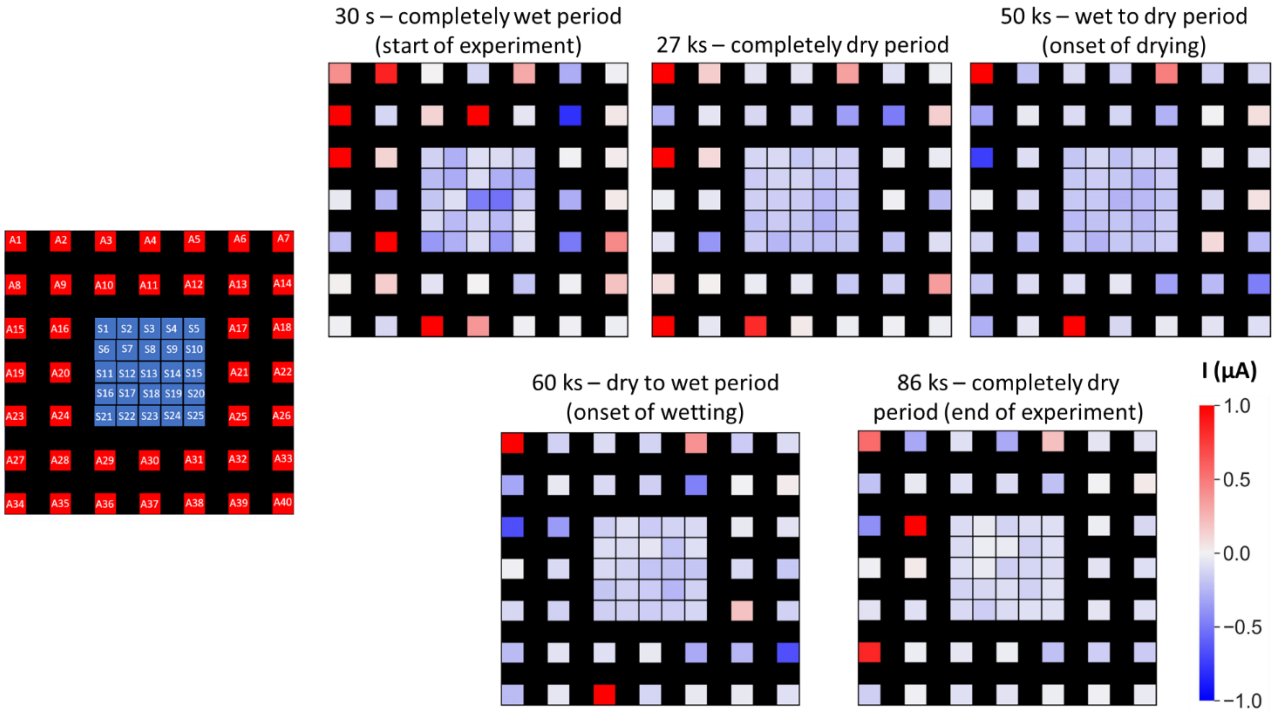

Figure 6.19. Current maps of the AA7050-316SS CMEA at various times over a 24-h wet-dry cyclic exposure under a thick film of 0.6 M NaCl solution with the addition of 10^{-2} M chromate. The cycle was for 1 h at 98% RH and 3 h at 30% RH for a total of 6 cycles. Temperature was kept constant at 35° C.

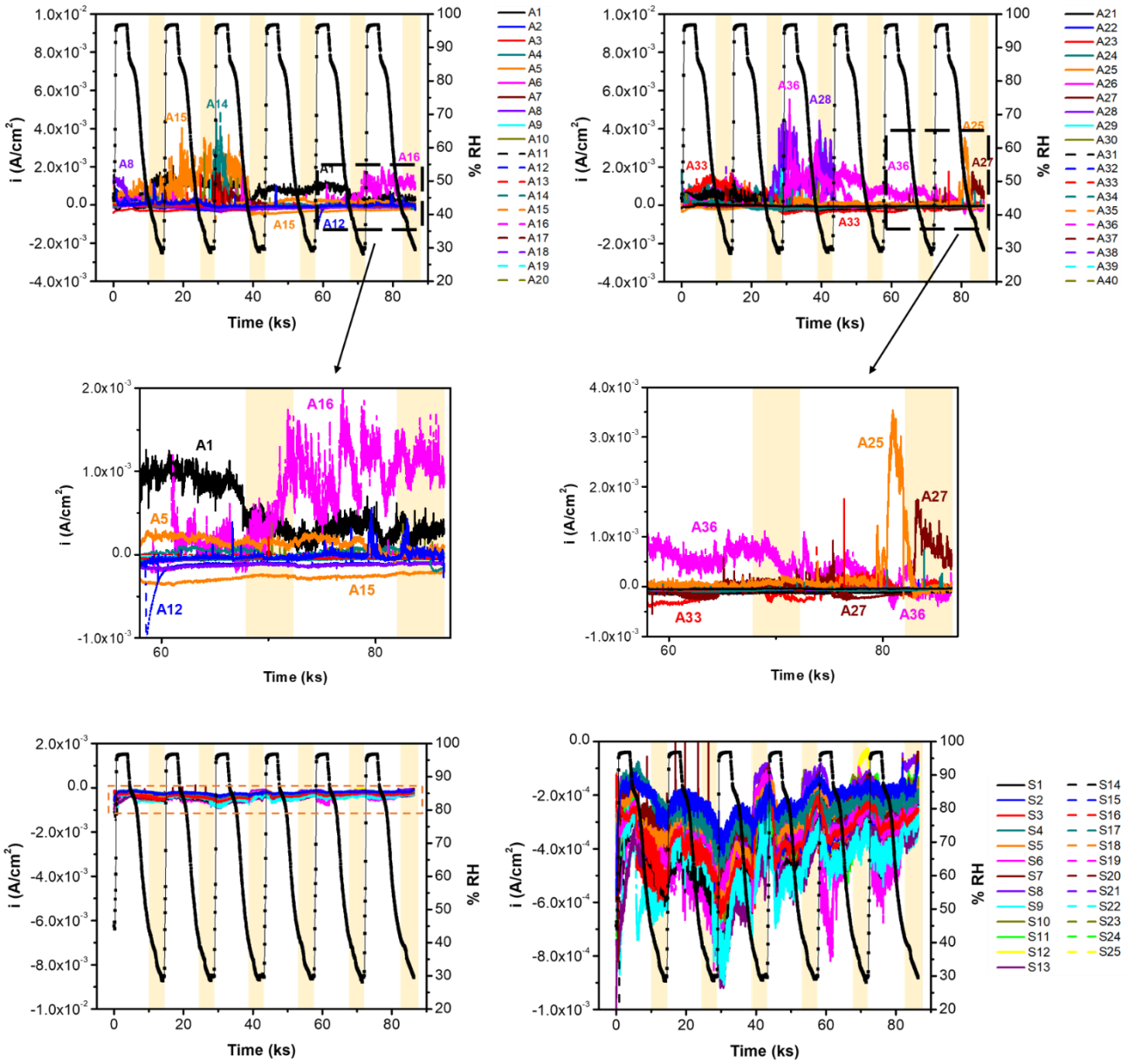

Figure 6.20. ZRA net galvanic current density as a function of time on the AA7050-316SS CMEA electrodes exposed to 24-h wet-dry cyclic conditions under a thick film of 0.6 M NaCl solution with the addition of 10^{-2} M chromate. The cycle was for 1 h at 98% RH and 3 h at 30% RH for a total of 6 cycles. Temperature was kept constant at 35° C. The RH data for the wet-dry cycle is shown on the right axis. Yellow bars indicate dry periods when the surface was deemed completely dry.

6.5 Discussion

6.5.1 The Effectiveness of Chromate Declines Under Wet-Dry Cycle Conditions in Comparison to Constant Thick Film Conditions with Stable Solution Chemistry

Aerospace structures experience a wide range of dynamic environmental conditions including periods of full immersion, thick film, thin film, humid and dry exposure as RH fluctuates. Corrosion kinetics under each of these conditions can be markedly different, and so it is important that an inhibitor be effective under this wide range of conditions. Figure 6.21 presents the total net anodic charge on the AA7050-316SS CMEA under constant thick films of 0.6 M NaCl and 5 M NaCl, in comparison to wet-dry cyclic conditions under a thick film of 0.6 M NaCl, and with additions of chromate. In inhibitor-free 0.6 M NaCl under constant thick film conditions at 98% RH, corrosion activity appeared to be rapid for the first 12 h of the experiment and then tapered for the remaining duration of the experiment. This decline in corrosion activity towards the end of the experiment could be attributed to the masking effect of precipitated corrosion products. The result was a decrease (~ 11%) in the total net anodic charge when compared to the case of 5 M NaCl at 80% RH where corrosion appeared to proceed at a more constant rate throughout the duration of the experiment. Under wet-dry cyclic conditions, the total net anodic charge significantly increased by ~ 62% due to the effect of dynamic electrolyte layer thickness and the associated changes in solution chemistry. As RH decreases, the thickness of the electrolyte layer decreases for a constant salt loading density, and the equilibrium chloride concentration increases. This situation results in an increase in the galvanic currents through enhanced ionic conductivity and decreases in the oxygen reduction reaction (ORR) diffusion distance even though oxygen solubility is reduced in concentrated salt solutions.[23,25] In this work, the increase in galvanic currents were evident during wet to dry (i.e., onset of drying) and dry to wet (i.e., onset of wetting) periods (Figure 6.16).

It has been reported that NaCl deliquesces at 75% RH at ambient temperature,[26] and so galvanic interactions should not occur below 75% RH. However, in this work, it is noted that the AA7050-316SS CMEA surface was not completely dry until 40% RH was reached. Therefore, the surface was considered to be completely dry for the last 1 h of each 4-h cycle. That said, because there was still some corrosion activity occurring – particularly with the addition of chromate –

during these deemed dry periods (summarized in Figure 6.22), it would not be surprising if the AA7050-316SS CMEA surface was still exposed to a hygroscopic electrolyte beneath the dry crystallized salt film. Schindelholz et al.[27] demonstrated that corrosion occurred on carbon steel exposed to NaCl down to a very low RH of 33%, which they attributed to capillary condensation between the NaCl and steel surface.

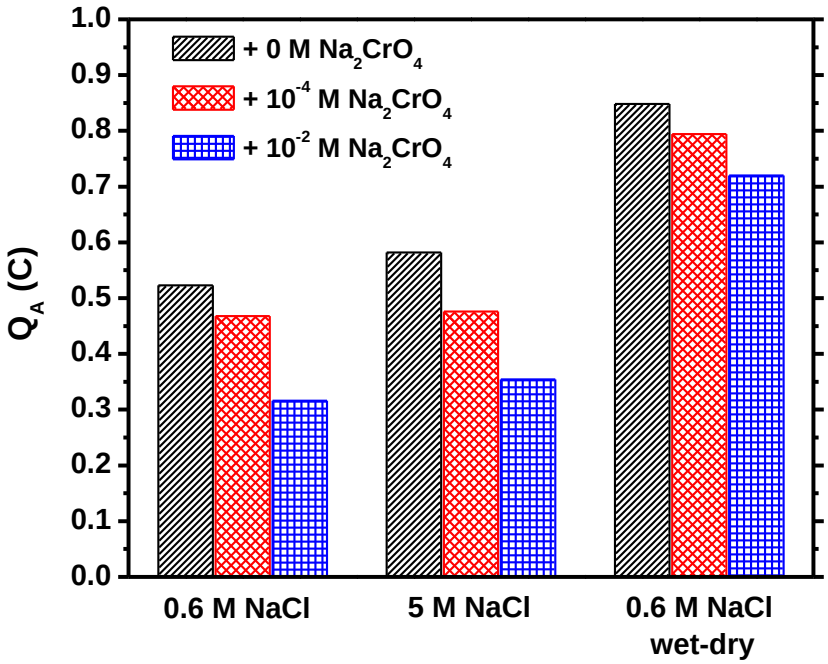

Figure 6.21. Total net anodic charge as a function of exposure environment on the AA7050-316SS CMEA.

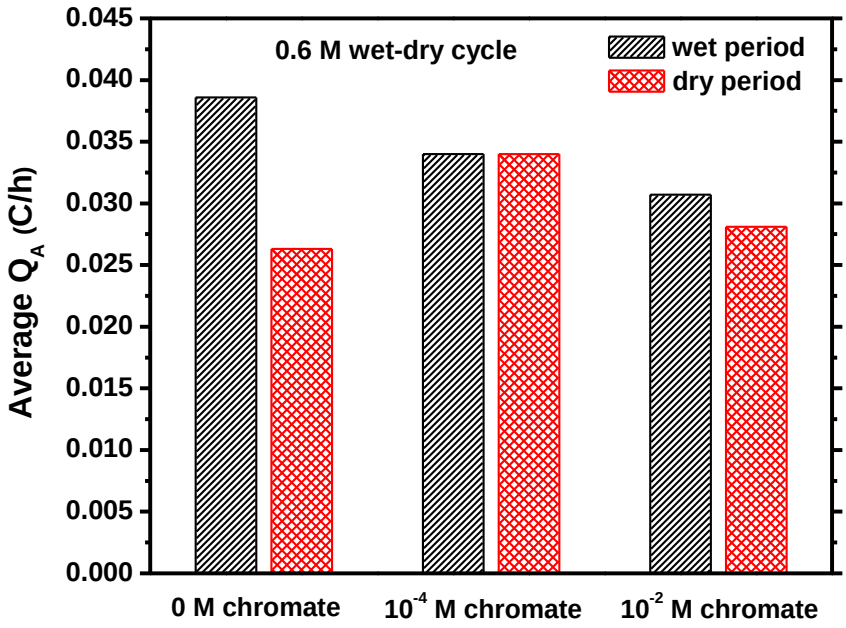

Figure 6.22. Comparison of the average net anodic charge per hour during a wet period vs. a dry period on the AA7050-316SS CMEA exposed to cyclic wet-dry conditions under a thick film of 0.6 M NaCl and with the additions of chromate. A wet period includes a completely wet period (i.e., at 98% RH), onset of drying (i.e., where the RH gradually ramps down from 98% to 40%), and onset of wetting (i.e., where the RH quickly ramps up from 40% to 98%). A dry period includes the period when the surface was deemed completely dry (i.e., 40% ≤ RH ≥ 30%).

The addition of chromate suppressed galvanic currents on the AA7050-316SS CMEA electrodes under in all three exposure environments, with the degree of suppression increasing with increasing chromate concentration (Figure 6.21). However, the inhibitive effect was observed to be much higher under constant thick film conditions in both 0.6 M NaCl and 5 M NaCl environments, more so for the 0.6 M NaCl environment, than under conditions of wet-dry cycling. The observation of superior effectiveness of chromate in 0.6 M NaCl compared to 5 M NaCl is consistent with the observations previously discussed in Chapter 3 where the addition of chromate to 5 M NaCl appeared to be less effective at suppressing ORR kinetics on planar 316SS and high-purity Cu electrodes, compared to the respective cases in 0.6 M NaCl (Figure 6.23). Speculations were made regarding the competitive adsorption between the chloride ion and the chromate ion where chloride would be disproportionately favored over chromate in terms of

surface adsorption and coverage of the electrodes due to its high mobility[28] and vast concentration in relation to chromate in the 5 M NaCl environment. That said, in this work in which AA7050 was coupled to 316SS, the difference in the total net anodic charge between the two solutions on addition of 10^{-2} M chromate was 0.038 C which was only a fraction when considering the case under wet-dry cycle conditions (Figure 6.21).

The addition of 10^{-4} M chromate to the cyclic wet-dry environment caused only a 7% decrease in the total net anodic charge in comparison to the inhibitor-free case (Figure 6.21). Furthermore, the average net charge per hour during a wet period was surprisingly approximately equal to that observed during a dry period at 0.034 C/hr. This observation was in contrast to the inhibitor-free case where the average net charge per hour during a wet period was about 35% higher than observed during a dry period. Another key observation was that with each progressive wet period, the total net charge increased. These observations implied that the apparent minimal degree of inhibition that may have been provided by this low concentration of chromate during the first cycle (Figure 6.18) may have been overwhelmed during subsequent cycles considering the evolving equilibrium concentration of chloride as the electrolyte layer thickness decreased. It is also plausible that after each cycle, the amount of chromate available to re-wet or solubilize was insufficient to provide further inhibition, evident by the proliferation of AA7050 net cathodes. It was observed that there was barely any cathodic inhibition provided on the AA7050 net cathodes (Figure 6.17). This result is consistent with the cathodic polarization data obtained on high-purity Cu (representative of Cu-IMPs and/or replated Cu on AA7050) and displayed in Figure 6.23. In Figure 6.23a, it can be seen that the addition of 10^{-4} M chromate to 0.6 M NaCl under a thick electrolyte layer (applicable to the beginning of the first cycle) provided very minimal suppression of ORR kinetics on high-purity Cu purity in comparison to 316SS. Under a thinner electrolyte layer of 5 M NaCl (applicable to a wet to dry period) in Figure 6.23b, the addition of 10^{-4} M chromate did not suppress ORR kinetics on high-purity Cu.

Increasing the chromate concentration to 10^{-2} M chromate in the cyclic wet-dry environment caused only a further 8% decrease in the total net anodic charge from 10^{-2} M chromate (Figure 6.21). This further decrease in the total net anodic charge resulted largely from

an improved, albeit small, current suppression on the AA7050 net cathodes, which is consistent with the small degree of ORR suppression on high-purity Cu in 5 M NaCl under a thin electrolyte layer when exposed to the same chromate concentration (Figure 6.23). Although lower than the case of 10^{-4} chromate, the average net anodic charge per hour during a dry period in this environment was still higher (~ 7%) than attained in inhibitor-free conditions (Figure 6.22). This sustainment of corrosion activity at considerable rates at such a low RH as 30% in the presence of chromate suggests that there may been some trapped concentrated electrolyte underneath the apparent dry crystallized salt film on the surface of the CMEA.

Another aspect to consider is the expected increase in the concentration of Al^{3+} under the cyclic wet-dry conditions compared to that under thick film conditions. It was shown in Chapter 3 that the presence of Al^{3+} accelerated cathodic kinetics on 316SS and high-purity Cu, and chromate was ineffective at providing adequate cathodic inhibition on the electrodes. In the current work, it is conceivable that the production of Al^{3+} with each progressive cycle would encourage further Cu replating on the AA7050 electrodes, in addition to the active Cu-rich IMPs and 316SS, providing more cathodic area with attendant substantial increase in cathodic current to sustain anodic dissolution. This situation would diminish the ability of chromate to provide inhibition, regardless of concentration.

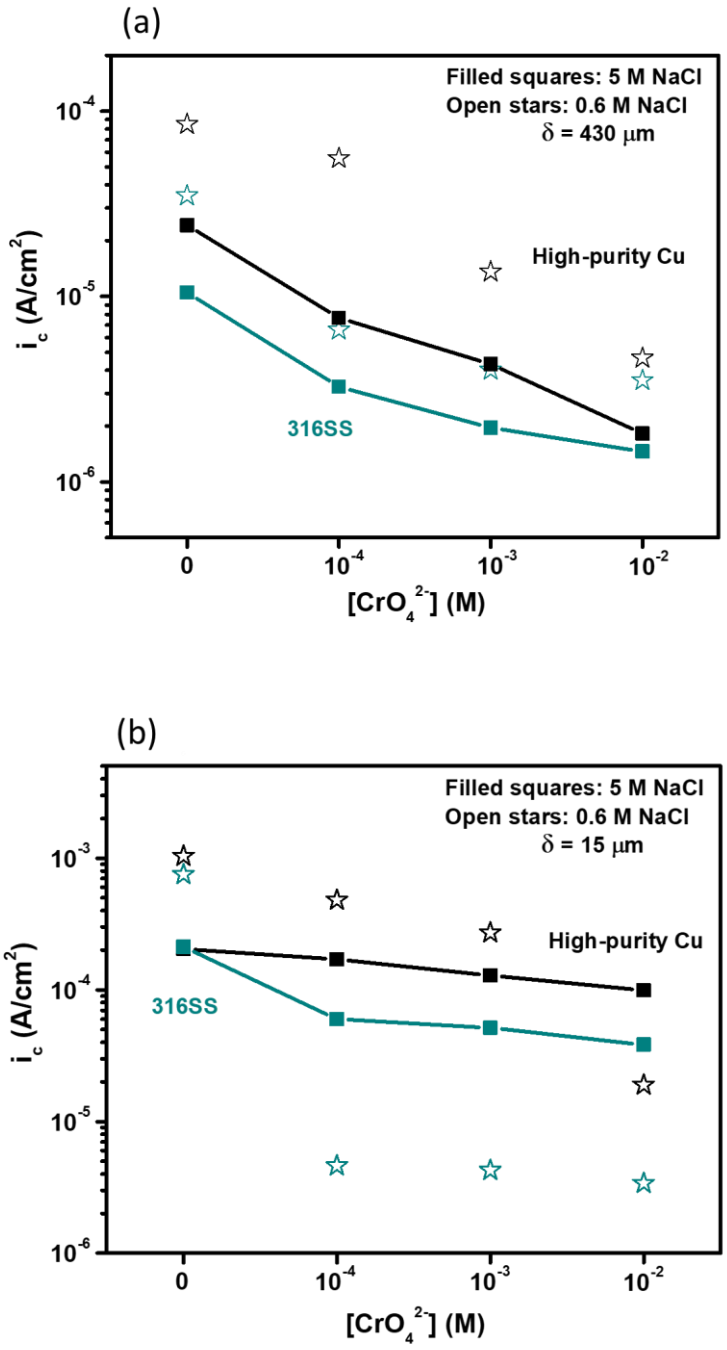

Figure 6.23. Comparison of the ORR behaviors of high-purity Cu and 316SS in 0.6 M NaCl and 5 M NaCl as a function of chromate concentration at (a) δ = 430 μm (thick film conditions), and (b) at δ = 15 μm (thin film conditions).

6.5.2 Significance of Cathodes – Cu-rich IMPs/Replated Cu on AA7050 vs. 316SS – as a Function of Exposure Environment

On a typical homogeneous macro-galvanic couple, corrosion damage on the anode tends to accelerate at/near the couple (i.e., anode-cathode) interface, and decreases with distance away from the couple interface. For instance, Liu et al.[29] studied the galvanic current interactions on a Zn-316SS galvanic couple and found that the corrosion depth on Zn was highest at the Zn-316SS interface and steeply declined with distance away from the couple interface. In the current work, it is noted that the above-described tendency was not observed on the AA7050-316SS CMEA across all exposure environments. There were no clear correlations of favored AA7050 net anodes in the immediate vicinity of the 316SS cathodes. Instead, the AA7050 electrodes often switch polarity sporadically. The switch from a net anode to a net cathode could be an indication of the preferential dealloying of active elemental constituent(s) of an initially anodic Cu-rich IMP, leaving behind a cluster of Cu-rich remnants and/or subsequent electrodeposition of Cu on the surface.[3,30,31] On the other hand, the switch from a net cathode to a net anode could indicate the mechanical detachment of the cluster of Cu-rich remnants,[32,33] leaving behind an exposed area of the Al matrix. Due to the heterogeneous nature of the AA7050 microstructure, it is speculated that the location of the AA7050 net anodes at any point in time was largely governed by metallurgically-driven propensity for localized corrosion and micro-galvanic coupling as opposed to proximity to the 316SS as would be the case for a homogeneous macro-galvanic couple.[23]

AA7050 electrodes played a significant role in supporting cathodic reactions on the CMEA. A summary of the contributions of AA7050 and 316SS to the total net cathodic charge as a function of exposure environment is presented in Figure 6.24. In the more aggressive environments, i.e., 5 M NaCl and conditions of wet-dry cycling, AA7050 net cathodes supplied over 50% of the total net cathodic charge, regardless of chromate concentration. In general, chromate displayed less propensity to inhibit cathodic reactions on AA7050 net cathodes in comparison to 316SS. That said, the degree of cathodic inhibition on the 316SS electrodes fell as the environment became more aggressive. The Cr(III)-rich oxide barrier film formed on reduction of chromate is irreversible and persistent,[34] thus it would be expected that further changes in RH that result in a concentrated solution chemistry during wet-dry cycling should have minimal

impact on corrosion kinetics. However, this was not the case in the current work which was evident by sharp increases in anodic currents after the first wet-dry cycle in chromate-containing environments. It therefore follows that higher chromate concentrations than utilized in this work may be required as the conductivity/aggressiveness of the environment increases. Such high concentrations may not be achievable in the field.[35,36] As noted previously in Chapter 3 and also evident in the current work, the inability of chromate to effect early and adequate cathodic inhibition on 316SS in an AA7050-316SS couple would likely increase the driving force for Cu replating. The replated Cu, in addition to the Cu-rich IMPs, may become the more significant cathode weakly affected by chromate that drives further attack, and so should not be underestimated when considering the current capacities of cathodes in AA-SS couples.

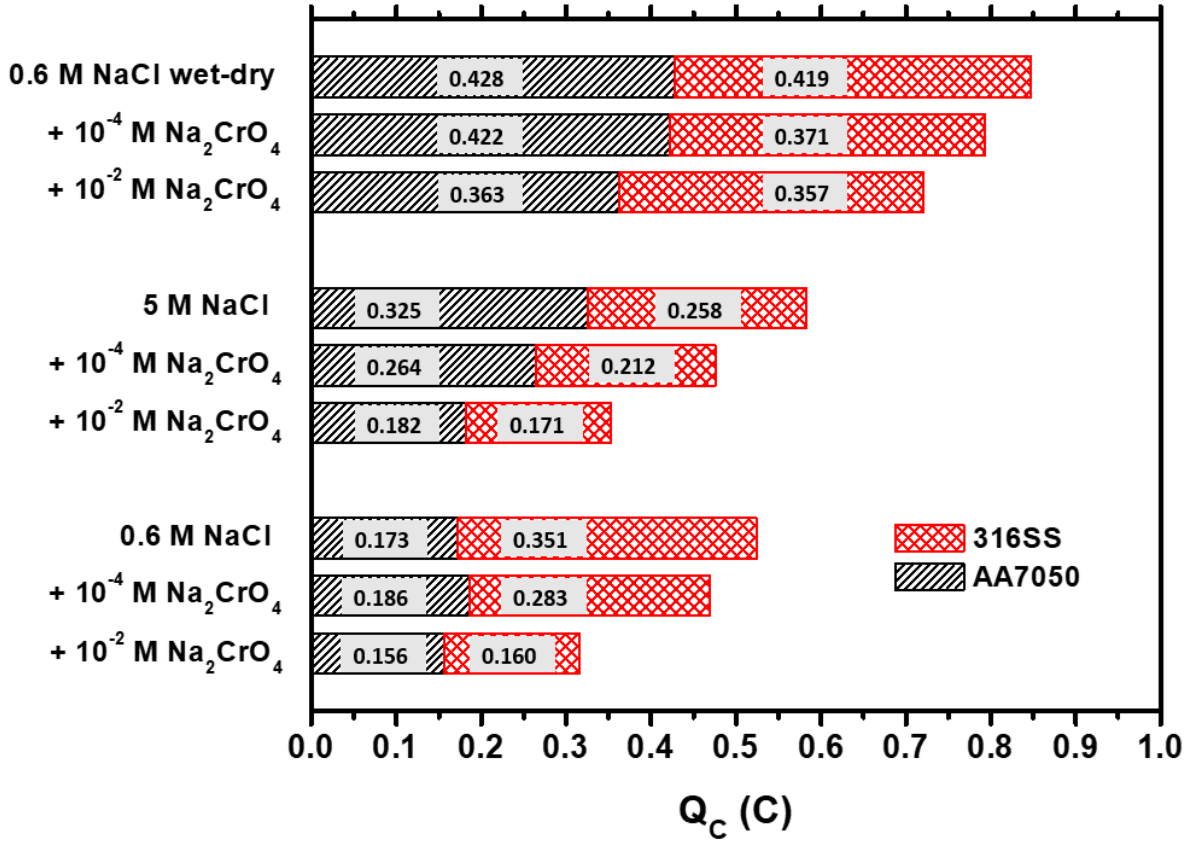

Figure 6.24. Summary of the contributions of AA7050 and 316SS to the total net cathodic charge as a function of exposure environment.

6.6 Conclusions

A galvanic CMEA was constructed with AA7050-T7451 and 316SS in a fastener configuration to interrogate the effect of chromate on the galvanic current interactions pertinent to the boldly exposed surface under conditions of thick film and wet-dry cycling in dilute and concentrated chloride solutions. The efficacy of chromate under these exposure conditions was evaluated through examination of the extent of current suppression on the AA7050 net cathodes and the 316SS electrodes. In summary, the following findings are highlighted:

- In inhibitor-free environments, the total net anodic charge increased with increasing conductivity and aggressiveness of the electrolyte. Under thick film conditions, the total net anodic charge increased by 11% when chloride concentration was increased from 0.6 M to 5 M. Under conditions of wet-dry cycling, the total net anodic charge increased by 62% when compared to relatively constant thick film conditions. This large increase in charge during wet-dry cycling was attributed to increases in equilibrium chloride concentration as the electrolyte thickness decreased, evident by the sharp current spikes observed during periods of onset of drying and wetting.
- There were no correlations of favored AA7050 net anodes in the immediate vicinity of the 316SS cathodes, regardless of exposure conditions. Instead, the AA7050 electrodes often switched polarity sporadically at random locations. It was speculated that the location of the AA7050 net anodes was influenced by metallurgical factors rather than the proximity to the 316SS electrodes as would be the case for a homogeneous macro-galvanic couple.
- Assessment of the contributions of the AA7050 and 316SS electrodes to the total net cathodic charge indicated that AA7050 played a significant role in supporting cathodic reactions on the CMEA. In the more aggressive environments, i.e., 5 M NaCl and conditions of wet-dry cycling, AA7050 net cathodes supplied more than 50% of the total net cathodic charge.
- The effectiveness of chromate was found to decline with increasing conductivity and aggressiveness (i.e., higher chloride-to-chromate concentration ratio) of the electrolyte. Under wet-dry cycling conditions, anodic current spikes observed after the

initial cycle indicated that any inhibition achieved during the first cycle was overwhelmed during subsequent cycles, and the quantity available to re-solubilize was insufficient to provide further inhibition. In addition, chromate exhibited less propensity to suppress cathodic currents on the AA7050 net cathodes in comparison to the 316SS electrodes.

6.7 References

1. T. Dursun and C. Soutis, *Mater. Des.*, **56**, 862–871 (2014).

2. J. R. Davis, *Corrosion of Aluminum and Aluminum Alloys*, ASM International, New York, (1999).

3. N. Birbilis and R. G. Buchheit, *J. Electrochem. Soc.*, **152**, B140–B151 (2005).

4. O. Schneider, G. O. Ilevbare, R. G. Kelly, and J. R. Scully, *J. Electrochem. Soc.*, **154**, C397–C410 (2007).

5. M. A. Jakab, D. A. Little, and J. R. Scully, *J. Electrochem. Soc.*, **152**, B311–B320 (2005).

6. G. O. Ilevbare, O. Schneider, R. G. Kelly, and J. R. Scully, *J. Electrochem. Soc.*, **151**, B453–B464 (2004).

7. D. Olson, T. Siewert, S. Liu, and G. Edwards, *ASM Handbook Vol 6: Welding, Brazing, and Soldering*, ASM International, New York, (1993).

8. C. A. Matzdorf et al., *Corrosion*, **69**, 1240–1246 (2013).

9. Z. Feng and G. S. Frankel, *Corrosion*, **70**, 95 (2014).

10. Z. Feng, G. S. Frankel, and C. A. Matzdorf, *J. Electrochem. Soc.*, **161**, C42–C49 (2014).

11. V. N. Rafla, A. D. King, S. Glanvill, A. Davenport, and J. R. Scully, *Corrosion*, **74**, 5–23 (2018).

12. R. S. Marshall, R. G. Kelly, A. Goff, and C. Sprinkle, *Corrosion*, **75**, 1461–1473 (2019).

13. Z. Feng, G. S. Frankel, W. H. Abbott, and C. A. Matzdorf, *Corrosion*, **72**, 342–355 (2016).

14. Z. Feng, J. Boerstler, G. S. Frankel, and C. A. Matzdorf, *Corrosion*, **71**, 771–783 (2015).

15. V. N. Rafla and J. R. Scully, *Corrosion*, **75**, 587–603 (2019).

16. U.-E. Charles-Granville, C. F. Glover, J. R. Scully, and R. G. Kelly, *J. Electrochem. Soc.*, **168**, 121509 (2021).

17. A. C. Bastos, M. C. Quevedo, O. V. Karavai, and M. G. S. Ferreira, *J. Electrochem. Soc.*, **164**, C973–C990 (2017).

18. G. Williams and H. Neil McMurray, *J. Electrochem. Soc.*, **155**, C340 (2008).

19. C. F. Glover, T. W. Cain, and J. R. Scully, *Corros. Sci.*, **149**, 195–206 (2019).

20. M. Saeedikhani, K. X. Kuah, S. Wijesinghe, S. Vafakhah, and D. J. Blackwood, *J. Electrochem. Soc.*, **168**, 081505 (2021).

21. P. Atz Dick, G. H. Knörnschild, and L. F. P. Dick, *Corros. Sci.*, **114**, 28–36 (2017).

22. B. Kannan, C. F. Glover, H. N. McMurray, G. Williams, and J. R. Scully, *J. Electrochem. Soc.*, **165**, C27–C41 (2018).

23. V. N. Rafla and J. R. Scully, *Corrosion*, **75**, 12–28 (2019).

24. V. N. Rafla, P. Khullar, R. G. Kelly, and J. R. Scully, *J. Electrochem. Soc.*, **165**, C562–C572 (2018).

25. W. Lang and R. Zander, *Ind. Eng. Chem. Fundam.*, **25**, 775–782 (1986).

26. E. Schindelholz and R. G. Kelly, *Corros. Rev.*, **30**, 135–170 (2012).

27. E. Schindelholz, B. E. Risteen, and R. G. Kelly, *J. Electrochem. Soc.*, **161**, 450–459 (2014).

28. C. A. Lucy and T. L. Mcdonald, *Anal. Chem*, **67**, 1074–1078 (1995).

29. C. Liu, G. W. Kubacki, and R. G. Kelly, *Corrosion*, **75**, 465–473 (2019).

30. Y. Zhu, K. Sun, and G. S. Frankel, *J. Electrochem. Soc.*, **165**, C807–C820 (2018).

31. A. Kosari et al., *J. Electrochem. Soc.*, **168**, 041505 (2021).

32. R. G. Buchheit, M. A. Martinez, and L. P. Montes, *J. Electrochem. Soc.*, **147**, 119–124 (2000).

33. M. B. Vukmirovic, N. Dimitrov, and K. Sieradzki, *J. Electrochem. Soc.*, **149**, B428–B439 (2002).

34. U.-E. Charles-Granville, C. Liu, J. R. Scully, and R. G. Kelly, *J. Electrochem. Soc.*, **167**, 111507 (2020).

35. L. Xia, E. Akiyama, G. Frankel, and R. Mccreery, *J. Electrochem. Soc.*, **147**, 2556–2562 (2000).

36. J. D. Ramsey, L. Xia, M. W. Kendig, and R. L. McCreery, *Corros. Sci.*, **43**, 1557–1572 (2001).

7. Conclusions and Recommendations for Future Work

7.1 Conclusions

This dissertation utilized a number of laboratory methods in addition to modeling to advance the mechanistic understanding of the galvanic-induced localized corrosion of AA7050-T7451 coupled to 316SS in simulated atmospheric environments from the perspectives of damage dependence on cathodic activity and chromate action on the main cathodic contributors. Although extensive research into potential chromate replacements have been underway for the last three decades, only minor advances have been made with regards to finding a sustainable alternative that meets the versatility and cost effectiveness of chromates. For this reason, the aerospace industry is still heavily reliant on chromates, and research is still ongoing to advance the mechanistic understanding of chromate protection particularly in relation to the galvanic corrosion behavior of complex structures complicated with micro- and macro-galvanic couples. To this end, this dissertation work characterized the mechanism(s) and shortfalls of chromate inhibition of AA7050-T7451 coupled to 316SS under various environmental conditions pertinent to a plate-fastener geometry. The understanding achieved with this work should aid in optimizing testing frameworks and serve as a benchmark in the engineering design of future corrosion mitigation strategies.

The RDE technique was utilized to experimentally assess the effects of chromate on the mass-transport-limited ORR behavior of AA7XXX alloys under thin film electrolyte conditions representative of atmospheric exposure. Chromate suppressed ORR kinetics on AA7050 by up to two orders of magnitude over the chromate-free case; the effect became greater with thinner diffusional boundary layer as electrode rotation rate increased. Chromate was reduced irreversibly to form a Cr(III)-rich film on the electrode surface that blocked cathodic sites and hindered ORR. ORR inhibition was sustained when chromate was subsequently removed from solution. Comparison of the electrochemical behaviors of AA7050 and AA7075 indicated that same trends may apply across AA7XXX alloys; however, the degree of inhibition may be lower as the Cu content of alloy increases. Better corrosion performance on AA7075 upon addition of chromate was attributed to its lower Cu content, and hence, reduced cathodic area (fewer Cu-

rich IMPs and/or less Cu replating) requiring lower concentration of chromate to adequately suppress ORR kinetics. The surface film on AA7050 after cathodic polarization in chromate consisted of mixed Cr(III) / Cr(VI) oxides with some underpotentially deposited Cr^0. Cu-rich IMPs on AA7050 were speculated to promote underpotential deposition of Cr. Chromate acted as an intrinsic cathodic inhibitor on Pt by forming a Cr(III)-rich surface film that reduced ORR kinetics on Pt by up to one order of magnitude. In summary, chromate exhibited its inherent capability as an effective cathodic inhibitor for the ORR regardless of the nature of the electrode surface.

The RDE technique was extended to evaluate the current capacities of the individual cathodic contributors in AA7050-316SS galvanic couple to drive localized corrosion of AA7050 in the presence of chromate under simulated atmospheric conditions. The addition of 10^{-4} M chromate into dilute NaCl solution significantly reduced ORR kinetics on both 316SS and Cu-rich IMPs on AA7050. However, at least 10^{-2} M chromate was required to achieve a similar effect on high-purity Cu. It was speculated based on this result that early cathodic inhibition of 316SS may mitigate AA7050 corrosion and subsequent Cu replating. However, if Cu replates, it may become the more significant cathode weakly affected by chromate that drives further attack. It was also determined that the degree of chromate inhibition on the cathodes decreased with increasing chloride concentration. In order to simulate pre-corrosion of AA7050 leading to the release of Al^{3+} into a concentrated chloride environment, experiments were carried out where 10^{-1} M Al^{3+} was added to the 5 M NaCl environment. The addition of 10^{-1} M Al^{3+} to 5 M Cl^- solution enhanced HER kinetics making it the dominant cathodic reaction as opposed to the ORR. Chromate exhibited a diminished ability to inhibit the HER compared to the ORR. Furthermore, in the presence of 10^{-1} M Al^{3+}, 316SS was determined to be the more significant cathode in comparison to high-purity Cu, with an increased current capacity of up to one order of magnitude. In summary, it is plausible that following a coating breakdown, replated Cu on AA may be the more important cathode that sustains damage initiation and/or drives early-stage damage propagation on AA, leading to accumulation of Al ions which in turn increases the supply of protons in solution and accelerates cathodic kinetics on the 316SS and replated Cu to advance damage propagation on the AA. It therefore follows that early mitigation of Cu replating through ORR inhibition on SS by chromate would be crucial in limiting macro-galvanic corrosion of AAs.

The performance of chromate in protecting AA7050 against macro-galvanic induced attack when *actually* coupled to 316SS in simulated crevice environments, compared to external conditions was also assessed, with the aim of providing an explanation as to why chromate appears to be less effective at suppressing active corrosion vs. initiation of corrosion on AAs coupled to SS fasteners as reported in the literature. It was observed that chromate suppressed initiation of damage on AA7050 by suppressing cathodic kinetics on 316SS and anodic kinetics on AA7050, however, the degree of inhibition decreased with decreasing pH. The decreased level of chromate inhibition in acidic solutions was attributed to the predominance of the bichromate ion ($HCrO_4^-$) which is more difficult to reduce compared to either the dichromate ion ($Cr_2O_7^{2-}$) or the chromate ion (CrO_4^{2-}). Although chromate exhibited a diminished ability to inhibit the HER compared to the ORR, low solution pH by itself was not considered to be the main damage driver in an AA7050-316SS fastener crevice. The presence of 10^{-1} M Al^{3+} inside the crevice enhanced HER kinetics and acted as a strong buffer such that chromate became ineffective at providing cathodic inhibition on the 316SS/high-purity Cu or raising the pH of the environment. Minimal anodic inhibition, realized via electrostatic adsorption, was insufficient to mitigate damage initiation and/or propagation on AA7050. With no Al^{3+} added to the environment, high-purity Cu was determined to be the more significant cathode, whereas 316SS became the more significant cathode in the presence of 10^{-1} M Al^{3+}. This result was consistent with the results obtained on the uncoupled individual cathodes in Chapter 3. In summary, chromate exhibited a propensity to inhibit damage initiation rather than damage propagation in simulated AA7050-316SS fastener crevice environments.

The scanning vibrating electrode technique (SVET) was utilized to experimentally validate the applicability of finite element modeling (FEM) in simulating macro-galvanic-induced corrosion of AA7050 coupled to 316SS.[1] The SVET and FEM both provided local current density distributions, which were then compared. The discrepancy between the two techniques was traced to several sources including experimental complexities of non-steady-state, lack of charge conservation, and inhomogeneities in electrode surface conditions and/or local electrolyte

[1] This work was a collaboration with R.S. Marshall and C.V. Moraes. RSM and CVM performed the modeling while I carried out the experimental analyses.

chemistry. However, once the boundary conditions were optimized to tune the framework to better reflect the local electrolyte conditions expected at the electrode surface, the model was validated. With the validated model, better agreements in the *total currents* calculated with both techniques were achieved. That said, the local current density distributions as measured experimentally could not be predicted by the model, owing to the model's incapability to capture localized corrosion events such as pitting and precipitation of corrosion products. Furthermore, it was determined that the electrolyte current densities measured by the SVET at a distance of 100 µm from the electrode surface can be significantly different from the actual current density at the electrode surface, and the difference depends on the position above the galvanic couple surface. It was predicted that there was a 10% difference at locations far away from the galvanic couple interface while at the vicinity between the two electrodes, the difference was as high as 200%. In summary, as current densities measured with the SVET are typically an underestimation of the actual values at the electrode/electrolyte interface, combining the SVET with a validated model – capable of predicting the electrolyte current density as a function of distance from the electrode surface – may be advantageous in bridging this gap and better interpreting the results obtained with the SVET.

A galvanic coupled micro-electrode array (CMEA) was constructed with AA7050-T7451 and 316SS in a fastener configuration to interrogate the effect of chromate on the galvanic current interactions pertinent to the boldly exposed surface under conditions of thick film and wet-dry cycling in dilute and concentrated chloride solutions. The efficacy of chromate under these exposure conditions was evaluated through examination of the extent of current suppression on the AA7050 net cathodes and the 316SS electrodes. In inhibitor-free environments, the total net anodic charge increased with increasing conductivity and aggressiveness of the electrolyte. Under thick film conditions, the total net anodic charge increased by 11% when chloride concentration was increased from 0.6 M to 5 M. Under conditions of wet-dry cycling, the total net anodic charge increased by 62% when compared to thick film conditions. This large increase in charge during wet-dry cycling was attributed to increases in equilibrium chloride concentration as the electrolyte thickness decreased during each cycle, evident by the sharp current spikes observed during periods of onset of drying and

wetting. There were no correlations of favored AA7050 net anodes in the immediate vicinity of the 316SS cathodes, regardless of exposure conditions. Instead, the AA7050 electrodes often switch polarity sporadically at random locations. It was speculated that the location of the AA7050 net anodes was dominated by metallurgical factors rather than the proximity to the 316SS electrodes as would be the case for a homogeneous macro-galvanic couple. Assessment of the contributions of the AA7050 and 316SS electrodes to the total net cathodic charge indicated that AA7050 played a significant role in supporting cathodic reactions on the CMEA. In the more aggressive environments, i.e., 5 M NaCl and conditions of wet-dry cycling, AA7050 electrodes serving as net cathodes supplied more than 50% of the total net cathodic charge. The effectiveness of chromate was found to decline with increasing conductivity and aggressiveness of the electrolyte. Under wet-dry cycling conditions, anodic current spikes observed after the initial cycle indicated that any inhibition achieved during the first cycle was overwhelmed during subsequent cycles, and the quantity available to re-wet was insufficient to provide further inhibition. In addition, chromate exhibited less propensity to suppress cathodic currents on the AA7050 net cathodes in comparison to the 316SS electrodes. In summary, under wet-dry cycling conditions, the effectiveness of chromate was diminished when compared to constant thick film conditions, due to the alternation in equilibrium chloride concentration as electrolyte thickness changed upon onset of drying and wetting.

It was established in this work that chromate provided adequate protection by precipitating a low porosity, electronically insulating film over the substrate that hindered oxygen and chloride adsorption and/or restricted the transfer of electrons from the electrode-film interface to the film-solution interface. Under conditions where the formation of this film was discouraged, chromate inhibition was minimal or not realized, and attack on the AA anode was sustained. Therefore, it is imperative that candidates for chromate replacement must possess these film-forming characteristics across a wide range of environmental pH, considering the aggressive nature of electrolyte chemistry in atmospheric environments, including the large buffering effect of metal ions in bimetallic crevices as observed with the addition of Al ions in this work. Another important aspect to consider when evaluating non-chromate inhibitor systems is the optimization of inhibitor leach rates from coating in light of mitigation of damage propagation

as opposed to damage initiation, while minimizing the risk of premature inhibitor depletion through controlled release. As regards bimetallic crevices, e.g., AA-SS, it is plausible that coating the SS fastener prior to installation when joining AA-based structures might slow damage propagation inside the crevice by limiting the area of available active cathode (i.e., SS and replated Cu) in the event that the coating fails. As mentioned previously, early cathodic inhibition on the SS is likely to mitigate macro-galvanic corrosion of AA and consequent Cu replating.

7.2 Recommended Future Work

- Investigate the effect of environmentally friendly inhibitors such as Mg-rich primers, zinc ions, cerium ions, molybdates, and vanadates on the individual actors in AA-SS couples employing similar testing methods and environments as utilized in this work. A metal pigment concept in combination with a chemical inhibitor could also be explored. These inhibitors have been shown to precipitate protective films on AAs. It may be worthwhile to assess the extent to which these inhibitors suppress cathodic reactions on 316SS and Cu-rich IMPs/replated Cu in comparison to chromate across a wide range of environments and pH. A more effective cathodic inhibitor than chromate would prove more beneficial in protecting AAs against micro- and macro-galvanic corrosion.
- Further characterize the effects of geometric variables such as crevice gap width, crevice length, and external cathode area that control galvanic interactions in AA-SS galvanic couples. This work could be accomplished by constructing improved coupled micro-electrode arrays that permit precise crevice gap adjustments and use of pH probes inside the crevice for pH measurements, as well as the use of a sintered Ag/AgCl counter/reference electrode embedded inside the crevice to conduct polarization experiments. Assessment of the pH profile along the length of the crevice could provide further insights on the pH-induced distribution of macro-galvanic damage on AA in occluded regions as well as the effect of pH on chromate inhibition along the length of the crevice.

- Further characterize and elucidate how the corrosion damage mode of AA7050 evolves under changing environmental conditions such as variations in chromate concentration, pH, and Al ion concentration.
- In Chapter 5 as well as in other recent literature by R. S. Marshall, a validated FEM modeling framework was proposed to predict the current distributions/damage on the surface and within the fastener hole of AA7XXX-316SS fastener assembly. However, these studies did not consider the influence of replated Cu and the effect of chromate in solution. It is suggested to adapt the FEM modeling with the inclusion of transport of minor species to predict the galvanic interactions between AA7050, replated Cu, and 316SS with different geometric and environmental considerations as a function of chromate concentration. Determine the throwing power of 316SS and replated Cu as a function of cathode size and chromate concentration, as well as the associated damage distribution as a function of position along the AA7050-316SS couple surface vs. inside the fastener crevice. Anodic hotspots could be assigned on AA7050 at the surface and within the fastener crevice to investigate how the interplay of chromate and replated Cu vs. 316SS interacts with the anodic areas.
- Experimentally determine the distribution of chromate released from a chromate coating system into a fastener crevice as a function of time using inductive coupled plasma-optical emission spectroscopy (ICP-OES). Compare the concentration profile to the concentrations utilized in this work. The polarization data generated on the electrodes for each chromate concentration as a function of environment could serve as boundary conditions for modeling the damage distribution along AA7050-316SS fastener crevice as a function of time.